Stockholm
University

From irrotational flows to turbulent dynamos

Fabio Del Sordo

Cover image: The Stockholm Archipelago seen from Storholmen.
(Photo: Fabio Del Sordo, June 2011)

ISBN 978-91-7447-573-9

Printed in Sweden by Universitetsservice, US-AB, Stockholm 2012
Distributor: Department of XX, Stockholm University

If you have built castles in the air,
your work need not be lost;
that is where they should be.
Now put the foundations under them.
(Henry David Thoreau - Walden)

O' assaje finisc'
e o' poc' bast'
(Popular saying)

To my roots and foundations,
Antonella, Tino e Sara

Abstract

Many of the celestial bodies we know are found to be magnetized: the Earth, many of the planets so far discovered, the Sun and other stars, the interstellar space, the Milky Way and other galaxies. The reason for that is still to be fully understood, and this work is meant to be a little step in that direction.

The dynamics of the interstellar medium is dominated by events like supernovae explosions that can be modelled as irrotational flows. The first part of this thesis is dedicated to the analysis of some characteristics of these flows, in particular how they influence the typical turbulent magnetic diffusivity of a medium, and it is shown that the diffusivity is generally enhanced, except for some specific cases such as steady potential flows, where it can be lowered. Moreover, it is examined how such flows can develop vorticity when they occur in environments affected by rotation or shear, or that are not barotropic.

Secondly, we examine helical flows, that are of basic importance for the phenomenon of the amplification of magnetic fields, namely the dynamo. Magnetic helicity can arise from the occurrence of an instability: here we focus on the instability of purely toroidal magnetic fields, also known as Tayler instability. It is possible to give a topological interpretation of magnetic helicity. Using this point of view, and being aware that magnetic helicity is a conserved quantity in non-resistive flows, it is illustrated how helical systems preserve magnetic structures longer than non-helical ones.

The final part of the thesis deals directly with dynamos. It is shown how to evaluate dynamo transport coefficients with two of the most commonly used techniques, namely the imposed-field and the test-field methods. After that, it is analyzed how dynamos are affected by advection of magnetic fields and material away from the domain in which they operate. It is demonstrated that the presence of an outflow, like stellar or galactic winds in real astrophysical cases, alleviates the so-called catastrophic quenching, that is the damping of a dynamo in highly conductive media, thus allowing the dynamo process to work better.

Contents

Foreword

If we shadows have offended,
Think but this, and all is mended,
That you have but slumbered here
While these visions did appear.

(Puck, in "A Midsummer Night's Dream")

Many astrophysical bodies are nowadays known to be cradles of magnetic fields: in their cradles they grow and change. Two classes of phenomena are responsible for their evolution: dissipation and amplification. The latter is named dynamo. The evolution of magnetic fields is influenced by turbulence, which occurs in many astrophysical contexts. This work deals with problems related to the study of magnetic fields, dynamos and turbulent transport in astrophysics, with a special focus on the interstellar medium. It is divided into four parts.

- Chapter 1 introduces the essentials of the physics that will be used in the rest of the thesis: basic concepts of magnetohydrodynamics, mean-field theory and mean-field diffusivities. These topics are among the subjects of **Paper I**, that deal, for the first time, with their applications to irrotational flows.
- Chapter 2 brings us from irrotational flows to irrotationally forced flows, in which vorticity could be produced. Such a forcing resembles the action of supernova explosions in the interstellar medium. After seeing how these events can develop vorticity through the interaction with rotation, shear, and baroclinicity (**Paper II**) we return to the mean-field point of view on some aspect of irrotational flows and magnetic fields transport (**Paper I**). It was known that the turbulent magnetic diffusivity should be negative for purely irrotational forcing, but now we show that this is only true on large length scales and for the rare case of stationary flows.
- Chapter 3 focuses on magnetic helicity, a basic element in large-scale dynamos. In **Paper III** it is shown how a non-helical system can evolve into a helical one through the occurrence of an instability. In particular, we address the case of the global instability of toroidal fields, namely the Tayler instability. We study an example of spontaneous symmetry breaking that leads to the spontaneous formation of helical structures during its early nonlinear evolution. This system is then modeled quantitatively through amplitude equations that characterize the nature of the symmetry breaking in our case. Then we study how magnetic helicity evolves during the decay of interlocked flux rings configurations.

This is done in **Paper IV** through a topological interpretation of helicity. It is demonstrated that helical systems preserve magnetic structures longer than non-helical ones – even though both are interlinked in seemingly similar ways.

- Finally, in Chapter 4 we present examples of dynamos at work. These dynamos are a consequence of a forced turbulent flow. We begin by reviewing in **Paper V** the application of the so-called test-field method to dynamo problems, and emphasize its validity in the nonlinear case. **Paper VI** discusses one of the problems that can arise in the evaluation of the dynamo coefficients in numerical simulations by comparing two ways to measure the so-called α effect. It is shown that the commonly used method of imposing a uniform magnetic field, also known as imposed-field method, can produce up to 4 different results. None of such results give the physically relevant set of coefficients that can be obtained by applying the test-field method and resetting the fluctuations to zero, over regular time intervals, the fluctuating meso-scale dynamo-generated fields. The occurrence of such fields on the scale of the investigated domain is indeed found to be the cause of errors arising when using the imposed-field method.

  We then turn to a more realistic application of dynamos. It is known that many astrophysical bodies are characterized by outflows of material from the domain in which the dynamo operates; turbulent dynamos can be affected by such outflows. It is also known that systems with high magnetic Reynolds numbers are affected by the 'catastrophic quenching,' which means that the dynamo is adversely affected with increasing magnetic Reynolds number. How do outflows influence such a quenching? This topic is addressed in **Paper VII**, where we measure magnetic helicity fluxes and show that they become important for magnetic Reynolds numbers above one thousand and begin to alleviate catastrophic quenching. This requires a numerical resolution of $1024 \times 1024 \times 2048$ meshpoints in our elongated domain covering part of a turbulent disk on both sides of the equator.

List of Papers

The following papers, referred to in the text by their Roman numerals, are included in this thesis.

Turbulent transport and vorticity production for potential flows

I. Rädler, K.-H., Brandenburg, A., **Del Sordo, F.**, & Rheinhardt, M.: 2011, "Mean-field diffusivities in passive scalar and magnetic transport in irrotational flows," *Phys. Rev. E* **84**, 4

II. **Del Sordo, F.**, & Brandenburg, A.: 2011, "Vorticity production through rotation, shear and baroclinicity," *Astron. Astrophys.*, **528**, A145

Spontaneous helicity production and conservation

III. Bonanno, A., Brandenburg, A., **Del Sordo, F.**, & Mitra, D.: 2012, "Breakdown of chiral symmetry during saturation of the Tayler instability," *Phys. Rev. E* **86**, 016313

IV. **Del Sordo, F.**, Candelaresi, S., & Brandenburg, A.: 2010, "Magnetic field decay of three interlocked flux rings with zero linking number," *Phys. Rev. E* **81**, 036401

Turbulent dynamo and dynamo transport coefficients

V. Brandenburg, A., Chatterjee, P., **Del Sordo, F.**, Hubbard, A., Käpylä, P. J., & Rheinhardt, M. "Turbulent transport in hydromagnetic flows," *Phys. Scr. 2010, T142, 014028*

VI. Hubbard, A., **Del Sordo, F.**, Käpylä, P. J., & Brandenburg, A.: 2009, "The α effect with imposed and dynamo-generated magnetic fields," *Monthly Notices Roy. Astron. Soc.* **398**, 1891–1899

VII. **Del Sordo, F.**, Guerrero, G., & Brandenburg, A.: 2012, "Turbulent dynamo with advective magnetic helicity flux," *Monthly Notices Roy. Astron. Soc.*, submitted, arXiv:1205.3502

Papers not included in the thesis

1. Dosopoulou, F., Del Sordo, F., Tsagas, C. G., & Brandenburg A. : 2012, "Vorticity production and survival in viscous and magnetized cosmologies," *Phys. Rev. D* **85**, 063514

Conference papers not included in the thesis

1. Brandenburg, A., & Del Sordo, F.: 2010, "Turbulent diffusion and galactic magnetism," in *Highlights of Astronomy, Vol.* **15**, ed. E. de Gouveia Dal Pino, CUP, pp. 432-433 , Vol 15
2. Candelaresi, S., Del Sordo, F., & Brandenburg, A.: 2011, "Influence of Magnetic Helicity in MHD," in *Astrophysical Dynamics: from Stars to Galaxies*, ed. IAU Symp. 271, N. Brummell and A.S. Brun, pp. 369-370
3. Cantiello, M., Braithwaite, J., Brandenburg, A., Del Sordo, F., Käpylä, P., & Langer, N.: 2011, "3D MHD simulations of subsurface convection in OB stars," in *Active OB stars: structure, evolution, mass loss and critical limits*, ed. IAU Symp. 272, C. Neineret al., pp. 32-37
4. Del Sordo, F., & Brandenburg, A.: 2011, "Vorticity from irrotationally forced flow," in *Astrophysical Dynamics: from Stars to Galaxies*, ed. IAU Symp. 271, N. Brummell and A.S. Brun, pp. 375-376
5. Cantiello, M., Braithwaite, J., Brandenburg, A., Del Sordo, F., Käpylä, P., & Langer, N.: 2011, "Turbulence and magnetic spots at the surface of hot massive stars," in *Physics of Sun and Starspots*, ed. IAU Symp. 273, D.P. Choudhary & K.G. Strassmeier, pp. 200-203
6. Candelaresi, S., Del Sordo, F., & Brandenburg, A.: 2011, " Decay of trefoil and other magnetic knots," in *Advances in Plasma Astrophysics*, ed. IAU Symp. S274, A. Bonanno, E. de Gouveia dal Pino, & A. Kosovichev, pp. 461-463 , Vol. 6
7. Del Sordo, F., & Brandenburg, A.: 2011, "How can vorticity be produced in irrotationally forced flows?," in *Advances in Plasma Astrophysics*, ed. IAU Symp. 274, A. Bonanno, de Gouveia dal Pino, & A. Kosovichev, pp. 373-375 Vol. 6
8. Del Sordo, F., Bonanno, A., Brandenburg, A., & Mitra, D.: 2012, "Spontaneous chiral symmetry breaking in the Tayler instability," in *Comparative Magnetic Minima: Characterizing quiet times in the Sun and stars*, ed. IAU Symp. S286, C. H. Mandrini in press

Reprints were made with permission from the publishers.

My contribution to the papers

- **Paper I**: I contributed to it running simulations of irrotational flow using a setup coming from the work made in **PaperII**.

- **Paper II**: I shared the work with my supervisor since the beginning. I have set up the different cases to be studied, I performed the analysis and wrote extensive parts of the paper.

- **Paper III**: I was in charge of running all the numerical simulations and analyze them, I also wrote a big part of the paper and made all the plots.

- **Paper IV**: It came out during some discussion in a course on solar physics. I had the idea to study the setup and the configuration described in the paper, then I run some of the simulations and wrote extensive part of the introduction and the results.

- **Paper V**is a review paper on turbulent transport to which I contributed writing part of the introduction.

- **Paper VI**: It was done at the very beginning of my PhD. I helped in running some of the simulations and took the occasion for learning much about the code. Then I also contribute in some parts of the text.

- **Paper VII**: It was born from a common idea with the co-authors and I run many of the simulations, wrote extensive parts of the paper and made almost all the figures.

1. Magnetized interstellar gases

All that you touch
And all that you see
All that you taste
All you feel

(Pink Floyd - "Eclipse")

1.1 Why bother about magnetic fields?

The first celestial body we know of is the spaceship that is carrying us through the space-time, namely the Earth. And it is known that it is magnetized, since much earlier than the discovery of any other cosmic magnetic field.

William Gilbert was the first, in his six-volume treatise *De Magnete, Magneticisque Corporibus, et de Magno Magnete Tellure* (1600), to say that the Earth possesses a dipolar magnetic field. The magnetic flux density at the poles is about 0.6 G (gauss). Then, at the beginning of the 20th century, Hale (1908) had the idea that some line splitting observed in sunspot spectra might have been a consequence of the presence of magnetic fields in the Sun via the Zeeman-effect. After that, in the late forties, observations of Zeeman splitting led to the discovery of magnetic fields on stars of spectral type A. Later on, a similar discovery was made for stars in the late stages of their evolution, like white dwarfs. These stars showed very strong magnetic fields, up to 10^8 G, that is five orders of magnitude higher than those observed in sunspots. Even stronger, of the order of 10^{12} G, are the fields observed in neutron stars. During the last decades of the 20th century, thanks to spacecraft missions, magnetic fields have been found to be harboured by all the planet of the solar system, with strengths ranging from 10^{-4} to 10 G. Recently also exoplanets have been found to be magnetized – see for instance Fares et al. (2012).

Dealing with magnetic fields of much larger objects, like galaxies, is possible mainly through the detection of the Faraday effect, or Faraday rotation. When passing through a magnetized medium, the plane of polarization rotates in proportion to the component of the magnetic field in the direction of propagation. Thus the interstellar medium (hereafter ISM) is measured to have fields of the order of 10^{-5} G.

So, it seems that almost anywhere in the known universe there are magnetic fields. The Universe is full of electrically charged particles, located in low densities plasmas with very large mean-free paths and, therefore, with high electrical conductivities. We will see that, whenever a magnetic field happens to exist, the only way to get rid of it is to let it decay via dissipation. This is a very slow process, which would be accelerated by turbulence, but turbulence also regenerates magnetic fields through the dynamo process, which will be introduced next.

1.2 A glimpse into hydro- and magneto-hydrodynamics

1.2.1 Hydrodynamics

Since we will deal with fluids throughout this thesis, let us briefly introduce the mathematical tools that will be used. A fluid is an assembly of microscopic particles that, when under the action of stress, offers no resistance to it in the initial stages of its deformations.

It is possible to describe a *continuum* as a fluid when there is good scale-separation. This means that the fluid description works on length scales that are much bigger than those typical of the interactions of the microscopic particles, but much smaller than the global scales of the systems.

The Newtonian mechanics for such systems can be rewritten as follows:

$$\frac{\partial \rho}{\partial t} + \boldsymbol{\nabla} \cdot (\rho \boldsymbol{U}) = 0, \tag{1.1}$$

is the continuity equation, expressing the conservation of mass, where ρ is the density and $\boldsymbol{U}$ the velocity of the fluid. In the case of a fluid with constant density, we are in the so-called incompressible case, for which eq. (1.1) becomes

$$\boldsymbol{\nabla} \cdot \boldsymbol{U} = 0. \tag{1.2}$$

The momentum equation, also known as the Navier-Stokes equation, is

$$\frac{\mathrm{D}\boldsymbol{U}}{\mathrm{D}t} = -\rho^{-1}\boldsymbol{\nabla} p + \boldsymbol{g} + \rho^{-1}\boldsymbol{\nabla} \cdot (2\rho\nu\mathsf{S}) + \boldsymbol{F}_{\mathrm{ext}}, \tag{1.3}$$

where ν is the kinematic viscosity,

$$\mathsf{S}_{ij} = \tfrac{1}{2}(U_{i,j} + U_{j,i}) - \tfrac{1}{3}\delta_{ij}U_{k,k} \tag{1.4}$$

is the traceless rate of strain tensor (commas indicate partial differentiation), p is the pressure, $\boldsymbol{g}$ the gravitational acceleration and $\boldsymbol{F}_{\mathrm{ext}}$ an external force, which acts on the fluid. The expression $\mathrm{D}/\mathrm{D}t = \partial/\partial t + \boldsymbol{U} \cdot \boldsymbol{\nabla}$ is called the Lagrangian derivative, that is a derivative with respect to the co-moving fluid.

Comparing the advective term $\boldsymbol{U}\cdot\boldsymbol{\nabla}\boldsymbol{U}$ with the viscous term $\nu\boldsymbol{\nabla}^2\boldsymbol{U}$, one has:

$$\frac{|\boldsymbol{U}\cdot\boldsymbol{\nabla}\boldsymbol{U}|}{|\nu\boldsymbol{\nabla}^2\boldsymbol{U}|} \approx \frac{u_0^2}{L}\bigg/\frac{\nu u_0}{L^2} = \frac{Lu_0}{\nu} \equiv \mathrm{Re}, \tag{1.5}$$

where u_0 is a typical velocity and L a typical length of the system. The ratio of these two terms is defined as the *Reynolds number* $\mathrm{Re} = Lu_0/\nu$ and it will be widely used in the rest of this work. We define

$$\mathrm{Re} = u_{\mathrm{rms}}/\nu k_{\mathrm{f}}, \tag{1.6}$$

where u_{rms} is the root-mean-square velocity of a system and k_{f} is the inverse length scale on which turbulent motions are driven.

1.2.2 Magnetohydrodynamics

When we are studying a fluid which is electrically conducting, but globally neutral, and its flow is non-relativistic, we are dealing with classical magnetohydrodynamics (hereafter MHD). The origin of MHD is based on Maxwell's equations for the magnetic field $\boldsymbol{B}$ and the electric field $\boldsymbol{E}$

$$\boldsymbol{\nabla}\cdot\boldsymbol{E} = \frac{\rho_e}{\varepsilon_0} \quad , \quad \text{[Gauss' law]} \tag{1.7}$$

$$\boldsymbol{\nabla}\cdot\boldsymbol{B} = 0 \quad , \quad \text{[No magnetic monopoles]} \tag{1.8}$$

$$\boldsymbol{\nabla}\times\boldsymbol{E} = -\frac{\partial\boldsymbol{B}}{\partial t} \quad , \quad \text{[Faraday's law]} \tag{1.9}$$

$$\boldsymbol{\nabla}\times\boldsymbol{B} = \mu_0\boldsymbol{J} + \mu_0\varepsilon_o\frac{\partial\boldsymbol{E}}{\partial t} \quad , \quad \text{[Ampere's and Maxwell's law]}, \tag{1.10}$$

where ρ_e is the charge density, ε_0 the vacuum permittivity and μ_0 the vacuum permeability. The speed of light is defined as $c = 1/\sqrt{\varepsilon_0\mu_0}$.

Using (1.7)–(1.10) and the equations in Sect. 1.2.1 we have the basic equations of MHD

$$\frac{\partial\boldsymbol{B}}{\partial t} = \boldsymbol{\nabla}\times(\boldsymbol{U}\times\boldsymbol{B} - \eta\mu_0\boldsymbol{J}) \quad , \quad \text{[Induction]} \tag{1.11}$$

$$\frac{\mathrm{D}\rho}{\mathrm{D}t} + \rho\boldsymbol{\nabla}\cdot\boldsymbol{U} = 0 \quad , \quad \text{[Continuity]} \tag{1.12}$$

$$\frac{\mathrm{D}\boldsymbol{U}}{\mathrm{D}t} = -\rho^{-1}\boldsymbol{\nabla}p + \boldsymbol{g} + \boldsymbol{F}_{\mathrm{visc}} + \rho^{-1}\boldsymbol{J}\times\boldsymbol{B} + \boldsymbol{F}_{\mathrm{ext}} \quad , \quad \text{[Momentum]} \tag{1.13}$$

where $\boldsymbol{J} = \boldsymbol{\nabla}\times\boldsymbol{B}/\mu_0$ is the current density, $\eta = 1/\mu_0\sigma$ the magnetic diffusivity, σ is the conductivity, $\boldsymbol{J}\times\boldsymbol{B}$ is the Lorentz force, $\boldsymbol{F}_{\mathrm{visc}} = \rho^{-1}\boldsymbol{\nabla}\cdot(2\rho\nu\mathsf{S})$ is the viscous force and the displacement current $\partial\boldsymbol{E}/\partial t$ has been dropped in favor of the much larger $\mu_0 \boldsymbol{J}$ term. Also in this case we can obtain a nondimensional number, this time comparing the inductive term $\boldsymbol{\nabla} \times (\boldsymbol{U} \times \boldsymbol{B})$ with the dissipative term $-\boldsymbol{\nabla} \times (\eta \mu_0 \boldsymbol{J}) = \eta \boldsymbol{\nabla}^2 \boldsymbol{B}$:

$$\frac{|\boldsymbol{\nabla} \times (\boldsymbol{U} \times \boldsymbol{B})|}{|\eta \boldsymbol{\nabla}^2 \boldsymbol{B}|} \approx \frac{u_0 B_0}{L} \bigg/ \frac{\eta B_0}{L^2} = \frac{u_0 L}{\eta} \equiv \mathrm{Re_M}. \tag{1.14}$$

The ratio of these two terms is called the *magnetic Reynolds number* $\mathrm{Re_M} = L u_0 / \eta$ and in our work is defined in terms of u_{rms} and k_{f} as

$$\mathrm{Re_M} = u_{\mathrm{rms}} / \eta k_{\mathrm{f}} \tag{1.15}$$

Both the definitions of Re and $\mathrm{Re_M}$ can result in values that are actually different from the ratio of the advective and viscous terms (Re) and the inductive and dissipative term ($\mathrm{Re_M}$). Chatterjee et al. (2011b) found that the discrepancies between the two values are within the 20% in numerical simulations in which the turbulence is driven only by a hydromagnetic instability (see Sect. 3) and with $\mathrm{Re} \lesssim 10$.

A concept that will be used is that of *equipartition*. Saying that a magnetic field is at equipartition means that the magnetic energy and the kinetic energy of the fluid are of the same order of magnitude, that is

$$\frac{\boldsymbol{B}^2}{2\mu_0} = \frac{1}{2} \rho \boldsymbol{U}^2. \tag{1.16}$$

Correspondingly, we define the so-called equipartition field strength as the volume average $B_{\mathrm{eq}} = \langle \mu_0 \rho \boldsymbol{u}^2 \rangle^{1/2}$, which is often used to express $\boldsymbol{B}$ in units of B_{eq}.

Throughout this work we solve the non-linear partial differential equations of hydrodynamics and MHD numerically using the PENCIL CODE[1], a high-order finite difference PDE solver.

1.3 Turning kinetic into magnetic energy: the dynamo

A dynamo is a flow that can sustain magnetic field against Ohmic dissipation. Through a dynamo, kinetic energy is transformed into magnetic energy.

Most dynamos allow growth from a weak initial seed magnetic field until some saturation level is reached. There are also dynamos whose velocity field is driven by the interaction with the magnetic field itself. An example is the magneto-rotational instability (Balbus and Hawley, 1991), which can lead to reinforcing the magnetic field by dynamo action (Brandenburg et al., 1995; Hawley et al., 1996; Stone et al., 1996).

At a first glance, dynamo problems can be divided in two classes:

---

[1] http://pencil-code.googlecode.com

- The kinematic dynamo problem, in which the velocity field $\boldsymbol{U}$ is given *a priori* and does not suffer any back-reaction from the subsequently amplified magnetic field;
- The full dynamo problem, where the flow has to be identified as a solution of the full set of MHD equations.

Magnetic fields exist either through permanent magnetization or through electric currents. In the first case magnetic fields are stationary: this is a feature that is rarely found in astrophysical objects, because their temperatures are well above the Curie point, i.e. they cannot behave as ferromagnets. This is the main reason for thinking that electric currents from the motion of charged particles are responsible for astrophysical fields, from planets to stars and galaxies.

The main idea of dynamo theory is that a magnetic field can be amplified through self-excitation. In 1854, for the first time, Søren Hjort proposed the idea that conducting matter can possibly carry electric currents when in motion and can so amplify pre-existent fields. After a few years, Samuel Alfred Varley, Ernst Werner von Siemens and Charles Wheatstone announced independently the same discovery (for further details see Brandenburg, 2011).

This was the beginning of the so-called dynamo theory. Translated into mathematics, looking for a dynamo means to find an exponentially growing solution of eq. (1.11). Equation (1.11) illustrates how the time evolution of a magnetic field depends on the velocity of the medium as well as the magnetic field itself and its back-reaction on the flow. It also tells us that when having a strictly vanishing magnetic field initially, it cannot experience any growth by induction. A dynamo is in fact a process of amplification of a field rather than one of generation.

What happens when a dynamo is acting? In its basic picture, a field line rises, stretches and twists and can form a loop. Let us take the example of a cartoon-like galactic environment to see the consequences of this. In a galaxy, turbulence is present since its formation. Cyclonic motions arise because of stratification and the Coriolis force due to the galactic rotation. In such a way toroidal fields, that is fields in the azimuthal direction of a galaxy, can be transformed into a poloidal fields, as was pointed out by Parker (1955). The scale for this phenomenon to happen is that of the largest turbulent eddies. This effect is also known as α effect. On the other hand we have the so-called Ω effect: differential azimuthal rotation produces toroidal fields from poloidal ones. In most of the cases in astrophysics the general assumption is that the magnetic field satisfies the so-called "frozen-in" condition. This means that a magnetic line moves along with a flow line. This is an approximation that can be made in the cases of a perfectly conducting fluid: motions along the field lines do not change the structure of the magnetic field. Instead, when the flow

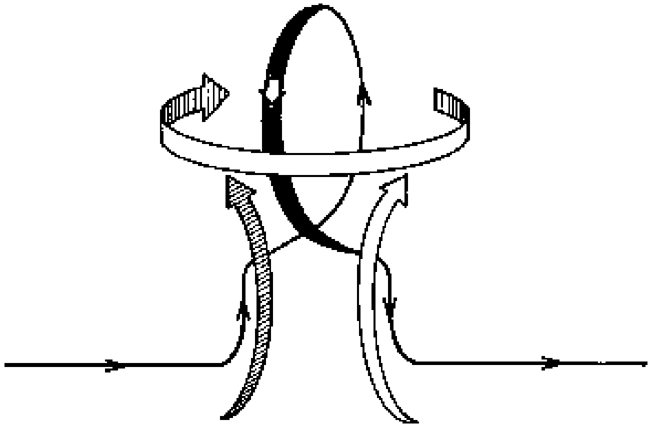

Figure 1.1: A schematic representation of the α-effect: a field line rises and twists creating an α-like structure, thus generating a radial component from an azimuthal one. (Figure from Parker (1970).)

lines move transversely to the field lines they carry the magnetic field along with them. In terms of the MHD equations we can write such a condition as

$$\boldsymbol{E} = -\boldsymbol{U} \times \boldsymbol{B}. \tag{1.17}$$

In general, however, the effect of magnetic diffusion has to be considered, especially when we deal with dynamos and reconnection. In some situations, and especially at small scales, the frozen-in condition is not valid.

With the frozen-in condition holding, the α and Ω effects can be easily illustrated. In fact, the field lines follow the flow of matter: they can stretch, twist and raise, giving thereby birth to tangled lines from straight ones, and so to radial components from and azimuthal ones and vice-versa, like in Fig. 1.1. Equation (1.11) shows indeed that one of the factors determining the time evolution of the magnetic field is the velocity field. However it is important to point out that these effects can take place also in the case in which diffusion is important, that is the case of finite Reynolds number, although in this case they are less efficient in producing a dynamo.

1.4 Mean-field theory and dynamo action

The typical theoretical framework through which an MHD dynamo is described is the so-called mean-field theory (Krause and Rädler, 1980; Moffatt, 1978; Parker, 1955). The main idea of mean-field theory is that turbulent systems, of which MHD dynamos are an example, can be studied using a two-scale approach, where velocities and magnetic fields are decomposed into mean and fluctuating components:

$$\boldsymbol{U} = \overline{\boldsymbol{U}} + \boldsymbol{u} \quad \text{and} \quad \boldsymbol{B} = \overline{\boldsymbol{B}} + \boldsymbol{b}. \tag{1.18}$$

In the following, we assume that the Reynolds rules hold, in particular $\overline{\overline{\boldsymbol{U}} \times \boldsymbol{b}} = \overline{\boldsymbol{u} \times \overline{\boldsymbol{B}}} = 0$ and $\overline{\overline{\boldsymbol{U}} \times \overline{\boldsymbol{B}}} = \overline{\boldsymbol{U}} \times \overline{\boldsymbol{B}}$. The mean parts $\overline{\boldsymbol{U}}$ and $\overline{\boldsymbol{B}}$ generally vary slowly both in space and time, compared with other features of the system under consideration, and describe the global, and often the more prominent behavior of the system. On the other side we define as fluctuating fields those components that describe irregular, often chaotic, small-scale effects. Using the aforementioned decomposition, eq. (1.11) can be averaged to obtain an equation for $\partial\overline{\boldsymbol{B}}/\partial t$, which, in turn, can be subtracted from eq. (1.11) to obtain an equation for $\partial\boldsymbol{b}/\partial t$. We thus obtain a set of two equations for the mean and fluctuating quantities,

$$\frac{\partial\overline{\boldsymbol{B}}}{\partial t} = \boldsymbol{\nabla} \times \left(\overline{\boldsymbol{U}} \times \overline{\boldsymbol{B}}\right) + \nabla \times \overline{\boldsymbol{\mathcal{E}}} + \eta\nabla^2\overline{\boldsymbol{B}}, \tag{1.19}$$

$$\frac{\partial\boldsymbol{b}}{\partial t} = \boldsymbol{\nabla} \times \left(\overline{\boldsymbol{U}} \times \boldsymbol{b}\right) + \boldsymbol{\nabla} \times \left(\boldsymbol{u} \times \overline{\boldsymbol{B}}\right) + \boldsymbol{\nabla} \times \boldsymbol{\mathcal{E}}' + \eta\nabla^2\boldsymbol{b}, \tag{1.20}$$

where $\boldsymbol{\mathcal{E}} \equiv \boldsymbol{u} \times \boldsymbol{b}$ is the electromotive force and $\boldsymbol{\mathcal{E}}' = \boldsymbol{\mathcal{E}} - \overline{\boldsymbol{\mathcal{E}}}$ is the fluctuating part. One of the goals of this description is to write $\overline{\boldsymbol{\mathcal{E}}}$ in terms of the mean-field $\overline{\boldsymbol{B}}$. To obtain the desired relation one can consider the underlying symmetries that constrain the form of this relation. Let us take the example of a homogeneous system and assume that the turbulence is isotropic, but lacking mirror symmetry. Under such conditions the vector $\overline{\boldsymbol{\mathcal{E}}}$ can have components both along the mean magnetic field $\overline{\boldsymbol{B}}$ and along the mean current density $\overline{\boldsymbol{J}} = \boldsymbol{\nabla} \times \overline{\boldsymbol{B}}/\mu_0$. Ignoring higher order spatial and time derivatives, one can write

$$\overline{\boldsymbol{\mathcal{E}}} = \alpha\overline{\boldsymbol{B}} - \eta_{\mathrm{t}}\mu_0\overline{\boldsymbol{J}}. \tag{1.21}$$

The coefficients linking correlations such as $\overline{\boldsymbol{\mathcal{E}}}$ to mean quantities such as $\overline{\boldsymbol{B}}$ and $\overline{\boldsymbol{U}}$ are named mean-field transport coefficients, with each one describing a distinct physical effect. In eq. (1.21), α quantifies the α effect, described qualitatively in Sect. 1.3, while η_{t} quantifies the turbulent diffusion of the mean magnetic field and it is called *turbulent magnetic diffusivity*. It has been shown both theoretically and through numerical simulations (Sur et al., 2007b) that the transport coefficients α and η_{t} are proportional to the magnetic Reynolds number if this is below unity and constant with $\alpha \approx \alpha_0 \equiv -u_{\mathrm{rms}}/3$ and $\eta_{\mathrm{t}} \approx \eta_{\mathrm{t0}} \equiv u_{\mathrm{rms}}/3k_{\mathrm{f}}$ for the fully helical case with positive helicity. Here, k_{f} is the wavenumber of the energy-carrying eddies, i.e., roughly where the kinetic energy spectrum has its peak.

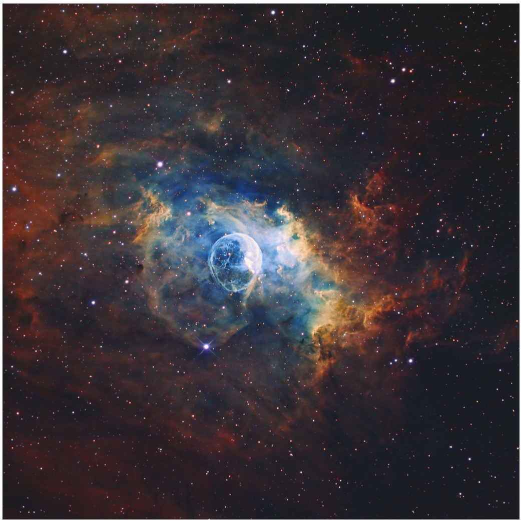

Figure 1.2: The bubble Nebula, NGC 7635 is a H II (ionized atomic hydrogen) region emission nebula in the constellation Cassiopeia. The bubble is created by a strong stellar wind whose origin is in the hot central star SAO 20575. (Image Credit & Copyright: Larry Van Vleet.)

1.5 Mean-field diffusivities

The induction equations (1.19) and (1.20), governing respectively the mean and fluctuating magnetic fields in an electrically conducting fluid contain diffusion terms with the magnetic diffusivity η. In the mean-field induction equation there appears for isotropic turbulence, $\eta + \eta_\mathrm{t}$ in place of η, where the turbulent magnetic diffusivity η_t, introduced in eq. (1.21), is determined by the turbulent motions.

Equation (1.20) contains terms that can sometimes be neglected. When we are in the low conductivity limit for small magnetic Reynolds number, $\mathrm{Re}_\mathrm{M} = UL/\eta \ll 1$, or in the high conductivity limit for small Strouhal number, $\mathrm{St} = U\tau_\mathrm{c}/L \ll 1$ (where τ_c indicates a characteristic correlation time of the turbulence), we can ignore $\boldsymbol{\nabla} \times \boldsymbol{\mathcal{E}}'$ in eq. (1.20). Under this approximation, known as SOCA (Second Order Correlation Approximation) or FOSA (First Order Smoothing Approximation), eq. (1.20) takes the form

$$\frac{\partial \boldsymbol{b}}{\partial t} = \boldsymbol{\nabla} \times \left(\overline{\boldsymbol{U}} \times \boldsymbol{b}\right) + \boldsymbol{\nabla} \times \left(\boldsymbol{u} \times \overline{\boldsymbol{B}}\right) + \eta \nabla^2 \boldsymbol{b} \tag{1.22}$$

and it is possible to perform an analytical calculation of the transport coefficients (e.g. Krause and Rädler, 1980; Rädler and Rheinhardt, 2007). Under the assumptions $\boldsymbol{\nabla}\cdot\boldsymbol{u}=0$ and $\overline{\boldsymbol{U}}=0$, this yields in the high conductivity limit

$$\alpha=-\frac{\tau_{\rm c}}{3}\overline{\boldsymbol{\omega}\cdot\boldsymbol{u}},\quad \eta_{\rm t}=\frac{\tau_{\rm c}}{3}\overline{\boldsymbol{u}^2}, \tag{1.23}$$

where $\boldsymbol{\omega}=\boldsymbol{\nabla}\times\boldsymbol{u}$ is the vorticity of the fluctuating velocity, and in the low conductivity limit

$$\alpha=-\frac{1}{3\eta}\overline{\boldsymbol{\psi}\cdot\boldsymbol{u}},\quad \eta_{\rm t}=\frac{1}{3\eta}\overline{\boldsymbol{\psi}^2}, \tag{1.24}$$

where $\boldsymbol{\psi}$ is the vector potential of $\boldsymbol{u}=\boldsymbol{\nabla}\times\boldsymbol{\psi}$ in the Coulomb gauge $\boldsymbol{\nabla}\cdot\boldsymbol{\psi}=0$. Even though neither $\mathrm{St}\ll 1$ nor $\mathrm{Re}_{\rm M}\ll 1$ apply directly to virtually any astrophysical environment, it gives an analytical expression for the transport coefficient, that are otherwise possible to know only via numerical simulations.

At first glance it seems plausible that turbulence enhances the effective diffusion, with positive $\eta_{\rm t}$. In a compressible fluid, however, this is not always true. A counter example for the magnetic case has long been known. Represent the compressible velocity field in the form

$$\boldsymbol{u}=\boldsymbol{\nabla}\times\boldsymbol{\psi}+\boldsymbol{\nabla}\phi, \tag{1.25}$$

where ϕ is a scalar potential. We can define u_c, λ_c, and τ_c as characteristic magnitude, length, and time, respectively, of the velocity field. Assume that the magnetic Reynolds number $u_c\lambda_c/\eta$ is small compared to unity and that τ_c considerably exceeds the free-decay time λ_c^2/η of a magnetic structure of size λ_c. Then it turns out (Krause and Rädler, 1980; Rädler and Rheinhardt, 2007) that α remains unchanged, but

$$\eta_{\rm t}=\frac{1}{3\eta}(\overline{\boldsymbol{\psi}^2}-\overline{\phi^2})\,. \tag{1.26}$$

That is, negative $\eta_{\rm t}$ are well possible if the part of $\boldsymbol{U}$ determined by the potential ϕ dominates. Then, the mean-field diffusivity is smaller than the molecular one. By contrast, for an incompressible flow, $\boldsymbol{\nabla}\cdot\boldsymbol{u}=0$, $\eta_{\rm t}$ can never be negative, while it can never be positive for an irrotational flow eq. (2.1), $\boldsymbol{W}=\nabla\times\boldsymbol{U}=0$. This result is the main motivation of **Paper I**, and it is of some interest for modelling the turbulence in the ISM.

Another possible application of such results could be in studies of the very early Universe, where phase transition bubbles are believed to be generated in connection with the electroweak phase transition (Kajantie and Kurki-Suonio, 1986, Ignatius et al., 1994). The relevant equation of state is that of an ultra-relativistic gas with constant sound speed $c/\sqrt{3}$, where c is the speed of light. This is a barotropic equation of state, so the baroclinic term vanishes. Hence, there is no obvious source of vorticity in the (non-relativistic) bulk motion inside these bubbles so that it should be essentially irrotational. This changes, however, if there is a magnetic field of significant strength, because the resulting Lorentz force is in general not a potential one.

However, as we will see when discussing **Paper II**, even though the aforementioned astrophysical situations can be modeled by irrotationally forced flows, one has to take into account that, when rotation or shear are important or the Mach number is close to or in excess of unity and the baroclinic effect present, vorticity production becomes progressively more important.

1.6 Magnetic fields in the interstellar medium

1.6.1 The Galactic field

The first idea about the origin of the galactic magnetic field was that it had its origin prior to the formation of the galaxy, or at least the galactic disk. Later, Parker (1971) pointed out that dynamic motions would have expelled such magnetic fields on a timescale shorter than a billion years (Parker, 1970, 1971). The idea that the Galactic field was produced by a dynamo was proposed independently by Parker (1971) and Vainshtein and Ruzmaikin (1971). It would be driven by cyclonic turbulence and differential rotation of the ISM.

During the formation of the Galaxy there would have been the possibility of a Biermann battery that could lead to weak magnetic fields. Then this field has to be amplified by dynamo action, mainly powered by supernova-driven turbulence and stellar winds. In general, a battery is a mechanism that can produce electric currents from zero initial currents. The main idea behind the word “battery” is that electric currents can arise due to physical differences between positively and negatively changed particles. For example, the proton-to-electron mass ratio m_p/m_e is about 1836, but their charges have the same modulus e.

As consequence, in a gas composed of ionized hydrogen, a given pressure gradient will accelerate differently the positive and negative components, so leading to the occurrence of an electric field coupling positive and negative charges. In a two-fluid description, for a given ionization fraction χ, one needs to add a new term in eq. (1.11), that therefore reads (Brandenburg and Subramanian, 2005c)

$$\frac{\partial \boldsymbol{B}}{\partial t} = \boldsymbol{\nabla} \times (\boldsymbol{U} \times \boldsymbol{B} - \eta \mu_0 \boldsymbol{J}) - \frac{m_p}{e(1+\chi)} \frac{\boldsymbol{\nabla}\rho \times \boldsymbol{\nabla} p}{\rho^2}. \qquad (1.27)$$

The last term of the right-hand-side represents the battery, that is a source term that exists independently of the value of the initial magnetic field. This new term is similar to the baroclinic term in the equation for the evolution of vorticity – see also **Paper II**. It is described by a cross product, and therefore it is non-vanishing only if the gradients of density and pressure are not parallel to each other. This can happen, for instance, as consequence of rotation or shear. Apart from differences in the driving mechanism of the turbulence, the underlying theory of large-scale galactic magnetic field generation by turbulence was analogous to that of the Sun. That theory became widely known through the work of Steenbeck et al. (1966) a few years earlier, and is based on early work by Parker (1955). The mean-field theory of stellar and galactic dynamos continues to be an active research field, as is evidenced through the progress reviewed extensively in recent years (Beck et al., 1996, Kulsrud, 1999, Brandenburg and Subramanian, 2005c).

The ISM is a very inhomogeneous and active environment. It is subject to the action of stellar wind (see fig. 1.2 for an example) and above all because harbours star formation and death. Especially massive stars contribute to this dynamics, evolving in short (for a star!) period of time of the order of 10^6 years and ending their lives exploding as supernovae: such events release energies of the order of 10^{51} ergs. After the explosion, the remnants of the supernova remain filled with hot gas with high pressure that drives the supersonic expansion in the unperturbed interstellar gas that was surrounding the star. This expansion keeps going until the pressure inside the remnant is comparable with the pressure outside it. These explosions take places in random locations of a galaxy and act as a forcing for supersonic motions and turbulence in the ISM. They act on length scales of up to 100 pc.

The action of supernova explosions and star formation can be relevant on a galactic scale, not only for the formation of turbulence, but also generating a global galactic outflow (Mac Low and McCray, 1988, Mac Low and Ferrara, 1999). Fig. 1.2 shows an example of a galaxy in which the high star formation rate is thought to be responsible for the observed global outflow. We will see in Sect. 3 and in **Paper VII** how an outflow can affect in a decisive way the efficiency of dynamo action.

1.6.2 Observations of interstellar magnetic fields

Let us say something about magnetic fields that are observed in the ISM and in galaxies. To observe magnetic fields in a galaxy one needs to find at least one polarized background source to perform a Faraday rotation measurement, that is a measure of the angle formed by the polarization vector and the field at different radio wave lengths. This process becomes quite challenging especially for distant galaxies, mainly due to their small angular size. Intermediate redshift galaxies can occasionally lie in the line of sight of some distant quasar. In such a case a magnetic field in the galaxy might then be revealed (Stil, 2009).

In nearby spiral galaxies the average total field that is obtained from total

Figure 1.3: A starburst galaxy, M82, showing a strong wind. The red filaments that are expanding from the galactic plane are due to the effect of a galactic wind caused by the intense star formation. (Image Credit & Copyright: Dietmar Hager, Torsten Grossmann.)

synchrotron intensity ranges from $4\mu G$ in M31 up to about $15\mu G$ in M51, with a mean value of $9\mu G$ for a sample of 74 galaxies (Shukurov and Sokoloff, 2008). The ratio of energy densities between random and regular magnetic fields components is $b^2/\overline{B}^2 \simeq 3$ (Shukurov and Sokoloff, 2008). One example of a magnetic field configuration in a spiral galaxy is shown in Fig. 1.4.

In the Milky Way (or the Galaxy) it has been observed a magnetic field with a global quadrupolar parity, while this has not yet been observed elsewhere (Frick et al., 2001). The global pattern of the field is that of a spiral, similar to the spiral arms, but there is also a huge variety of structures, like magnetic arms and field reversals between discs and halo Fletcher et al. (2011). One of these reversals can be observed close to the solar system; the strength of the field nearby the Sun is $\simeq 2\mu G$, which is therefore indeed not representative of the average field of spiral galaxies. In spiral galaxies it is common that the spiral pattern is followed by the magnetic field, but the random component is usually of the same order of magnitude as the regular one. The total value of the equipartition field in the solar neighborhood is $B = 6 \pm 2\mu G$. This is obtained from the synchrotron intensity of the diffuse galactic background: using these last two values it can be argued that the local regular field $\overline{\boldsymbol{B}}$ has a strength of $4 \pm 1\mu G$, while for the random component of the total field we have $b = (B^2 - \overline{B}^2)^{1/2} = 5 \pm 2\mu G$ (Shukurov and Sokoloff, 2008). Looking at some specific cases, for the equipartition field we find 4μ G for M33, 12μ G for NGC 6946, and 19μ G for NGC 2276 (Zweibel and Heiles, 1997).

The random component of the field is in general stronger than the regular

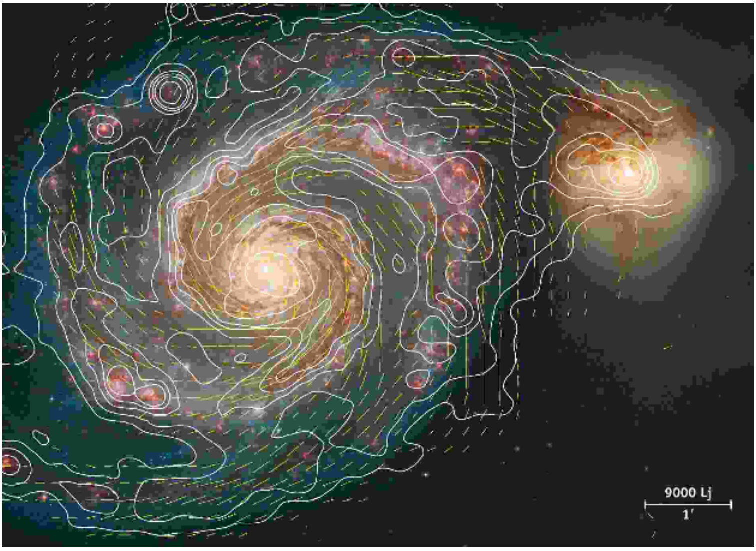

Figure 1.4: Magnetic fields mapped on an optical image of M51. The image shows the contours of the total radio intensity and polarization vectors at 6 cm wavelength, combined from radio observations. The magnetic field seems to follow rather well the optical spiral structure. However, also the regions between the spiral arms contain strong and ordered fields. (Figure from Fletcher et al. (2011).)

one. It has to be pointed out that there is a discrepancy between the $\overline{B}$ observed in the Milky Way and the one measured for other spiral galaxies. In fact, for the Galaxy we observe $\overline{B} = 1\text{–}2\mu\,\mathrm{G}$, that is, a lower value than the aforementioned ones. There could be several explanations for this problem, as showed for example by Beck et al. (2003) and Sokoloff et al. (1998). One of these could be the difference in depth probed by the total synchrotron emission and Faraday rotation measures in observations of extragalactic and galactic sources.

A few words about other types of galaxies. In barred galaxies the global configuration of the magnetic field would be expected to be different from that of spiral galaxies. Interstellar magnetic field are in fact strongly affected by the non-axisymmetric gas flow and large scale shocks. In particular the regular magnetic field might be enhanced by velocity gradients, while the dynamo action would be influenced by the presence of a bar (Beck et al., 2005).

Dwarf galaxies are the most numerous species of galaxies in the universe; nevertheless they are very difficult to be observed because they are very faint objects, especially in the radio domain. Consequently, not much is known much about the generation of magnetic fields in these galaxies. Recently, thanks to investigations of the radio emission of nearby dwarf galaxies (Chyży, 2010), a trend has been observed. Dwarf galaxies seem to have predominately weak magnetic fields, with strength of about 4 μG, that is about two or three times smaller than in normal spirals. On the other hand, recently a strong polarized emission was discovered in an optically bright dwarf galaxy, NGC 4449. In this case the strength of the total magnetic field is about 12 μG, while the regular component is about 8 μG (Chyży, 2010). These values are comparable with those related to radio-bright spirals: they are surprising large, since the structure of the galaxy itself is lacking an ordered rotation pattern that was expected to be necessary to for dynamo action. Nevertheless, rotation could play a role on scales smaller than the global one, thereby helping the dynamo process to take place. In general it is found that magnetic fields depend on the surface density through the galactic star formation rate. It is common to find, in galaxies with a regular structure, that the random component of the field is stronger than the ordered one.

2. Studies of (ir)rotational flows

I've heard it said, that we can all be defined
Only by looking twice at our past
And I agree but I'm still failing to see
Just what is there to me without my dreams?

(Viktoria Tolstoy, in "Word by Word")

2.1 Understanding how a fluid becomes vortical

The ISM is a turbulent environment whose dynamics is determined by several astrophysical processes. As explained in Sect. 1.6, the turbulence is believed to be driven mainly by supernova explosions, injecting energy that sustains turbulence with rms velocities of $\sim 10\,\mathrm{km/s}$ and correlation lengths of up to $100\,\mathrm{pc}$ (Beck et al., 1996). These supersonic events involve strong shocks in the surroundings of the explosions sites. It is therefore numerically demanding to simulate supernova explosions. Nevertheless, nowadays there are several examples of numerical models able to reproduce their physics, like the observed volume fractions of hot, warm, and cold gas (Rosen and Bregman, 1995, Korpi et al., 1999), the statistics of pressure fluctuations (Mac Low et al., 2005), the effects of the magnetic field (de Avillez and Breitschwerdt, 2005), and even dynamo action (Gressel et al., 2008, Hanasz et al., 2009, Gissinger et al., 2009).

In many of these simulations significant amounts of vorticity are being produced. Nevertheless, observing vortical structures can appear, on one hand, to be a surprising result, given that each supernova drives the gas radially outward and can be described approximatively by radial expansion waves. This way of modelling an explosion, through a time-dependent spherical blob, leads to an irrotational forcing acting on the fluid, which does not produce any vorticity.

Therefore we aim to study how vorticity is generated in irrotational flows, described by a particular case of eq. (1.25) that, when $\boldsymbol{\psi} = 0$, reads

$$\boldsymbol{U} = \boldsymbol{\nabla}\phi. \tag{2.1}$$

For a given velocity field $\boldsymbol{U}$ we can define the vorticity as its curl,

$$\boldsymbol{W} = \nabla \times \boldsymbol{U}. \tag{2.2}$$

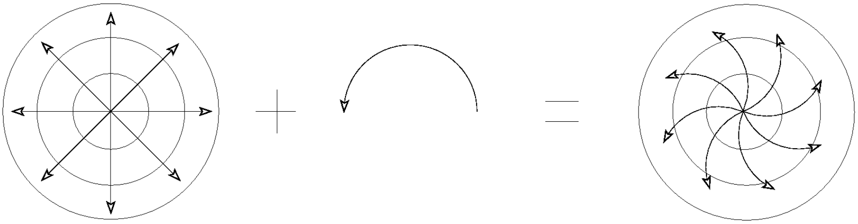

Figure 2.1: A fluid that is expanding can develop vorticity if rotating. This is the first case of vorticity generation that is studied in **Paper II**.

This definition arises from the need to quantify the rotation and the angular momentum of a fluid system. In fact, this can be done by calculating the circulation Γ on a closed path C embedded in the fluid, and using the Stokes's theorem as follows:

$$\Gamma = \int_C \boldsymbol{U}\,\mathrm{d}l = \int_S \boldsymbol{\nabla}\times\boldsymbol{U}\cdot\hat{\boldsymbol{n}}\,\mathrm{d}S = \int_S \boldsymbol{W}\cdot\hat{\boldsymbol{n}}\,\mathrm{d}S, \tag{2.3}$$

where S and $\hat{\boldsymbol{n}}$ define a surface bounded to C. For an inviscid barotropic fluid, Γ is conserved in time: this result is known as Kelvin's theorem. This means that the flux of vorticity across a surface S bounded by a closed loop C advected by the fluid is constant in time.

The evolution equation for $\boldsymbol{W}$ can be obtained by taking the curl of the Navier Stokes equation. In the incompressible case, $\boldsymbol{\nabla}\cdot\boldsymbol{U} = 0$, we have

$$\frac{D\boldsymbol{U}}{Dt} = -\boldsymbol{\nabla}\left(\frac{p}{\rho}+\Phi\right) - \boldsymbol{\nabla}\times(\nu\boldsymbol{\nabla}\times\boldsymbol{U}), \tag{2.4}$$

from which, for constant ν,

$$\frac{D\boldsymbol{W}}{Dt} = \boldsymbol{W}\cdot\boldsymbol{\nabla}\boldsymbol{U} + \nu\boldsymbol{\nabla}^2\boldsymbol{W}. \tag{2.5}$$

A more general expression for the evolution equation of $\boldsymbol{W}$ is given below in eq. (2.6) for the compressible case.

In an isothermal model, with constant viscosity ν, the general evolution equation for the vorticity is (see, e.g., Mee and Brandenburg, 2006)

$$\frac{\partial\boldsymbol{W}}{\partial t} = \boldsymbol{\nabla}\times(\boldsymbol{U}\times\boldsymbol{W} - \nu\boldsymbol{\nabla}\times\boldsymbol{W}) + \nu\boldsymbol{\nabla}\times\boldsymbol{G}. \tag{2.6}$$

Here,

$$G_i = 2\mathsf{S}_{ij}\nabla_j \ln\rho \tag{2.7}$$

is a part of the viscous force that has non-vanishing curl even when the flow is purely irrotational to begin with, and S_{ij} was defined in eq. (1.4).

Figure 2.2: Circular expansion waves in water, resembling the setup studied in **Paper II**. The water might be considered isothermal, and the waves are travelling with a very low Mach number. Indeed, at first glance no vortex is seen where wave fronts encounter each other. (Picture taken in Tyresta National Park, 2011. Credit: Fabio Del Sordo.)

Qualitatively, vorticity can arise as a consequence of the interplay between an otherwise potential velocity field and background flows. A first example is that of a fluid that is rotating around a certain axes. If a spherical expansion wave is driven in this fluid, the interplay between rotation and expansion leads to the generation of vorticity. This is sketched qualitatively in fig. 2.1. In case there is neither rotation, nor shear, nor any other thermodynamical effects, no vorticity is produced, as visible in fig. 2.2.

Mathematically one has to add the Coriolis force $2\boldsymbol{\Omega} \times \boldsymbol{U}$ to the evolution equation of the velocity field, and its curl $2\boldsymbol{\nabla} \times \boldsymbol{\Omega} \times \boldsymbol{U}$ to eq. (2.6). In **Paper II** we have examined this case, which is summarized in Fig. 2.3. The intensity of rotation can be quantified by the Coriolis number

$$\mathrm{Co} = 2\Omega\tau, \quad \text{where} \quad \tau = (u_{\mathrm{rms}} k_{\mathrm{f}})^{-1} \tag{2.8}$$

is the turnover time, that is the ratio between the length scale k_{f}^{-1} on which the forcing is acting and the root-mean-square velocity of the flow u_{rms}. It is found that, for $\mathrm{Co} \lesssim 10$, there is a linear relationship between the vorticity and rotation. In other words, the ratio $k_\omega / k_{\mathrm{f}}$ is proportional to Co, where $k_\omega = \omega_{\mathrm{rms}} / u_{\mathrm{rms}}$. The enstrophy spectra are peaked close to the value of the forcing wavenumber and decrease clearly for big values of k, that is, for small scales. In **Paper II** we also show that similar results are obtained in case there is an underlying shear flow that adds to the expansion wave.

Moreover, in **Paper II** we quantify the role played by the baroclinic term $\boldsymbol{\nabla}\rho \times \boldsymbol{\nabla}p$. This term vanishes in the isothermal case, which belongs to the class of barotropic flows for which $p \propto \rho$. This mechanism is the most efficient one among those investigated for the production vorticity. As soon as the flow becomes supersonic the vorticity shows up where shock fronts encounter each other, as illustrated in fig. 2.4. As for the dependence of vorticity on a magnetic field, Kahniashvili et al. (2012) found that the root-mean-square vorticity turns out to be approximately proportional to the magnetic energy density, up to $\mathrm{Re} \sim 250$.

In principle, vorticity could also be amplified by a dynamo effect. Indeed in the evolution equation there is the $\boldsymbol{\nabla} \times (\boldsymbol{U} \times \boldsymbol{W})$ term, which is analogous to the induction term in dynamo theory for magnetic fields. In this case $\boldsymbol{W}$ plays the role of the magnetic field. Nevertheless, so far this effect has not been observed in simulations up to numerical resolution of 512^3 meshpoints. Mee and Brandenburg (2006) showed that, under isothermal conditions, only the viscous force can produce vorticity. This vorticity becomes negligible in the limit of large Reynolds numbers or small viscosity. However, Federrath et al. (2010, 2011) have shown that this changes for Mach numbers approaching unity. The exact amount of vorticity production through the $\boldsymbol{G}$ term is still unclear, and so is the possible dependence on the numerical scheme in cases where there is no explicit viscosity.

Does the presence of vorticity affect a dynamo? Typically, the α effect in a dynamo is generated from helicity, which, in turn, is produced by the combined action of stratification and rotation. Therefore, α is directly proportional to the angular velocity which affects the fluid (Krause and Rädler, 1980). However, for the case in which the angular velocity varies spatially, Brandenburg and Donner (1997) found numerical evidence that the α effect is proportional to the vorticity of the fluid.

2.2 Passive scalar vs. magnetic field transport

A passive scalar is a contaminant that is present in a fluid flow with such low concentration that it has no dynamical effect on the motion of the fluid itself. For instance, when a person breathes out in a typical Swedish winter day, the weakly heated flow mixes in a passive scalar fashion with the cooler air that is entrained from the surroundings. Moisture mixing in air and dye in water provide other typical examples. When two chemicals are independently introduced into a fluid, turbulence provides efficient mixing that enables the reactions or combustion to occur at the molecular level (Warhaft, 2000).

The equation governing the behavior of a passive scalar in a fluid contains a diffusion term with a diffusion coefficient, say κ. In the corresponding mean-field equation there appears, in the simple case of isotropic turbulence, the effective mean-field diffusivity $\kappa + \kappa_{\mathrm{t}}$ in place of κ, where κ_{t} is determined by

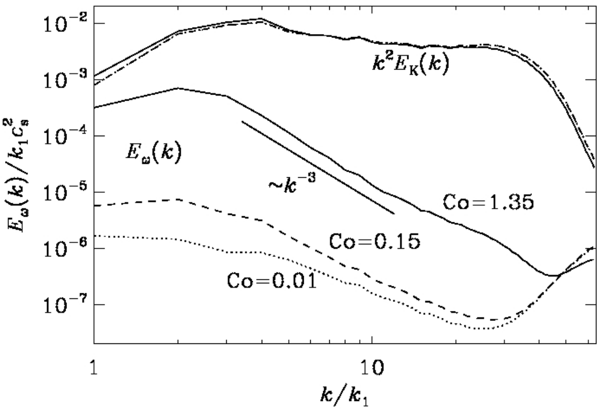

Figure 2.3: Time-averaged enstrophy spectra, $E_\omega(k)$, compared with $k^2E_K(k)$, as function of inverse wavenumber k (scaled with k_1, the smallest wavenumber of the periodic domain). The study for three values of the Coriolis number Co is here depicted. The curves of $k^2E_K(k)$ are close together and overlap for Co $=$ 0.01 (dotted) and 0.15 (dashed), so it becomes a single dash-dotted line. The k^{-3} slope is shown for comparison. In all three cases we have $k_f/k_1 = 4$.
(Figure from **Paper II**.)

the turbulent motion and therefore sometimes called *turbulent diffusivity*.

When the diffusivity κ is independent of position, a passive scalar C, describing for instance the concentration of dust or chemicals per unit volume of a fluid, satisfies

$$\frac{\partial C}{\partial t} + \boldsymbol{\nabla} \cdot (\boldsymbol{U}C) - \kappa \Delta C = 0, \tag{2.9}$$

where $\boldsymbol{U}$ is the fluid velocity. (We have here ignored the possibility that the fluid density could enter in the expression for the diffusion term.)

In **Paper I** we show that the behavior on η_t described in eq. (1.26), can be found also for κ_t, i.e. it can be negative at low Péclet numbers $\mathrm{Pe} = u_{\rm rms}/\kappa k_f$. We find, however, that there are also the requirements of good scale separation and of slow temporal variations of the flow. If these requirements are not obeyed, κ_t and η_t are no longer necessarily negative – even at small values of Péclet and magnetic Reynolds numbers. This is the reason why a reduction of the effective diffusivity has never been seen in physically meaningful compressible flows; see Brandenburg and Del Sordo (2010) for such an example, where η_t has been determined for a time-dependent, irrotationally forced turbulent flow.

A first example of the study presented in **Paper I** is shown in Fig. 2.5, where results for a homogeneous isotropic irrotational steady potential flow

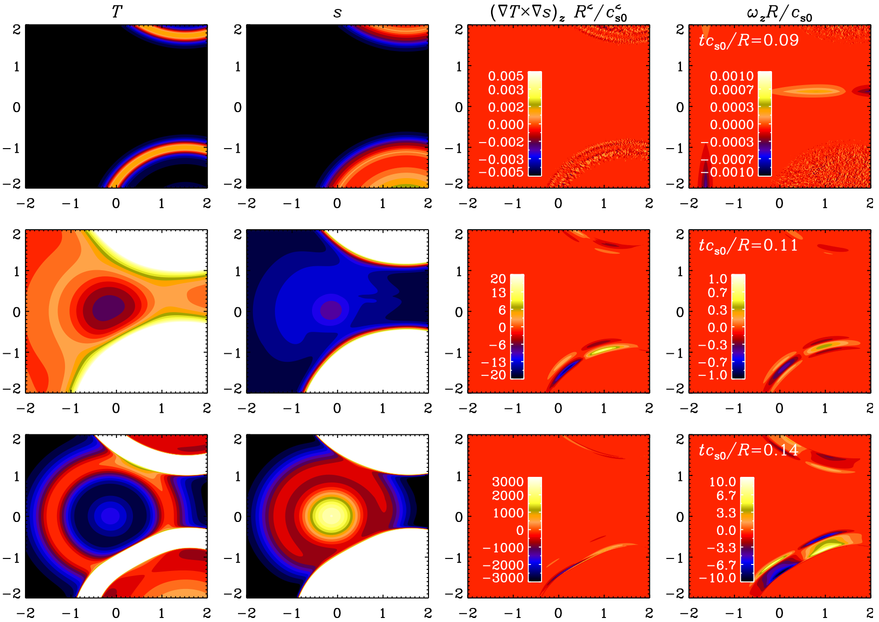

Figure 2.4: Images of T, s, $(\boldsymbol{\nabla} T \times \boldsymbol{\nabla} s)_z$, and normalized vertical vorticity for a two-dimensional run with 512^2 mesh points. It is shown an instant shortly before the second expansion wave is launched (top row), and shortly after the second expansion wave is launched (second and third row). Note the vorticity production from the baroclinic term in the second and third row, while in the top row, $(\boldsymbol{\nabla} T \times \boldsymbol{\nabla} s)_z$ and ω_z are just at the noise level of the calculation. Even under our weakly supersonic conditions shock surfaces are well localized and the zones of maximum production of vorticity appear to be those in which the fronts encounter each other. Only the inner part of the domain is shown. (Figure from **Paper II**.)

are displayed. The forcing is provided by

$$\boldsymbol{U} = \boldsymbol{\nabla}\phi, \tag{2.10}$$

$$\phi = \frac{u_0}{k_0}\cos k_0(x+\chi_x)\,\cos k_0(y+\chi_y)\,\cos k_0(z+\chi_z). \tag{2.11}$$

Here, u_0 and k_0 are positive constants and χ_x, χ_y, and χ_z can be interpreted as random phases. This steady flow might, in principle, generate inhomogeneities in the mass density, and this is the reason for which the applicability of our results has to be restricted to a limited time range.

In Fig. 2.5, $\tilde{\kappa}_\mathrm{t}$ and $\tilde{\eta}_\mathrm{t}$ are the turbulent diffusivity and turbulent magnetic diffusivity evaluated when the constraint of a good separation is relaxed. For small enough Pe and Re_M we indeed find negative values for these diffusivities, where the scale of variation of $\overline{C}$ is large compared with the scale of the

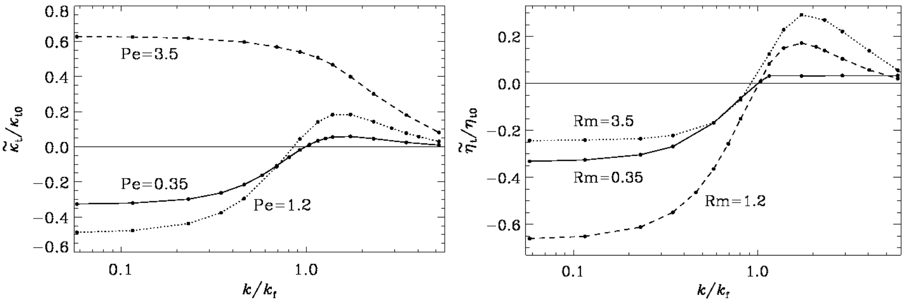

Figure 2.5: Left panel: $\tilde{\kappa}_t/\kappa_{t0}$ versus k/k_f for some values of Pe. Right panel: $\tilde{\eta}_t/\eta_{t0}$ versus k/k_f for some values of Re_M. (Figure from **Paper I**.)

turbulence, i.e. $k/k_f \ll 1$. When k/k_f becomes larger than unity, κ_t and η_t become positive.

One might wonder whether or not the spatial structure of the flow can affect the reduction of the effective diffusivity. Results of **Paper I** suggest that this is not the case. In fact, even in a nearly one-dimensional flow, turbulent diffusivities can become negative. However, in that case, if the underlying flow pattern displays propagating wave motions, there can be transport of the mean scalar in the direction of wave propagation – even in the absence of any mean material motion. Furthermore, in this case the wavenumber dependence shows a singularity at $k = k_f$ when SOCA is applied.

To better understand this we have then used the test-field method. This is a numerical procedure that allows to calculate the transport coefficients in eq. (1.21) using some known functions, also known as test fields (see **Paper V** and Chapter 4 for further details). When the test-field method is applied instead, the singularity disappears, but there is still a dramatic increase of the negative value of κ_t such that $\kappa_t + \kappa$ is close to zero. The 'naive' application of the test-field method suggests that the decay of $\overline{C}$ should then be 10 times slower than in the absence of any motions. However, using a direct numerical calculation of this simple flow pattern, we found that the actual decay is 200 times slower.

It turns out that the reason for this discrepancy is the so-called *memory effect*. This means that there is a non-instantaneous connection between the mean flux of the passive scalar and its mean concentration. Consequently one has to apply time-dependent test fields to get the correct result. The same happens in the magnetic case, in which assuming an instantaneous connection between the mean electromotive force and the mean magnetic field leads to ignoring the memory effect. When the test-field method is instead applied to a slowly decaying mean passive scalar concentration, we find that the value of $\kappa_t + \kappa$ in this time-dependent case is indeed 200 times smaller than κ, thereby confirming what found with direct numerical calculations. Although this study is not straightforwardly applicable to astrophysics, it is a step towards further analysis of similar processes, like the turbulent transport of momentum or heat. Another problem that can be better understood via the determination of turbulent transport coefficients for irrotationally forced flows is the mixing of species in a supernova-driven ISM. de Avillez and Mac Low (2002) found diffusion coefficients that increase exponentially with time, rather than remaining constant. This can be due to turbulent diffusivity.

3. Occurrence and conservation of magnetic helicity

Look on this result with a sense of wonder!
It is the evolution equation for the magnetic helicity.

(Steve Shore - An Introduction to Astrophysical Hydrodynamics)

3.1 The role of helicity in dynamos

When in MHD we speak about helicity, we might refer to different quantities. A hydrodynamic flow can be characterized by its kinetic helicity H_K, that is the volume integral of the scalar product between the velocity field and its curl, the vorticity $\boldsymbol{W} = \boldsymbol{\nabla} \times \boldsymbol{U}$,

$$H_K = \int_V \boldsymbol{W} \cdot \boldsymbol{U} \, \mathrm{d}V. \tag{3.1}$$

The value of H_K quantifies the mutual linkage of $\boldsymbol{W}$ lines (Moffatt, 1969). Likewise, one can define the flow helicity $H_U = \int_V \boldsymbol{\psi} \cdot \boldsymbol{U} \, \mathrm{d}V$, where $\boldsymbol{\psi}$ is the vector potential of the solenoidal part of $\boldsymbol{U}$; see **Paper I** and eq. (1.25). This quantity is a measure of the linkage of flow lines. When, instead, we are dealing with a magnetized environment, relevant quantities are the magnetic helicity

$$H_M = \int_V \boldsymbol{A} \cdot \boldsymbol{B} \, \mathrm{d}V \tag{3.2}$$

and the current helicity

$$H_C = \int_V \boldsymbol{J} \cdot \boldsymbol{B} \, \mathrm{d}V. \tag{3.3}$$

These two quantities describe the linkage of magnetic flux tubes and electric current lines, respectively. A quantity describing the linkage between magnetic flux tubes and vortex tubes is the so-called cross helicity

$$H_X = \int_V \boldsymbol{U} \cdot \boldsymbol{B} \, \mathrm{d}V. \tag{3.4}$$

We can then say that the helicity allows one to quantify the amount of twisting of a vector field. The most obvious and clear connection can be seen in the kinetic helicity, which is non-zero only if some helical structures can be identified in a flow. For instance, the trajectory of a person climbing a spiral staircase has a preferred handedness and hence a non-zero kinetic helicity. Nevertheless, one does not necessarily need to follow a spiral path to have a non-zero helicity. Take the example of a dancer following a straight line during a part of her dance-show, but moving through pirouettes. As long as she moves on a flat surface, her motion will be non-helical, because her velocity is a vector lying on the plane, while her twisting corresponds to a vector perpendicular to the plane, therefore their dot product vanishes. Nevertheless, if she keeps turning while jumping, her motion will be helical, even though her body is not following any helical path. In this case, her motion on a "large scale" will have zero helicity, while the "small scale" motion will be helical. We can then say that, in general, for a vector field, we can define its kinetic helicity as the sum of mean and fluctuating helicity

$$H_K = H_{K\mathrm{m}} + H_{K\mathrm{f}} \tag{3.5}$$

These two new quantities indicate respectively the large-scale helicity, $H_{Km} = \int_V \overline{\boldsymbol{W}} \cdot \overline{\boldsymbol{U}}\, \mathrm{d}V$, and the small-scale, or fluctuating, helicity, $H_{Kf} = \int_V \boldsymbol{\omega} \cdot \boldsymbol{u}\, \mathrm{d}V$.

However, the acting of a single dancer can be representative of the motion of a single fluid particle rather than of a fluid. This can be rather thought of as the action of a whole ballet group, for which the distinguishing of a collective helical motion from a non-helical one might be non-trivial. In this case, as we will see, a topological interpretation of the helicity, connecting this quantity to the linkage of field lines, will be helpful. The same concept applies to magnetic and current helicities, therefore representing the swirling of magnetic field and current lines, respectively.

The connection between the presence of helicity and the occurrence of an α effect and of a dynamo process was first investigated by Steenbeck et al. (1966). Figure 3.1 illustrates how the combined action of rotation, expansion with upward or compression with downward motions can generate helicity, so creating ordered magnetic structures that can lead to the formation of α-like structures (see Fig. 1.1). For small-scale dynamos it has been shown that they can work in non-helical flows (e.g. Kazantsev, 1968, Hughes et al., 1996). Using a two-scale analysis, Gilbert et al. (1988) showed that helicity is not strictly required for an α effect and the dynamo instability. A velocity field that is not parity-invariant can support α effect even if non-helical. Nevertheless, as stated in the same work, the presence of helicity helps the dynamo action. Even though there exist in the literature examples of flows acting as dynamos without involving the occurrence of helicity to develop (e.g. Vishniac and Brandenburg, 1997, Vishniac and Cho, 2001, Rogachevskii and Kleeorin, 2003, 2004), it is more difficult to produce coherent large-scale structures similar to those observed in stars and galaxies with non-helical dynamos rather

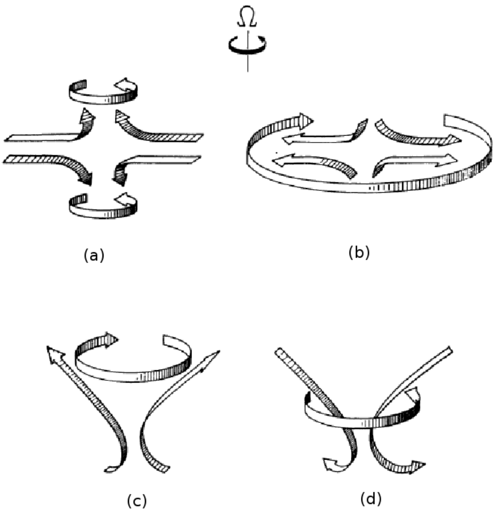

Figure 3.1: For a flow rotating with angular velocity Ω, Parker (1971) explained qualitatively through this figure the change in angular velocity under the action of compression (a), expansion (b), upward (c) or downward (d) expansion in the direction of the midplane. As consequence of these combined motions, net kinetic helicity is generated. (Figure from Parker (1971).)

than with helical ones (Brandenburg, 2005).

3.2 Spontaneous formation of helical structures

In nature there are systems for which their ground state does not share the same symmetries of the underlying equations of motion (Umezawa et al., 1982). This phenomenon is well known, e.g. in equilibrium statistical physics. One example is the paramagnetic-ferromagnetic transition: when decreasing the temperature down below the critical point, all the molecules of a magnet attain the same orientation, thereby breaking the up-down symmetry. This is then a typical example of spontaneously broken symmetry.

In non-equilibrium physics, spontaneous symmetry breaking is often observed as consequence of the occurrence of an instability: a system does not return to its initial state after being perturbed at a point where some control parameter is above a critical threshold. A well–studied example from fluid dynamics is the case of Rayleigh–Bénard convection (Swinney and Gollub, 1985)

In general, a state of a dynamical system is defined to be stable when an infinitesimal change of it leads to an infinitesimal change in future states (Drazin,

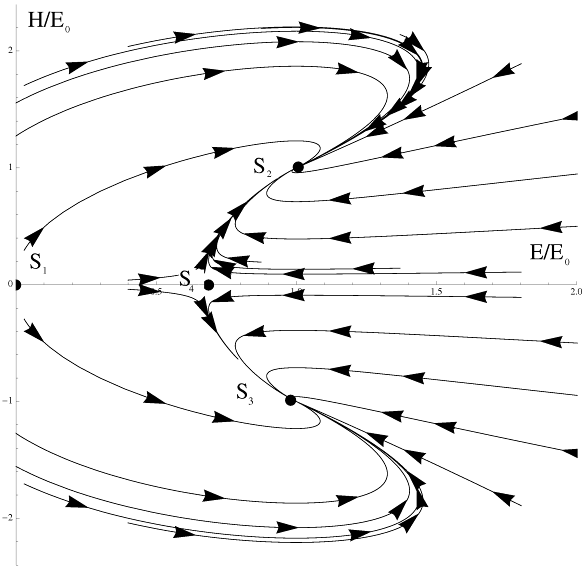

Figure 3.2: The phase portrait for $\mu < \mu_*$. This is the typical situation in which S_2 and S_3 are attractive and S_4 is a saddle point. (Figure from **Paper III**.)

2002). When, on the other hand, an infinitesimal variation in the present state can bring, in a finite time, the system into a state finitely away from the present one, then the state is said to be unstable [1].

What is relevant to our discussion is the fact that non-helical states can evolve into helical ones due to the occurrence of an instability. This means that a system, which does not show any handedness in its ground state, evolves in a finite time into a state of finite helicity if infinitesimally disturbed by a chiral perturbation. It consists then of left-handed (***L***) or right-handed (***R***) fully helical modes. The original chiral symmetry is therefore broken. We focus here on spontaneous chiral symmetry breaking in the non-linear phase of an instability due to the presence of a magnetic field. This might be relevant in astrophysics because helical flows are ubiquitous, and they are often the cause of a dynamo at work. In most cases the occurrence of helicity can be under-

---

[1] A more mathematically rigorous definition can be found in (Alligood et al., 1997, pag. 290): An equilibrium point $\bar{v}$ is called stable or Lyapunov stable if every initial point v_0 that is chosen very close to $\bar{v}$ has the property that the solution $F(t, v_0)$ stays close to $\bar{v}$ for $t \geq 0$. More formally, for any neighborhood N of $\bar{v}$ there exists a neighborhood N_1 of $\bar{v}$, contained in N, such that for each initial point v_0 in N_1, the solution $F(t, v_0)$ is in N for all $t \geq 0$. An equilibrium is called asymptotically stable if it is both stable and attracting. An equilibrium is called unstable if it is not stable. Finally, an equilibrium is globally asymptotically stable if it is asymptotically stable and all initial values converge to the equilibrium.

stood as a result of broken parity due to the presence of a pseudoscalar. For example, in the northern hemisphere of the Sun flows are expected to have negative helicity, because the pseudoscalar $\Omega \cdot \boldsymbol{\nabla}(\ln\rho)$ is negative. But, even in the absence of such pseudoscalar, could helicity emerge as a result of spontaneously broken symmetry? We address this question in **Paper III**, where we demonstrate the occurrence of spontaneous chiral symmetry breaking due to a global instability of a purely toroidal magnetic field, known as Tayler instability (Markey and Tayler, 1973; Tayler, 1973). A sufficient condition for this instability is (Bonanno and Urpin, 2008b)

$$\frac{\partial \ln B_\varphi}{\partial \ln r} > -\frac{1}{2}, \tag{3.6}$$

where r is the radial coordinate of the cylindrical domain. A spectrum of infinite unstable modes is excited by this instability: all of them are characterized by pairs of opposite azimuthal wave number $m = \pm 1$, 2, 3, ..., but with precisely the same growth rate. In particular, $m = \pm 1$ are the modes with the fastest growth rate. We thus discuss the possibility of generating a final state with finite helicity starting from a non-helical basic state, using a very small controlled helical perturbation. The nonlinear coupling between the different modes eventually leads to the formation of a final helical state. In the linear phase the system attains a helicity that is determined essentially by the helicity of the perturbation, while the nonlinear evolution can be rather complex and it is not clear *a priori* what the final selected helical state would be. Moreover we point out some aspects of the underlying nonlinear mechanism determining the evolution from a mirror-symmetric state to a final state with a preferred handedness or helicity. Such instability has recently been studied for its possible astrophysical applications, especially in radiative zones of stars (Spruit, 1999, Braithwaite and Nordlund, 2006, Braithwaite, 2006, Bonanno and Urpin, 2008a, Bonanno and Urpin, 2008b, Bonanno and Urpin, 2011, Bonanno and Urpin, 2012, Gellert et al., 2011).

We consider a cylindrical domain with a purely toroidal magnetic field. The Lorentz force is balanced by a gradient of the pressure of the fluid, so that the system is in equilibrium. To describe the evolution of this unstable system, we assume that we are dealing with an instability with two growing modes with opposite helicity but exactly the same growth rate. The amplitude of the left- and right-handed modes is given by vectors $\hat{\boldsymbol{L}}$ and $\hat{\boldsymbol{R}}$, respectively. In physical space we have

$$\boldsymbol{L}(\boldsymbol{x}) = \hat{\boldsymbol{L}}\phi(\boldsymbol{n}), \tag{3.7}$$

$$\boldsymbol{R}(\boldsymbol{x}) = \hat{\boldsymbol{R}}\phi(\boldsymbol{n}). \tag{3.8}$$

In cylindrical coordinate, ϕ is a combination of trigonometric and Bessel functions.

Similar to what was done by Fauve et al. (1991) we assume that the dynamical evolution of the unstable mode is determined by an effective Lagrangian. For a single left-handed mode, total helicity and energy are given by

$$
\begin{aligned}
E_L &= \frac{1}{2}\int \boldsymbol{L}^2(\boldsymbol{x})\,d^3x = \frac{1}{2}\hat{\boldsymbol{L}}\cdot\hat{\boldsymbol{L}}^*, && (3.9)\\
\mathcal{H}_L &= \int \boldsymbol{L}\cdot\nabla\times\boldsymbol{L}\,d^3x = -2\Lambda E_L. && (3.10)
\end{aligned}
$$

where an asterisk denotes complex conjugation and Λ is a measure of the helicity. Analogously we define E_R and $\mathcal{H}_R = +2\Lambda E_R$. In **Paper III** we show how this description of E_R, E_L, $\mathcal{H}_R$ and $\mathcal{H}_L$ leads to the following form for the Lagrangian of the system

$$
\mathcal{L}[\hat{\boldsymbol{L}},\hat{\boldsymbol{R}}] = \gamma\left[|\hat{\boldsymbol{L}}|^2+|\hat{\boldsymbol{R}}|^2\right] - \mu\left[|\hat{\boldsymbol{L}}|^4+|\hat{\boldsymbol{R}}|^4\right] - \mu_*\left(|\hat{\boldsymbol{L}}|^2|\hat{\boldsymbol{R}}|^2\right), \qquad (3.11)
$$

where the coefficient γ is the linear growth rate and μ and μ_* are adjustable parameters that determine the saturation of the instability in the weakly nonlinear regime.

It follows that the evolution equations for energy E and helicity $H = \mathcal{H}/2\Lambda$ are

$$
\begin{aligned}
\frac{dE}{dt} &= 2\gamma E - 2(\mu+\mu_*)E^2 - 2(\mu-\mu_*)H^2, && (3.12a)\\
\frac{dH}{dt} &= 2\gamma H - 4\mu EH. && (3.12b)
\end{aligned}
$$

The dynamical system described by eq. (3.12) is depicted in Fig. 3.2. It has four fixed points in the (E,H) plane, $S_1 = (0,0)$, $S_{2,3} = (E_0, \pm E_0)$, and $S_4 = (2E_\mathrm{a}, 0)$ with eigenvalues $\lambda_1 = (2\gamma, 2\gamma)$, $\lambda_2 = \lambda_3 = (-2\gamma, 2(\mu-\mu_*)/\gamma)$, and $\lambda_4 = (-2\gamma, 2\gamma - 4\gamma\mu/(\mu+\mu_*))$. The origin is always repulsive, showing that the ground state is unstable. S_2 and S_3 are sinks or saddle points depending on the values of parameters μ and μ_*. S_4, corresponding to an achiral solution, can be an attractive fixed point only if $\mu_* < \mu$, otherwise it is a saddle point. So we can say that the initially achiral dynamical system evolves into a chiral system in a finite time if $\mu < \mu_*$.

Fig. 3.3 shows how the description given in eq. (3.11) fits the results of the DNS. The linear phase is well described by the coefficient γ, while μ and μ_* allow a good fit up to the weakly nonlinear phase of the instability. We can note from eq. (3.11) that when $H = 0$ at $t = 0$, the system evolves into a non-helical state, because $\mathrm{d}H/\mathrm{d}t = 0$ for all t.

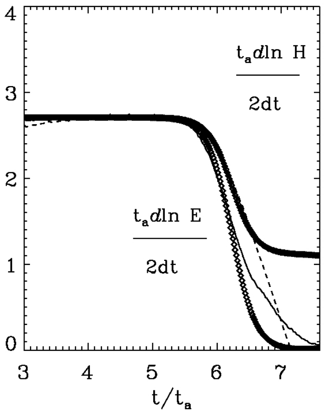

Figure 3.3: Time evolution for the logarithmic derivative of kinetic energy (solid line) E and kinetic helicity H (dashed) as measured in DNS for models `Hel` and `Helm1` in **Paper III**. t is in units of the Alfvén travel time t_A. We overplot a fit of the model with equations (3.12). The best fit is obtained for $\gamma = 2.71/t_A$, $\mu = 7.5 \cdot t_A/s_{\text{out}}^2$ and $\mu_* = 18 \cdot t_A/s_{\text{out}}^2$ and the solutions are over-plotted on the DNS results. (Figure from **Paper III**.)

3.3 Why do hydromagnetic flows conserve magnetic helicity?

Magnetic helicity H_M, defined in eq. (3.2), plays an important role in plasma physics (Taylor, 1974, Berger and Field, 1984, Jensen and Chu, 1984), solar physics (Rust and Kumar, 1994, 1996, Low, 1996), cosmology (Brandenburg et al., 1996, Field and Carroll, 2000, Christensson et al., 2005), and dynamo theory (Pouquet et al., 1976, Brandenburg and Subramanian, 2005c). This is due to the fact that H_M is a conserved quantity in ideal MHD (Woltjer, 1958). Even in the presence of finite magnetic diffusivity, the magnetic helicity can still only change on a resistive time scale.

This can be seen by starting from the definition of H_M, taking its time derivative, using eq. (1.8) and uncurling eq. (1.9) such that

$$\frac{\partial \boldsymbol{A}}{\partial t} = -\boldsymbol{E} - \boldsymbol{\nabla}\psi, \tag{3.13}$$

where ψ is the electrostatic potential. Using standard vector identities,

$$\frac{\partial(\boldsymbol{A}\cdot\boldsymbol{B})}{\partial t} = (-\boldsymbol{E} - \boldsymbol{\nabla}\psi)\cdot\boldsymbol{B} + \boldsymbol{A}\cdot(-\boldsymbol{\nabla}\times\boldsymbol{E}) = \tag{3.14}$$

$$= -2\boldsymbol{E}\cdot\boldsymbol{B} - \boldsymbol{\nabla}\cdot(\psi\boldsymbol{B} + \boldsymbol{E}\times\boldsymbol{A}). \tag{3.15}$$

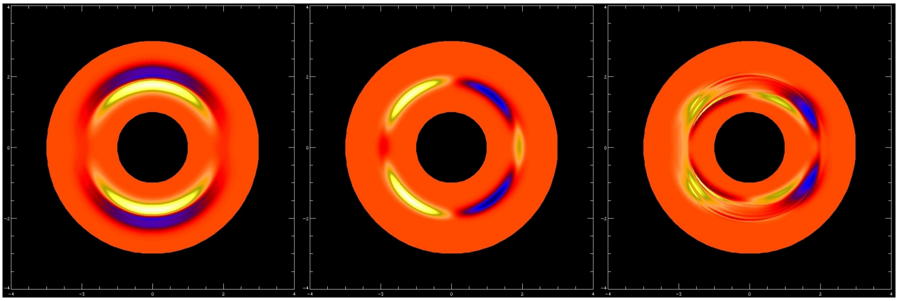

Figure 3.4: Formation of zones with different values for the kinetic helicity. Here we visualize three different snapshots of one of the simulations studied in **Paper III**. In the first snapshot we are at the beginning of the simulation, then at the beginning of the linear phase of the instability and, last, during the nonlinear phase. In the last snapshot we see how the yellow, corresponding to positive helicity, is dominant over the blue (negative helicity).

Therefore we have

$$\frac{dH_M}{dt} = -2\int_V \boldsymbol{E}\cdot\boldsymbol{B}\,\mathrm{d}V - \oint_S (\boldsymbol{E}\times\boldsymbol{A} + \psi\cdot\boldsymbol{B})\cdot\hat{\boldsymbol{n}}\,\mathrm{d}S = \tag{3.16}$$

$$= -2\eta\mu_0\int_V \boldsymbol{J}\cdot\boldsymbol{B}\,\mathrm{d}V. \tag{3.17}$$

We have here assumed that for closed domains the surface integral vanishes. In the non-resistive case, with $\eta = 0$, the magnetic helicity is therefore conserved. Nevertheless, in real astrophysical cases, characterized by a very large Re_M, even though the magnetic diffusivity is small, we have $\eta \neq 0$. Does this condition ensure that we can deal with the magnetic helicity treating it as a conserved quantity? In general we can: for example Brandenburg and Subramanian (2005c) argued that, as η approaches to zero, the magnetic helicity decreases with an upper bound given by the scaling $\eta^{1/2}$, which is not the case with kinematic helicity, even though that quantity would also be conserved in the ideal case.

Such conservation law is ultimately responsible for inverse cascade behavior that can be relevant for spreading primordial magnetic field over large length scales (Brandenburg et al., 1996, Field and Carroll, 2000, Christensson et al., 2005). It is also likely the reason why the magnetic fields of many astrophysical bodies have length scales that are larger than those of the turbulent motions responsible for driving these fields, as well as larger than the body itself. In the presence of finite magnetic diffusivity, the magnetic helicity can only change on a resistive time scale.

In a closed or periodic domain, if there is no external energy supply, a magnetic field decays with a speed depending critically on the value of the

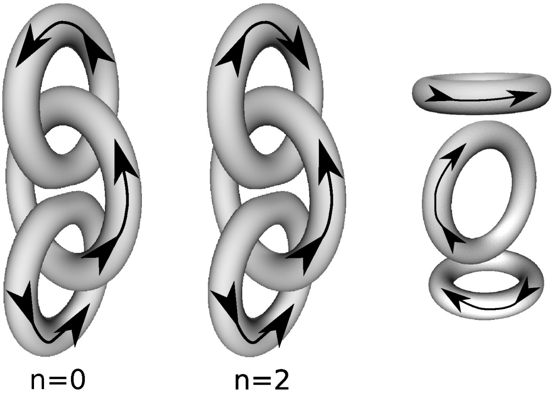

Figure 3.5: Visualization of the triple ring configuration studied in **Paper IV**. Arrows indicate the direction of the field lines in the rings, corresponding to a configuration with $n = 0$ (left) and $n = 2$ (center). On the right the non-interlocked configuration with $n = 0$ is shown. (Figure from **Paper IV**.)

magnetic helicity. To understand this statement, we can consider spectra of magnetic energy and magnetic helicity. The magnetic energy spectrum $M(k)$ is normalized such that

$$\int M(k)\,dk = \langle \boldsymbol{B}^2 \rangle / 2\mu_0, \tag{3.18}$$

where k is the wave number (ranging from 0 to ∞). The magnetic helicity spectrum $H_M(k)$ is normalized such that

$$\int H_M(k)\,dk = \langle \boldsymbol{A} \cdot \boldsymbol{B} \rangle. \tag{3.19}$$

In a closed or periodic domain, $H_M(k)$ is gauge-invariant, i.e., it does not change after adding a gradient term to $\boldsymbol{A}$. Indeed, if we choose a vector potential $\boldsymbol{A}^{'} = \boldsymbol{A} + \nabla\Psi$ we find

$$H_M^{'}(k)\,dk = \int_V \boldsymbol{A}^{'} \cdot \boldsymbol{B}\,\mathrm{d}V = H_M(k) + \int_V \nabla\psi \cdot \boldsymbol{B}\,\mathrm{d}V = \tag{3.20}$$

$$= H_M(k) - \int_V \psi\nabla \cdot \boldsymbol{B}\,\mathrm{d}V + \oint_S \psi\boldsymbol{B} \cdot \hat{\boldsymbol{n}}\,\mathrm{d}S = H_M(k). \tag{3.21}$$

Woltjer (1958) found that, for finite magnetic helicity, the magnetic energy spectrum has to fulfill the so-called realizability condition (Moffatt, 1969)

$$M(k) \geq k|H(k)|/2\mu_0. \tag{3.22}$$

As consequence, the decay of a magnetic field is subject to a corresponding decay of its associated magnetic helicity. Given that in a closed or periodic

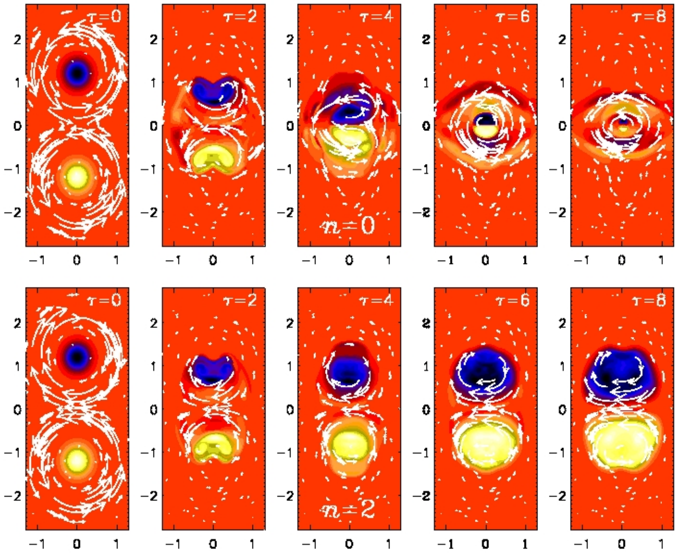

Figure 3.6: Cross-sections in the xy plane of the magnetic field with zero linking number (upper row) and finite linking number (lower row). The z component (pointing out of the plane) is shown together with vectors of the field in the plane. Light (yellow) shades indicate positive values and dark (blue) shades indicate negative values. Intermediate (red) shades indicate zero value. (Figure from **Paper IV**.)

domain the magnetic helicity changes only on resistive time scales (Berger, 1984), the decay of magnetic energy is slowed down correspondingly.

The decay of turbulent magnetic fields is often described by a power-law where the magnetic energy is proportional to $t^{-\sigma}$. In the absence of magnetic helicity, $\langle \boldsymbol{A} \cdot \boldsymbol{B} \rangle = 0$, a relatively rapid decay with $\sigma \approx 1.3$ (Mac Low, 1999; Mac Low et al., 1998, 2005) has been found, while with $\langle \boldsymbol{A} \cdot \boldsymbol{B} \rangle \neq 0$, the decay is slower with σ between 1/2 (Christensson et al., 2005) and 2/3 (Biskamp and Müller, 1999).

3.4 A topological interpretation of magnetic helicity

Magnetic helicity happens to have an interesting topological interpretation. When we deal with isolated flux tubes that do not present any internal twist, it is indeed possible to write its value as the product of their linking number times their fluxes (Moffatt, 1978). This means that a system of two or more interlocked flux tubes has a magnetic helicity, even if they are untwisted. If we have two interlocked flux tubes C_1 and C_2, with magnetic fluxes ϕ_1 and ϕ_2, respectively, we have $\boldsymbol{B}_1 \mathrm{d}V = \phi_1 \mathrm{d}\boldsymbol{l}$ and $\boldsymbol{B}_2 \mathrm{d}V = \phi_2 \mathrm{d}\boldsymbol{l}$. Therefore

$$H_M = \phi_1 \oint_{C_1} \boldsymbol{A} \cdot \mathrm{d}\boldsymbol{l} + \phi_2 \oint_{C_2} \boldsymbol{A} \cdot \mathrm{d}\boldsymbol{l} = 2\phi_1\phi_2. \tag{3.23}$$

The sign of the linking number becomes negative if the field lines in one of the tubes is reversed. Therefore, in this case, the magnetic helicity is more generally given by $H_M = \pm 2\phi_1\phi_2$.

This way to look at magnetic helicity turns out to be important. When we are able to connect magnetic helicity to physical structures we can then directly connect the stability, or instability, to the value of H_M. In particular, in **Paper IV** it is shown that a structure of interlocked magnetic flux rings characterized by a non-vanishing value of H_M can be longer lived than a similar one in which $H_M = 0$. We have analyzed the evolution of the three different configurations shown in Fig. 3.5. In particular, the configurations indicated as $n = 0$ and $n = 2$ have been compared in their evolution, for their topologically equality. A visualization of their evolution can be seen in Fig. 3.6: the configuration with $n = 0$, and therefore $H_M = 0$, decays much more quickly than the configuration with $n = 2$ and $H_M \neq 0$. As can be seen from this figure, at the non-dimensional time $\tau = 2$ (in Alfvén times) the field in the $n = 0$ case suffers from mutual cancellation of anti-parallel magnetic fields on both sides of $y = 0$.

The conservation of magnetic helicity appears, therefore, to play a major role in the stability of magnetic structures. Moreover, it is important in dynamo theory as well: firstly, it provides diagnostic evidence of large-scale dynamo action, and, secondly, it leads to a constraint on dynamo action itself, as we will see in detail in 4.3. In particular, as the work of Pouquet et al. (1976) shows, the α effect is proportional to the difference of kinetic and current helicity densities of the small-scale fields, $H_{Kf} - H_{Cf}$.

4. Helical turbulence at work: turbulent dynamo

Leave the gun. Take the cannoli.

(Peter Clemenza, in "The Godfather")

4.1 Imposed-field vs. test-field method

In the previous section we have discussed two possible contributions to α, namely those proportional to kinetic and current helicities. These two contributions might result in a small residual between two large values. In addition, in the presence of a strong magnetic field, α becomes certainly anisotropic. Indeed, earlier work using the test-field method (Brandenburg et al., 2008b) has shown that, even in the simplest case, α_{ij} takes the tensorial form $\alpha_0(\overline{B})\delta_{ij} + \alpha_1(\overline{B})\hat{B}_i\hat{B}_j$, where $\hat{B}_i = \overline{B}_i/|\overline{\boldsymbol{B}}|$ is the unit vector of the mean field. The goal of this section is to determine the functions $\alpha_0(\overline{B})$ and $\alpha_1(\overline{B})$ in some cases and to compare the results with those obtained using another simpler method that is, however, limited in its capabilities.

Approaching this general problem through numerical simulations is a common way to find these coefficients, although we are talking about techniques that are still on their way to being fully developed. Direct Numerical Simulations (DNS) offer a good way to evaluate these coefficients and they avoid the restricting approximations that are unavoidable in analytical approaches.

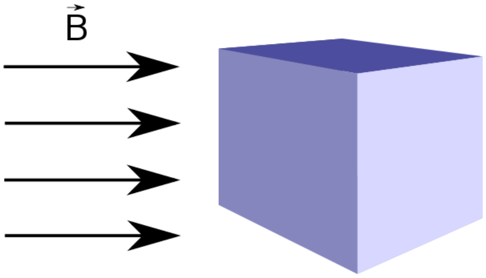

Figure 4.1: Qualitative illustration of the imposed-field method.

In the context of mean-field electrodynamics, the simplest way to accomplish such a measurement is the so-called *imposed-field method*, sketched in Fig. 4.1. The domain in which a DNS is performed (a box, in Fig. 4.1) is put under the action of an externally imposed large-scale field. Its influence on the fluctuations of magnetic and velocity fields is used to infer some of the full set of transport coefficients. It was originally used by Brandenburg et al. (1990) to show that in rotating stratified convection the vertical components of the α tensor have an opposite sign respect to the horizontal ones. The same result was found also later in theoretical works by Ferriere (1993) and Ruediger and Kichatinov (1993).

Let us translate this into mathematics. For a triply periodic vector potential $\boldsymbol{A}$, it is convenient to express the magnetic field in the form $\boldsymbol{B} = \boldsymbol{B}_0 + \boldsymbol{\nabla} \times \boldsymbol{A}$, where $\boldsymbol{B}_0$ is the imposed field. It is automatically equal to $\langle \boldsymbol{B} \rangle$, because the volume average of $\boldsymbol{\nabla} \times \boldsymbol{A}$ vanishes. The volume-averaged electromotive force is given by

$$\langle \mathcal{E} \rangle = \langle \mathcal{E} \rangle(t) \equiv \langle \boldsymbol{u} \times \boldsymbol{b} \rangle, \tag{4.1}$$

where $\boldsymbol{u} = \boldsymbol{U} - \langle \boldsymbol{U} \rangle$ and $\boldsymbol{b} = \boldsymbol{B} - \boldsymbol{B}_0$ are the fluctuating components of velocity and magnetic field. For mean fields defined as volume averages, and because of periodic boundary conditions, it also holds $\langle \boldsymbol{J} \rangle = \boldsymbol{0}$. Under isotropic conditions there is therefore only the α effect connecting $\langle \mathcal{E} \rangle$ with $\boldsymbol{B}_0$, via $\langle \mathcal{E} \rangle = \alpha_{\text{imp}} \boldsymbol{B}_0$, so

$$\alpha_{\text{imp}} = \langle \mathcal{E} \rangle \cdot \boldsymbol{B}_0 / B_0^2. \tag{4.2}$$

A different tool, more universal in its use, is the *test-field method* (Schrinner et al., 2005, 2007): in a single DNS it allows to determine all the wanted transport coefficients. This method could be summarized as follows: a fluctuating velocity field is taken from a DNS and inserted into a properly customized set of equations named *test equations*. Their solutions, the test solutions, give the response of chosen mean fields to the interaction with the fluctuating velocity field, that is a fluctuating magnetic field. The chosen mean fields are called *test fields*. The full details are given in **Paper V**. This is a review paper that highlights in particular the usefulness of the test-field method in nonlinear cases, for example in the case where the α effect is due to magnetic buoyancy (Chatterjee et al., 2011b). In that case one talks about the quasi-kinematic test-field method which applies as long as the magnetic fluctuations are only due to tangling of a large-scale field (Rheinhardt and Brandenburg, 2010).

This method has been applied to several models, like the ones with homogeneous turbulence with helicity (Sur et al., 2008), with shear and no helicity (Brandenburg et al., 2008a) and with both of them (Mitra et al., 2009), as well as to the study of magnetorotational instability (Gressel, 2010). This means that this method is actually able to cover several astrophysical situations, being able to calculate the transport coefficients in the aforementioned cases. On the other hand one still has to deal with the problem of the big computational power that is required to simulate through DNS such a physical situation. Real astrophysical values are therefore out of the range of the applicability of the test-field method.

4.2 Estimating the α effect

When simulating an MHD environment in which a large-scale magnetic field is generated the problem of the identification of the mechanism driving such a field arises naturally. For example, Hughes and Proctor (2009) measured the virtual absence of α effect in simulations of convection thus finding a result that appears to be in conflict with others, like Schrinner et al. (2005, 2007).

In **Paper VI** different ways to measure α are used and compared. The imposed-field method and the test-field method are applied to a helically turbulent environment, with positive helicity and $\mathrm{Re_M} > 1$ for which the kinematic value of α is known (Sur et al., 2008),

$$\alpha_0 = -\frac{\tau}{3} u_{\mathrm{rms}}. \tag{4.3}$$

When under the action of an external field, α should be catastrophically quenched according to Vainshtein and Cattaneo (1992),

$$\alpha_{\mathrm{fit}} = \frac{\alpha_0}{1 + \mathrm{Re_M} \overline{\boldsymbol{B}}^2 / B_{\mathrm{eq}}^2}. \tag{4.4}$$

This equation is a special case of the more general quenching formula of Kleeorin and Ruzmaikin (1982),

$$\alpha_{\mathrm{KR82}} = \frac{\alpha_0 + \mathrm{Re_M} \eta_{\mathrm{t}} \overline{\boldsymbol{J}} \cdot \overline{\boldsymbol{B}} / B_{\mathrm{eq}}^2}{1 + \mathrm{Re_M} \overline{\boldsymbol{B}}^2 / B_{\mathrm{eq}}^2}. \tag{4.5}$$

If the mean field is an imposed one, it is uniform in space, so $\overline{\boldsymbol{J}} = \mathbf{0}$, and we recover eq. (4.4).

In **Paper VI**, we found eq. (4.4) to be true only for strong imposed magnetic fields, $\mathrm{Re_M} \boldsymbol{B}_0^2 / B_{\mathrm{eq}}^2 > 1$. Surprising results have been found for weaker fields: In these cases the imposed-field method does not recover the kinematic value of α. Instead, α_{imp} can attain strongly suppressed values, but it can actually also attain strongly enhanced values. This is caused by the unavoidable emergence of so-called meso-scale dynamo action, that is the emergence of dynamo-generated magnetic fields on the scale of the domain. In principle, such meso-scale dynamo action could have been suppressed by restricting

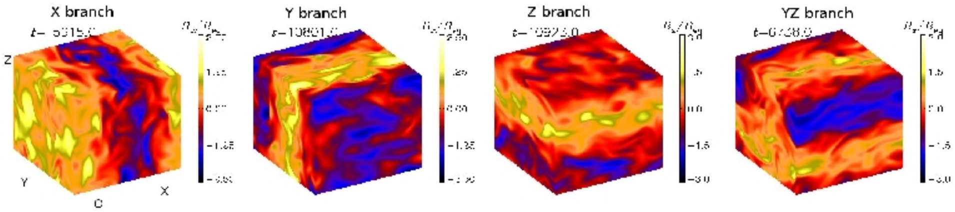

Figure 4.2: Visualization of B_z on the periphery of the computational domain for the X branch and B_x for the Y, Z, and YZ branches. The coordinate directions are indicated on the first panel. (Figure from **Paper VI**.)

oneself to scale-separation ratios, k_f/k_1, of less than 2 or so, as done, for example, in some of the runs of Brandenburg and Subramanian (2005a). In this case, with a triply-periodic box, four different magnetic field configurations can emerge, as illustrated in Fig. 4.2. The first three correspond to Beltrami fields, of the form $\overline{\boldsymbol{B}} = (\cos kz, \sin kz, 0)$, where the wave-vector points in one of the three coordinate directions. The fourth possibility is also a Beltrami field, but one that varies diagonally in a direction perpendicular to the direction of the imposed-field.

In general, neither the imposed-field method nor the test-field one are able to fully reproduce the kinematic value of the α effect. for the test-field method drives the growing of meso-scale fields as well. However the results obtained with the test-fields are closer to those that one would expect, showing that it is actually necessary to use a someway more complex strategy to measure α. What can be done is the following: resetting the meso-scale fluctuating fields over some regular time-intervals. In this way a more accurate value of α can be obtained for weak imposed field as well.

Determining the nature of the dynamo mechanism is an important part in the analysis of a successful simulation showing large-scale field generation. **Paper VI** shows that meaningful results for α can be obtained using either the imposed-field or the test-field methods under the condition that the departure of the magnetic field from the imposed one $\boldsymbol{B}_0$ is reset to zero to eliminate the effects of dynamo-generated meso-scale magnetic fields. Conversely, if such fields are not eliminated, the results can still be meaningful, but they need to be interpreted correspondingly and bear little relation to the imposed field. Strong imposed magnetic fields ($\mathrm{Re_M}\boldsymbol{B}_0^2/B_\mathrm{eq}^2 > 1$), on the other hand, do not drive any growth of meso-scale magnetic fields, so the resetting procedure is then neither necessary nor would it make much of a difference when the test-field method is used. However, when the imposed-field method is used, the resetting of the actual field reduces the quenching of u_rms. This affects the normalizations of B_0 and α_{ij} with B_eq and α_0, respectively, because both are proportional to u_rms.

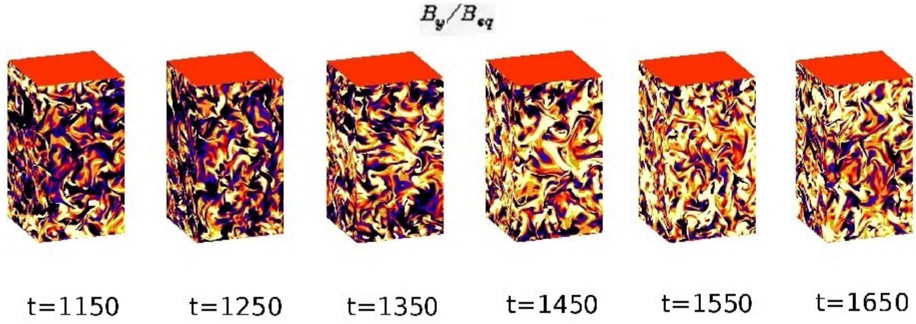

Figure 4.3: Visualization of B_y at six different times during the evolution of the system, for Model S3 in **Paper VII**. It is visible its variability, being this component of the magnetic field prevalently negative in the first snapshot and gradually turning positive in the others. Time is given in turnover times and spawns over half a cycle. (Figure from **Paper VII**.)

4.3 What happens in systems that conserve magnetic helicity?

We have talked about the evaluation of the transport coefficients and the dynamo effect. So now it is time to see the effect that a dynamo process has on the magnetic field of a system.

It has been demonstrated how the production of large-scale magnetic fields by a mean-field dynamo can be strongly suppressed at large magnetic Reynolds numbers as a consequence of the conservation of magnetic helicity. This phenomenon is known as *catastrophic quenching* (Kleeorin and Ruzmaikin, 1982; Vainshtein and Cattaneo, 1992). This is a consequence of magnetic helicity conservation and can be explained in the following way: the large-scale magnetic field generated by the α effect is helical, but in order to satisfy the conservation of total magnetic helicity, a small-scale field with magnetic helicity of opposite sign, but equal magnitude, must be generated in the system. The small-scale magnetic helicity is responsible for the creation of a magnetic α effect ($\alpha_{\rm M}$) which contributes with opposite sign to the kinetic α. Kleeorin and Ruzmaikin (1982) proposed this basic idea as the foundation of the so-called dynamical quenching model and this was later on confirmed by being able to reproduce catastrophic quenching in numerical simulations; see, for instance, Blackman and Brandenburg (2002). Nowadays this issue is still unclear when it comes to making predictions about the high-$\mathrm{Re_M}$ regime, difficult to be reproduced via numerics. One can state that the final amplitude reached by the magnetic α effect depends on the geometry of the system and on the value of the magnetic Reynolds number. For highly turbulent astrophysical objects

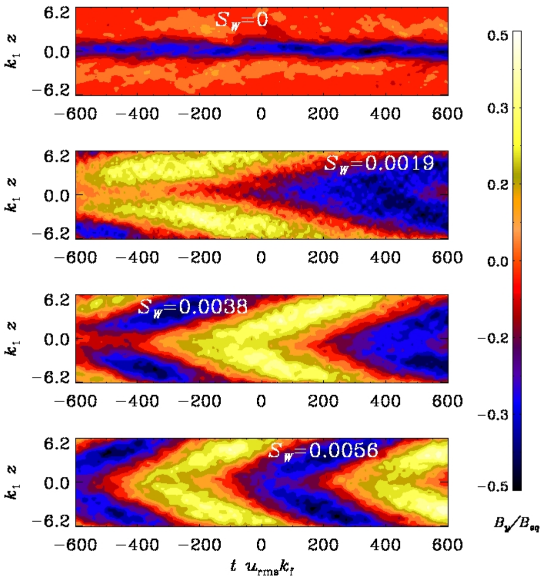

Figure 4.4: Space-time diagrams of $\overline{B}_y$ for different wind intensities S_W for models with similar $\mathrm{Re_M}$ in **Paper VII**. The time axes have been shifted such that for each run about 1200 turnover times are being displayed. Note that the cycle period decreases with increasing wind speed. (Figure from **Paper VII**.)

(high $\mathrm{Re_M}$) like the Sun or the Galaxy, α_M could get higher amplitudes, thereby decreasing the dynamo efficiency. However the dynamics of α_M also depends on the ability of the system to get rid of the small-scale magnetic helicity responsible for its creation. A critical parameter, on which the magnetic helicity annihilation in a closed or triply periodic domain depends, is the microscopic magnetic diffusivity. This annihilation is a very slow process given the scales and diffusivity values under consideration. However, an obvious solution to this catastrophic ($\mathrm{Re_M}$-dependent) quenching is to allow the system to get rid of helical small-scale magnetic fields. This issue is investigated in **Paper VII**.

4.4 Alleviating the dynamo quenching

In astrophysical bodies, systems characterised by high values of Re and $\mathrm{Re_M}$, large-scale magnetic fields are presently observed. Thus, catastrophic quenching is obviously not acting in those. As a consequence, there shall be ways to overcome the constraint given by the conservation of magnetic helicity which leads to the quenching of the dynamo. If, for instance, magnetic helicity is transported towards the outer boundaries and away from the dynamo, the quenching is expected to be alleviated. How can magnetic helicity can be

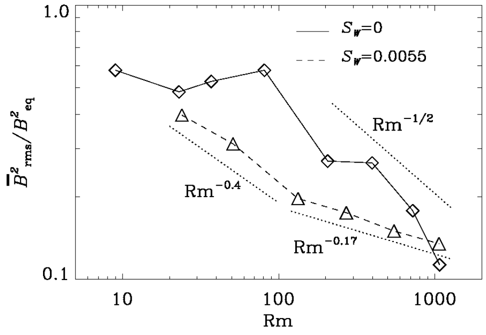

Figure 4.5: Scaling of $b_{\rm rms}$ with $\rm Re_M$ for a models without ($S_W = 0$) and with ($S_W \neq 0$) outflow. It is visible as for high enough $\rm Re_M$, $b_{\rm rms}$ decreases faster in the model without outflow. (Figure from **Paper VII**.)

transferred out of the domain in which the dynamo operates? One possibility is that small-scale magnetic helicity, responsible for the quenching of dynamo action, can be removed from the domain as consequence of the advection of material. In real astrophysical systems, this processes is generally expected to happen in a number of different ways. Typical examples of such advection can be stellar and galactic winds.

Among the various mechanisms for removing magnetic helicity from the system we focus on the role played by the turbulent–diffusive magnetic helicity flux and by the presence of advective flows or winds. The role of these magnetic helicity fluxes has already been tested in the context of mean-field dynamo models through a dynamical equation for the magnetic α-effect (Kleeorin et al., 2000, Brandenburg and Subramanian, 2005b, Sur et al., 2007a, Brandenburg et al., 2009, Guerrero et al., 2010, Chatterjee et al., 2011a).

These models have demonstrated the importance of magnetic helicity fluxes in solving the catastrophic quenching problem. Advection might be able to overcome the constraint imposed by the conservation of magnetic helicity, transporting a fraction of it outside the domain in which a dynamo is acting.

In **Paper VII** we study how the dynamo process is affected by advection; in particular we analyze the relative roles played by advective and diffusive fluxes of magnetic helicity. We do this by performing direct numerical simulations of a turbulent dynamo of α^2 type driven by forced turbulence in a Cartesian domain in the presence of a constant flow toward the upper and lower borders of the domain.

Figure 4.3 shows the system: we simulate a Cartesian domain under the action of helical plane wave forcing that drives a background helical turbulence. This drives a turbulent dynamo that amplifies a seed magnetic field. In Fig. 4.3 it can be seen that the y-component of the magnetic field oscillates

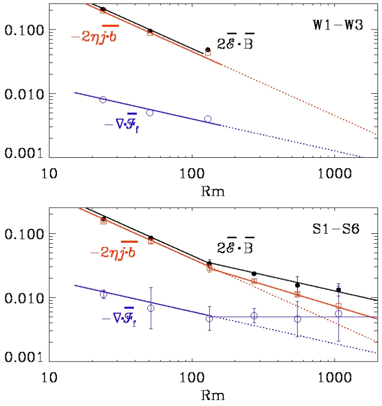

Figure 4.6: Scaling properties of the vertical slopes of $2\overline{\boldsymbol{\mathcal{E}}}\cdot\overline{\boldsymbol{B}}$, $-2\eta\mu_0\overline{\boldsymbol{j}\cdot\boldsymbol{b}}$, and $-\boldsymbol{\nabla}\cdot\overline{\mathcal{F}}_\mathrm{f}$ for models with weak wind (upper panel) and stronger wind (lower panel) in **Paper VII**. Given that the three quantities vary approximately linearly with z, the three labels indicate their non-dimensional values at $k_1z = 1$. The second panel shows that a stronger wind decreases the value of Re_M for which the contribution of the advective term becomes comparable to that of the resistive term. (Figure from **Paper VII**.)

from negative to positive polarity. This can be best seen in Fig. 4.4, where $\overline{B}_y$, that is the y-component averaged in the xy-plane, is shown. From the top panel of Fig. 4.4, one can also see that without an outflow our system does not show any oscillations. Fig. 4.5 illustrates what is the difference in b_rms for models with and without outflow, in function of Re_M. It is clear that for $\mathrm{Re}_\mathrm{M} \geq 200$ the b_rms decreases more slowly in case an outflow is present.

In Fig. 4.6 we plot the quantities playing a role in the evolution of the small scale magnetic helicity. This is characterized by the following quantities: the interaction between the mean magnetic field with the electromotive force ($2\overline{\boldsymbol{\mathcal{E}}}\cdot\overline{\boldsymbol{B}}$); a resistive term proportional to the current helicity, responsible for the magnetic contribution to the α effect ($-2\eta\mu_0\overline{\boldsymbol{j}\cdot\boldsymbol{b}}$); the advective helicity flux ($-\boldsymbol{\nabla}\cdot\overline{\mathcal{F}}_\mathrm{f}$).

We show in **Paper VII** that the alleviation of the catastrophic quenching happens when the advective flux becomes of the same order of magnitude of the diffusive one. This result might indicate that the presence of an outflow can actually play a decisive role in allowing high-Re_M astrophysical systems to harbour strong dynamo-generated magnetic fields.

5. Epilogue - A long way to go

It's a long way to the top
If you wanna rock 'n' roll.

(AC/DC)

Throughout this work we have seen examples of flows that can describe various astrophysical phenomena. We started looking at irrotational flows, as a model of expansions or explosions taking place in the ISM and we have seen how this flows can produce vorticity in the presence of rotation, shear, and baroclinicity. Also, irrotational flows are peculiar in terms of transport of magnetic fields as well as for a passive scalar. What's next? We need to include the effect of stratification to simulate a more realistic galactic environment and confirm the finding for α effect in the two galactic hemispheres. Moreover our three-dimensional simulations need to be pushed towards higher Mach numbers, to facilitate a better description of shock front encounters.

As a second kind of flow, we have considered helical ones. We know that magnetic helicity is a symptom of a dynamo at work, being associated with an α effect. We have pointed out how helicity can arise from the occurrence of an instability, which, in the case we have examined, is the Tayler instability. What will be interesting to analyze here is how a general instability can lead to the formation of helical structures and where there is the occurrence of symmetry breaking. Also, the importance of the Tayler instability in the development of the galactic field needs to evaluated. This might turn out to be relevant especially for elliptical galaxies, in which systematic rotation is relatively weak (Moss and Shukurov, 1996).

Coming to the dynamo problem, we have shown in Chapter 4 that one of the commonly used tools for analyzing the strength of the dynamo coefficient α can lead to misleading results. Currently, to our knowledge, the test-field method is the only reliable one to evaluate all the transport coefficients. One might need to reset the fluctuations due to the development of a meso-scale field in the computational domain. **Paper VII** shows that the magnetic helicity flux term becomes important in DNS of turbulent dynamos at large magnetic Reynolds numbers, but there is still a long way to go to make conclusive predictions about galactic dynamos. In forthcoming works we will need to include a more realistic galactic wind as well as the effect of shear, to have an $\alpha\Omega$ dynamo operating in the system. Moreover, the multi-phase nature of the ISM has to be taken into account. Nevertheless, there is the big constraint due to the restriction of simulating through DNS only flows with $\mathrm{Re_M} \lesssim 2000$. This is still a value that is only just entering what looks like an asymptotic regime, and it is far away from the real astrophysical ones.

Sammanfattning

Många av de himlakroppar vi känner till har visat sig vara magnetiserade: jorden, många av de hittills upptäckta planeterna, solen och andra stjärnor, den interstellära rymden, vintergatan och andra galaxer. Orsakerna till detta återstår fortfarande att förstå fullt ut, och denna avhandling är ett litet steg i den riktningen.

Dynamiken hos det interstellära mediet domineras av händelser som supernovaexplosioner, som kan modelleras som irrotationella flöden. Avhandlingens första del ägnas en analys av sådana flödens karakteristika, särskilt hur de påverkar den typiska turbulenta magnetiska diffusiviteten i ett medium, och det visas att diffusiviteten ökar utom i några få specialfall. Dessutom visas hur sådana flöden faktiskt kan utveckla virvelströmmar i miljöer som kännetecknas av rotation eller skjuvning eller inte är barotropiska.

För det andra undersöker vi helikala (spiralformade) flöden som är av grundläggande betydelse för dynamon, ett fenomen som förstärker magnetiska fält. Magnetisk helicitet kan uppstå i samband med en instabilitet: här fokuserar vi på instabiliteter i rent toridoala magnetiska fält, så kallade Tayler - instabiliteter. Man kan ge magnetisk helicitet en topologisk tolkning. Utgående från detta perspektiv, och med hänsyn tagen till att magnetisk helicitet är en bevarad storhet i icke-resistiva flöden, visas hur system som är helikala bevarar magnetiska strukturer längre än icke-helikala system.

Avhandlingens avslutande del behandlar dynamos.

Här visas hur man utvärderar dynamotransportkoeffecienter med de två vanligast använda teknikerna, nämligen metoderna "imposed-field"(pålagt fält) resp. test-field"(testfält). Därefter analyseras hur dynamos påverkas av advektion hos magnetiska fält och material utanför den domän där de verkar. Det visas att närvaron av ett utflöde, som t.ex. stjärnvindar eller galaktiska vindar i verkliga astrofysikaliska fall, mildrar så kallad "catastrophic quenching", en process som dämpar dynamos i högkonduktiva medier, och därigenom gör det möjligt för dynamon att fungera bättre.

(Thanks to Hans v. Zur-Mülen and Simon Candelaresi
for the translation from English)

Riassumendo

Molti dei corpi celesti che conosciamo sono magnetizzati: la Terra, molti tra i pianeti scoperti finora, il Sole e altre stelle, lo spazio interstellare, la Via Lattea e altre galassie. Molta strada ci separa da una totale comprensione di tutto ciò e questo lavoro intende essere un passo in questa direzione.

La dinamica del mezzo interstellare è dominata da eventi come le esplosioni di supernovae e venti stellari che possono essere schematizzati come flussi irrotazionali. La prima parte di questa tesi è stata dedicata all'analisi di alcune caratteristiche di questi flussi, con particolare enfasi su quale sia la loro influenza sulla diffusività megnetica turbolenta del mezzo. Si mostra come la diffusività aumenti, fatta eccezione per alcuni casi specifici. Inoltre abbiamo visto come i flussi irrotazionali possano sviluppare vorticità nel caso in cui avvengano in mezzi soggetti a rotazione o tensione tangenziale (shear), o nel caso in cui non siano barotropici.

Nella seconda parte abbiamo parlato di flussi elicoidali, di importanza basilare per il fenomeno dell'amplificazione dei campi magnetici, ossia la dinamo. L'elicità magnetica può sorgere a causa di un'instabilità: in questo lavoro ci siamo occupati dell'instabilità dei campi puramente toroidali, conosciuta anche come instabilità di Tayler. È possibile dare un'interpretazione topologica dell'elicità magnetica. Partendo da questo punto di vista, consapevoli che l'elicità magnetica è conservata in magnetoidrodinamica non resistiva, abbiamo mostrato come un sistema con elicità magnetica tenda a conservare le strutture magnetiche più a lungo di un suo analogo non elicoidale.

Nella parte conclusiva della tesi ci siamo occupati di dinamo. È possibile quantificare i coefficienti di trasporto per una dinamo con due tecniche differenti, ossia il metodo di campo imposto (imposed-field) e il metodo di campo test (test-field). Successivamente abbiamo analizzato come una dinamo venga affetta da trasporto di campo magnetico, o di materia, al di fuori del dominio in cui essa opera. Abbiamo dimostrato che la presenza di un efflusso, come un vento stellare o galattico in astrofisica, diminuisce la cosiddetta estinzione catastrofica della dinamo (catastrophic quenching), ossia l'attenuazione della dinamo in fluidi altamente conduttivi, e permette così una migliore efficienza del funzionamento di una dinamo.

Acknowledgements

Allá en mi infancia, yo estaba convencido de que a la luna
iba a parar todo lo que en la tierra se perdía.
Sin embargo, los astronautas no han encontrado sueños
peligrosos, ni promesas traicionadas, ni esperanzas rotas.
Si no están en la luna, ¿ dónde están?
¿Será que en la tierra no se perdieron?
¿Será que en la tierra se escondieron?

(Eduardo Galeano - Espejos)

Here we go. It seems that four years have passed in one second. But when I realize how many people have actually helped me in completing this thesis - and in how many ways! - I can feel that it was actually more than one second. It is true that in this world one can find dangerous dreams, but, thanks to the presence of some people, during these last years I have never been scared of trying to turn into reality the dreams that crowd my soul. This thesis is actually one of those.

Axel, whose energy is someway probably dynamo-generated and whose enthusiasm for science never reach saturation, for having showed me that, walking one step after another, one can actually cover a big distance.

Dhruba and his careful and clear way to teach the most difficult mysteries of hydromagnetism, making of them something someway human.

Karl-Heinz and Mattias, kind and humble people with limitless knowledge.

John, with whom I shared nice chats about physics, mountains, explorations and life.

Kambiz, Alexis, Garrelt, Gösta, whose doors have always been open for chat, advice and encouragement.

All the administrative staff at Nordita and the Astronomy Department, especially Hans who has a solution for every issue, from computers to apartments and ping pong.

All the people that contribute to make of NORDITA a great place for doing physics, relaxed and productive.

Andrea, Luca, Daniela e Alfio, per le grandi motivazioni e per avermi fatto sentire a casa a Catania.

Che Gustavo, maestro de español y de física, compañero de cervezas y ping pong.

Three great office mates:

Simon, compagno dei giri in bici, di cene a tarda sera a Nordita, di mille idee su una miriade di viaggi possibili e impensabili.

Jörn and his contageous smile.

Koen, who shared the office with me since the very beginning.

Javier, Angela, Nuria, Chicha, Jaime, Radek, Robert, Atefeh, Alessandra, Giuseppe, Francesco, Oliver, Sarah, Andong, CK, Thor, Alex, Mikaela and aMatti for being great company.

Lene&Leon, two beautiful people who love life.

Tim, for all the music played together and all the times you picked me up driving the boat on the baltic. Living together with the three of you on The Island has been unique.

All the people who gave me a ride in their cars and boats when hitchhiking for going back home on The Island, Storholmen, in the ice-walking and sea-crossing period of my life, at the same time helter-skelter and gold cave.

Sophie, for all the moments spent together that will lead towards new summits.

Elisa, Emilio, Karin e Domenico e la loro perfetta ospitalità a Goteborg. Dome, ricordi che 7-8 anni fa scrivesti per scherzo, in una mail, che avrei dovuto fare il dottorato in Svezia?

Francesca e Raphael, preziose certezze quotidiane.

Stefano, insostituibile compagno di discussioni di lavoro e qualche volta anche di hobby, dei mezzi chili di pasta, vino, soppressate, caciocavalli ...

Il Grandissimo Professore Fahmi, for all the lessons about life, whisky and work.

All the people in GalileMobile, an inspirational team full of ideas and energy. Hasta siempre Galileo!

Fede, Michi, Nestor y Eva, por ser una familia perfecta por el Chakano.

Ruben y Eduardo, por ser dos guías geniales para explorar el Sudamérica.

All of those who visited during these last 4 years, with whom I have shared the excitement of discovering Stockholm and Scandinavia, driving for hours, skiing, drinking, blathering and who knows in how many other ways. In particular Aloha, Silvia, Nacla, Fabio, Adeile, Luca, Dario, Mario, Antonio cap'e mongolfiera, Clemente, Giacomo, Tye, Gianlu.

And all the people who permitted me to always find a roof, all around Europe: Mario, Goffredo, Fabiano, Silvia, Ivana (e Martina!), Stefano, Beppe, Riccardo e i ragazzi del Rifugio Citelli sull'Etna.

I miei amici di una vita, Ric, Massimo, Matteo, Gipo, Paolié, Luigi, Toni, Simona, Rachele, Andrea, e Lorenzino, Davide, Giulia. Sapere che da qualche parte nel mondo siete sempre pronti ad ascoltarmi e sostenermi è quanto di più importante possa immaginare.

And then, all the way down to my roots and foundations: Sara, Tino, Antonella, my family.

All of you deserve a sincere, true Thank you! Gracias! Grazie! Tack! because the time spent together has been a great way to let this incredible jigsaw, that my life is, falling into place.

Stockholm - October 9, 2012

References

K. T. Alligood, T. D. Sauer, J. A. Yorke, and J. D. Crawford. Chaos: An Introduction to Dynamical Systems. *Physics Today*, 50:67, 1997. 26

S. A. Balbus and J. F. Hawley. A powerful local shear instability in weakly magnetized disks. I - Linear analysis. II - Nonlinear evolution. *Astrophys. J.*, 376:214–233, 1991. 4

R. Beck, A. Brandenburg, D. Moss, A. Shukurov, and D. Sokoloff. Galactic magnetism: recent developments and perspectives. *Ann. Rev. Astron. Astrophys.*, 34:155–206, 1996. 11, 15

R. Beck, A. Shukurov, D. Sokoloff, and R. Wielebinski. Systematic bias in interstellar magnetic field estimates. *Astron. Astrophys.*, 411:99–107, 2003. 13

R. Beck, A. Fletcher, A. Shukurov, A. Snodin, D. D. Sokoloff, M. Ehle, D. Moss, and V. Shoutenkov. Magnetic fields in barred galaxies. IV. NGC 1097 and NGC 1365. *Astron. Astrophys.*, 444:739–765, 2005. 13

M. A. Berger. Rigorous new limits on magnetic helicity dissipation in the solar corona. *Geophys. Astrophys. Fluid Dyn.*, 30:79–104, 1984. 32

M. A. Berger and G. B. Field. The topological properties of magnetic helicity. *J. Fluid Mech.*, 147:133–148, 1984. 29

D. Biskamp and W.-C. Müller. Decay laws for three-dimensional magnetohydrodynamic turbulence. *Phys. Rev. Lett.*, 83:2195–2198, 1999. 32

E. G. Blackman and A. Brandenburg. Dynamic nonlinearity in large-scale dynamos with shear. *Astrophys. J.*, 579:359–373, 2002. 39

A. Bonanno and V. Urpin. Stability of magnetic configurations containing the toroidal and axial fields. *Astron. Astrophys.*, 477:35–41, 2008a. 27

A. Bonanno and V. Urpin. Non-axisymmetric instability of axisymmetric magnetic fields. *Astron. Astrophys.*, 488:1–7, 2008b. 27

A. Bonanno and V. Urpin. Resonance instability of axially symmetric magnetostatic equilibria. *Phys. Rev. E*, 84(5):056310, 2011. 27

A. Bonanno and V. Urpin. Stability of the Toroidal Magnetic Field in Stellar Radiation Zones. *Astrophys. J.*, 747:137, 2012. 27

J. Braithwaite. The stability of toroidal fields in stars. *Astron. Astrophys.*, 453:687–698, 2006. 27

J. Braithwaite and Å. Nordlund. Stable magnetic fields in stellar interiors. *Astron. Astrophys.*, 450:1077–1095, 2006. 27

A. Brandenburg. Importance of magnetic helicity in dynamos. In R. Wielebinski and R. Beck, editors, *Cosmic Magnetic Fields*, volume 664 of *Lecture Notes in Physics, Berlin Springer Verlag*, page 219, 2005. 25

A. Brandenburg. Simulations of astrophysical dynamos. In A. Bonanno, E. de Gouveia Dal Pino, and A. G. Kosovichev, editors, *IAU Symposium*, volume 274 of *IAU Symposium*, pages 402–409, 2011. 5

A. Brandenburg and F. Del Sordo. Turbulent diffusion and galactic magnetism. *Highlights of Astronomy*, 15:432–433, 2010. 19

A. Brandenburg and K. J. Donner. The dependence of the dynamo alpha on vorticity. *Month. Not. Roy. Astron. Soc.*, 288:L29–L33, 1997. 18

A. Brandenburg and K. Subramanian. Minimal tau approximation and simulations of the alpha effect. *Astron. Astrophys.*, 439:835–843, 2005a. 38

A. Brandenburg and K. Subramanian. Strong mean field dynamos require supercritical helicity fluxes. *Astron. Nachr.*, 326:400–408, 2005b. 41

A. Brandenburg and K. Subramanian. Astrophysical magnetic fields and nonlinear dynamo theory. *Phys. Rep.*, 417:1–209, 2005c. 10, 11, 29, 30

A. Brandenburg, I. Tuominen, A. Nordlund, P. Pulkkinen, and R. F. Stein. 3-D simulation of turbulent cyclonic magneto-convection. *Astron. Astrophys.*, 232:277–291, 1990. 36

A. Brandenburg, A. Nordlund, R. F. Stein, and U. Torkelsson. Dynamo-generated turbulence and large-scale magnetic fields in a keplerian shear flow. *Astrophys. J.*, 446:741, 1995. 4

A. Brandenburg, K. Enqvist, and P. Olesen. Large-scale magnetic fields from hydromagnetic turbulence in the very early universe. *Phys. Rev. D*, 54:1291–1300, 1996. 29, 30

A. Brandenburg, K.-H. Rädler, M. Rheinhardt, and P. J. Käpylä. Magnetic Diffusivity Tensor and Dynamo Effects in Rotating and Shearing Turbulence. *Astrophys. J.*, 676:740–751, 2008a. 36

A. Brandenburg, K.-H. Rädler, M. Rheinhardt, and K. Subramanian. Magnetic Quenching of α and Diffusivity Tensors in Helical Turbulence. *Astrophys. J. Lett.*, 687:L49–L52, 2008b. 35

A. Brandenburg, S. Candelaresi, and P. Chatterjee. Small-scale magnetic helicity losses from a mean-field dynamo. *Month. Not. Roy. Astron. Soc.*, 398:1414–1422, 2009. 41

P. Chatterjee, G. Guerrero, and A. Brandenburg. Magnetic helicity fluxes in interface and flux transport dynamos. *Astron. Astrophys.*, 525:A5, 2011a. 41

P. Chatterjee, D. Mitra, M. Rheinhardt, and A. Brandenburg. Alpha effect due to buoyancy instability of a magnetic layer. *Astron. Astrophys.*, 534:A46, 2011b. 4, 36

M. Christensson, M. Hindmarsh, and A. Brandenburg . Scaling laws in decaying helical hydromagnetic turbulence. *Astron. Nachr.*, 326:393–399, 2005. 29, 30, 32

K. T. Chyży. Magnetic fields in dwarfs versus early-type galaxies. *Highlights of Astronomy*, 15:454–455, 2010. 13, 14

M. A. de Avillez and D. Breitschwerdt. Testing global ISM models: a detailed comparison of O VI column densities with FUSE and Copernicus data. *Astrophys. J. Lett.*, 634:L65–L68, 2005. 15

M. A. de Avillez and M.-M. Mac Low. Mixing timescales in a supernova-driven Interstellar Medium. *Astrophys. J.*, 581:1047–1060, 2002. 22

P. G. Drazin. *Introduction to Hydrodynamic Stability*. 2002. 25

R. Fares, J.-F. Donati, C. Moutou, M. Jardine, A. C. Cameron, A. F. Lanza, D. Bohlender, S. Dieters, A. F. Martínez Fiorenzano, A. Maggio, I. Pagano, and E. L. Shkolnik. Magnetic field, differential rotation and activity of the hot-Jupiter-hosting star HD 179949. *Month. Not. Roy. Astron. Soc.*, 423:1006–1017, 2012. 1

S. Fauve, S. Douady, and O. Thual. Drift instabilities of cellular patterns. *J. Phys. II*, 1:311–322, 1991. 28

C. Federrath, J. Roman-Duval, R. S. Klessen, W. Schmidt, and M.-M. Mac Low. Comparing the statistics of interstellar turbulence in simulations and observations. Solenoidal versus compressive turbulence forcing. *Astron. Astrophys.*, 512:A81, 2010. 18

C. Federrath, G. Chabrier, J. Schober, R. Banerjee, R. S. Klessen, and D. R. G. Schleicher. Mach number dependence of turbulent magnetic field amplification: solenoidal versus compressive flows. *Phys. Rev. Lett.*, 107(11):114504, 2011. 18

K. Ferriere. The full alpha-tensor due to supernova explosions and superbubbles in the Galactic disk. *Astrophys. J.*, 404:162–184, 1993. 36

G. B. Field and S. M. Carroll. Cosmological magnetic fields from primordial helicity. *Phys. Rev. D*, 62 (10):103008, 2000. 29, 30

A. Fletcher, R. Beck, A. Shukurov, E. M. Berkhuijsen, and C. Horellou. Magnetic fields and spiral arms in the galaxy M51. *Month. Not. Roy. Astron. Soc.*, 412:2396–2416, 2011. 12, 13

P. Frick, R. Stepanov, A. Shukurov, and D. Sokoloff. Structures in the rotation measure sky. *Month. Not. Roy. Astron. Soc.*, 325:649–664, 2001. 12

M. Gellert, G. Rüdiger, and R. Hollerbach. Helicity and α-effect by current-driven instabilities of helical magnetic fields. *Month. Not. Roy. Astron. Soc.*, 414:2696–2701, 2011. 27

A. D. Gilbert, U. Frisch, and A. Pouquet. Helicity is unnecessary for alpha effect dynamos, but it helps. *Geophys. Astrophys. Fluid Dyn.*, 42:151–161, 1988. 24

C. Gissinger, S. Fromang, and E. Dormy. Direct numerical simulations of the galactic dynamo in the kinematic growing phase. *Month. Not. Roy. Astron. Soc.*, 394:L84–L88, 2009. 15

O. Gressel. A mean-field approach to the propagation of field patterns in stratified magnetorotational turbulence. *Month. Not. Roy. Astron. Soc.*, 405:41–48, 2010. 36

O. Gressel, D. Elstner, U. Ziegler, and G. Rüdiger. Direct simulations of a supernova-driven galactic dynamo. *Astron. Astrophys.*, 486:L35–L38, 2008. 15

G. Guerrero, P. Chatterjee, and A. Brandenburg. Shear-driven and diffusive helicity fluxes in $\alpha\Omega$ dynamos. *Month. Not. Roy. Astron. Soc.*, 409:1619–1630, 2010. 41

G. E. Hale. On the Probable Existence of a Magnetic Field in Sun-Spots. *Astrophys. J.*, 28:315, 1908. 1

M. Hanasz, K. Otmianowska-Mazur, G. Kowal, and H. Lesch. Cosmic-ray-driven dynamo in galactic disks. A parameter study. *Astron. Astrophys.*, 498:335–346, 2009. 15

J. F. Hawley, C. F. Gammie, and S. A. Balbus. Local three-dimensional simulations of an accretion disk hydromagnetic dynamo. *Astrophys. J.*, 464:690, 1996. 4

D. W. Hughes and M. R. E. Proctor. Dynamo action in the presence of an imposed magnetic field. *Roy. Soc. Lond. Proc. Ser. A*, 465:1599–1616, 2009. 37

D. W. Hughes, F. Cattaneo, and K. Eun-Jin. Kinetic helicity, magnetic helicity and fast dynamo action. *Phys. Lett. A*, 223:167–172, 1996. 24

J. Ignatius, K. Kajantie, H. Kurki-Suonio, and M. Laine. Growth of bubbles in cosmological phase transitions. *Phys. Rev. D*, 49:3854–3868, 1994. 9

T. H. Jensen and M. S. Chu. Current drive and helicity injection. *Phys. Fluids*, 27:2881–2885, 1984. 29

T. Kahniashvili, A. Brandenburg, L. Campanelli, B. Ratra, and A. G. Tevzadze. Evolution of inflation-generated magnetic field through phase transitions. *ArXiv e-prints*, 2012. 18

K. Kajantie and H. Kurki-Suonio. Bubble growth and droplet decay in the quark-hadron phase transition in the early Universe. *Phys. Rev. D*, 34:1719–1738, 1986. 9

A. P. Kazantsev. Enhancement of a Magnetic Field by a Conducting Fluid. *Sov. J. Exp. Theor. Phys.*, 26: 1031, 1968. 24

N. Kleeorin, D. Moss, I. Rogachevskii, and D. Sokoloff. Helicity balance and steady-state strength of the dynamo generated galactic magnetic field. *Astron. Astrophys.*, 361:L5–L8, 2000. 41

N. I. Kleeorin and A. A. Ruzmaikin. *Magnetohydrodynamics*, 18:116, 1982. 37, 39

M. J. Korpi, A. Brandenburg, A. Shukurov, I. Tuominen, and Å. Nordlund. A supernova-regulated interstellar medium: simulations of the turbulent multiphase medium. *Astrophys. J. Lett.*, 514:L99–L102, 1999. 15

F. Krause and K.-H. Rädler. *Mean-field magnetohydrodynamics and dynamo theory*. Pergamon Press, Oxford, 1980. 6, 8, 9, 18

R. M. Kulsrud. A critical review of galactic dynamos. *Ann. Rev. Astron. Astrophys.*, 37:37–64, 1999. 11

B. C. Low. Solar Activity and the Corona. *Sol. Phys.*, 167:217–265, 1996. 29

M.-M. Mac Low. The Energy Dissipation Rate of Supersonic, Magnetohydrodynamic Turbulence in Molecular Clouds. *Astrophys. J.*, 524:169–178, 1999. 32

M.-M. Mac Low and A. Ferrara. Starburst-driven Mass Loss from Dwarf Galaxies: Efficiency and Metal Ejection. *Astrophys. J.*, 513:142–155, 1999. 11

M.-M. Mac Low and R. McCray. Superbubbles in disk galaxies. *Astrophys. J.*, 324:776–785, 1988. 11

M.-M. Mac Low, R. S. Klessen, A. Burkert, and M. D. Smith. Kinetic Energy Decay Rates of Supersonic and Super-Alfvénic Turbulence in Star-Forming Clouds. *Phys. Rev. Lett.*, 80:2754–2757, 1998. 32

M.-M. Mac Low, D. S. Balsara, J. Kim, and M. A. de Avillez. The distribution of pressures in a supernova-driven interstellar medium. I. Magnetized medium. *Astrophys. J.*, 626:864–876, 2005. 15, 32

P. Markey and R. J. Tayler. The adiabatic stability of stars containing magneticfields-II. Poloidal fields. *Month. Not. Roy. Astron. Soc.*, 163:77, 1973. 27

A. J. Mee and A. Brandenburg. Turbulence from localized random expansion waves. *Month. Not. Roy. Astron. Soc.*, 370:415–419, 2006. 16, 18

D. Mitra, P. J. Käpylä, R. Tavakol, and A. Brandenburg. Alpha effect and diffusivity in helical turbulence with shear. *Astron. Astrophys.*, 495:1–8, 2009. 36

H. K. Moffatt. The degree of knottedness of tangled vortex lines. *J. Fluid Mech.*, 35:117–129, 1969. 23, 31

H. K. Moffatt. *Magnetic field generation in electrically conducting fluids*. Cambridge, England, Cambridge University Press, 1978. 353 p., 1978. 6, 32

D. Moss and A. Shukurov. Turbulence and magnetic fields in elliptical galaxies. *Month. Not. Roy. Astron. Soc.*, 279:229–239, 1996. 43

E. N. Parker. Hydromagnetic Dynamo Models. *Astrophys. J.*, 122:293, 1955. 5, 6, 11

E. N. Parker. The generation of magnetic fields in astrophysical bodies. I. The dynamo equations. *Astrophys. J.*, 162:665, 1970. 6, 10

E. N. Parker. The generation of magnetic fields in astrophysical bodies. II. the galactic field. *Astrophys. J.*, 163:255, 1971. 10, 25

A. Pouquet, U. Frisch, and J. Leorat. Strong MHD helical turbulence and the nonlinear dynamo effect. *J. Fluid Mech.*, 77:321–354, 1976. 29, 33

K.-H. Rädler and M. Rheinhardt. Mean-field electrodynamics: critical analysis of various analytical approaches to the mean electromotive force. *Geophys. Astrophys. Fluid Dyn.*, 101:117–154, 2007. 8, 9

M. Rheinhardt and A. Brandenburg. Test-field method for mean-field coefficients with MHD background. *Astron. Astrophys.*, 520:A28+, 2010. 36

I. Rogachevskii and N. Kleeorin. Electromotive force and large-scale magnetic dynamo in a turbulent flow with a mean shear. *Phys. Rev. E*, 68(3):036301, 2003. 24

I. Rogachevskii and N. Kleeorin. Nonlinear theory of a “shear-current” effect and mean-field magnetic dynamos. *Phys. Rev. E*, 70(4):046310, 2004. 24

A. Rosen and J. N. Bregman. Global models of the interstellar medium in disk galaxies. *Astrophys. J.*, 440: 634, 1995. 15

G. Ruediger and L. L. Kichatinov. Alpha-effect and alpha-quenching. *Astron. Astrophys.*, 269:581–588, 1993. 36

D. M. Rust and A. Kumar. Helical magnetic fields in filaments. *Sol. Phys.*, 155:69–97, 1994. 29

D. M. Rust and A. Kumar. Evidence for helically kinked magnetic flux ropes in solar eruptions. *Astrophys. J. Lett.*, 464:L199+, 1996. 29

M. Schrinner, K.-H. Rädler, D. Schmitt, M. Rheinhardt, and U. Christensen. Mean-field view on rotating magnetoconvection and a geodynamo model. *Astron. Nachr.*, 326:245–249, 2005. 36, 37

M. Schrinner, K.-H. Rädler, D. Schmitt, M. Rheinhardt, and U. R. Christensen. Mean-field concept and direct numerical simulations of rotating magnetoconvection and the geodynamo. *Geophys. Astrophys. Fluid Dyn.*, 101:81–116, 2007. 36, 37

A. Shukurov and D. Sokoloff. *Astrophysical dynamos*. Elsevier B.V., 2008. 12

D. D. Sokoloff, A. A. Bykov, A. Shukurov, E. M. Berkhuijsen, R. Beck, and A. D. Poezd. Depolarization and Faraday effects in galaxies. *Month. Not. Roy. Astron. Soc.*, 299:189–206, 1998. 13

H. C. Spruit. Differential rotation and magnetic fields in stellar interiors. *Astron. Astrophys.*, 349:189–202, 1999. 27

M. Steenbeck, F. Krause, and K.-H. Rädler. Berechnung der mittleren LORENTZ-Feldstärke für ein elektrisch leitendes Medium in turbulenter, durch CORIOLIS-Kräfte beeinflußter Bewegung. *Zeitschrift Naturforschung Teil A*, 21:369, 1966. 11, 24

J. M. Stil. Magnetic Fields in Distant Spiral Galaxies. In D. J. Saikia, D. A. Green, Y. Gupta, & T. Venturi, editor, *Astron. Pac. Conf. Ser.*, volume 407 of *Astron. Soc. Pac. Conf. Ser.*, page 147, 2009. 11

J. M. Stone, J. F. Hawley, C. F. Gammie, and S. A. Balbus. Three-dimensional magnetohydrodynamical simulations of vertically stratified accretion disks. *Astrophys. J.*, 463:656, 1996. 4

S. Sur, A. Shukurov, and K. Subramanian. Galactic dynamos supported by magnetic helicity fluxes. *Month. Not. Roy. Astron. Soc.*, 377:874–882, 2007a. 41

S. Sur, K. Subramanian, and A. Brandenburg. Kinetic and magnetic α-effects in non-linear dynamo theory. *Month. Not. Roy. Astron. Soc.*, 376:1238–1250, 2007b. 7

S. Sur, A. Brandenburg, and K. Subramanian. Kinematic α-effect in isotropic turbulence simulations. *Month. Not. Roy. Astron. Soc.*, 385:L15–L19, 2008. 36, 37

H. L. Swinney and J. P. Gollub. *Hydrodynamic instabilities and the transition to turbulence*. 1985. 25

R. J. Tayler. The adiabatic stability of stars containing magnetic fields-I.Toroidal fields. *Month. Not. Roy. Astron. Soc.*, 161:365, 1973. 27

J. B. Taylor. Relaxation of toroidal plasma and generation of reverse magnetic fields. *Phys. Rev. Lett.*, 33: 1139–1141, 1974. 29

H. Umezawa, H. Matsumoto, and M. Tachiki. *Thermo field dynamics and condensed states.* 1982. 25

S. I. Vainshtein and F. Cattaneo. Nonlinear restrictions on dynamo action. *Astrophys. J.*, 393:165–171, 1992. 37, 39

S. I. Vainshtein and A. A. Ruzmaikin. Generation of the large-scale galactic magnetic field. *Astron. Zh.*, 48:902, 1971. 10

E. T. Vishniac and A. Brandenburg. An Incoherent alpha - Omega Dynamo in Accretion Disks. *Astrophys. J.*, 475:263, 1997. 24

E. T. Vishniac and J. Cho. Magnetic helicity conservation and astrophysical dynamos. *Astrophys. J.*, 550: 752–760, 2001. 24

Z. Warhaft. Passive scalars in turbulent flows. *Ann. Rev. Fluid Mech.*, 32:203–240, 2000. 18

L. Woltjer. A theorem on force-free magnetic fields. *Proc. Nat. Acad. Sci.*, 44:489–491, 1958. 29, 31

E. G. Zweibel and C. Heiles. Magnetic fields in galaxies and beyond. *Nature*, 385:131–136, 1997. 12

I

PHYSICAL REVIEW E **84**, 046321 (2011)

Mean-field diffusivities in passive scalar and magnetic transport in irrotational flows

Karl-Heinz Rädler,[1,2,3,*] Axel Brandenburg,[2,4,3] Fabio Del Sordo,[2,4] and Matthias Rheinhardt[2]
[1]*Astrophysikalisches Institut Potsdam, An der Sternwarte 16, D-14482 Potsdam, Germany*
[2]*NORDITA, AlbaNova University Center, Roslagstullsbacken 23, SE-10691 Stockholm, Sweden*
[3]*Kavli Institute for Theoretical Physics, University of California, Santa Barbara, California 93106, USA*
[4]*Department of Astronomy, Stockholm University, SE-10691 Stockholm, Sweden*

(Received 8 April 2011; revised manuscript received 13 June 2011; published 25 October 2011)

Certain aspects of the mean-field theory of turbulent passive scalar transport and of mean-field electrodynamics are considered with particular emphasis on aspects of compressible fluids. It is demonstrated that the total mean-field diffusivity for passive scalar transport in a compressible flow may well be smaller than the molecular diffusivity. This is in full analogy to an old finding regarding the magnetic mean-field diffusivity in an electrically conducting turbulently moving compressible fluid. These phenomena occur if the irrotational part of the motion dominates the vortical part, the Péclet or magnetic Reynolds number is not too large, and, in addition, the variation of the flow pattern is slow. For both the passive scalar and the magnetic cases several further analytical results on mean-field diffusivities and related quantities found within the second-order correlation approximation are presented, as well as numerical results obtained by the test-field method, which applies independently of this approximation. Particular attention is paid to nonlocal and noninstantaneous connections between the turbulence-caused terms and the mean fields. Two examples of irrotational flows, in which interesting phenomena in the above sense occur, are investigated in detail. In particular, it is demonstrated that the decay of a mean scalar in a compressible fluid under the influence of these flows can be much slower than without any flow, and can be strongly influenced by the so-called memory effect, that is, the fact that the relevant mean-field coefficients depend on the decay rates themselves.

DOI: 10.1103/PhysRevE.84.046321 PACS number(s): 47.65.−d, 52.65.Kj, 52.30.Cv, 52.35.Vd

I. INTRODUCTION

Many investigations of transport processes in turbulently moving fluids have been done in the framework of the mean-field concept. A simple example is the transport of a passive scalar quantity like the number density of particles in a turbulent fluid [1–5]. Another important example is the magnetic-field transport in electrically conducting turbulent fluids. The widely elaborated mean-field electrodynamics, or magnetofluiddynamics, delivers in particular the basis of the mean-field theory of cosmic dynamos [6,7].

The original equation governing the behavior of a passive scalar in a fluid contains a diffusion term with a diffusion coefficient, say κ. In the corresponding mean-field equation there appears, in the simple case of isotropic turbulence, the effective mean-field diffusivity $\kappa + \kappa_t$ in place of κ, where κ_t is determined by the turbulent motion and therefore sometimes called the "turbulent diffusivity." Likewise, the induction equation governing the magnetic field in an electrically conducting fluid contains a diffusion term with the magnetic diffusivity η. In the mean-field induction equation there appears, again for isotropic turbulence, $\eta + \eta_t$ in place of η, where η_t is again determined by the turbulent motion and sometimes called the "turbulent magnetic diffusivity."

At first glance it seems plausible that turbulence enhances the effective diffusion, corresponding to positive κ_t and η_t. In a compressible fluid, however, this is not always true. A counterexample for the magnetic case has been long known. Represent the velocity in the form $\boldsymbol{u} = \nabla \times \boldsymbol{\psi} + \nabla\phi$ by a vector potential $\boldsymbol{\psi}$ satisfying the gauge condition $\nabla \cdot \boldsymbol{\psi} = 0$ and a scalar potential ϕ. Let u_c, λ_c, and τ_c be a characteristic magnitude, length, and time, respectively, of the velocity field. Assume that the magnetic Reynolds number $u_c\lambda_c/\eta$ is small compared to unity and that τ_c considerably exceeds the free-decay time λ_c^2/η of a magnetic structure of size λ_c. Then it turns out [7–10] that

$$\eta_t = \frac{1}{3\eta}(\overline{\boldsymbol{\psi}^2} - \overline{\phi^2}). \tag{1}$$

That is, negative η_t are certainly possible if the part of $\boldsymbol{u}$ determined by the potential ϕ dominates. Then, the mean-field diffusivity is smaller than the molecular one. This surprising result deserves more thorough examination, which is indeed one of the motivations behind this paper. Here it will be shown that a result analogous to (1) applies to κ_t, too. These results apply not only to turbulence in the narrow sense, but also to other kinds of random and even nonrandom (including steady) flows.

Results of that kind might be of some interest for the turbulence in the interstellar medium. It is widely believed that it is mostly driven by supernova explosions [11–14]. In this case the driving force, and so the flow, too, could have noticeable irrotational parts, i.e., parts that are described by gradients of potentials. However, when rotation or shear is important, or the Mach number is close to or in excess of unity and the baroclinic effect present, vorticity production becomes progressively more important—even when the forcing of the flow is purely irrotational [15].

Another possible application of such results could be in studies of the very early Universe, where phase transition bubbles are believed to be generated in connection with the electroweak phase transition [16,17]. The relevant equation

---

[*] khraedler@arcor.de

of state is that of an ultrarelativistic gas with constant sound speed $c/\sqrt{3}$, where c is the speed of light. This is a barotropic equation of state, so the baroclinic term vanishes. Hence, there is no obvious source of vorticity in the (nonrelativistic) bulk motion inside these bubbles so that it should be essentially irrotational. This changes, however, if there is a magnetic field of significant strength, because the resulting Lorentz force is in general not a potential one.

In Sec. II of this paper we give an outline of the mean-field theory of passive scalar transport, prove the passive-scalar version of relation (1), and derive some further results in the framework of the second-order correlation approximation. We also give an analogous outline of mean-field electrodynamics and present some specific results. In Sec. III we formulate the mean-field concept for the case of nonlocal relationships between the turbulence-dependent terms in the mean-field equations and the mean fields, and we explain the test-field method for the determination of transport coefficients. In Sec. IV we then present analytical and numerical results for two simple models which reflect mean-field properties of irrotational flows. Finally a discussion of our findings is given in Sec. V.

II. OUTLINE OF MEAN-FIELD THEORIES

A. Passive scalar transport

Let us focus attention on passive scalars C which describe the concentration of, e.g., dust or chemicals per unit volume of a fluid. We assume that C satisfies

$$\partial_t C + \nabla \cdot (\boldsymbol{U} C) - \nabla \cdot (\kappa \nabla C) = 0, \tag{2}$$

where $\boldsymbol{U}$ is the fluid velocity and κ a diffusion coefficient, which in general depends on both the mass density ϱ and the temperature T. In the case of an incompressible isothermal fluid, Eq. (2) applies with κ independent of position so that $\nabla \cdot (\kappa \nabla C)$ turns into $\kappa \Delta C$. We want, however, to include compressible fluids, too. We may justify (2), e.g., if C describes the concentration of an admixture of light particles in a compressible isothermal fluid. The diffusion coefficient is then given by $\kappa = f(T)/\varrho$, with some function f; see [18], Chap. 11, p. 39. We expect the validity of (2) with some dependency of κ on ϱ also in more general cases. In a flow of such a fluid, its density, even when uniform initially, will in general become position dependent in the course of time. For the sake of simplicity we shall nevertheless ignore any consequence of inhomogeneous density. Hence, our results are applicable only for either the limited time interval or the limited velocity amplitude range for which the density inhomogeneity is still negligible. Overcoming these limitations requires a theory which includes momentum and continuity equations and is beyond the scope of this paper.

With this in mind we consider, in what follows, κ always as independent of position, and replace (2) by

$$\partial_t C + \nabla \cdot (\boldsymbol{U} C) - \kappa \Delta C = 0. \tag{3}$$

We further assume that the fluid motion and therefore also C show turbulent fluctuations, define mean quantities like $\overline{C}$ or $\overline{\boldsymbol{U}}$ by a proper averaging procedure which ensures the validity of the Reynolds rules, and put $C = \overline{C} + c$ and $\boldsymbol{U} = \overline{\boldsymbol{U}} + \boldsymbol{u}$. The evolution of $\overline{C}$ is then governed by

$$\partial_t \overline{C} + \nabla \cdot (\overline{\boldsymbol{U}}\, \overline{C}) + \overline{\mathcal{G}} - \kappa \Delta \overline{C} = 0 \tag{4}$$

with

$$\overline{\mathcal{G}} = \nabla \cdot \overline{\boldsymbol{\mathcal{F}}}, \quad \overline{\boldsymbol{\mathcal{F}}} = \overline{\boldsymbol{u} c}\,. \tag{5}$$

For c we have

$$\partial_t c + \nabla \cdot [\boldsymbol{u}\overline{C} + \overline{\boldsymbol{U}} c + (\boldsymbol{u} c)'] - \kappa \Delta c = 0, \tag{6}$$

where $(\boldsymbol{u}c)'$ stands for $\boldsymbol{u}c - \overline{\boldsymbol{u}c}$. Clearly, $\overline{\boldsymbol{\mathcal{F}}}$ is a functional of $\boldsymbol{u}$, $\overline{\boldsymbol{U}}$, and $\overline{C}$ in the sense that $\overline{\boldsymbol{\mathcal{F}}}$ at a given point in space and time depends in general on $\boldsymbol{u}$, $\overline{\boldsymbol{U}}$, and $\overline{C}$ at other points, too. This functional is linear in $\overline{C}$.

Let us, for simplicity, consider the case $\overline{\boldsymbol{U}} = \boldsymbol{0}$ and assume that $\boldsymbol{u}$ corresponds to homogeneous turbulence. Until further notice we adopt the assumption that $\overline{C}$ varies only weakly in space and time so that $\overline{\boldsymbol{\mathcal{F}}}$, at a given point in space and time, can be simply represented as a function of $\overline{C}$ and its first spatial derivatives, i.e., $\nabla\overline{C}$, taken just at this point. We will refer to this assumption as "perfect scale separation." We may then conclude that

$$\overline{\mathcal{F}}_i = \gamma_i^{(C)} \overline{C} - \kappa_{ij} \frac{\partial \overline{C}}{\partial x_j}, \tag{7}$$

with $\gamma_i^{(C)}$ and κ_{ij} being coefficients determined by $\boldsymbol{u}$, which are independent of position.[1]

Clearly, $\gamma_i^{(C)}$ gives the velocity of advection of $\overline{C}$, and κ_{ij} is a contribution to the total mean-field diffusivity tensor, which is then equal to $\kappa\delta_{ij} + \kappa_{ij}$. From (7) we conclude that

$$\overline{\mathcal{G}} = \gamma_i^{(C)} \frac{\partial \overline{C}}{\partial x_i} - \kappa_{ij} \frac{\partial^2 \overline{C}}{\partial x_i \partial x_j}. \tag{8}$$

Of course, κ_{ij} may be assumed to be symmetric in i and j. For isotropic turbulence we have $\gamma_i^{(C)} = 0$ and $\kappa_{ij} = \kappa_t \delta_{ij}$ with some constant coefficient κ_t so that

$$\overline{\boldsymbol{\mathcal{F}}} = -\kappa_t \nabla \overline{C}, \tag{9}$$

and consequently

$$\overline{\mathcal{G}} = -\kappa_t \Delta \overline{C}. \tag{10}$$

Although we have defined $\boldsymbol{u}$ as the turbulent velocity, only its statistical symmetry properties like homogeneity or isotropy have in fact been utilized. Here and later in this paper, the term "turbulence" should, accordingly, be understood in a wider sense, including random or even nonrandom flows with such properties.

---

[1] Consequently, a spatially constant $\overline{C}$ is not influenced by $\boldsymbol{u}$ and thus stationary; nevertheless it causes a fluctuation c that is, for stationary $\boldsymbol{u}$, again stationary. Hence, there is then a nontrivial *stationary* solution of (2) with constant average. For potential flows $\boldsymbol{u} = \nabla\phi$ it can be given explicitly as $C = C_0 \exp(\phi/\kappa)$. We thank our referee for having made us aware of it.

In specific calculations often the second-order correlation approximation (SOCA) is used. It consists in neglecting the term $(\boldsymbol{u}c)'$ in Eq. (6) for c, so that this equation turns into

$$\partial_t c - \kappa \Delta c = -\nabla \cdot (\boldsymbol{u}\overline{C}). \tag{11}$$

The applicability of this approximation is restricted to not too large velocities $\boldsymbol{u}$. If we characterize the velocity field again by a typical magnitude u_c and by typical length and time scales λ_c and τ_c, respectively, we may define the parameter $q_\kappa = \lambda_c^2/\kappa\tau_c$, which gives the ratio of the free-decay time λ_c^2/κ to τ_c; further, the Péclet number $\mathrm{Pe} = u_c\lambda_c/\kappa$ and the Strouhal number $\mathrm{St} = u_c\tau_c/\lambda_c$. Note that $q_\kappa = \mathrm{Pe}/\mathrm{St}$. A sufficient condition for the applicability of SOCA in the case $q_\kappa \gg 1$ reads $\mathrm{St} \ll 1$; in the case $q_\kappa \ll 1$ it reads $\mathrm{Pe} \ll 1$.

B. Diffusivity in a special case

Let us focus attention on homogeneous isotropic turbulence and determine κ_t in a limiting case. Since κ_t depends neither on $\overline{C}$ nor on position, we may choose simply $\overline{C} = \boldsymbol{G}\cdot\boldsymbol{x}$ with a constant $\boldsymbol{G}$ so that $\nabla\overline{C} = \boldsymbol{G}$, and consider at the end only $\boldsymbol{x} = \boldsymbol{0}$. We represent $\boldsymbol{u}$ in the form

$$\boldsymbol{u} = \nabla \times \boldsymbol{\psi} + \nabla\phi, \quad \nabla\cdot\boldsymbol{\psi} = 0, \tag{12}$$

by a vector potential $\boldsymbol{\psi}$ and a scalar potential ϕ, and set further

$$\boldsymbol{\psi} = \nabla \times \boldsymbol{\chi}, \quad \phi = -\nabla\cdot\boldsymbol{\chi}, \tag{13}$$

where we utilized the freedom in defining the new vector potential $\boldsymbol{\chi}$ such that both $\boldsymbol{\psi}$ and ϕ are now derived from this single quantity. We then have

$$\boldsymbol{u} = -\nabla^2\boldsymbol{\chi}. \tag{14}$$

We further assume that $\boldsymbol{u}$ varies so slowly in time that we may consider it as independent of t. Finally we adopt SOCA so that (11) applies. We may write it in the form

$$\Delta(\kappa c - X) = 0 \tag{15}$$

with

$$X = -\boldsymbol{\chi}\cdot\boldsymbol{G} - 2\nabla\Phi\cdot\boldsymbol{G} + \phi\,\boldsymbol{G}\cdot\boldsymbol{x}, \quad \Delta\Phi = \phi. \tag{16}$$

From (15) we conclude that

$$c = \frac{1}{\kappa}X + c_0, \tag{17}$$

where c_0 is some constant. Calculating then $\overline{\boldsymbol{\mathcal{F}}}$ at $\boldsymbol{x} = \boldsymbol{0}$ we obtain

$$\overline{\mathcal{F}}_i = -\frac{1}{\kappa}(\overline{u_i\chi_k} + 2\overline{u_i\partial\Phi/\partial x_k})G_k. \tag{18}$$

Due to the isotropy of the turbulence we have

$$\overline{u_i\chi_k} = \tfrac{1}{3}\overline{\boldsymbol{u}\cdot\boldsymbol{\chi}}\,\delta_{ik}, \quad \overline{u_i\partial\Phi/\partial x_k} = \tfrac{1}{3}\overline{\boldsymbol{u}\cdot\nabla\Phi}\,\delta_{ik}. \tag{19}$$

Using (12) and (13) and considering the homogeneity of the turbulence, we find

$$\overline{\boldsymbol{u}\cdot\boldsymbol{\chi}} = \overline{\boldsymbol{\psi}^2} + \overline{\phi^2}, \quad \overline{\boldsymbol{u}\cdot\nabla\Phi} = -\overline{\phi^2}. \tag{20}$$

Consequently we have

$$\overline{\boldsymbol{\mathcal{F}}} = -\frac{1}{3\kappa}(\overline{\boldsymbol{\psi}^2} - \overline{\phi^2})\boldsymbol{G}. \tag{21}$$

Comparing this with (9), we obtain

$$\kappa_{\mathrm{t}} = \frac{1}{3\kappa}(\overline{\boldsymbol{\psi}^2} - \overline{\phi^2}), \tag{22}$$

a result in full analogy to (1). For an incompressible flow κ_t can never be negative, while it can never be positive for an irrotational flow.

C. Relations for transport coefficients

We consider now homogeneous, but not necessarily isotropic turbulence and use a Fourier transformation of the form

$$F(\boldsymbol{x},t) = \iint \hat{F}(\boldsymbol{k},\omega)\exp(i\boldsymbol{k}\cdot\boldsymbol{x} - i\omega t)\,d^3k\,d\omega. \tag{23}$$

Further we adopt SOCA. Then standard derivations (see, e.g., [7]) yield

$$\gamma_i^{(C)} = -\iint \frac{ik_k}{\kappa k^2 - i\omega}\hat{Q}_{ik}(\boldsymbol{k},\omega)\,d^3k\,d\omega, \tag{24}$$

$$\kappa_{ij} = \iint \left(\frac{\hat{Q}_{ij}(\boldsymbol{k},\omega) + \hat{Q}_{ji}(\boldsymbol{k},\omega)}{2(\kappa k^2 - i\omega)} - \frac{2\kappa[\hat{Q}_{ik}(\boldsymbol{k},\omega)k_j + \hat{Q}_{jk}(\boldsymbol{k},\omega)k_i]k_k}{(\kappa k^2 - i\omega)^2} \right) d^3k\,d\omega, \tag{25}$$

where $\hat{Q}_{ij}(\boldsymbol{k},\omega)$ is the Fourier transform of the correlation tensor $Q_{ij}(\boldsymbol{\xi},\tau)$, defined by

$$Q_{ij}(\boldsymbol{\xi},\tau) = \overline{u_i(\boldsymbol{x},t)\,u_j(\boldsymbol{x}+\boldsymbol{\xi},t+\tau)}. \tag{26}$$

Since $Q_{ij}(\boldsymbol{\xi},\tau)$ is real, we have $\hat{Q}_{ij}(\boldsymbol{k},\omega) = \hat{Q}_{ij}^*(-\boldsymbol{k}, -\omega)$, where the asterisk means complex conjugation.

We recall here Bochner's theorem (see, e.g., [7], Chap. 6), according to which, for any homogeneous turbulence, $\hat{Q}_{ij}(\boldsymbol{k},\omega)$ is positive semidefinite, that is,

$$\hat{Q}_{ij}(\boldsymbol{k},\omega)\,X_i\,X_j^* \geqslant 0 \tag{27}$$

for any complex vector $\boldsymbol{X}$.

Assume first incompressible turbulence, that is, $\nabla\cdot\boldsymbol{u} = 0$. Then we have

$$\hat{Q}_{ij}k_j = 0, \quad \hat{Q}_{ij}k_i = 0. \tag{28}$$

In this case, (24) yields $\gamma_i^{(C)} = 0$ (even if the flow is not isotropic), and (25) turns into

$$\kappa_{ij} = \frac{1}{2}\iint \frac{1}{\kappa k^2 - i\omega}\left(\hat{Q}_{ij}(\boldsymbol{k},\omega) + \hat{Q}_{ji}(\boldsymbol{k},\omega)\right)d^3k\,d\omega. \tag{29}$$

From (27) and (29) we may conclude that κ_{ij} is positive semidefinite. If the flow is statistically isotropic we have $\kappa_{ij} = \kappa_t\delta_{ij}$ and we may conclude that κ_{t} is non-negative.

Assume next irrotational turbulence, that is, $\boldsymbol{u} = \nabla\phi$ with any potential ϕ. Then we have

$$\hat{Q}_{ij}(\boldsymbol{k},\omega) = k_ik_j\hat{R}(\boldsymbol{k},\omega) \tag{30}$$

with some real function $\hat{R}$ related to ϕ. Owing to (27), $\hat{R}$ must be non-negative (cf. [7], Chap. 6). With (24), (25), and (30) we find

$$\gamma_i^{(C)} = -\iint \frac{ik_i \hat{R}(\boldsymbol{k},\omega)k^2}{\kappa k^2 - i\omega}\, d^3k\, d\omega, \tag{31}$$

$$\kappa_{ij} = -\iint \frac{(3\kappa k^2 + i\omega)k_i k_j \hat{R}(\boldsymbol{k},\omega)}{(\kappa k^2 - i\omega)^2}\, d^3k\, d\omega. \tag{32}$$

For statistically isotropic flows $\hat{R}$ depends only via k on $\boldsymbol{k}$. Hence, we obtain as expected $\gamma_i^{(C)} = 0$ and

$$\kappa_t = -\frac{1}{3}\iint \frac{(3\kappa k^2 + i\omega)k^2 \hat{R}(k,\omega)}{(\kappa k^2 - i\omega)^2}\, d^3k\, d\omega. \tag{33}$$

Assume now in addition that the variations of $\boldsymbol{u}$ in time are slow. Then $\hat{R}$ is markedly different from zero only for very small ω. Consequently, κ_t is nonpositive.

D. Magnetic-field transport

We now consider a magnetic field $\boldsymbol{B}$ in a homogeneous electrically conducting fluid and assume that it is governed by

$$\partial_t \boldsymbol{B} - \nabla \times (\boldsymbol{U} \times \boldsymbol{B}) - \eta\nabla^2 \boldsymbol{B} = \boldsymbol{0}, \quad \nabla\cdot\boldsymbol{B} = 0, \tag{34}$$

with $\boldsymbol{U}$ being again the velocity and η the magnetic diffusivity of the fluid. Focusing attention on a turbulent situation, we define again mean fields, in particular $\overline{\boldsymbol{B}}$ and $\overline{\boldsymbol{U}}$, and put $\boldsymbol{B} = \overline{\boldsymbol{B}} + \boldsymbol{b}$ and $\boldsymbol{U} = \overline{\boldsymbol{U}} + \boldsymbol{u}$. Then we have

$$\partial_t \overline{\boldsymbol{B}} - \nabla \times (\overline{\boldsymbol{U}} \times \overline{\boldsymbol{B}} + \overline{\boldsymbol{\mathcal{E}}}) - \eta\nabla^2 \overline{\boldsymbol{B}} = \boldsymbol{0}, \quad \nabla\cdot\overline{\boldsymbol{B}} = 0, \tag{35}$$

where

$$\overline{\boldsymbol{\mathcal{E}}} = \overline{\boldsymbol{u}\times\boldsymbol{b}} \tag{36}$$

and

$$\partial_t \boldsymbol{b} - \nabla \times [\overline{\boldsymbol{U}} \times \boldsymbol{b} + \boldsymbol{u} \times \overline{\boldsymbol{B}} + (\boldsymbol{u}\times\boldsymbol{b})'] - \eta\nabla^2 \boldsymbol{b} = \boldsymbol{0}, \qquad \nabla\cdot\boldsymbol{b} = 0. \tag{37}$$

Here $(\boldsymbol{u}\times\boldsymbol{b})'$ means $\boldsymbol{u}\times\boldsymbol{b} - \overline{\boldsymbol{u}\times\boldsymbol{b}}$. The mean electromotive force $\overline{\boldsymbol{\mathcal{E}}}$ due to the fluctuations $\boldsymbol{u}$ and $\boldsymbol{b}$ is a functional of $\boldsymbol{u}$, $\overline{\boldsymbol{U}}$, and $\overline{\boldsymbol{B}}$, which is linear in $\overline{\boldsymbol{B}}$.

Let us restrict ourselves again to $\overline{\boldsymbol{U}} = \boldsymbol{0}$. Assuming perfect scale separation, defined analogously to the passive scalar case considered before, we may conclude that

$$\overline{\mathcal{E}}_i = a_{ij}\overline{B}_j - \eta_{ij}(\nabla\times\overline{\boldsymbol{B}})_j - c_{ijk}(\nabla\overline{\boldsymbol{B}})^s_{jk}, \tag{38}$$

where $(\nabla\overline{\boldsymbol{B}})^s_{jk} = \frac{1}{2}(\partial\overline{B}_j/\partial x_k + \partial\overline{B}_k/\partial x_j)$. Here a_{ij}, η_{ij}, and c_{ijk} are quantities determined by $\boldsymbol{u}$. [Instead of the traditional b_{ijk} we use here $\eta_{ij} = \frac{1}{2}b_{imn}\epsilon_{jmn}$ and $c_{ijk} = -\frac{1}{2}(b_{ijk} + b_{ikj})$.][2]

In this context SOCA consists in dropping the term $(\boldsymbol{u}\times\boldsymbol{b})'$ in (37) so that

$$\partial_t \boldsymbol{b} - \eta\nabla^2\boldsymbol{b} = \nabla\times(\boldsymbol{u}\times\overline{\boldsymbol{B}}), \quad \nabla\cdot\boldsymbol{b} = 0. \tag{39}$$

Sufficient conditions under which this applies are again analogous to those explained below (11). We have only to replace the parameter q_κ by $q_\eta = \lambda_c^2/\eta\tau_c$ and the Péclet number Pe by the magnetic Reynolds number $\mathrm{Rm} = u_c\lambda_c/\eta$. Note that $q_\eta = \mathrm{Rm}/\mathrm{St}$.

The relevant relations for a_{ij}, η_{ij}, and c_{ijk}, derived under SOCA for homogeneous turbulence, are given in the Appendix. Let us restrict ourselves here to homogeneous nonhelical turbulence. Then the correlation tensor $\hat{Q}_{ij}$ may not contain any pseudoscalar or any other pseudoquantity. As a consequence, the symmetric part of a_{ij} and the antisymmetric part of η_{ij} are equal to zero, and we have

$$\begin{aligned} a_{ij} &= \epsilon_{ijk}\gamma_k^{(B)}, \\ \gamma_i^{(B)} &= \frac{1}{2}\iint ik_k \frac{\hat{Q}_{ik}(\boldsymbol{k},\omega) + \hat{Q}_{ki}(\boldsymbol{k},\omega)}{\eta k^2 - i\omega}\, d^3k\, d\omega, \end{aligned} \tag{40}$$

and

$$\eta_{ij} = \frac{1}{2}\iint \left(\frac{[2\delta_{ij}\delta_{kl} - (\delta_{ik}\delta_{jl} + \delta_{jk}\delta_{il})]\hat{Q}_{kl}(\boldsymbol{k},\omega)}{2(\eta k^2 - i\omega)} - \frac{\eta[2\delta_{ij}k_k - (k_i\delta_{jk} + k_j\delta_{ik})]k_l\hat{Q}_{kl}(\boldsymbol{k},\omega)}{(\eta k^2 - i\omega)^2} \right) d^3k\, d\omega. \tag{41}$$

Moreover, c_{ijk} is equal to zero.

Consider now incompressible turbulence, for which (28) applies. Then we have, even in the anisotropic case, $\gamma_i^{(B)} = 0$ [see also [7], Chap. 7.1, statement (i)]. Furthermore,

$$\eta_{ij} = \frac{1}{4}\iint \frac{[2\delta_{ij}\delta_{kl} - (\delta_{ik}\delta_{jl} + \delta_{jk}\delta_{il})]\hat{Q}_{kl}(\boldsymbol{k},\omega)}{\eta k^2 - i\omega}\, d^3k\, d\omega, \tag{42}$$

which, together with (27), implies that η_{ij} is positive semidefinite. If the turbulence is in addition isotropic, we have $\eta_{ij} = \eta_t\delta_{ij}$ with

$$\eta_t = \frac{1}{3}\iint \frac{\hat{Q}_{kk}(\boldsymbol{k},\omega)}{\eta k^2 - i\omega}\, d^3k\, d\omega. \tag{43}$$

Like κ_t, η_t also has to be non-negative [see also [7], Chap. 7.4, Eq. (7.47)].

Consider next irrotational turbulence, for which (30) applies. Then,

$$\gamma_i^{(B)} = \iint \frac{ik_i k^2 \hat{R}(\boldsymbol{k},\omega)}{\eta k^2 - i\omega}\, d^3k\, d\omega, \tag{44}$$

$$\eta_{ij} = -\frac{1}{2}\iint \frac{(\eta k^2 + i\omega)(k^2\delta_{ij} - k_i k_j)\hat{R}(\boldsymbol{k},\omega)}{(\eta k^2 - i\omega)^2}\, d^3k\, d\omega. \tag{45}$$

If the variations of $\boldsymbol{u}$ in time are slow, $\hat{R}$ is markedly different from zero only for small ω. Then it can be readily shown that η_{ij} is negative semidefinite. In the isotropic case, $\hat{R}$ depends, as already noted above, only via k on $\boldsymbol{k}$. Therefore we have, independent of the time behavior of $\boldsymbol{u}$, $\gamma_i^{(B)} = 0$ and

$$\eta_\mathrm{t} = -\frac{1}{3}\iint \frac{(\eta k^2 + i\omega)\hat{R}(k,\omega)k^2}{(\eta k^2 - i\omega)^2}\, d^3k\, d\omega. \tag{46}$$

If then the time variations of $\boldsymbol{u}$ are slow, η_t has to be nonpositive [see also [7], Chap. 7, Eq. (7.51)].

---

[2] In analogy to what was noted for the passive scalar case, stationary solutions of (34) with constant mean parts of $\boldsymbol{B}$ are conceivable.

III. GENERALIZATIONS AND TEST-FIELD PROCEDURE

A. Lack of scale separation

In applications, the assumption of perfect scale separation, used so far, might be violated; see, e.g., [19]. We now relax it. Considering first again the passive scalar case we admit now a dependence of $\overline{\boldsymbol{\mathcal{F}}}$, at a given point in space, on $\overline{C}$ (or its derivatives) at other points, that is, we admit a nonlocal connection between $\overline{\boldsymbol{\mathcal{F}}}$ and $\overline{C}$. For the sake of simplicity, however, we assume until further notice that $\overline{\boldsymbol{\mathcal{F}}}$, at a given time, is only connected with $\overline{C}$ (or its derivatives) at the same time, that is, we remain with an instantaneous connection between $\overline{\boldsymbol{\mathcal{F}}}$ and $\overline{C}$. Again, we restrict ourselves to homogeneous turbulence.

We further assume here, again for simplicity, that mean fields are defined as averages over all x and y. Hence, they depend on z and t only.

In what follows it is then sufficient to consider the z component of $\overline{\boldsymbol{\mathcal{F}}}$ only. As a straightforward generalization of the relation for $\overline{\mathcal{F}}_z$ contained in (7), with derivatives with respect to z only, we now write

$$\overline{\mathcal{F}}_z(z,t) = \int \left(\gamma_z^{(C)}(\zeta)\, \overline{C}(z-\zeta,t) - \kappa_{zz}(\zeta) \frac{\partial \overline{C}(z-\zeta,t)}{\partial z} \right) d\zeta, \tag{47}$$

with two functions $\gamma_z^{(C)}(\zeta)$ and $\kappa_{zz}(\zeta)$, which are assumed to be symmetric in ζ, and with the integration being over all ζ. (In the case of inhomogeneous turbulence, $\gamma_z^{(C)}$ and κ_{zz} would also depend on z.) With the specifications $\gamma_z^{(C)}(\zeta) = \gamma_z^{(C)}\delta(\zeta)$ and $\kappa_{zz}(\zeta) = \kappa_{zz}\delta(\zeta)$, where $\gamma_z^{(C)}$ and κ_{zz} on the right-hand sides are understood as constants, we return just to the relation for $\overline{\mathcal{F}}_z$ given by (7). Utilizing integrations by parts, we may rewrite (47) as

$$\overline{\mathcal{F}}_z(z,t) = \int \Gamma(\zeta) \overline{C}(z-\zeta,t)\, d\zeta \tag{48}$$

with

$$\Gamma(\zeta) = \gamma_z^{(C)}(\zeta) - \frac{\partial \kappa_{zz}(\zeta)}{\partial \zeta}. \tag{49}$$

In what follows, it is convenient to work with a Fourier transformation defined by

$$F(\zeta) = \frac{1}{2\pi} \int \tilde{F}(k) \exp(ik\zeta)\, dk. \tag{50}$$

[Apart from the fact that here only a function of the single variable ζ is considered, this definition differs from (23) also by the factor $1/2\pi$ on the right-hand side.] Equation (48) is then equivalent to

$$\overline{\mathcal{F}}_z(z,t) = \frac{1}{2\pi} \int \tilde{\Gamma}(k) \tilde{\overline{C}}(k,t) \exp(ikz)\, dk, \tag{51}$$

and (49) implies

$$\tilde{\gamma}_z^{(C)}(k) = \mathrm{Re}[\tilde{\Gamma}(k)], \quad \tilde{\kappa}_{zz}(k) = -k^{-1}\mathrm{Im}[\tilde{\Gamma}(k)]. \tag{52}$$

For $\gamma_z^{(C)}$ and κ_{zz} on the right-hand sides of (7) and (8) we have then

$$\gamma_z^{(C)} = \tilde{\gamma}_z^{(C)}(0), \quad \kappa_{zz} = \tilde{\kappa}_{zz}(0). \tag{53}$$

Let us admit that $\overline{\mathcal{F}}_z$, at a given time, depends on $\overline{C}$ (and its spatial derivatives) not only at this but also at earlier times. This noninstantaneous connection between $\overline{\mathcal{F}}_z$ and $\overline{C}$ can be described as a *memory effect*; see, e.g., [20]. We then have to generalize (47) such that

$$\overline{\mathcal{F}}_z(z) = \iint \left(\gamma_z^{(C)}(\zeta,\tau)\, \overline{C}(z-\zeta,t-\tau) - \kappa_{zz}(\zeta,\tau) \frac{\partial \overline{C}(z-\zeta,t-\tau)}{\partial z} \right) d\zeta\, d\tau \tag{54}$$

with $\gamma_z^{(C)}$ and κ_{zz} symmetric in ζ and equal to zero for $\tau < 0$; the integration is then over all ζ and $\tau \geqslant 0$. It is straightforward to generalize the relations (48) to (53) in that sense. Then, Fourier transforms with respect to ζ and τ occur, and $\tilde{\gamma}_z^{(C)}$ and $\tilde{\kappa}_{zz}$ depend not only on k but also on an additional variable ω.

The generalizations explained here can easily be extended to the magnetic case discussed in Sec. II D. Then, $\gamma_z^{(B)}$, η_{xx}, and η_{yy} occur as functions of ζ, or of ζ and τ, and their Fourier transforms $\tilde{\gamma}_z^{(B)}$, $\tilde{\eta}_{xx}$, and $\tilde{\eta}_{yy}$ as functions of k, or of k and ω.

B. Test-field procedure

In Sec. II we have presented results for quantities like $\gamma_i^{(C)}$ or κ_{ij} which apply only under SOCA. As soon as we are able to solve equations like (6), e.g., numerically, we may determine these quantities, or $\tilde{\gamma}_z^{(C)}$ and $\tilde{\kappa}_{zz}$ introduced in the preceding section, also beyond this approximation. A proper tool for that is the test-field method, first developed in mean-field electrodynamics [21,22]. We apply the ideas of this method here first to the passive scalar case. As in the preceding section we assume again that the mean fields are defined by averaging over all x and y and relax spatial scale separation, but ignore at first scale separation in time, that is, the memory effect.

Suppose that we have solved (6) for two different *test fields* $\overline{C}$, say

$$\overline{C}^c = C_0 \cos kz \quad \text{and} \quad \overline{C}^s = C_0 \sin kz \tag{55}$$

with given C_0 and k, and calculated the corresponding $\overline{\mathcal{F}}_z$, say $\overline{\mathcal{F}}_z^c(z)$ and $\overline{\mathcal{F}}_z^s(z)$. Specifying (47) to $\overline{\mathcal{F}}_z^c$ and $\overline{\mathcal{F}}_z^s$ and considering that, due to (50) and the assumed symmetry of $\gamma_z^{(C)}(\zeta)$ and $\kappa_{zz}(\zeta)$ in ζ,

$$\begin{aligned} \int \gamma_z^{(C)}(\zeta) \cos k\zeta\, d\zeta &= \tilde{\gamma}_z^{(C)}(k), \\ \int \kappa_{zz}(\zeta) \cos k\zeta\, d\zeta &= \tilde{\kappa}_{zz}(k), \end{aligned} \tag{56}$$

we find

$$\begin{aligned} \overline{\mathcal{F}}_z^c(z) &= C_0\big[\tilde{\gamma}_z^{(C)}(k)\, \cos kz + \tilde{\kappa}_{zz}(k)\, k\, \sin kz\big], \\ \overline{\mathcal{F}}_z^s(z) &= C_0\big[\tilde{\gamma}_z^{(C)}(k)\, \sin kz - \tilde{\kappa}_{zz}(k)\, k\, \cos kz\big]. \end{aligned} \tag{57}$$

This in turn leads to

$$\tilde{\gamma}_z^{(C)}(k) = \frac{1}{C_0}\left[\overline{\mathcal{F}}_z^{c}(z)\,\cos kz + \overline{\mathcal{F}}_z^{s}(z)\,\sin kz\right],$$
$$\tilde{\kappa}_{zz}(k) = \frac{1}{C_0 k}\left[\overline{\mathcal{F}}_z^{c}(z)\,\sin kz - \overline{\mathcal{F}}_z^{s}(z)\,\cos kz\right]. \qquad (58)$$

Note that, although constituents of the right-hand sides depend on z, the left-hand sides do not.

If the memory effect is taken into account, Eq. (6) has to be solved with time-dependent test fields $\overline{C}$. Let us define such fields by multiplying the right-hand sides in (55) by a factor $e^{i\omega t}$. Integrate then the relevant equations numerically with any initial condition until all transient parts of the solutions have disappeared. For steady flows, the remaining solutions then show the same harmonic time variation as the test fields (approximately possible also for unsteady flows). That is, the same time-dependent factors occur on both sides of the equations analogous to (57) and can be removed. These equations then allow the determination of $\tilde{\gamma}_z^{(C)}(k,\omega)$ and $\tilde{\kappa}_{zz}(k,\omega)$, that is, the Fourier transforms of $\gamma_z^{(C)}(\zeta,\tau)$ and $\kappa_{zz}(\zeta,\tau)$. Of course, $\tilde{\gamma}_z^{(C)}(k,\omega)$ and $\tilde{\kappa}_{zz}(k,\omega)$ are in general complex. We may also replace the factor $e^{i\omega t}$ by $e^{\sigma t}$ with a complex σ. Instead of the Fourier transformation with respect to time we have then to use a Laplace transformation.

A test-field procedure, as described here for passive scalars, can also be established for the magnetic case as discussed in Sec. II D. It allows then the calculation of quantities like $\gamma_z^{(B)}$, η_{xx}, and η_{yy} or their Fourier or Laplace transforms. Such procedures have already been used elsewhere (e.g., [20,22]).

For the numerical computations presented below we use the PENCIL CODE [23], where the test-field methods both for passive scalars and for magnetic fields have already been implemented [4]. All results presented in this paper have been obtained with a version of the code compatible with revision 16408.

IV. EXAMPLES AND ILLUSTRATIONS

A. Three-dimensional flow

In an attempt to model properties of homogeneous isotropic irrotational turbulence we wish to consider first a steady potential flow. Thus, we choose

$$\boldsymbol{u} = \nabla\phi, \qquad (59)$$

$$\phi = \frac{u_0}{k_0}\cos k_0(x+\chi_x)\,\cos k_0(y+\chi_y)\,\cos k_0(z+\chi_z). \qquad (60)$$

Here, u_0 and k_0 are positive constants and χ_x, χ_y, and χ_z are understood as random phases. Of course, this steady flow must lead to growing inhomogeneities of the mass density. Therefore the applicability of our results is restricted to a limited time range; see the discussion below (2).

Starting from original fields C and $\boldsymbol{B}$, which may depend on x, y, z, and t, and also on χ_x, χ_y, and χ_z, we define mean fields $\overline{C}$ and $\overline{\boldsymbol{B}}$ by averaging over all x and y and, in addition, over χ_z. Consequently, mean fields no longer depend on x, y, or χ_z, but they may depend on z and t. Clearly, the Reynolds averaging rules apply exactly. For mean quantities determined by $\boldsymbol{u}$ only, averaging over x and y is equivalent to averaging over χ_x and χ_y. Therefore, such quantities can also be understood as averages over χ_x, χ_y, and χ_z. Clearly, $\overline{\boldsymbol{u}^2}$ is independent of x, y, and also of z.

From (59) and (60), we conclude that

$$u_{\rm rms} = \frac{1}{2}\sqrt{\frac{3}{2}}\,u_0 \qquad (61)$$

and we define a wave number k_f of $\boldsymbol{u}$ by

$$k_f = \sqrt{3}k_0. \qquad (62)$$

In what follows, κ_t and η_t, as well as $\tilde{\kappa}_t$ and $\tilde{\eta}_t$, will be expressed in units of κ_{t0} and η_{t0}, given by

$$\kappa_{t0} = \eta_{t0} = \frac{u_{\rm rms}}{3k_f}. \qquad (63)$$

Furthermore, we define the Péclet number Pe and the magnetic Reynolds number Rm by

$${\rm Pe} = \frac{u_{\rm rms}}{\kappa k_f}, \quad {\rm Rm} = \frac{u_{\rm rms}}{\eta k_f}. \qquad (64)$$

Calculations in the framework of SOCA under the assumption of perfect scale separation yield

$$\kappa_t = -\kappa_{t0}{\rm Pe}, \quad \eta_t = -\eta_{t0}{\rm Rm}. \qquad (65)$$

Clearly, κ_t and η_t are nonpositive. If scale separation is, in the sense of (47), relaxed, we obtain

$$\tilde{\kappa}_t(k) = -\kappa_{t0}{\rm Pe}\, f(k/k_f), \quad \tilde{\eta}_t(k) = -\eta_{t0}{\rm Rm}\, f(k/k_f),$$
$$f(v) = \frac{1-v^2}{1+(2/3)v^2+v^4}. \qquad (66)$$

In all following discussions we consider k as positive. Like κ_t and η_t, also $\tilde{\kappa}_t$ and $\tilde{\eta}_t$ are negative as long as $k/k_f < 1$.

In what follows, we present results for the quantities $\tilde{\kappa}_t$ and $\tilde{\eta}_t$ obtained by the test-field procedure described in Sec. III B, utilizing numerical integrations of Eq. (6) for c or Eq. (37) for $\boldsymbol{b}$. Averaging over χ_z was performed by averaging over z.

Figure 1 shows $\tilde{\kappa}_t/\kappa_{t0}$ as well as $\tilde{\eta}_t/\eta_{t0}$ for a small value of k/k_f, at which these quantities should be very close to κ_t/κ_{t0} and η_t/η_{t0}, as functions of Pe and Rm, respectively. (These values could also be obtained with a test field that is independent of z and another one linear in z.) In agreement with the results presented in Sec. II and with (65), κ_t and η_t are negative for not too large values of Pe and Rm, respectively. Remarkably the functions $\tilde{\kappa}_t({\rm Pe})$ and $\tilde{\eta}_t({\rm Rm})$ coincide formally for small values of Pe and Rm only, but are otherwise clearly different from each other. In particular, $\tilde{\eta}_t$ remains negative, at least for ${\rm Rm} \leqslant 70$, while $\tilde{\kappa}_t$ becomes positive for ${\rm Pe} \gtrsim 2$. The total diffusivities, $\eta + \tilde{\eta}_t$ and $\kappa + \tilde{\kappa}_t$, are always found to be positive.

Figures 2 and 3 show examples of the dependence of $\tilde{\kappa}_t/\kappa_{t0}$ and $\tilde{\eta}_t/\eta_{t0}$ on k/k_f. Again, $\tilde{\kappa}_t$ and $\tilde{\eta}_t$ with ${\rm Pe} = 0.35$ and ${\rm Rm} = 0.35$, respectively, that is, in the validity range of SOCA, take coinciding negative values in the limit of small k/k_f. However, $\tilde{\kappa}_t$ and $\tilde{\eta}_t$ become positive for large values of k/k_f, regardless of the values of Pe and Rm. The dependence of $\tilde{\kappa}_t$ on Pe and that of $\tilde{\eta}_t$ on Rm are in general clearly different from each other.

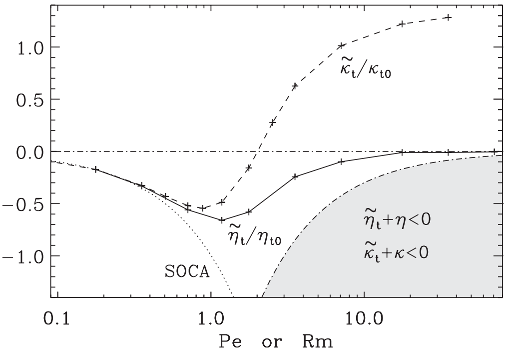

FIG. 1. $\tilde{\kappa}_t/\kappa_{t0}$ and $\tilde{\eta}_t/\eta_{t0}$ as functions of Pe and Rm, respectively, for the model given by (59) and (60); $k/k_f = 1/10\sqrt{3} \approx 0.06$. The dotted line on the lower left gives SOCA result and the shaded area on the lower right marks the regime where the total diffusivities would become negative.

The results regarding negative contributions of κ_t to the mean-field diffusivity for passive scalars, or negative contributions of η_t to the magnetic mean-field diffusivity, have been found under the assumption that the velocity $\boldsymbol{u}$ is steady or varies only weakly in time. In order to see the influence of the variability of $\boldsymbol{u}$ we consider now a *renovating flow*. It is assumed that, during some time interval, a steady flow as given by (60) with some values of χ_x, χ_y, and χ_z exists, and likewise in the following interval, but with randomly changed χ_x, χ_y, and χ_z, and so forth. Hence, there is no correlation between the flows in the different intervals. It is further assumed that all intervals are equally long. Denoting their durations by τ, we define now the dimensionless parameters

$$q_\kappa = \left(\kappa k_f^2 \tau\right)^{-1}, \quad q_\eta = \left(\eta k_f^2 \tau\right)^{-1}. \tag{67}$$

Steadiness of the velocity corresponds to $q_\kappa = q_\eta = 0$.

Figure 4 shows the dependency of $\tilde{\kappa}_t/\kappa_{t0}$Pe on q_κ and that of $\tilde{\eta}_t/\eta_{t0}$Rm on q_η for $k/k_f = 1/\sqrt{3} \approx 0.6$. We see that $\tilde{\kappa}_t$ and $\tilde{\eta}_t$ are no longer negative if q_κ and q_η exceed 0.2 and 0.3, respectively.

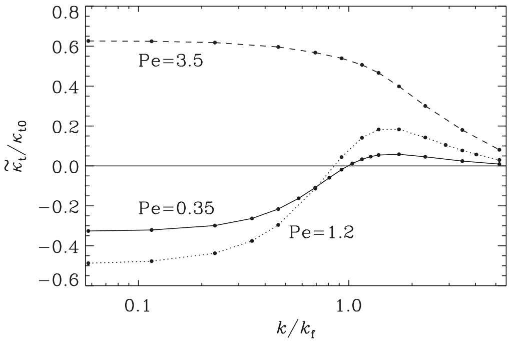

FIG. 2. $\tilde{\kappa}_t/\kappa_{t0}$ versus k/k_f for some values of Pe.

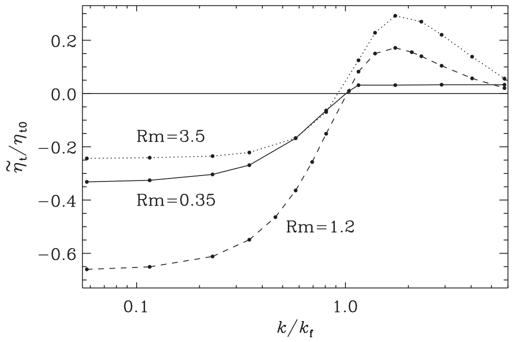

FIG. 3. $\tilde{\eta}_t/\eta_{t0}$ versus k/k_f for some values of Rm.

B. Plane-wave-like flow

With the idea of establishing a simple model reflecting features of homogeneous *anisotropic* turbulence, we remain with (59), that is $\boldsymbol{u} = \nabla\phi$, but replace (60) by

$$\phi = \frac{u_0}{k_0}\cos[k_0(sx + z) - \omega_0 t - \chi]. \tag{68}$$

If $s = 0$, the velocity $\boldsymbol{u}$ corresponds to a sound wave traveling in the z direction, with wavelength and frequency determined by k_0 and ω_0 and with a phase angle χ. We assume, for simplicity, $k_0 > 0$ and $\omega_0 \geqslant 0$ so that the wave travels in the positive z direction. If we admit nonzero values of s, the wave propagates no longer in the z direction, but in the direction of the vector $(s,0,1)$. For $\omega_0 = 0$ the velocity $\boldsymbol{u}$ does not depend on time, that is, we have a "frozen-in" wave.

Similarly to the preceding example, we define mean fields here by averaging over all x and y and, if the original field depends on χ, also over χ. Then, mean fields may depend only on z and t. Again, the Reynolds averaging rules apply exactly. If an original field is determined by $\boldsymbol{u}$ only and s is unequal to zero, averaging over x is equivalent to averaging over χ.

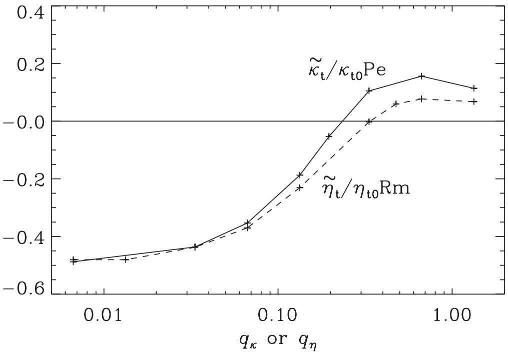

FIG. 4. $\tilde{\kappa}_t/\kappa_{t0}$Pe and $\tilde{\eta}_t/\eta_{t0}$Rm versus q_κ or q_η, respectively, for a renovating flow with $u_{\rm rms} k_f \tau = 5.3$ and $k/k_f = 1/\sqrt{3} \approx 0.6$. In the calculations, τ was held constant. Consequently, $q_\kappa = \mathrm{Pe}/5.3$ and $q_\eta = \mathrm{Rm}/5.3$.

Instead of (61) we now have

$$u_{\rm rms} = u_0\sqrt{\frac{s^2+1}{2}}\,, \tag{69}$$

and instead of (62) and (63) we put

$$k_f = k_0, \quad \kappa_{t0} = \eta_{t0} = \frac{u_{\rm rms}}{k_f}, \tag{70}$$

and we define Pe and Rm again according to (64). Finally we set

$$q_\kappa = \frac{\omega_0}{\kappa k_0^2}, \quad q_\eta = \frac{\omega_0}{\eta k_0^2}\,. \tag{71}$$

Due to the definition of mean fields, which implies that $\overline{C}$ and $\overline{\boldsymbol{B}}$ do not depend on x and y, we also have $(\boldsymbol{\nabla}\times\overline{\boldsymbol{B}})_z = 0$. In addition, we assume that $\overline{B}_z = 0$.

Adopting SOCA and assuming again perfect scale separation, we find

$$\begin{aligned} \gamma_z^{(C)} &= u_{\rm rms}{\rm Pe}\, g(s,q_\kappa), \\ \gamma_z^{(B)} &= u_{\rm rms}{\rm Rm}\, g(s,q_\eta), \\ g(s,q) &= \frac{(1+s^2)q}{(1+s^2)^2+q^2}, \end{aligned} \tag{72}$$

and

$$\begin{aligned} \kappa_{zz} &= -\kappa_{\rm t0}{\rm Pe}\ h(s,q_\kappa), \\ \eta_{xx} &= \eta_{yy} = -\eta_{\rm t0}{\rm Rm}\, h(s,q_\eta), \\ h(s,q) &= \frac{(1+s^2)[(1+s^2)^2-3q^2]}{[(1+s^2)^2+q^2]^2}. \end{aligned} \tag{73}$$

In the case $q_\kappa = q_\eta = 0$, that is, for frozen-in waves, the $\gamma_z^{(C)}$ and $\gamma_z^{(B)}$ vanish. This is due to the fact that, then, there is no preference for the positive or negative z direction. For $q_\kappa \neq 0$, however, $\gamma_z^{(C)}$ is positive so that $\overline{C}$ is advected in the positive z direction. Further, κ_{zz} is negative for not too large q_κ, but it becomes positive for larger q_κ. This applies analogously with q_η, $\gamma_z^{(B)}$, and $\eta_{xx} = \eta_{yy}$.

Relaxing perfect spatial scale separation and assuming that $\overline{C}$ and $\overline{\boldsymbol{B}}$ vary in time as $\exp(\sigma t)$ with a real σ, we find further

$$\begin{aligned} \tilde{\gamma}_z^{(C)} &= u_{\rm rms}{\rm Pe}\, g\big(s,q_\kappa,k/k_f,\sigma/\kappa k_f^2\big), \\ \tilde{\gamma}_z^{(B)} &= u_{\rm rms}{\rm Rm}\, g\big(s,q_\eta,k/k_f,\sigma/\eta k_f^2\big), \\ g(s,q,v,w) &= \frac{q}{2}\left(\frac{1+s^2+v}{[(1+v)^2+s^2+w]^2+q^2}\right. \\ &\quad \left. +\ \delta\frac{1+s^2-v}{[(1-v)^2+s^2+w]^2+q^2}\right), \end{aligned} \tag{74}$$

and

$$\begin{aligned} \tilde{\kappa}_{zz} &= -\kappa_{t0}{\rm Pe}\, h\big(s,q_\kappa,k/k_{\rm f},\sigma/\kappa k_f^2\big), \\ \tilde{\eta}_{xx} &= \tilde{\eta}_{yy} = -\eta_{t0}{\rm Rm}\, h\big(s,q_\eta,k/k_f,\sigma/\eta k_f^2\big), \\ h(s,q,v,w) &= -\frac{1}{2v}\left(\frac{(1+s^2+v)[(1+v)^2+s^2+w]}{[(1+v)^2+s^2+w]^2+q^2}\right. \\ &\quad \left. -\ \delta\frac{(1+s^2-v)[(1-v)^2+s^2+w]}{[(1-v)^2+s^2+w]^2+q^2}\right). \end{aligned} \tag{75}$$

The factor δ is in general equal unity but equal to zero if $1-v=s=w=q=0$, that is, if the following denominator vanishes. All coefficients $\gamma_i^{(C)}$, $\gamma_i^{(B)}$, $\tilde{\gamma}_i^{(C)}$, $\tilde{\gamma}_i^{(B)}$, κ_{ij}, η_{ij}, $\tilde{\kappa}_{ij}$, and $\tilde{\eta}_{ij}$, which are not explicitly mentioned, are equal to zero.

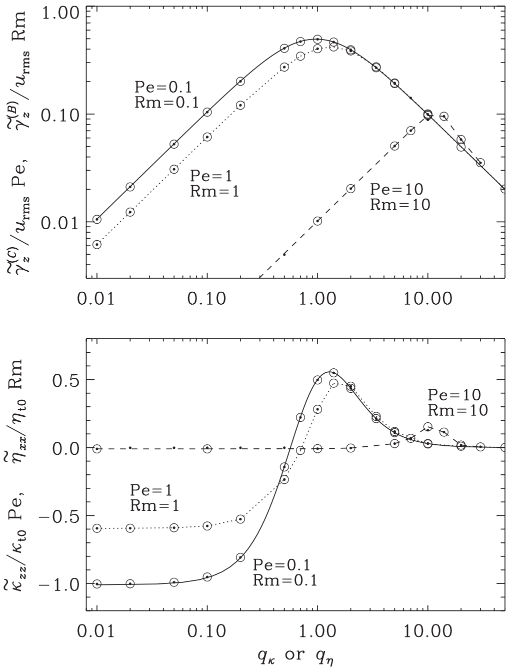

FIG. 5. Dependence of $\tilde{\gamma}_z^{(C)}/u_{\rm rms}{\rm Pe}$ and $\tilde{\kappa}_{zz}/\kappa_{t0}{\rm Pe}$ on q_κ as well as that of $\tilde{\gamma}_z^{(B)}/u_{\rm rms}{\rm Rm}$ and $\tilde{\eta}_{xx}/\eta_{t0}{\rm Rm}$ on q_η for the model given by Eq. (68) for $k/k_f = 0.1$, $s = 0.01$, $\sigma = 0$, and three values of Pe or Rm, respectively. Solid lines give SOCA results, symbols the values obtained by the test-field method; dots correspond to $\tilde{\gamma}_z^{(C)}/u_{\rm rms}{\rm Pe}$ and $\tilde{\kappa}_{zz}/\kappa_{t0}{\rm Pe}$, open circles to $\tilde{\gamma}_z^{(B)}/u_{\rm rms}{\rm Rm}$, and $\tilde{\eta}_{xx}/\eta_{t0}{\rm Rm}$. Clearly, $\tilde{\gamma}_z^{(C)}/u_{\rm rms}{\rm Pe}$ and $\tilde{\kappa}_{zz}/\kappa_{t0}{\rm Pe}$ coincide completely with $\tilde{\gamma}_z^{(B)}/u_{\rm rms}{\rm Rm}$ and $\tilde{\eta}_{xx}/\eta_{t0}{\rm Rm}$ if Pe and Rm coincide.

Numerical calculations of $\tilde{\gamma}_z^{(C)}$ and $\tilde{\kappa}_{zz}$ as well as $\tilde{\gamma}_z^{(B)}$ and $\tilde{\eta}_{xx} = \tilde{\eta}_{yy}$ by the test-field method, without restriction to SOCA, have been carried out with $k/k_f = 0.1$ and some specific values of Pe and Rm. Only cases with $s \neq 0$ were included, for which the χ and x averages are equivalent. Hence the standard test-field procedure with horizontal averages could be employed. Figure 5 shows these quantities for $s = 0.01$ as functions of q_κ or q_η. The results for Pe $= 0.1$ and Rm $= 0.1$ are in good agreement with our SOCA calculations, that is, (74) and (75). Those for higher Pe and Rm clearly deviate from them. Interestingly, the dependence of $\tilde{\gamma}_z^{(C)}$ and $\tilde{\kappa}_{zz}$ on Pe is always the same as those of $\tilde{\gamma}_z^{(B)}$ and $\tilde{\eta}_{xx}$ or $\tilde{\eta}_{yy}$ on Rm.

A remarkable feature of SOCA results (75) for $\tilde{\kappa}_{zz}$, and also for $\tilde{\eta}_{xx} = \tilde{\eta}_{yy}$, is that these quantities show singularities at $k/k_f = 1$ if $q_\kappa = q_\eta = s = \sigma = 0$. Nevertheless they are well defined at this point; $\tilde{\kappa}_{zz}/\kappa = {\rm Pe}^2/4$ and $\tilde{\eta}_{xx}/\eta = \tilde{\eta}_{yy}/\eta = {\rm Rm}^2/4$ at $k/k_f = 1$.

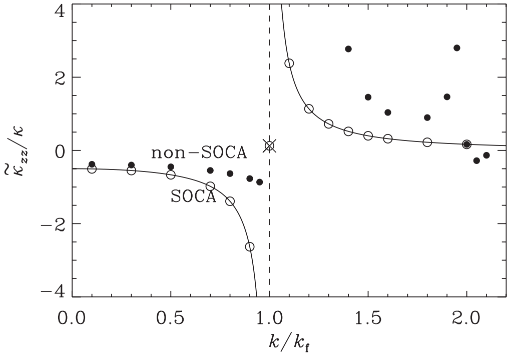

FIG. 6. Dependence of $\tilde{\kappa}_{zz}/\kappa$ with $\mathrm{Pe} = 0.707$ and $q_\kappa = \sigma = 0$ on k/k_f. Solid lines as well as the cross at $k/k_f = 1$ result from analytic SOCA calculations with $s = 0$. Symbols give numerical results obtained with Eq. (6) using $s = 0.01$; filled circles, full equation; open circles, SOCA, term $(\boldsymbol{u}c)'$ dropped. Note the second "resonance" at $k/k_f = 2$.

Let us, in what follows, focus attention on passive scalars only. Consider a mean scalar of the form $\overline{C} = F(t)\cos kz$ with F being positive. For $q_\kappa = 0$, its time behavior is exclusively determined by the quantity $\kappa + \tilde{\kappa}_{zz}$. Clearly $\overline{C}$ is bound to decay if $\kappa + \tilde{\kappa}_{zz} > 0$. Now consider the dependence of $\tilde{\kappa}_{zz}$ on k/k_f for $q_\kappa = s = \sigma = 0$, depicted in Fig. 6. If k/k_f is smaller than but close to unity, $\tilde{\kappa}_{zz}$ may, even for small Pe, take arbitrarily large negative values, and $\kappa + \tilde{\kappa}_{zz}$ becomes negative. This will then lead to a growth of the modulus of $\overline{C}$. Of course, this conclusion is drawn from a result obtained under SOCA and may hence be questionable. Indeed, the sufficient condition for the applicability of SOCA given so far, $\mathrm{Pe} \ll 1$, has been derived for $k/k_f \ll 1$ only. If, by contrast, $k/k_f \approx 1$, we find, when comparing the terms $\boldsymbol{\nabla} \cdot (\boldsymbol{u}c)'$ and $\kappa \Delta c$ in (6) under the assumption that c is dominated by contributions with wave numbers $k + k_f$ and $k - k_f$, for $q_\kappa = \sigma = 0$ and $s \ll 1$ the more stringent condition

$$\mathrm{Pe} \ll 3\frac{(1 - k/k_f)^2 + s^2}{1 - k/k_f + s^2}. \tag{76}$$

It supports the doubts in the above conclusion concerning the growth of the modulus of $\overline{C}$.

The aforementioned SOCA calculations for $s = 0$ have been extended by the inclusion of fourth-order terms in $\boldsymbol{u}$, that is, in Pe. Apart from some quantitative changes of $\tilde{\kappa}_{zz}/\kappa$ in the neighborhood of $k/k_f = 1$, which occur with larger Pe, a new singularity emerges at $k/k_f = 2$. As can be seen in Fig. 6, the numerical (non-SOCA) calculations with $s = 0.01$ reflect this feature, too. They also give indications of a further resonance at $k/k_f = 3$ (not shown).

Figure 7 shows $\tilde{\kappa}_{zz}$ for steady test fields (that is, $\sigma = 0$) with $k/k_f = 0.9$ and $s = 0.01$ as a function of Pe. The results clearly deviate from those obtained by SOCA as soon as Pe exceeds, say, 0.2. Considering that $\kappa + \tilde{\kappa}_{zz} \geqslant 0$ is equivalent to $-\tilde{\kappa}_{zz}/\kappa_{t0} \leqslant 1/\mathrm{Pe}$, Fig. 7 tells us further that $\kappa + \tilde{\kappa}_{zz}$ becomes very small with growing Pe, but suggests that it remains positive. We may suppose that the modulus of the considered $\overline{C}$ never grows but its decay becomes very slow for large Pe. For example, for $\mathrm{Pe} = 1$ we expect that $\lambda = -(\kappa + \tilde{\kappa}_{zz})k^2 \approx -0.1\kappa k^2$, that is, the decay of $\overline{C}$ should be about ten times slower than in the absence of any motion.

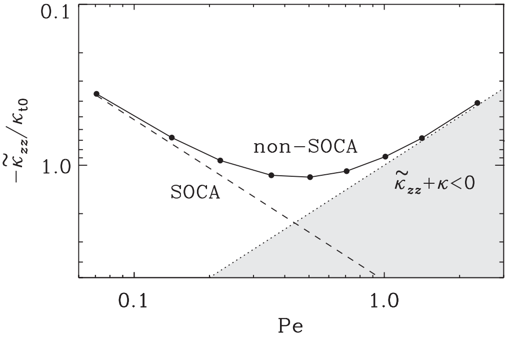

FIG. 7. Dependence of $\tilde{\kappa}_{zz}/\kappa_{t0}$ on Pe for $k/k_f = 0.9$ and $s = 0.01$, $\sigma = q_\kappa = 0$. The dashed line gives SOCA result and the shaded area marks the range where the total diffusivity would become negative.

In these considerations, however, the memory effect, that is, the dependence of the value of $\tilde{\kappa}_{zz}$, relevant for the decay of $\overline{C}$, on the decay rate λ itself, has been ignored. As explained in Sec. III B, we have to include this dependence by using time-dependent test fields. Let us assume that they vary as $\exp(\sigma t)$ but consider σ first as independent of λ. Then $\tilde{\kappa}_{zz}$ and $\lambda = -(\kappa + \tilde{\kappa}_{zz})k^2$ occur as functions of σ. Figure 8, obtained by test-field calculations, shows this dependence of λ on σ. If we then identify σ with λ we find, as indicated in Fig. 8, $\lambda \approx -0.005\kappa k^2$. That is, the decay of $\overline{C}$ is about 200 times slower than in the absence of any motion.

In order to check this surprising result, we perform two-dimensional direct numerical simulations based on Eq. (2) with a flow given by (68) using $k_0 = 10k_1$, where $k_1 = 2\pi/L_z$ is the smallest wave number in the z direction with extent L_z. Our computational domain is periodic in both directions. We

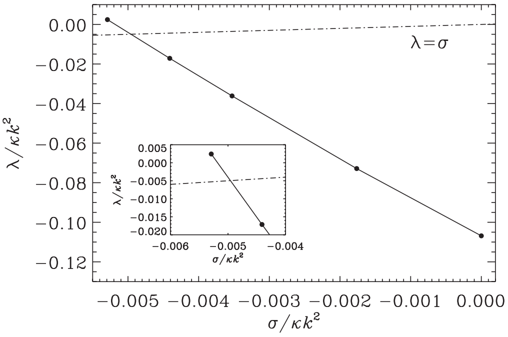

FIG. 8. Dependence $\lambda(\sigma) = -[(\kappa + \tilde{\kappa}_{zz}(k,\sigma)]k^2$ for $\mathrm{Pe} = 1.0$, $k/k_f = 9/10$, $s = 0.01$, and $q_\kappa = 0$. The curve representing $\lambda(\sigma)/\kappa k^2$ intersects the dash-dotted line $\lambda = \sigma$ at $\lambda(\sigma)/\kappa k^2 = -0.005$, which is shown more clearly in the inset.

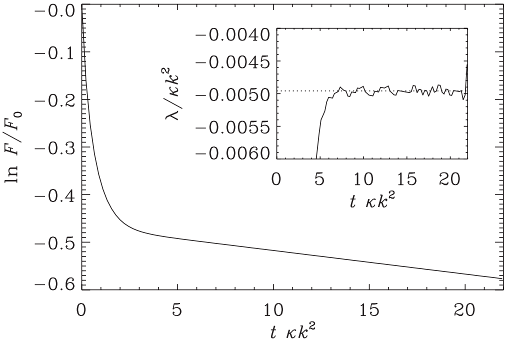

FIG. 9. Direct simulation showing the decay of the amplitude F of $\overline{C}(z)$ in units of its initial value F_0. Parameters as in Fig. 8. The inset shows the time dependence of the growth rate λ, leveling off at $\lambda \approx -0.005\kappa k^2$ after some initial adjustment time.

choose $L_x = 10L_z$ so as to accommodate the variation in the x direction with wave number $k_0 s$ and $s = 0.01$. The initial condition is $C = C_0 \cos kz$, with $C_0 > 0$ and $k = 9k_1$. We use 128^2 mesh points and choose Pe $= 1$, which is clearly beyond the applicability of SOCA; cf. Fig. 7.

As we expect that $\overline{C} = F(t) \cos kz$, we have identified the maximum of the x average of C with respect to z with F and determined the growth rate by calculating first its instantaneous value $\lambda(t) = d \ln F/dt$; see Fig. 9. It turns out that the average of λ over the time interval in which it is approximately constant is in excellent agreement with the test-field result $\lambda \approx -0.005\kappa k^2$ described above. The snapshot in Fig. 10 shows that $C(x,z)$ varies mainly in the z direction with the dominant wave number $k = 9k_f/10$. In units of κk^2, the *free-decay rate* of a mode with this wave number would be 0.01, or 0.012, if the variation in x is taken into account. Note, however, that the dominant constituent of C belongs, by virtue of its x dependence, to the *fluctuating* field c and that the actual decay rate of the *mean field* $\overline{C}$ is at least two times smaller than the given free-decay rate. The fluctuations are not decaying freely, but follow the mean field, and hence adopt its decay rate. In this particular case, the rms values of the fluctuations exceed those of the mean field by a factor of 14.

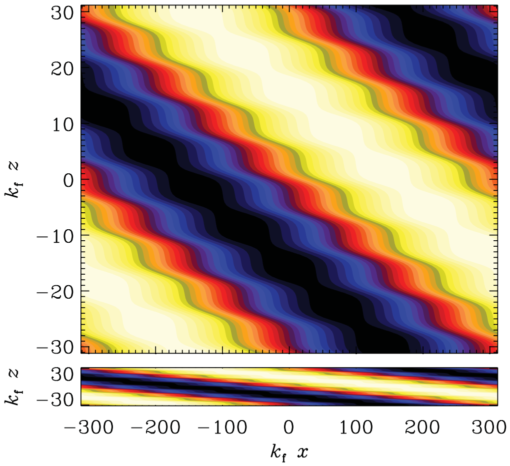

FIG. 10. (Color online) Snapshot of $C(x,z)$ for the simulation shown in Fig. 9 at $t\kappa k^2 = 17$. Bright (yellow) shades indicate positive values and dark (blue) shades negative values. The lower panel shows $C(x,z)$ with the correct aspect ratio of the box.

The question could be raised as to whether a resonance effect in the above sense can also occur for solenoidal flows. Numerical experiments with the (stationary) ABC flow (for its definition see, e.g., [24]) indicate clearly that the decay of $\overline{C}$ is always accelerated in the presence of this flow, irrespective of the value of k/k_f.

V. CONCLUSIONS

In this work we have shown that the turbulent diffusivity κ_t for the concentration of a passive scalar in a potential flow can be negative at low Péclet numbers. This result is analogous to an earlier finding for the turbulent magnetic diffusivity η_t in such a flow at low magnetic Reynolds numbers, originally derived in the context of astrophysical dynamo theory. The numerical calculations presented in this paper confirm Eq. (1) quantitatively for an irrotational flow. We have not yet considered the case of the combined action of solenoidal and irrotational flows where the question arises of how strong the solenoidal part has to be to render the turbulent diffusivities positive. Our calculations also show that negative values of κ_t do not occur for larger Péclet numbers, whereas negative η_t may well exist for moderate to large Reynolds numbers. In neither case have negative turbulent diffusivities yet been seen in laboratory experiments. Nevertheless, for possible physical applications of our results one may think of microfluidic devices [25], in which the flow can be compressible [26] and the Péclet number small.

In addition to the condition of small Péclet and magnetic Reynolds numbers, there are also the requirements of good scale separation and of slow temporal variations of the flow. If these requirements are not obeyed, κ_t and η_t are no longer necessarily negative – even at small values of Péclet and magnetic Reynolds numbers. This may be the reason why a reduction of the effective diffusivity has never been seen in physically meaningful compressible flows and why Eq. (1) is virtually unknown in the turbulence community. In fact, previous attempts to verify this equation in simulations have failed because of the fact that the time dependence has been too vigorous in those flows [27].

The spatial structure of the flow does not appear to be critical for obtaining a reduction of the effective diffusivity. Even in a nearly one-dimensional flow, turbulent diffusivities can become negative. However, in that case there are two new effects. First, if the underlying flow pattern displays propagating wave motions, there can be transport of the mean scalar in the direction of wave propagation—even in the absence of any mean material motion. Again, this effect may have applications to microfluidic devices. Second, the wave number characteristics display a singular behavior under SOCA, but even beyond SOCA there can be a dramatic slowdown of the decay by factors of several hundreds compared with the molecular values. This result is completely unexpected because no such behavior has ever been seen for any other turbulent transport process. Furthermore, the memory effect proves to be markedly important in such cases, so the common assumption of an instantaneous relation between the mean flux of the scalar and its mean concentration or the mean electromotive force and the mean magnetic field breaks down near the singularity.

In addition to finding out more about possible applications of the turbulent transport phenomena discussed above, it would be natural to study the possibility of similar processes for the turbulent transport of other quantities including momentum and heat or other active scalars. Further, a complementary effort to determine the transport coefficients for *turbulent* irrotational flows numerically would be of high interest, the more as there are no simple analytical results available. Supernova-driven turbulence in the interstellar medium would of course be the most suggestive application.

Clearly, both analytical and numerical approaches using the test-field method proved to be invaluable in that they are able to predict unexpected phenomena that can then also be verified using direct numerical simulations and in future hopefully also laboratory experiments.

ACKNOWLEDGMENTS

We thank the anonymous referee for fruitful hints that helped to improve the paper. K.-H.R. and A.B. are grateful for the opportunity to work on this paper while participating in the program “The Nature of Turbulence” at the Kavli Institute for Theoretical Physics in Santa Barbara, CA. This work was supported in part by the European Research Council under the AstroDyn Research Project No. 227952, the Swedish Research Council Grant No. 621-2007-4064, and the National Science Foundation under Grant No. NSF PHY05-51164. We acknowledge the allocation of computing resources provided by the Swedish National Allocations Committee at the Center for Parallel Computers at the Royal Institute of Technology in Stockholm and the National Supercomputer Centers in Linköping.

APPENDIX: RELATIONS FOR a_{ij}, η_{ij}, AND c_{ijk}

Under SOCA we may derive, for homogeneous turbulence,

$$a_{ij} = \iint i(\epsilon_{ilm}k_j - \epsilon_{ilj}k_m)\frac{\hat{Q}_{lm}(\boldsymbol{k},\omega)}{\eta k^2 - i\omega}\,d^3k\,d\omega, \tag{A1}$$

$$\eta_{ij} = \frac{1}{2}\iint \left(\delta_{ij}\delta_{lm} - \delta_{im}\delta_{jl} - \frac{2\eta(\delta_{ij}k_l k_m - k_i k_m \delta_{jl})}{\eta k^2 - i\omega}\right) \times \frac{\hat{Q}_{lm}(\boldsymbol{k},\omega)}{\eta k^2 - i\omega}d^3k\,d\omega, \tag{A2}$$

$$c_{ijk} = -\frac{1}{2}\iint \left(2\epsilon_{imn}\delta_{jk} - (\epsilon_{imj}\delta_{kn} + \epsilon_{imk}\delta_{jn}) - 2\eta\frac{2\epsilon_{imn}k_j k_k - (\epsilon_{imj}k_k + \epsilon_{imk}k_j)k_n}{\eta k^2 - i\omega}\right) \times \frac{\hat{Q}_{mn}(\boldsymbol{k},\omega)}{\eta k^2 - i\omega}\,d^3k\,d\omega. \tag{A3}$$

---

[1] T. Elperin, N. Kleeorin, and I. Rogachevskii, Phys. Rev. Lett. **52**, 2617 (1995).

[2] T. Elperin, N. Kleeorin, and I. Rogachevskii, Phys. Rev. Lett. **76**, 224 (1996).

[3] T. Elperin, N. Kleeorin, and I. Rogachevskii, Phys. Rev. E **55**, 2713 (1997).

[4] A. Brandenburg, A. Svedin, and G. M. Vasil, Mon. Not. R. Astron. Soc. **395**, 1599 (2009).

[5] N. E. L. Haugen, N. Kleeorin, I. Rogachevskii, and A. Brandenburg, e-print arXiv:1101.4188.

[6] H. K. Moffatt, *Magnetic Field Generation in Electrically Conducting Fluids* (Cambridge University Press, Cambridge, 1978).

[7] F. Krause and K.-H. Rädler, *Mean-Field Magnetohydrodynamics and Dynamo Theory* (Pergamon Press, Oxford, 1980).

[8] K.-H. Rädler, in *From the Sun to the Great Attractor*, edited by D. Page and J. G. Hirsch, Lecture Notes in Physics, Vol. 556 (Springer, Berlin, 2000), p. 101.

[9] K.-H. Rädler, in *Magnetohydrodynamics: Historical Evolution and Trends*, edited by S. Molokov, R. Moreau, and H. K. Moffatt (Springer, Dordrecht, 2007), p. 55.

[10] K.-H. Rädler and M. Rheinhardt, Geophys. Astrophys. Fluid Dynam. **101**, 11 (2007).

[11] M. J. Korpi, A. Brandenburg, A. Shukurov, I. Tuominen, and Å. Nordlund, Astrophys. J. **514**, L99 (1999).

[12] M. A. de Avillez and M.-M. Mac Low, Astrophys. J. **581**, 1047 (2002).

[13] D. S. Balsara, J. Kim, M.-M. Mac Low, and G. J. Mathews, Astrophys. J. **617**, 339 (2004).

[14] O. Gressel, D. Elstner, U. Ziegler, and G. Rüdiger, Astron. Astrophys. **486**, L35 (2008).

[15] F. Del Sordo and A. Brandenburg, Astron. Astrophys. **528**, A145 (2011).

[16] K. Kajantie and H. Kurki-Suonio, Phys. Rev. D **34**, 1719 (1986).

[17] J. Ignatius, K. Kajantie, H. Kurki-Suonio, and M. Laine, Phys. Rev. D **49**, 3854 (1994).

[18] E. M. Lifshitz and L. P. Pitaevskii, *Physical Kinetics*, 1st ed. (Pergamon Press, Oxford, 1981).

[19] P. Chatterjee, D. Mitra, M. Rheinhardt, and A. Brandenburg, Astron. Astrophys. **534**, A46 (2011).

[20] A. Hubbard and A. Brandenburg, Astrophys. J. **706**, 712 (2009).

[21] M. Schrinner, K.-H. Rädler, D. Schmitt, M. Rheinhardt, and U. R. Christensen, Geophys. Astrophys. Fluid Dynam. **101**, 81 (2007).

[22] A. Brandenburg, K.-H. Rädler, and M. Schrinner, Astron. Astrophys. **482**, 739 (2008).

[23] The PENCIL CODE is a high-order finite-difference code (sixth order in space and third order in time); http://pencil-code.googlecode.com.

[24] T. Dombre, U. Frisch, J. M. Greene, M. Hénon, A. Mehr, and A. M. Soward, J. Fluid Mech. **167**, 353 (1986).

[25] J. Koo and C. Kleinstreuer, J. Micromech. Microeng. **13**, 568 (2003).

[26] Z. Yao, P. Hao, and X. Zhang, Sci. China Phys., Mech. Astron. **54**, 711 (2011).

[27] A. Brandenburg and F. Del Sordo, in *Highlights of Astronomy*, edited by E. de Gouveia Dal Pino, Vol. 15 (Cambridge University Press, Cambridge, 2010), p. 432.

II

Astronomy & Astrophysics manuscript no. paper
August 14, 2012

Vorticity production through rotation, shear, and baroclinicity

F. Del Sordo[1,2] and A. Brandenburg[1,2]

[1] Nordita, AlbaNova University Center, Roslagstullsbacken 23, SE-10691 Stockholm, Sweden
[2] Department of Astronomy, AlbaNova University Center, Stockholm University, SE 10691 Stockholm, Sweden

August 14, 2012, Revision: 1.94

ABSTRACT

Context. In the absence of rotation and shear, and under the assumption of constant temperature or specific entropy, purely potential forcing by localized expansion waves is known to produce irrotational flows that have no vorticity.
Aims. Here we study the production of vorticity under idealized conditions when there is rotation, shear, or baroclinicity, to address the problem of vorticity generation in the interstellar medium in a systematic fashion.
Methods. We use three-dimensional periodic box numerical simulations to investigate the various effects in isolation.
Results. We find that for slow rotation, vorticity production in an isothermal gas is small in the sense that the ratio of the root-mean-square values of vorticity and velocity is small compared with the wavenumber of the energy-carrying motions. For Coriolis numbers above a certain level, vorticity production saturates at a value where the aforementioned ratio becomes comparable with the wavenumber of the energy-carrying motions. Shear also raises the vorticity production, but no saturation is found. When the assumption of isothermality is dropped, there is significant vorticity production by the baroclinic term once the turbulence becomes supersonic. In galaxies, shear and rotation are estimated to be insufficient to produce significant amounts of vorticity, leaving therefore only the baroclinic term as the most favorable candidate. We also demonstrate vorticity production visually as a result of colliding shock fronts.

Key words. magnetohydrodynamics (MHD) – turbulence – Galaxies: magnetic fields – ISM: bubbles

1. Introduction

Turbulence in the interstellar medium (ISM) is believed to be driven by supernova explosions. Such events inject sufficient amounts of energy to sustain turbulence with rms velocities of $\sim 10\,\mathrm{km/s}$ and correlation lengths of up to $100\,\mathrm{pc}$ (Beck et al., 1996). Simulations of such events can be computationally quite demanding, because the bulk motions tend to be supersonic and the flows involve strong shocks in the vicinity of individual explosion sites, as was seen early on in two-dimensional simulations (Rosen & Bregman, 1995). Nevertheless, such simulations are able to reproduce a number of physical phenomena such as the observed volume fractions of hot, warm, and cold gas (Rosen et al., 1996; Korpi et al., 1999a), the statistics of pressure fluctuations (Mac Low et al., 2005), the effects of the magnetic field (de Avillez & Breitschwerdt, 2005), and even dynamo action (Gressel et al., 2008; Gissinger et al., 2009; Hanasz et al., 2009). These simulations tend to show the development of significant amounts of vorticity, which is at first glance surprising. Indeed, each supernova drives the gas radially outward and can roughly be described by radial expansion waves. In such a description, turbulence is forced by the gradient of a potential that consists of a time-dependent spherical blob at random locations. Obviously, such a forcing is irrotational, so no vorticity is produced.

Earlier work of Mee & Brandenburg (2006) showed that under isothermal conditions only the viscous force can produce vorticity and that this becomes negligible in the limit of large Reynolds numbers or small viscosity. In principle, vorticity can also be amplified akin to the dynamo effect by the $\boldsymbol{\nabla}\times(\boldsymbol{u}\times\boldsymbol{\omega})$ term, which is analogous to the induction term in dynamo theory, where $\boldsymbol{\omega}$ plays the role of the magnetic field. However, neither this nor the viscosity effect were found to operate – even at numerical resolutions of up to 512^3 meshpoints. This disagreed with subsequent simulations by Federrath et al. (2010), who solved the isothermal inviscid Euler equations with irrotational forcing using the FLASH CODE. They found significant vorticity generation in proximity to shocks where some kind of effective numerical viscosity must have acted.

Given that under isothermal conditions, only viscosity can lead to vorticity production, one must ask whether numerical viscosity or effective viscosity needed to stabilize numerical codes might have contributed to the production of vorticity in some of the earlier works. Indeed, it is possible that the directional operator splitting used in the FLASH CODE may have been responsible for spurious vorticity generation in the work of Federrath et al. (2010); (R. Rosner, private communication). On the other hand, when cooling and heating functions are included to perform more realistic simulations of the ISM, vorticity could be produced by the baroclinic term. Furthermore, even in the isothermal case, in which the baroclinic term vanishes, vorticity could be produced if there is rotation and/or shear.

The baroclinic term results from taking the curl of the pressure gradient term and is proportional to the cross product of the gradients of pressure and density. This term can play an important role when the assumptions of isothermality or adiabaticity are relaxed. Indeed, the baroclinic term can also be written as the cross product of the gradients of entropy and temperature. This formulation highlights the need for non-ideal effects, because in the absence of any other heating or cooling mechanisms, the entropy is just driven by viscosity. Again, it is not obvious that in the absence of additional heating and cooling much vorticity can be produced. On the other hand, it is clear that viscous heating must be significant even in the limit of vanishing viscosity, because the velocity gradients can be very large, especially in shocks. Of course, the assumption about additional heating and cooling is not realistic for the interstellar medium and will need to be relaxed. Finally, there are the effects of rotation and shear, that can contribute to the production of vorticity even in the absence of baroclinicity.

The goal of this paper is to study the relative importance of the individual effects that contribute to vorticity production. It is then advantageous to restrict oneself to simplifying conditions that allow one to identify the governing effects. An important simplification is the restriction to weakly supersonic conditions so that shocks and other sharp structures can still be resolved with just a uniform and constant viscosity. We also neglect the effects of stratification which can only indirectly contribute to vorticity production. In fact, a constant gravitational acceleration drops out when taking the curl. Only in the non-isothermal and non-isentropic case can gravity contribute to vorticity production by enhancing the effect of the baroclinic term. We begin with a preliminary discussion and a qualitative analysis of the important terms in the vorticity equation.

2. Preliminary considerations

We recall that in the absence of baroclinicity, rotation, and shear, the curl of the evolution equation of the velocity is given by (see, e.g., Mee & Brandenburg, 2006)

$$\frac{\partial \boldsymbol{\omega}}{\partial t} = \boldsymbol{\nabla} \times (\boldsymbol{u} \times \boldsymbol{\omega} - \nu \boldsymbol{\nabla} \times \boldsymbol{\omega}) + \nu \boldsymbol{\nabla} \times \boldsymbol{G}, \tag{1}$$

where ν is the kinematic viscosity (assumed constant) and $G_i = 2\mathsf{S}_{ij}\nabla_j \ln\rho$ is a part of the viscous force that has non-vanishing curl even when the flow is purely irrotational. Here,

$$\mathsf{S}_{ij} = \tfrac{1}{2}(u_{i,j} + u_{j,i}) - \tfrac{1}{3}\delta_{ij} u_{k,k} \tag{2}$$

is the traceless rate of strain matrix, and commas denote partial differentiation. The $\boldsymbol{G}$ term breaks the formal analogy with the induction equation. It is convenient to express the resulting rms vorticity in terms of the typical wavenumber k_ω of vortical structures which we define as

$$k_\omega = \omega_{\rm rms}/u_{\rm rms}. \tag{3}$$

We monitor the ratio $k_\omega/k_{\rm f}$, where $k_{\rm f}$ is the adopted nominal forcing wavenumber. In Mee & Brandenburg (2006), the resulting vorticity, expressed in terms of the ratio $k_\omega/k_{\rm f}$, was found to be zero within error bars. This result is compatible with the idea that the $\nu\boldsymbol{\nabla}\times\boldsymbol{G}$ term in Equation (1) is insignificant for vorticity production. By contrast, in vortical turbulence and at moderate values of the Reynolds number, $k_\omega/k_{\rm f}$ is found to be of the order of unity (Brandenburg, 2001), although one should expect a mild increase proportional to the square root of the Reynolds number as this number increases.

2.1. Rotation

Rotation leads to the addition of the Coriolis force, $2\boldsymbol{\Omega} \times \boldsymbol{u}$, in the evolution equation for the velocity. Taking the curl, we obtain the vorticity equation (1) with two additional terms, both proportional to $\boldsymbol{\Omega}$, so we have

$$\frac{\partial \boldsymbol{\omega}}{\partial t} = ... - 2\boldsymbol{\Omega}\boldsymbol{\nabla}_\perp \cdot \boldsymbol{u}_\perp + 2\boldsymbol{\Omega}\cdot\boldsymbol{\nabla}\boldsymbol{u}_\perp, \tag{4}$$

where the dots denote the other terms in Equation (1) that we discussed already. In order to estimate the production of vorticity, one could derive an evolution equation for the enstrophy density, $\frac{1}{2}\boldsymbol{\omega}^2$, by multiplying the right-hand side of Equations (1) and (4) by $\boldsymbol{\omega}$, and use a closure assumption for the resulting triple correlations. However, it is then difficult to obtain a useful prediction for $\omega_{\rm rms}$, because the right-hand side of such an equation would necessarily be proportional to $\boldsymbol{\omega}$ and would therefore vanish, unless $\omega_{\rm rms}$ was different from zero to begin with. Instead, we estimate $\omega_{\rm rms}$ by computing the rms value of $\partial\boldsymbol{\omega}/\partial t$ and replacing it by $\omega_{\rm rms}/\tau_\Omega$, where τ_Ω is a typical time scale of the problem. This leads to

$$\omega_{\rm rms} \approx 2\Omega\tau_\Omega \left\langle (\boldsymbol{\nabla}_\perp \cdot \boldsymbol{u}_\perp)^2 + (\nabla_\parallel \boldsymbol{u}_\perp)^2 \right\rangle^{1/2}, \tag{5}$$

where $\boldsymbol{\nabla}_\perp$ and $\nabla_\parallel$ denote derivatives in the directions perpendicular and parallel to the rotation axis and $\boldsymbol{u}_\perp$ is the velocity vector perpendicular to the rotation axis. Using Cartesian coordinates where $\boldsymbol{\Omega}$ points in the z direction, we have

$$\omega_{\rm rms} \approx 2\Omega\tau_\Omega \left\langle (u_{x,x} + u_{y,y})^2 + u_{x,z}^2 + u_{y,z}^2 \right\rangle^{1/2}. \tag{6}$$

We expect τ_Ω to be comparable to the turnover time, $\tau = (u_{\rm rms}k_{\rm f})^{-1}$. We expect the rms values of the velocity derivative term in Equation (6) to be comparable to the rms velocity and some inverse length scale. Typically, one would expect it to be proportional to $u_{\rm rms}k_{\rm f}$, although, again, there can be an additional dependence on the square root of the Reynolds number. However, for fixed Reynolds number, and not too rapid rotation, we expect $\omega_{\rm rms}$ to increase linearly with the Coriolis number, i.e.,

$$\mathrm{Co} = 2\Omega\tau, \quad \text{where} \quad \tau = (u_{\rm rms}k_{\rm f})^{-1}. \tag{7}$$

Thus, we expect $k_\omega/k_{\rm f} = \mathrm{St}_\Omega\,\mathrm{Co}$, where we have defined an effective rotational Strouhal number,

$$\mathrm{St}_\Omega = \tau_\Omega^{\rm eff} u_{\rm rms} k_{\rm f}. \tag{8}$$

We regard this as a fit parameter that will emerge as a result of the simulations. We have here introduced the quantity $\tau_\Omega^{\rm eff}$, where $\tau_\Omega^{\rm eff}/\tau_\Omega$ is given by the ratio of the velocity gradient terms divided by $u_{\rm rms}k_{\rm f}$. However, for larger values of Co there may be a departure from a linear dependence between $k_\omega/k_{\rm f}$ and Co. (We note that, apart from a possible 4π factor, the Coriolis number is just the inverse Rossby number.) One aim of this paper is therefore to verify this dependence from simulations and to determine empirically the value of τ_Ω.

2.2. Shear

In the presence of linear shear with $\boldsymbol{u}^S = (0, Sx, 0)$, the evolution equation for the departure from the mean shear attains additional terms, $-\boldsymbol{u}^S\boldsymbol{\nabla}\cdot\boldsymbol{u} - \boldsymbol{u}\cdot\boldsymbol{\nabla}\boldsymbol{u}^S$. This implies a dependence of $\omega_{\rm rms}$ on S, analogous to the Ω dependence discussed above. In components form, this means that

$$\omega_{\rm rms} \approx S\tau_S \left\langle (u_{x,x} + u_{y,y})^2 + u_{x,z}^2 + u_{z,y}^2 + O(xu'') \right\rangle^{1/2}, \tag{9}$$

which is quite similar to Equation (5), except that in the penultimate term in angular brackets the indices are now interchanged, i.e. we now have $u_{z,y}$ instead of $u_{y,z}$. In analogy to τ_Ω, we define τ_S as a typical time scale of the problem and we expect it to be again related to the turnover time τ. The $O(xu'')$ denotes the presence of additional terms that are proportional to x and to second derivatives of $\boldsymbol{u}$. However, when adopting the shearing box approximation with shearing-periodic boundaries (Goldreich & Lynden-Bell, 1965; Wisdom & Tremaine, 1988), each point in the xy plane is statistically equivalent. We would therefore not expect there to be a systematic x dependence, which corresponds to the assumption of Galilean invariance that is sometimes used in the study of turbulent transport coefficients in linear shear flows (Sridhar & Subramanian, 2009). We will postpone the possibility of additional terms until later. Since we expect τ_S to be comparable to $\tau=(u_{\rm rms}k_{\rm f})^{-1}$, the rms vorticity should be proportional to the shear parameter,

$$\mathrm{Sh}=S\tau\equiv S/u_{\rm rms}k_{\rm f}, \tag{10}$$

although for large values of $|\mathrm{Sh}|$ we may expect departures from a linear dependence. Determining this dependence is another aim of this paper. Again, a linear dependence is characterized by the values of τ_S and $\tau_S^{\rm eff}$, where, in analogy with the previous case with rotation, the ratio $\tau_S^{\rm eff}/\tau_S$ is given by the derivative term in Equation (9), normalized by $u_{\rm rms}k_{\rm f}$. A convenient non-dimensional measure of the value of $\tau_S^{\rm eff}$ is what we call the shear Strouhal number,

$$\mathrm{St}_S=\tau_S^{\rm eff}u_{\rm rms}k_{\rm f}, \tag{11}$$

which can be determined provided there is a range in Sh over which $\omega_{\rm rms}$ increases linearly with Sh.

The study of vorticity production by rotation and shear is quite independent of thermodynamics and can in principle be studied even in the incompressible case. However, in the present paper we study this effect in the weakly compressible case of low Mach numbers and under the assumption of an isothermal equation of state, where the baroclinic term vanishes.

2.3. Baroclinicity

As mentioned in the introduction, the baroclinic term, proportional to $\boldsymbol{\nabla}\rho\times\boldsymbol{\nabla}p$, emerges when taking the curl of the pressure gradient term, $\rho^{-1}\boldsymbol{\nabla}p$. This term can also be written as

$$\rho^{-1}\boldsymbol{\nabla}p=\boldsymbol{\nabla}h-T\boldsymbol{\nabla}s, \tag{12}$$

where h and s are specific enthalpy and specific entropy, respectively, and T is the temperature. Thus, we have

$$\frac{\partial\boldsymbol{\omega}}{\partial t}=...+\boldsymbol{\nabla}T\times\boldsymbol{\nabla}s. \tag{13}$$

In order to study the effect of the baroclinic term, it is useful to look at the dependence of the mean angle θ between the gradients of s and T, defined via

$$\sin^2\theta=\langle(\boldsymbol{\nabla}T\times\boldsymbol{\nabla}s)^2\rangle/\langle(\boldsymbol{\nabla}T)^2\rangle\langle(\boldsymbol{\nabla}s)^2\rangle. \tag{14}$$

An important aspect is then to study first the dependence of the rms values of the gradients of s and T. We can do this by looking at a one-dimensional model where, of course, $\theta=0$.

Next, we need to determine θ from three-dimensional simulations. The hope is then that we can express baroclinic vorticity production in the form

$$k_\omega/k_{\rm f}=\mathrm{St}_{\rm baro}(\boldsymbol{\nabla}T)_{\rm rms}(\boldsymbol{\nabla}s)_{\rm rms}\sin\theta/u_{\rm rms}^2k_{\rm f}^2. \tag{15}$$

On dimensional grounds we expect the product of $(\boldsymbol{\nabla}T)_{\rm rms}$ and $(\boldsymbol{\nabla}s)_{\rm rms}$ to be of the order of $u_{\rm rms}^2k_{\rm f}^2$, and so a possible ansatz would be

$$k_\omega/k_{\rm f}=\mathrm{St}_{\rm baro}^{\rm eff}\sin\theta, \tag{16}$$

where we have subsumed the scalings of $(\boldsymbol{\nabla}T)_{\rm rms}$ and $(\boldsymbol{\nabla}s)_{\rm rms}$ in that of an effective baroclinic Strouhal number $\mathrm{St}_{\rm baro}^{\rm eff}$.

An important issue is the fact that viscous heating leads to a continuous increases of the temperature. As a result, the sound speed changes and it becomes then impossible to study the behavior of the system in a steady state. In order to avoid this inconvenience, we add a volume cooling term that is non-vanishing when the local sound speed $c_{\rm s}$ is different from a given target value, $c_{\rm s0}$. Thus, in the presence of finite thermal diffusivity χ, and with a cooling term governed by a cooling time $\tau_{\rm cool}$, our entropy equation takes the form

$$T\frac{{\rm D}s}{{\rm D}t}=2\nu\mathbf{S}^2+\rho^{-1}\boldsymbol{\nabla}\cdot(c_p\rho\chi\boldsymbol{\nabla}T)-\frac{1}{\tau_{\rm cool}}(c_{\rm s}^2-c_{\rm s0}^2), \tag{17}$$

where $c_{\rm s}$ is the adiabatic sound speed. We assume a perfect gas so that $c_{\rm s}^2=(\gamma-1)c_pT$, where $\gamma=c_p/c_v=5/3$ for a monatomic gas, and c_p and c_v are the specific heats at constant pressure and constant volume, respectively. The value of $\tau_{\rm cool}$ can have an influence on the results, so we need to consider different values. We express $\tau_{\rm cool}$ in terms of $c_{\rm s0}$ and $k_{\rm f}$, and define the nondimensional quantity $\mathrm{St}_{\rm cool}=\tau_{\rm cool}c_{\rm s0}k_{\rm f}$.

3. The model

In this paper we solve the continuity equation for the density ρ,

$$\frac{{\rm D}\ln\rho}{{\rm D}t}=-\boldsymbol{\nabla}\cdot\boldsymbol{u}, \tag{18}$$

together with the momentum equation for the velocity $\boldsymbol{u}$,

$$\frac{{\rm D}\boldsymbol{u}}{{\rm D}t}=-\rho^{-1}\boldsymbol{\nabla}p-2\boldsymbol{\Omega}\times\boldsymbol{u}-Su_x\hat{\boldsymbol{y}}+\boldsymbol{\nabla}\phi+\boldsymbol{F}_{\rm visc}, \tag{19}$$

where ${\rm D}/{\rm D}t=\partial/\partial t+(\boldsymbol{u}+\boldsymbol{u}^S)\cdot\boldsymbol{\nabla}$ is the advection operator with respect to the sum of turbulent flow $\boldsymbol{u}$ and laminar shear flow $\boldsymbol{u}^S$, p is the pressure, ϕ is the forcing potential, and

$$\boldsymbol{F}_{\rm visc}=\rho^{-1}\boldsymbol{\nabla}\cdot(2\nu\rho\mathbf{S}) \tag{20}$$

is the viscous force, where $\mathbf{S}$ was defined in Equation (2). The forcing potential is given by

$$\phi(\boldsymbol{x},t)=\phi_0\,N\exp\left\{-[\boldsymbol{x}-\boldsymbol{x}_{\rm f}(t)]^2/R^2\right\}, \tag{21}$$

where $\boldsymbol{x}=(x,y,z)$ is the position vector, $\boldsymbol{x}_{\rm f}(t)$ is the random forcing position that changes abruptly after a time interval Δt, R is the radius of the Gaussian, and N is a non-dimensional factor proportional to $\Delta t^{-1/2}$. This ensures that the amplitude of the correlation function of ϕ is independent of Δt. Thus, we choose $N=\sqrt{R/c_{\rm s0}\Delta t}$. Since N is non-dimensional, the prefactor ϕ_0 has the same dimension as ϕ, which is that of velocity squared. We consider two forms for the time dependence of $\boldsymbol{x}_{\rm f}$. First, we take $\boldsymbol{x}_{\rm f}$ such that the forcing is δ-correlated in time. In that case, Δt is equal to the length of the time step δt. Alternatively, we choose a finite forcing time $\delta t_{\rm force}$ that defines the interval during which $\boldsymbol{x}_{\rm f}$ remains constant, after which the forcing changes again abruptly. Thus,

$$\Delta t=\max\left(\delta t,\delta t_{\rm force}\right) \tag{22}$$

is equal to δt in the δ-correlated case or equal to $\delta t_{\rm force}$ in the case of finite correlation time.

The work of Mee & Brandenburg (2006) showed that the peak of the energy spectrum depends on the radius R of the Gaussian. Indeed, the Fourier transform of $\exp(-r^2/R^2)$ is also a Gaussian with $\exp(-k^2/k_{\rm f}^2)$, where

$$k_{\rm f}=2/R. \tag{23}$$

In the following we use this as our definition of $k_{\rm f}$ and check a posteriori that this is close to the position of the peak of the energy spectrum. In the following, we characterize our simulations in terms of the ratio $k_{\rm f}/k_1$, and consider values between 2 and 10.

We use the PENCIL CODE,[1] which is a non-conservative, high-order, finite-difference code (sixth order in space and third order in time) for solving the compressible hydrodynamic and hydromagnetic equations. We adopt non-dimensional variables by measuring speed in units of a reference sound speed, $c_{\rm s0}$, and length in units of $1/k_1$, where k_1 is the smallest wavenumber in the periodic domain. This implies that the nondimensional size of the domain is $(2\pi)^3$.

In order to study the effects of rotation and shear, we ignore entropy effects and restrict ourselves to an isothermal equation of state with constant sound speed $c_{\rm s}$. This means that $\rho^{-1}\boldsymbol{\nabla} p$ reduces to $c_{\rm s}^2\boldsymbol{\nabla}\ln\rho = \boldsymbol{\nabla}h$, which has vanishing curl. Here, $h = c_{\rm s}^2\ln\rho$ is the relevant enthalpy in the isothermal case. On the other hand, in order to study the effects of baroclinicity, we do need to allow the entropy to vary, so we also need to solve Equation (17), and study the dependence of $k_\omega/k_{\rm f}$ on the Mach number,

$$\mathrm{Ma} = u_{\rm rms}/c_{\rm s}. \tag{24}$$

In order to characterize the degree of turbulence, we define the Reynolds number based on the energy-carrying scale, corresponding to the typical wavenumber where the spectrum peaks, i.e.

$$\mathrm{Re} = u_{\rm rms}/\nu k_{\rm f}. \tag{25}$$

For vortical turbulence, this definition is known to be a good measure of the ratio of the resulting turbulent viscosity divided by the molecular diffusivity (Yousef et al., 2003). The two numbers, Ma and Re, can be varied by changing ν and/or the strength of the forcing. In all cases we use $\chi = \nu$. Another input parameter is the forcing Strouhal number

$$\mathrm{St}_{\rm force} = \tau_{\rm force}u_{\rm rms}k_{\rm f}, \tag{26}$$

which is zero for δ-correlated forcing and equal to about 0.3 in cases with finite correlation time. These are also the values used by Mee & Brandenburg (2006).

In the following we also consider kinetic energy and enstrophy spectra, $E_{\rm K}(k)$ and $E_\omega(k)$, respectively. They are normalized such that (Lesieur, 1990)

$$\int E_{\rm K}(k)\,{\rm d}k = \tfrac{1}{2}\langle\boldsymbol{u}^2\rangle, \quad \int E_\omega(k)\,{\rm d}k = \tfrac{1}{2}\langle\boldsymbol{\omega}^2\rangle, \tag{27}$$

where $\frac{1}{2}\langle\boldsymbol{u}^2\rangle$ and $\frac{1}{2}\langle\boldsymbol{\omega}^2\rangle$ are kinetic energy and enstrophy, respectively. For comparison we also consider spectra of enthalpy, $E_{\rm h}(k)$, which are normalized such that $\int E_{\rm h}(k)\,{\rm d}k = \frac{1}{2}\langle h^2\rangle$.

Throughout this paper we assume periodic boundary conditions, except that in the presence of shear we employ shearing-periodic boundary conditions where the x direction is periodic with respect to positions in y that shift with time, i.e.

$$f(-\tfrac{1}{2}L_x, y, z, t) = f(\tfrac{1}{2}L_x, y + L_xSt, z, t), \tag{28}$$

where f represents any one of our four dependent variables $(\boldsymbol{u}, \rho)$. This boundary condition was first proposed by Goldreich & Lynden-Bell (1965) and has been routinely used in local simulations of accretion disk turbulence (Hawley et al., 1995). Note, however, that recent work of Regev & Umurhan (2008) and Bodo et al. (2008) called attention to the possibility of problems with the shearing sheet approximation when the size of the perturbations is large. In somewhat weaker form, this problem also applies to a non-shearing periodic box. Indeed, we shall kept this in mind when interpreting some of the results presented below.

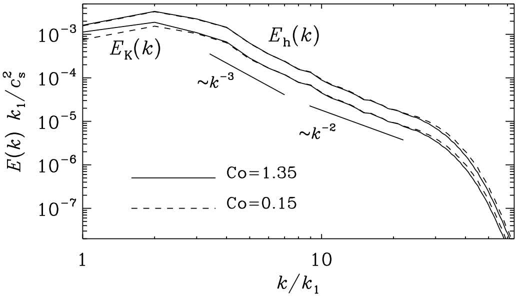

Fig. 1. Time-averaged kinetic energy and enthalpy spectra for two values of the Coriolis number for $\mathrm{Re} = 25$ and $\mathrm{St}_{\rm force} = 0.4$. The two straight lines give the slopes -2 and -3, respectively. In both cases we have $k_{\rm f}/k_1 = 4$.

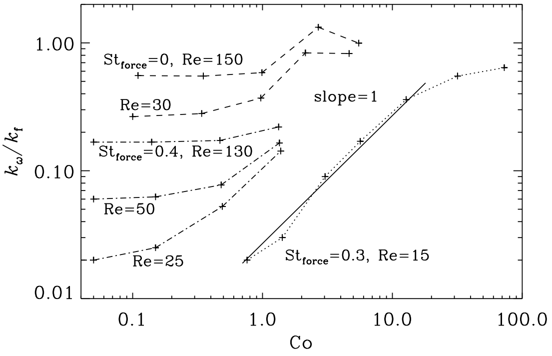

Fig. 2. Dependence of $k_\omega/k_{\rm f}$ on Co for three groups of runs: group 1 with $\mathrm{Re} = 15$, $k_{\rm f}/k_1 = 10$, $\mathrm{St}_{\rm force} = 0.3$; group 2 with Re between 25 and 130, $k_{\rm f}/k_1 = 4$, $\mathrm{St}_{\rm force} = 0.4$; and group 3 with $\mathrm{Re} = 30$ and 150, $k_{\rm f}/k_1 = 2$, $\mathrm{St}_{\rm force} = 0$.

4. Results

We begin by studying the effect of rotation. In Figure 1 we plot time-averaged kinetic energy and enthalpy spectra, $E_{\rm K}(k)$ and $E_{\rm h}(k)$, respectively. Note that rotation has a tendency to move the peak of $E_{\rm K}(k)$ to the left of the nominal value of $k_{\rm f}$. However, at the Reynolds number of 25 shown here, there is no inertial range, but in all cases, the energy spectra show a clear viscous dissipation range, suggesting that these runs are sufficiently well resolved. At somewhat larger Reynolds number or smaller forcing wavenumber, earlier work of Mee & Brandenburg (2006) began to show a short k^{-2} subrange. Such a slope is predicted for shock turbulence (Kadomtsev & Petviashvili, 1973), and it has also been seen in the irrotational component of transonic turbulence (Porter et al., 1998).

---

[1] `http://pencil-code.googlecode.com/`

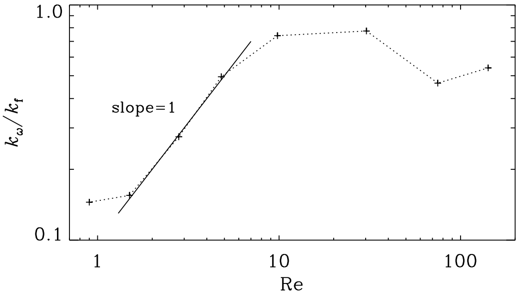

Fig. 3. Dependence of $k_\omega/k_{\rm f}$ on Re for Co $\approx$ 1, $k_{\rm f}/k_1 = 2$, and $\mathrm{St}_{\rm force} = 0$ (δ-correlated forcing).

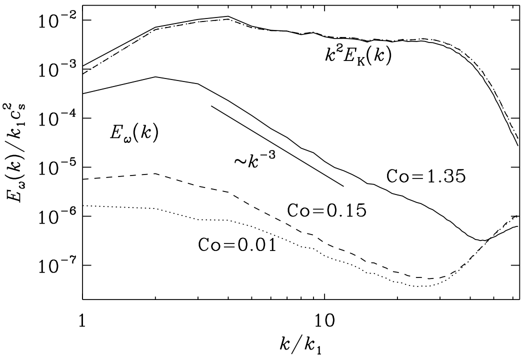

Fig. 4. Time-averaged enstrophy spectra, $E_\omega(k)$, compared with $k^2E_{\rm K}(k)$, for Re = 25, $\mathrm{St}_{\rm force} = 0.4$, and three values of the Coriolis number. The curves of $k^2E_{\rm K}(k)$ are close together and overlap for Co = 0.01 (dotted) and 0.15 (dashed), so it becomes a single dash-dotted line. The k^{-3} slope is shown for comparison. In all three cases we have $k_{\rm f}/k_1 = 4$.

In Figure 2 we plot the dependence of $k_\omega/k_{\rm f}$ on Co for three groups of runs: group 1 with Re = 15, $k_{\rm f}/k_1 = 10$, $\mathrm{St}_{\rm force} = 0.3$; group 2 with Re between 25 and 130, $k_{\rm f}/k_1 = 4$, $\mathrm{St}_{\rm force} = 0.4$; and group 3 with Re = 30 and 150, $k_{\rm f}/k_1 = 2$, $\mathrm{St}_{\rm force} = 0$. In all cases we use 128^3 mesh points, average the results over at least 200 turnover times and, in some cases, even several thousand turnover times. It turns out that for $\mathrm{St}_{\rm force} \neq 0$ a linear relationship between $k_\omega/k_{\rm f}$ and Co is a good approximation for Co $\lesssim$ 10, where $k_\omega/k_{\rm f} \approx 0.03\,\mathrm{Co}$, i.e. $\mathrm{St}_\Omega = 0.03$. Furthermore, we see from Table 1 that the normalized velocity derivative terms are all about 0.5, so the root of the sum of their squares is slightly larger than unity, corresponding to $\tau_\Omega^{\rm eff}/\tau_\Omega \approx 1.3$. For Co > 10 the value of $k_\omega/k_{\rm f}$ seems to saturate at about unity.

A similar result is also found for $\mathrm{St}_{\rm force} = 0$, except that there remains a spurious contamination of vorticity even for small values of Co, a limit in which we expect to observe no vorticity production. By varying the value of Re, while keeping Co $\approx$ 1 fixed, we see that $k_\omega/k_{\rm f}$ asymptotes to zero for sufficiently small values of Re; see Figure 3. This suggests that there can easily be spurious vorticity generation, possibly due to marginally sufficient resolution. The possibility of spurious vorticity is indeed verified by Figure 4, where we compare enstrophy spectra, $E_\omega(k)$, with $k^2E_{\rm K}(k)$. Note that for large values of Co, the enstrophy spectrum decays like k^{-3}. However, for smaller values of Co the level of enstrophy at the mesh scale remains approximately unchanged and is thus responsible for the spurious vorticity found above for small values of Co and not too small values of Re. Nevertheless for larger values of Co, the production of vorticity is an obvious effect of rotation in an otherwise potential velocity field, and it is most pronounced at large length scales, as can also be seen in Figure 4.

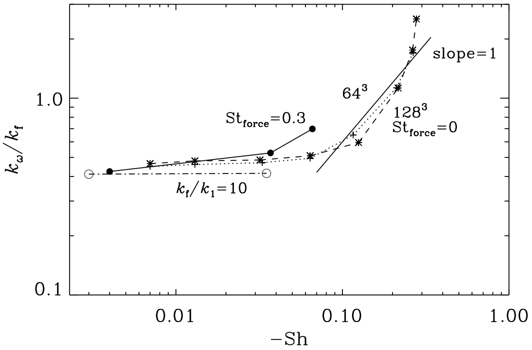

Fig. 5. Dependence of $k_\omega/k_{\rm f}$ on Sh for Re $\approx$ 40 and $k_{\rm f}/k_1 = 2$ and δ-correlated forcing ($\mathrm{St}_{\rm force} = 0$). Different resolutions are shown to give similar results. At small values of |Sh|, comparisons with $\mathrm{St}_{\rm force} = 0.3$ (keeping $k_{\rm f}/k_1 = 2$) or $k_{\rm f}/k_1 = 10$ (keeping $\mathrm{St}_{\rm force} = 0$) are also shown.

Next, we study the dependence of the ratio $k_\omega/k_{\rm f}$ on shear; see Figure 5. We use a resolution of 64^3 or 128^3 mesh points, average the results over at least 200 turnover times and, in cases of lower resolution, over several thousand turnover times. It turns out that in the presence of shear, some level of helicity production can never be avoided – even in the limit of small Sh. Again, this appears spurious and demonstrates the general sensitivity of vorticity generation on resolution effects. An additional problem is of course the finite size of the shearing box (Regev & Umurhan, 2008; Bodo et al., 2008), which may be responsible for spurious vorticity generation. On the other hand, there is vorticity generation even for large scale-separation ratios, $k_{\rm f}/k_1 = 10$; see the dash-dotted line in Figure 5. This suggests the possibility of a more general problem that would

Table 1. Root-mean-squared values of components of the velocity derivative tensor, normalized by $u_{\rm rms}k_{\rm f}$, as well as the three diagonal components of the $\langle u_iu_j\rangle$ tensor for 4 values of Co.

Co	0.11	0.35	0.99	2.80
$(\boldsymbol{\nabla}_\perp\boldsymbol{u}_\perp)_{\rm rms}/u_{\rm rms}k_{\rm f}$	1.26	1.20	1.21	1.04
$u_{x,x}^{\rm rms}/u_{\rm rms}k_{\rm f}$	0.76	0.74	0.75	0.70
$u_{y,y}^{\rm rms}/u_{\rm rms}k_{\rm f}$	0.79	0.74	0.75	0.70
$u_{x,z}^{\rm rms}/u_{\rm rms}k_{\rm f}$	0.49	0.47	0.48	0.63
$u_{y,z}^{\rm rms}/u_{\rm rms}k_{\rm f}$	0.49	0.47	0.48	0.63
$u_{z,y}^{\rm rms}/u_{\rm rms}k_{\rm f}$	0.49	0.47	0.46	0.58
$\langle u_x^2\rangle/u_{\rm rms}^2$	0.32	0.33	0.35	0.42
$\langle u_y^2\rangle/u_{\rm rms}^2$	0.34	0.34	0.35	0.41
$\langle u_z^2\rangle/u_{\rm rms}^2$	0.35	0.34	0.29	0.18

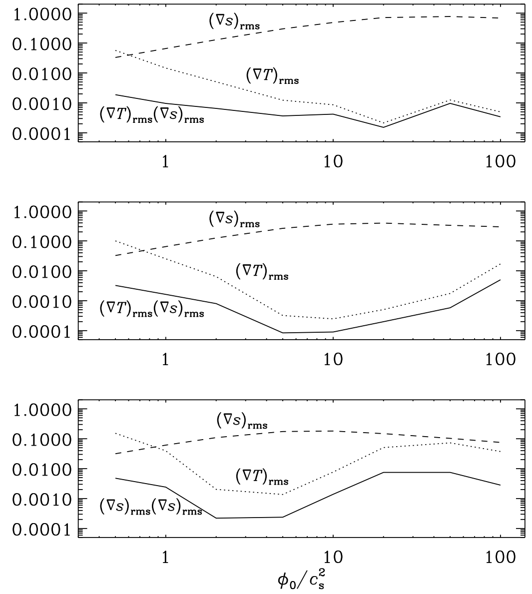

Fig. 6. Dependence of the rms values of temperature and entropy on ϕ_0 for $\nu/c_{\rm s}R = 1$ and $\mathrm{St_{cool}} = 0.2$ (top panel), 0.6 (middle panel), and 2 (bottom panel).

not go away even in the limit of small eddies and small values of $|\mathrm{Sh}|$. Nevertheless, there is a clear rise of $k_\omega/k_{\rm f}$ when $|\mathrm{Sh}| > 0.1$, which is in agreement with our expectations outlined in Section 2.2. However, the slope in this relationship is rather steep, $\mathrm{St}_S \approx 6$. The velocity derivative terms are only slightly larger than in the case with rotation, corresponding to $\tau_S^{\rm eff}/\tau_S \approx 1.5$; see also Table 2. Tentatively, this suggests that for comparable values of Co and Sh, $\tau_S \gg \tau_\Omega$. On the other hand, given that even for small values of Sh there is spurious vorticity generation, we cannot be certain that the results are reliable for larger ones either. The case with shear must therefore remain somewhat inconclusive.

Finally, we consider the possibility of vorticity generation by the baroclinic term. In a preparatory step we study first the dependence of the product $(\boldsymbol{\nabla}T)_{\rm rms}(\boldsymbol{\nabla}s)_{\rm rms}$ on both Ma and Re in a one-dimensional model. In all cases we vary the strength of the forcing amplitude in the range $1 \leq \phi_0/c_{\rm s0}^2 \leq 500$ for different values of viscosity and cooling time. As we increase the value of ϕ_0, the Reynolds number increases for a given value of the viscosity. For small values of ϕ_0, the Mach number also increases linearly, where the ratio of Ma/Re increases with increasing viscosity. However, for larger values of ϕ_0 there is saturation and Ma no longer increase with ϕ_0.

Table 2. Similar to Table 1, but for the case with shear.

Sh	-0.01	-0.03	-0.06	-0.12	-0.26
$(\boldsymbol{\nabla}_\perp\boldsymbol{u}_\perp)_{\rm rms}/u_{\rm rms}k_{\rm f}$	1.35	1.36	1.36	1.37	0.87
$u_{x,x}^{\rm rms}/u_{\rm rms}k_{\rm f}$	0.87	0.87	0.90	0.97	0.75
$u_{y,y}^{\rm rms}/u_{\rm rms}k_{\rm f}$	0.81	0.81	0.76	0.66	0.47
$u_{x,z}^{\rm rms}/u_{\rm rms}k_{\rm f}$	0.51	0.50	0.51	0.53	0.72
$u_{y,z}^{\rm rms}/u_{\rm rms}k_{\rm f}$	0.46	0.47	0.47	0.46	0.74
$u_{z,y}^{\rm rms}/u_{\rm rms}k_{\rm f}$	0.46	0.48	0.46	0.43	0.57
$\langle u_x^2\rangle/u_{\rm rms}^2$	0.37	0.38	0.37	0.36	0.25
$\langle u_y^2\rangle/u_{\rm rms}^2$	0.31	0.31	0.32	0.34	0.56
$\langle u_z^2\rangle/u_{\rm rms}^2$	0.32	0.31	0.31	0.31	0.25

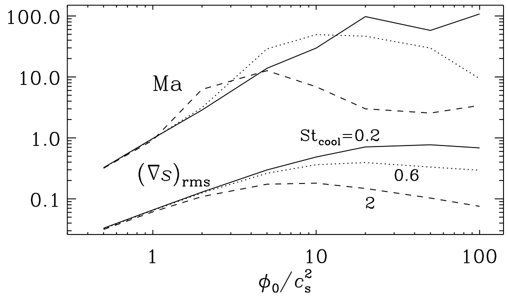

Fig. 7. Dependence of Mach number and the rms value of entropy on ϕ_0 for $\nu/c_{\rm s}R = 1$ and $\mathrm{St_{cool}} = 0.2$, 0.6, and 2 (solid, dotted, and dashed line types, respectively).

Furthermore, in the range where Ma still increases linearly with ϕ_0, the rms value of the entropy gradient increases, but it also saturates when Ma saturates. The rms value of the temperature gradient, however, decreases with increasing values of ϕ_0, but this seems to be a special property of the one-dimensional model that is not borne out by the three-dimensional simulations where it stays approximately constant.

Remarkably, the results are fairly independent of the cooling time, except that the break point where $(\nabla s)_{\rm rms}$ saturates occurs for smaller values of ϕ_0 as we increase the cooling time; see Figure 6. This break point is also related to the point where the Mach number saturates, as can be seen from Figure 7. However, for longer cooling times there can be longer transients, making it difficult to obtain good averages. Therefore we focus, in the rest of this paper, on the case of shorter cooling times using $\mathrm{St_{cool}} = 0.2$. Another remarkable result is that the normalized value of $(\boldsymbol{\nabla}T)_{\rm rms}(\boldsymbol{\nabla}s)_{\rm rms}$ is always of the order of about 10^{-3}, independent of resolution, cooling time, or the value of the viscosity.

Most of the basic features of the one-dimensional model are also reproduced by two- and three-dimensional calculations. Two-dimensional simulations have the advantage of being easily visualized and are therefore best suited for illustrating vorticity production by the baroclinic term. In Figure 8 we demonstrate that vorticity production is associated with the interaction between the fronts of different expansion waves. In this example we chose $\delta t_{\rm force}c_{\rm s0}/R = 0.1$, so the first expansion wave is launched at $t = 0$ and the second one at $tc_{\rm s0}/R = 0.1$. The top row of Figure 8 shows that at $tc_{\rm s0}/R = 0.09$, i.e. just before launching the second expansion wave, the baroclinic term and the vorticity are still just at the noise level. At that time the most pronounced feature is the discontinuity between the Gaussian expansion waves in the periodic domain. This leads to negligibly weak vorticity, and no baroclinic term. At $tc_{\rm s0}/R = 0.11$, the effect of the second expansion wave becomes noticeable in visualizations of both $(\boldsymbol{\nabla}T \times \boldsymbol{\nabla}s)_z$ and ω_z, while our visualizations of T and s barely show the second expansion wave. At $tc_{\rm s0}/R = 0.14$, the first expansion wave is clearly no longer circular, which is obviously associated with the second expansion

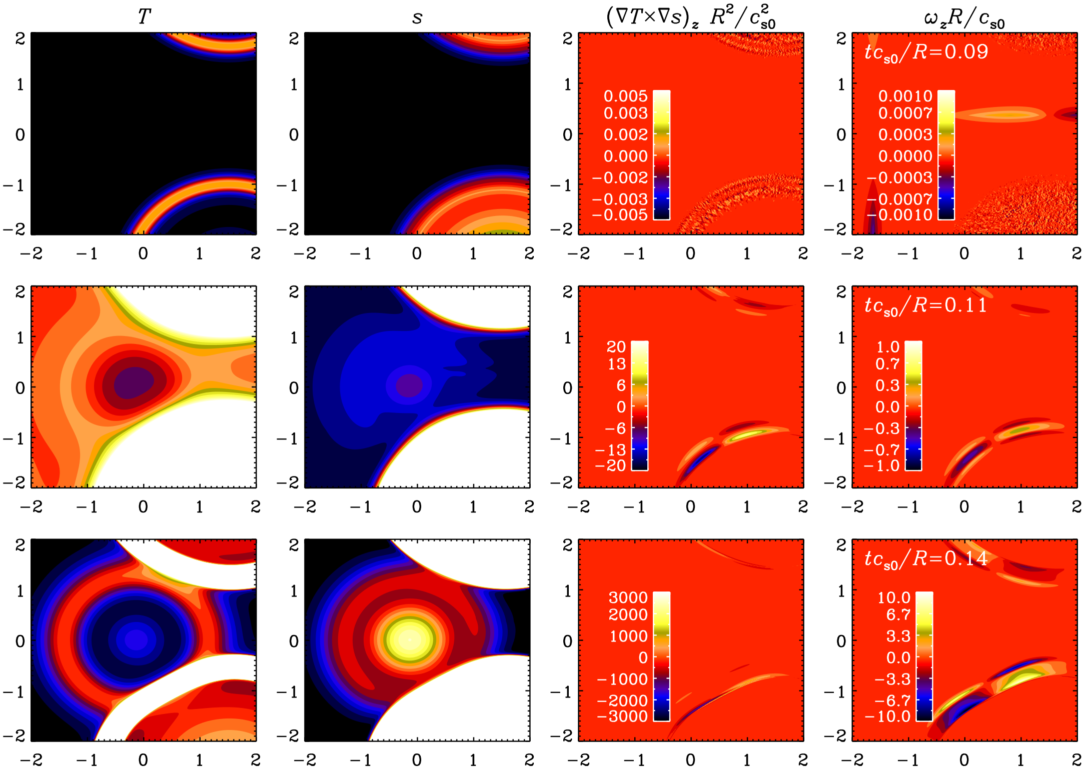

Fig. 8. Images of T, s, $(\nabla T \times \nabla s)_z$, and normalized vertical vorticity for a two-dimensional run with $\delta t_{\rm force} c_{\rm s0}/R = 0.1$ at an instant shortly before the second expansion wave is launched (top row), and shortly after the second expansion wave is launched (second and third row). Note the vorticity production from the baroclinic term in the second and third row, while in the top row, $(\nabla T \times \nabla s)_z$ and ω_z are just at the noise level of the calculation. Even under our weakly supersonic conditions shock surfaces are well localized and the zones of maximum production of vorticity appear to be those in which the fronts encounter each other. Here we have used $\phi_0/c_{\rm s0}^2 = 100$, $\nu = \chi = 0.1 c_{\rm s0} R$, with 512^2 mesh points. Only the inner part of the domain is shown.

wave that is now quite pronounced in our visualizations of both T and s.

In order to have a more accurate quantitative determination of vorticity production, we now consider three-dimensional models. In Figure 9 we show the dependence of various quantities on ϕ_0 for $\mathrm{St}_{\rm cool} = 0.2$ and $\nu/c_{\rm s}R = 1$. In all cases we use 128^3 mesh points and average the results over between 20 and 70 turnover times. Note that here $\mathrm{Re} \approx 0.05\,\phi_0/c_{\rm s0}^2$. Given that Re depends inverse proportionally on $\nu/Rc_{\rm s0}$, we can also write $\mathrm{Re} \approx 0.05\,\phi_0 R/c_{\rm s0}\nu$. The Mach number saturates at about $\mathrm{Ma} = 3$, and the rms value of the entropy gradient increases up until this point. Given that the rms value of the temperature gradient also stays approximately constant, we find a weak increase of $(\nabla T)_{\rm rms}(\nabla s)_{\rm rms}$. The value of $(\nabla T \times \nabla s)_{\rm rms}$ is always found to be a certain fraction below this value, resulting in a typical baroclinic angle of about 45 degrees; see the third panel of Figure 9. Finally, the amount of vorticity production in terms of $k_\omega/k_{\rm f}$ is about 0.3 for $\phi_0/c_{\rm s0}^2 \gtrsim 20$. For smaller values, on the other hand, there is an approximately linear increase with $k_\omega/k_{\rm f} \approx 0.014\,\phi_0/c_{\rm s0}^2$.

The possibility of spurious vorticity is easily eliminated in this case by looking at enstrophy spectra; see Figure 10, where we compare $E_\omega(k)$ with $k^2 E_{\rm K}(k)$. All spectra fall off rapidly with increasing k. Thus, even though the initial vorticity generation occurred evidently at the smallest available scales, once the flow becomes fully developed, most of the enstrophy resides at scales equal to or larger than the driving scale. Furthermore, the spectra of $E_\omega(k)$ and $k^2 E_{\rm K}(k)$ are close together, suggesting that the vorticity is close to its maximal value.

5. Applications

The level of vorticity that is produced in the usual case of solenoidal forcing of the turbulence is such that $k_\omega/k_{\rm f} \approx 1$ (see, e.g., Brandenburg, 2001). For turbulence whose driving force has finite correlation time ($\mathrm{St}_{\rm force} = 0.3$, for example), and small values of Re, we have $k_\omega/k_{\rm f} = O(1)$ when $\mathrm{Co} \gtrsim 10$. However, for larger values of Re, the turbulence becomes vortical already for smaller values of Co. Comparing with the galaxy, we have $\Omega \approx 10^{-15}\,\mathrm{s}^{-1}$, $u_{\rm rms} = 10\,\mathrm{km/s}$, and an estimated correlation length of about 70 pc, so $k_{\rm f} = 3 \times 10^{-20}\,\mathrm{cm}$, so $\mathrm{Co} = 0.07$, which is rather small. Thus, rotation may not be able to produce sufficient levels of vorticity. Given that in galaxies with flat rotation curves, $S \approx -\Omega$, shear should not be very efficient ei-

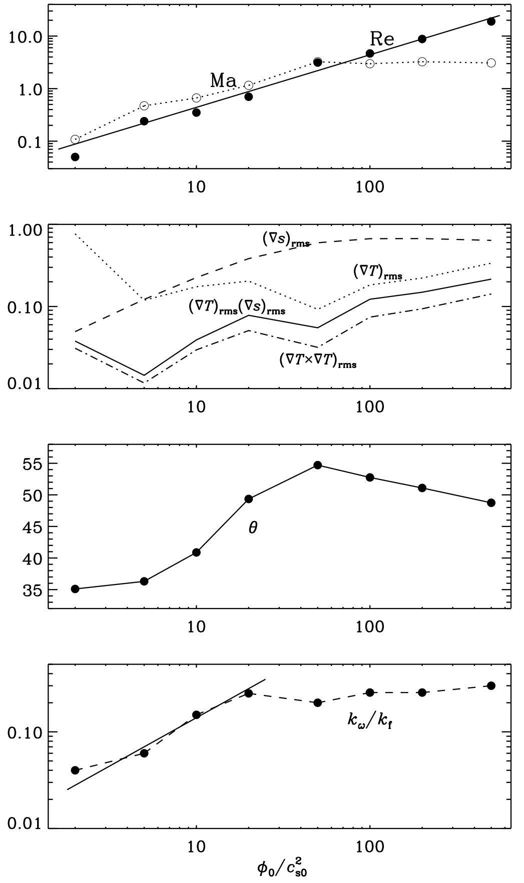

Fig. 9. Dependence of Ma, Re, the rms values of $\boldsymbol{\nabla}s$ and $\boldsymbol{\nabla}T$, the angle θ between them, as well as $k_\omega/k_{\rm f}$, on $\phi_0/c_{\rm s}^2$ for $\nu/c_{\rm s}R=1$.

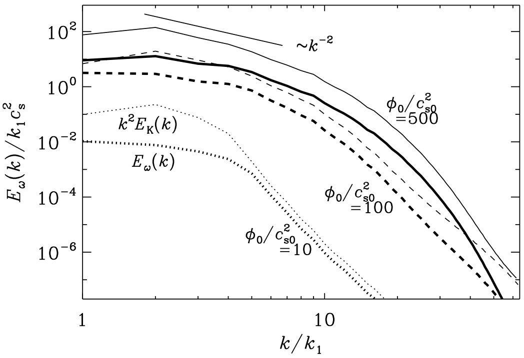

Fig. 10. Time-averaged enstrophy spectra, $E_\omega(k)$ (thick lines), compared with $k^2E_{\rm K}(k)$ (thin lines below the corresponding thick lines), for the three-dimensional baroclinic case with $\phi_0/c_{\rm s0}^2=10$ (dashed), 100 (dotted), and 500 (solid lines). The k^{-2} slope is shown for comparison. In all three cases we have $k_{\rm f}/k_1=4$.

ther. However, the Mach numbers are undoubtedly larger than unity in the interstellar medium, so this should lead to values of $k_\omega/k_{\rm f}\approx 0.3$, which is the saturation value found in Figure 9. Given that one of the reasons for studying the production of vorticity is the question of dynamo action, we should point out that such values of $k_\omega/k_{\rm f}$ are large enough for the small-scale dynamo. Large-scale dynamo action should be possible in galaxies as well, because of their large length scales, but it suffers from the well-known problem of a small growth rate. It then remains difficult to explain large-scale magnetic fields in very young galaxies (Beck et al., 1996).

The question of vorticity generation is also important in studies of the very early Universe, where phase transition bubbles are believed to be generated in connection with the electroweak phase transition (Kajantie & Kurki-Suonio, 1986; Ignatius et al., 1994). Here the equation of state is that of a relativistic fluid, $p=\rho c^2/3$, where c is the speed of light. Thus, there is no baroclinic term and no obvious source of vorticity. However, the relativistic equation of state may be modified at small length scales, but it is not clear that this can facilitate significant vorticity production.

6. Conclusions

The present work has demonstrated that vorticity production is actually quite ubiquitous once there is rotation, shear, or baroclinicity. This implies that the assumption of potential flows as a model for interstellar turbulence might be of academic interest and could only be realized under special conditions of weak forcing, weak rotation, and no shear. In galaxies, however, the shear and Coriolis number are well below unity, leaving only the baroclinic term as a viable candidate for the production of vorticity. This agrees with early work of Korpi et al. (1999b), who analyzed the production terms in supersonic, supernova-driven turbulence quantitatively; see also Glasner et al. (1997), who showed that on long enough time scales significant vorticity can also be produced for subsonic flows. We have also observed how vorticity is mainly produced close to shock front encounters. This motivates a more detailed investigation of these zones as the next step in the study of vorticity generation in the interstellar medium. It should also be pointed out that the baroclinic term corresponds to the battery term in the induction equation Kulsrud et al. (1997); Brandenburg & Subramanian (2005). Thus, when studying the possibility of dynamo action, this battery term provides an intrinsic and well defined seed for the dynamo and should therefore be included as well.

Acknowledgements. We thank an anonymous referee for making a number of useful suggestions that have improved our paper. We acknowledge the allocation of computing resources provided by the Swedish National Allocations Committee at the Center for Parallel Computers at the Royal Institute of Technology in Stockholm and the National Supercomputer Centers in Linköping. This work was supported in part by the European Research Council under the AstroDyn Research Project 227952 and the Swedish Research Council grant 621-2007-4064.

References

Beck, R., Brandenburg, A., Moss, D., Shukurov, A., & Sokoloff, D. 1996, ARA&A, 34, 155
Bodo, G., Mignone, A., Cattaneo, F., Rossi, P., & Ferrari, A. 2008, A&A, 487, 1

Brandenburg, A. 2001, ApJ, 550, 824
Brandenburg, A., & Subramanian, K. 2005, Phys. Rep., 417, 1
de Avillez, M. A., & Breitschwerdt, D. 2005, A&A, 436, 585
Federrath, C., Roman-Duval, J., Klessen, R. S., Schmidt, W., & Mac Low, M.-M. 2010, A&A, 512, A81
Gissinger, C., Fromang, S., & Dormy, E. 2009, MNRAS, 394, L84
Glasner, A., Livne, E., & Meerson, B. 1997, Phys. Rev. Lett., 78, 2112
Goldreich, P., & Lynden-Bell, D. 1965, MNRAS, 130, 125
Gressel, O., Elstner, D., Ziegler, U., & Rd̈iger, G. 2008, A&A, 486, L35
Hanasz, M., Otmianowska-Mazur, K., Kowal, G., & Lesch, H. 2009, A&A, 498, 335
Hawley, J. F., Gammie, C. F., & Balbus, S. A. 1995, ApJ, 440, 742
Ignatius, J., Kajantie, K., Kurki-Suonio, H., & Laine, M. 1994, Phys. Rev. D, 49, 3854
Kadomtsev, B. B., & Petviashvili, V. I. 1973, Sov. Phys. Dokl., 18, 115
Kajantie, K., & Kurki-Suonio, H. 1986, Phys. Rev. D, 34, 1719
Korpi, M. J., Brandenburg, A., Shukurov, A., Tuominen, I., & Nordlund, Å. 1999a, ApJ, 514, L99
Korpi, M. J., Brandenburg, A., Shukurov, A. & Tuominen, I. 1999b, in Interstellar Turbulence, ed. J. Franco & A. Carramiñana (Cambridge University Press), 127
Kulsrud, R. M., Cen, R., Ostriker, J. P., & Ryu, D. 1997, ApJ, 480, 481
Lesieur, M. 1990, Turbulence in Fluids (Martinius Nijhoff Publishers, Dordrecht)
Mac Low, M.-M., Balsara, D. S., Kim, J., & de Avillez, M. A. 2005, ApJ, 626, 864
Mee, A. J., & Brandenburg, A. 2006, MNRAS, 370, 415
Porter, D. H., Woodward, P. R., & Pouquet, A. 1998, Phys. Fluids, 10, 237
Regev, O., & Umurhan, O. M. 2008, A&A, 481, 21
Rosen, A. & Bregman, J. N. 1995, ApJ, 440, 634
Rosen, A., Bregman, J. N., & Kelson, D. D. 1996, ApJ, 470, 839
Sridhar, S. & Subramanian, K. 2009, Phys. Rev. E, 80, 066315
Wisdom, J., & Tremaine, S. 1988, AJ, 95, 925
Yousef, T. A., Brandenburg, A., & Rüdiger, G. 2003, A&A, 411, 321

`Header: /var/cvs/brandenb/tex/fabio/vortgen/paper.tex,v 1.34 2011-02-25 14:33:39 brandenb Exp $`

III

PHYSICAL REVIEW E **86**, 016313 (2012)

Breakdown of chiral symmetry during saturation of the Tayler instability

Alfio Bonanno,[1,2] Axel Brandenburg,[3,4] Fabio Del Sordo,[3,4] and Dhrubaditya Mitra[3]
[1]*INAF, Osservatorio Astrofisico di Catania, Via S. Sofia 78, 95123 Catania, Italy*
[2]*INFN, Sezione di Catania, Via S. Sofia 72, 95123 Catania, Italy*
[3]*Nordita, Royal Institute of Technology and Stockholm University, Roslagstullsbacken 23, SE-10691 Stockholm, Sweden*
[4]*Department of Astronomy, Stockholm University, SE 10691 Stockholm, Sweden*

(Received 30 March 2012; published 13 July 2012)

We study spontaneous breakdown of chiral symmetry during the nonlinear evolution of the Tayler instability. We start with an initial steady state of zero helicity. Within linearized perturbation calculations, helical perturbations of this initial state have the same growth rate for either sign of helicity. Direct numerical simulations (DNS) of the fully nonlinear equations, however, show that an infinitesimal excess of one sign of helicity in the initial perturbation gives rise to a saturated helical state. We further show that this symmetry breaking can be described by weakly nonlinear finite-amplitude equations with undetermined coefficients which can be deduced solely from symmetry consideration. By fitting solutions of the amplitude equations to data from DNS, we further determine the coefficients of the amplitude equations.

DOI: 10.1103/PhysRevE.86.016313 PACS number(s): 47.20.Bp, 52.35.Py, 11.30.Qc, 07.55.Db

I. INTRODUCTION

There are many examples in nature where the ground state does not share the same symmetries of the underlying equations of motion [1]. The most common examples include equilibrium phase transition, e.g., the case of a liquid-solid transition where the space translational symmetry is broken, or that of a paramagnetic-ferromagnetic transition where the spin-rotational symmetry is broken; see, e.g., Ref. [2] for a detailed discussion. However, the original symmetry is not lost but gives rise to the appearance of a regular structure with a specific length scale.

In nonequilibrium physics, spontaneous symmetry breaking is often observed when some control parameter is increased above a critical value; see, e.g., Ref. [3] for a comprehensive introduction. Two well-studied examples from fluid dynamics include the case of Rayleigh-Bénard convection [3] and the Mullins-Sekerka instability of a moving interface between two phases [4]. These systems, too, are invariant under translation and reflection, but the basic instability produces a symmetry-breaking bifurcation in which the continuous translational symmetry of the basic state is broken to a discrete one, although the mirror symmetry is often retained. If the instability parameter is raised further, secondary instabilities may break the periodic pattern and eventually a completely new symmetry-broken state may emerge, as has been seen in several experiments [5]. At very high values of the control parameter, turbulence sets in and most of the symmetries are statistically restored.

In a hydrodynamic system under rotation, spontaneous breakdown of chiral symmetry has been studied; see, e.g., Ref. [7]. Spontaneous chiral symmetry breaking is also found in liquid crystals [6]. Preliminary evidence showing spontaneous chiral symmetry breaking in magnetohydrodynamics (MHD), in the absence of rotation, has been presented for the magnetic buoyancy instability [8] and for the Tayler instability in a Taylor-Couette setup [9]. However, the role of the dynamics of the bifurcation process is still poorly understood.

The purpose of the present paper is twofold. First we demonstrate the occurrence of spontaneous chiral symmetry breaking in the context of a global instability of the toroidal field, and second we elucidate some aspects of the underlying nonlinear mechanism which determines the evolution from a mirror-symmetric state to a state with a preferred handedness or helicity. In particular, we shall be interested in the case of the Tayler instability [10,11], which has attracted much interest in recent times for its possible astrophysical applications [9,12–18]. We thus discuss the possibility of generating a final state with finite helicity starting from a nonhelical basic state, using a very small controlled helical perturbation.

Our setup has the advantage of better clarifying the complex nonlinear coupling between the different modes, which eventually leads to the formation of a final helical state. In fact, the Tayler instability, in its simplest realization, has no threshold field, at least in ideal MHD [13], where a sufficient condition for instability simply reads

$$\beta \equiv \frac{\partial \ln B_\varphi}{\partial \ln s} > -\frac{1}{2}, \tag{1}$$

s being the cylindrical radius. On the other hand, the spectrum is characterized by an infinite number of unstable modes all characterized by pairs of opposite azimuthal wave number $m = \pm 1, 2, 3, \ldots$, but with precisely the same growth rate. In particular, as is well known, $m = \pm 1$ are the modes with the fastest growth rate. Here our aim is to understand the dynamics of the bifurcation process which leads to the selection of a final state of finite helicity and to understand the evolution of the system after the bifurcation takes place. It should also be noted that in the linear stage, the preferred helicity is determined essentially by the helicity of the perturbation, but the nonlinear evolution can be rather complex and it is not clear *a priori* what the final selected helical state would be.

The rest of the paper is organized as follows. In Sec. II, we write down the finite-amplitude equations that govern the evolution of the instability in the weakly nonlinear phase. Our approach is based on symmetry arguments; a detailed analytical derivation of the amplitude equations is avoided here. We find that the amplitude equations predict a breakdown of parity for a certain choice of parameters. Direct numerical simulations (DNS) of the fully nonlinear equations describing the evolution of the Tayler instability are performed in Sec. III. In our DNS studies, we also find breakdown of parity. We fit data from DNS to solutions of the amplitude equations to numerically determine the parameters appearing in the amplitude equations. It turns out that the amplitude equations we deduce are identical to those used to describe the breakdown of mirror symmetry in studies of the biochemical origin of life. This connection is explored in Sec. IV. Finally, conclusions are drawn in Sec. V

II. AMPLITUDE EQUATIONS

To the best of our knowledge, the amplitude equations describing the spontaneous breakdown of mirror symmetry in hydrodynamic instabilities were first described in Ref. [19]. The basic idea is as follows.

Let us consider an instability with two growing modes with opposite helicity but exactly the same growth rate and let the amplitude in this basis of the left- and right-handed modes be given by vectors $\hat{\boldsymbol{L}}$ and $\hat{\boldsymbol{R}}$, respectively. In physical space, we have

$$\boldsymbol{L}(\boldsymbol{x}) = \hat{\boldsymbol{L}}\phi(\boldsymbol{n}), \tag{2}$$

$$\boldsymbol{R}(\boldsymbol{x}) = \hat{\boldsymbol{R}}\phi(\boldsymbol{n}). \tag{3}$$

For example, in Cartesian domains, with real-space coordinate $\boldsymbol{x}$, $\phi(\mathrm{n}) = \exp(i\boldsymbol{n}\cdot\boldsymbol{x})$. In cylindrical coordinate, ϕ is a combination of trigonometric and Bessel functions. As the modes are helical, they satisfy the Beltrami relation,

$$\nabla\times\boldsymbol{R} = \Lambda\boldsymbol{R} \quad \text{and} \quad \nabla\times\boldsymbol{L} = -\Lambda\boldsymbol{L}. \tag{4}$$

For the present problem, explicit expressions involve a linear combinations of the type $J_m(s\sqrt{\Lambda^2 + n^2\pi^2/h^2})\cos(m\phi)\cos(zn\pi/h)$, where J_m is the Bessel function of the first kind, $n,m = \pm 1,2,3\ldots$, h is the height of the cylinder, and s the cylindrical radius [20]. The set of such modes forms a complete set (a Hilbert basis) for the spatial distribution of the field.

Here we assume that the dynamical evolution of the unstable mode is determined by an effective Lagrangian. For the left-handed helical mode, total helicity and energy are given by

$$E_L = \frac{1}{2}\int \boldsymbol{L}^2(\boldsymbol{x})\,d^3x = \frac{1}{2}\hat{\boldsymbol{L}}\cdot\hat{\boldsymbol{L}}^*, \tag{5}$$

$$\mathcal{H}_L = \int \boldsymbol{L}\cdot\nabla\times\boldsymbol{L}\,d^3x = -2\Lambda E_L, \tag{6}$$

where an asterisk denotes complex conjugation. Analogous definitions apply also to E_R and $\mathcal{H}_R = +2\Lambda E_R$. We then have $E = E_L + E_R$ being the total energy and $\mathcal{H} = \mathcal{H}_L + \mathcal{H}_R$ the total helicity. In the weakly nonlinear regime, the amplitude equations can be written as

$$\frac{\partial\hat{\boldsymbol{L}}}{\partial t} = \frac{\delta\mathcal{L}}{\delta\hat{\boldsymbol{L}}} \quad \text{and} \quad \frac{\partial\hat{\boldsymbol{R}}}{\partial t} = \frac{\delta\mathcal{L}}{\delta\hat{\boldsymbol{R}}}, \tag{7}$$

where the simplest form of the Lagrangian is given by

$$\mathcal{L}[\hat{\boldsymbol{L}},\hat{\boldsymbol{R}}] = \gamma[|\hat{\boldsymbol{L}}|^2 + |\hat{\boldsymbol{R}}|^2] - \mu[|\hat{\boldsymbol{L}}|^4 + |\hat{\boldsymbol{R}}|^4]. \tag{8}$$

The form of the Lagrangian is determined by the symmetry of the problem. The coefficient γ is the linear growth rate and μ determines the saturation of the instability in the weakly nonlinear regime. We emphasize that the μ and γ for $\hat{\boldsymbol{L}}$ and $\hat{\boldsymbol{R}}$ could be different if and only if the chiral symmetry is broken from the outset, but this is *not* the case here. Now note that the Lagrangian must also be invariant under the parity transformation, under which

$$\mathcal{P}(\hat{\boldsymbol{L}}) = \hat{\boldsymbol{R}} \quad \text{and} \quad \mathcal{P}(\hat{\boldsymbol{R}}) = \hat{\boldsymbol{L}}. \tag{9}$$

This additional symmetry allows one additional term in the Lagrangian given by

$$-\mu_*(|\hat{\boldsymbol{L}}|^2|\hat{\boldsymbol{R}}|^2). \tag{10}$$

With this additional term in the Lagrangian, the evolution equations for the two eigenmodes are given by

$$\frac{\partial\hat{\boldsymbol{L}}}{\partial t} = \gamma\hat{\boldsymbol{L}} - (\mu|\hat{\boldsymbol{L}}|^2 + \mu_*|\hat{\boldsymbol{R}}|^2)\hat{\boldsymbol{L}}, \tag{11a}$$

$$\frac{\partial\hat{\boldsymbol{R}}}{\partial t} = \gamma\hat{\boldsymbol{R}} - (\mu|\hat{\boldsymbol{R}}|^2 + \mu_*|\hat{\boldsymbol{L}}|^2)\hat{\boldsymbol{R}}. \tag{11b}$$

These equations, for certain parameters, allow and can describe the growth of one handedness while the other is extinguished [19]. Similar equations, which describe the time dependence of the amplitudes of the leading modes, but without considering their spatial dependence, are often used to extend linear perturbation theory of hydrodynamic instabilities into the weakly nonlinear regime. In this form, they are often called the Landau equations [21].

The energy of the left- and right-handed modes is determined by

$$\frac{dE_L}{dt} = 2\gamma E_L - 4\mu E_L^2 - 4\mu_* E_L E_R, \tag{12a}$$

$$\frac{dE_R}{dt} = 2\gamma E_R - 4\mu E_R^2 - 4\mu_* E_L E_R. \tag{12b}$$

These equations show that both E_L and E_R grow exponentially at the rate 2γ until nonlinear effects become important and either E_L or E_R saturates at $E_0 \equiv \gamma/2\mu$ and the energy of the mode of opposite handedness vanishes. In principle, the achiral solution with $E_L = E_R \equiv E_\mathrm{a} = \gamma/2(\mu + \mu_*)$ is also possible, but, as we will see below, such a solution is unstable for $\mu < \mu_*$, which is what we find in Sec. III. The reason for this instability is the presence of the term proportional to μ_*, which represents a phenomenon known as “mutual antagonism” in studies of the origin of homochirality of biomolecules [22–24]. We will return to this issue in Sec. IV, where we discuss the analogy with chiral symmetry breaking in biomolecules in more detail.

Using Eqs. (6) and (11) and defining $H = \mathcal{H}/2\Lambda$, we have $E_R = (E + H)/2$ and $E_L = (E - H)/2$. We can thus obtain the following evolution equations:

$$\frac{dE}{dt} = 2\gamma E - 2(\mu + \mu_*)E^2 - 2(\mu - \mu_*)H^2, \tag{13a}$$

$$\frac{dH}{dt} = 2\gamma H - 4\mu E H. \tag{13b}$$

The dynamical system described by (13) and depicted in Fig. 1 has four fixed points in the (E,H) plane: $S_1 = (0,0)$, $S_{2,3} = (E_0, \pm E_0)$, and $S_4 = (2E_\mathrm{a},0)$ with eigenvalues $\lambda_1 = (2\gamma,2\gamma)$, $\lambda_2 = \lambda_3 = (-2\gamma, 2(\mu - \mu_*)/\gamma)$, and $\lambda_4 =$

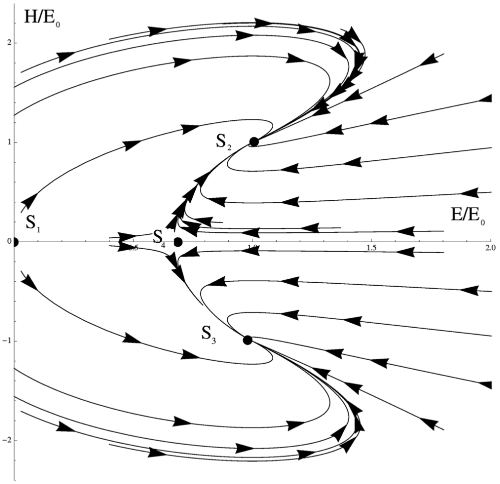

FIG. 1. The phase portrait for $\mu < \mu_*$. This is the typical situation in which S_2 and S_3 are attractive and S_4 is a saddle point.

$(-2\gamma, 2\gamma - 4\gamma\mu/(\mu + \mu_*))$. The origin is always repulsive while S_2 and S_3 are sinks or saddle points depending on the values of parameters μ and μ_*. S_4, corresponding to the achiral solution, can be an attractive point only if $\mu_* < \mu$, otherwise it is a saddle point.

A discussion of the amplitude equations is now in order. First, we have assumed that there are exactly two modes of opposite helicity that becomes critical at the onset of the instability. This assumption is based on linear perturbation analysis. As all the other modes in this case are stable, in the spirit of center manifold reduction, we have ignored their contributions to total energy and helicity. If several modes are simultaneously unstable at the onset, then we may expect a higher degree of complexity. Secondly, as our approach is based on symmetry, the form of the amplitude equations that we obtain is very general. This is also a weakness of our approach, as we cannot determine the expression for either μ or μ_*. In principle, the method of multiscale expansion or center manifold reduction can be applied to this problem to derive an analytical expression of μ and μ_*, but this is a difficult proposition in the present case as a solution of the linear problem itself is not known in an analytically closed form.

We can then compute the quantities γ, μ, and μ_* with the help of DNS by comparing the time evolution obtained for the left-hand side of (13) in the weakly nonlinear phase where our description is valid. We can anticipate that in most of our simulations, $\mu < \mu_*$ and therefore the system should relax to a state of finite helicity in a finite time, although we start from an infinitesimally small helicity. This is precisely what we observe in our DNS.

III. DIRECT NUMERICAL SIMULATIONS

To analyze the evolution of the Tayler instability, we choose our numerical domain to be a cylindrical shell with an inner radius $s_{\rm in} = 1$, outer radius $s_{\rm out} = 3$, and height $h = 2$. We perform simulations of the time-dependent resistive magnetohydrodynamic equations for a compressible isothermal gas: the pressure is thus given by $p = \rho c_{\rm s}^2$, where ρ is the density and $c_{\rm s}$ is the isothermal sound speed.

We use the PENCIL CODE[1] to solve the equations for the magnetic vector potential $\boldsymbol{A}$, ($\boldsymbol{B} = \nabla \times \boldsymbol{A}$) the velocity $\boldsymbol{U}$, and the logarithmic density $\ln\rho$ in the form

$$\frac{\partial \boldsymbol{A}}{\partial t} = \boldsymbol{U} \times \boldsymbol{B} + \eta \nabla^2 \boldsymbol{A}, \tag{14}$$

$$\frac{\mathrm{D}\boldsymbol{U}}{\mathrm{D}t} = -c_{\rm s}^2 \nabla \ln\rho + \boldsymbol{J} \times \boldsymbol{B}/\rho + \boldsymbol{F}_{\rm visc}, \tag{15}$$

$$\frac{\mathrm{D}\ln\rho}{\mathrm{D}t} = -\nabla \cdot \boldsymbol{U}, \tag{16}$$

where

$$\boldsymbol{F}_{\rm visc} = \rho^{-1} \nabla \cdot 2\nu\rho \mathsf{S}$$

is the viscous force, S is the traceless rate of strain tensor having components $\mathsf{S}_{ij} = \frac{1}{2}(U_{i,j} + U_{j,i}) - \frac{1}{3}\delta_{ij} \nabla \cdot \boldsymbol{U}$,

$$\boldsymbol{J} = \nabla \times \boldsymbol{B}/\mu_0$$

is the current density, ν is the kinematic viscosity, and η is the magnetic diffusivity.

We choose periodic boundary conditions in the vertical (z) and azimuthal (φ) directions, while at radial (s) boundaries we select a perfectly conducting boundary condition for the magnetic field and stress-free boundary conditions for velocity. The resolution of the simulations presented here is 128^3 mesh points in all three directions, but comparison with different resolution demonstrated that our results are converged.

We choose a basic state with zero velocity and zero axial component of the magnetic field (B_z). The azimuthal component of the magnetic field is

$$B_\varphi = B_0\,(s/s_0) \exp[-(s - s_0)^2/\sigma^2], \tag{17}$$

where B_0 is a normalization constant, $s_0 = 2$, and $\sigma = 0.2$. We choose B_0 and $c_{\rm s}$ in such a way that the sound speed is much larger than the Alfvén speed. In this way, we avoid magnetic perturbation to be dominant over hydrodynamical perturbations.

In the basic state, the Lorentz force due to the magnetic field is balanced by the gradient of pressure. Hence the pressure of the fluid is given by

$$p = p_0 - \frac{B_0^2}{4s_0^2} \left[(2\,s^2 - \sigma^2) e^{-2\frac{(s-s_0)^2}{\sigma^2}} + s_0 \sigma \sqrt{\pi} \sqrt{2}\, \mathrm{erf}\left(\frac{\sqrt{2}(s - s_0)}{\sigma} \right) \right], \tag{18}$$

where p_0 is a constant that must be large enough to ensure that the pressure is positive. If no perturbation is added, the system remains stationary. Therefore, we add at the beginning of the simulation a perturbation of the magnetic field with an infinitesimally small net helicity given by the following

---

[1] http://pencil-code.googlecode.com/

expression:

$$\boldsymbol{A} = \delta s \cos\left(z\frac{n_z\pi}{h}\right)\begin{pmatrix}\sin m\varphi \\ 0 \\ \cos m\varphi\end{pmatrix}, \tag{19}$$

where δ is an arbitrary small amplitude which we set to 10^{-7} for all the simulations and $k_z = q/s_{\rm in} = n_z\pi/h$ is the vertical wave number of the perturbation.

As discussed in [13], kink instabilities are a special case of the so-called quasi-interchange instabilities, where combined azimuthal and vertical fields are present in the basic state. In the incompressible limit, the unstable eigenmodes can be described by a (t,z,φ) dependence of the type $\propto \exp(\gamma t - ik_z z - im\varphi)$ where the growth rate γ is determined from a numerical solution of the nonlinear eigenvalue problem for the radial disturbance v_{1s},

$$\begin{aligned}&\frac{d}{ds}\left[\frac{1}{\lambda}\left(\gamma^2+\omega_A^2\right)\left(\frac{dv_{1s}}{ds}+\frac{v_{1s}}{s}\right)\right] - k_z^2\left(\gamma^2+\omega_A^2\right)v_{1s}\\ &\quad + 2\omega_B\left[\frac{m(1+\lambda)}{s^2\lambda^2}\left(1-\frac{\beta\lambda}{1+\lambda}\right)(\omega_{Az}+2m\omega_B)\right.\\ &\quad \left. + \frac{m\omega_{Az}}{s^2\lambda^2} - k_z^2\omega_B(1-\beta)\right]v_{1s} + \frac{4k_z^2\omega_A^2\omega_B^2}{\lambda\left(\gamma^2+\omega_A^2\right)}v_{1s} = 0.\end{aligned} \tag{20}$$

Here $\omega_A = (\boldsymbol{B}\cdot\boldsymbol{k})/\sqrt{\rho}$ with $\boldsymbol{k} = (0,m/s,k_z)$, so $\omega_{Az} = k_z B_z/\sqrt{\rho}$. Furthermore, we have defined $\omega_B = B_\varphi/s\sqrt{\rho}$ and $\lambda = 1 + m^2/s^2k_z^2$.

Equation (20) describes the stability problem as a nonlinear eigenvalue problem. This equation was first derived by Freidberg [25] in his study of MHD stability of a diffuse screw pinch (see also [13]). The author found that, for a given value of k_z, it is possible to obtain multiple values of the eigenvalue γ, each one corresponding to a different eigenfunction, and he calculated γ for the fastest growing fundamental mode. The most general form of Eq. (20), taking into account compressibility of plasma, was derived by Goedbloed [26]. Since we study the stability assuming that the magnetic energy is smaller than the thermal energy, the incompressible form of Eq. (20) can be a sufficiently accurate approximation, as we have verified. In the case at hand, $(\boldsymbol{B}\cdot\boldsymbol{k})/\sqrt{\rho} = m\omega_B = \omega_A$ because we are interested in pure kink (Tayler) instabilities, with $B_z \equiv 0$ in the basic state. Note that as $\omega_{Az} = 0$ in our case, Eq. (20) is invariant for $m \to -m$.

In this latter case, once (20) is solved and v_{1s} is obtained, the expressions for the other perturbed quantities denoted by the subscript "1" read

$$B_{1s} = -\frac{i}{\gamma s}B_\varphi\, v_{1s}, \tag{21a}$$

$$B_{1\varphi} = -\frac{i}{\gamma s}B_\varphi\, v_{1\varphi} - \frac{B_\varphi}{\gamma s}(\beta-1)v_{1s}, \tag{21b}$$

$$B_{1z} = -\frac{i}{\gamma s}B_\varphi\, v_{1z}, \tag{21c}$$

$$v_{1\varphi} = \frac{-im}{(k_z s)^2\lambda}\frac{\partial}{\partial s}(s\, v_{1s}) - \frac{2im\omega_B^2\, v_{1s}}{\lambda\left(\gamma^2+m^2\omega_B^2\right)}, \tag{21d}$$

$$v_{1z} = -\frac{i}{k_z s}\frac{\partial}{\partial s}(s\, v_{1s}) - \frac{m}{k_z s}v_{1\varphi}. \tag{21e}$$

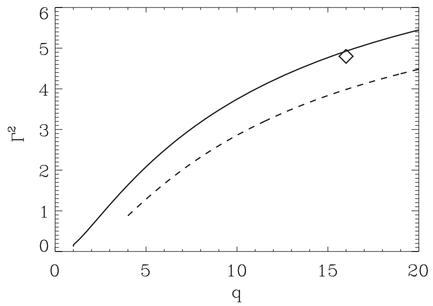

FIG. 2. The dispersion relation for the dimensionless growth rate Γ for the $m = \pm1$ mode (solid line) and for the $m = \pm2$ mode (dashed). Higher values of $|m|$ have even smaller growth rates. This curve is obtained for a linear model with physical parameters corresponding to the nonlinear model `Held`, for which we indicate, with a rhombus, the growth rate for its faster growing mode.

Unfortunately even for the case of pure kink instabilities, (20) cannot be solved analytically and one has to determine the dispersion relation numerically. Therefore, to test our numerical setup we have solved numerically Eq. (20) for the basic state (17) for various values of B_0 and σ in the limit of small v_A/c_s ratio to check that in the linear phase the growth rate extracted from the DNS is in agreement with the linear theory. In particular, as the inner radius of the cylinder is not at $s = 0$, we have set $v_{1s} = 0$ at both inner and outer boundaries. Note here that the growth rate and eigenfunctions of this instability are known for the ideal MHD limit. Hence to compare with those results, we choose viscosity and magnetic diffusivity such that the dissipative time scales are much *larger* than the characteristic growth time (inverse of γ) of the instability.

The results are shown in Fig. 2 for the dimensionless growth rate $\Gamma = \gamma t_A$, where $t_A = s_{\rm out}\sqrt{\rho}/B_0$ is the Alfvén travel time, as a function of the dimensionless vertical wave number $q = k_z s_{\rm in}$ for model `Held` in Table I, with $B_0 = 0.5$, and $n_z = 10$. In particular, to compare the growth rate obtained from our DNS, we have determined the characteristic vertical wave number of the unstable mode in the linear phase by means of the Fourier analysis of the magnetic fields. We also found that in all the simulations, the azimuthal wave number of the fastest growing mode turned out to be always $m = \pm1$ as higher values of $|m|$ have a smaller growth rate (as shown in Fig. 2). We found that the corresponding growth rate determined from the linear phase of our direct numerical simulation is about 7–5 % smaller than the linear value. We think this is acceptable in view of unavoidable numerical diffusion in three-dimensional numerical simulations.

We see that the eigenfunction is rather localized for $q \gg 1$, as is visible in the example shown in Fig. 3. We can exploit this property to obtain approximate explicit expressions for the growth rate at large values of q. In fact, we can consider the magnetic field approximately constant around $s = s_0$ and apply the small-gap approximation (see [13] for details) so that $v_{1s} \propto \sin[\pi(s-s_0)/\sigma]$ and the dimensionless growth rate

TABLE I. For every model, s goes from 1 to 3, z from -1 to 1, and the perturbation has an amplitude $\delta = 10^{-7}$, $\sigma = 0.2$.

Model	B_0^2/p_0	v_A/c_s	c_s	m	n_z	γt_A	$\mu \frac{s_{\rm out}^2}{t_A}$	$\mu_* \frac{s_{\rm out}^2}{t_A}$	μ_*/μ
`Hel`	10^{-1}	0.3	10	-1	1	2.71	7.5	18	2.4
`Helm1`	10^{-1}	0.3	10	$+1$	1	2.71	7.5	18	2.4
`Helc`	10^{-1}	0.3	20	-1	1	6.2	7	18.5	2.6
`Helmb`	2.5×10^{-2}	0.15	10	-1	1	2.2	1	2.3	2.3
`Held`	2.5×10^{-2}	0.15	10	-1	10	2.2	3	7.3	2.4
`Heln10`	10^{-1}	0.3	10	-1	10	2.75	4.5	10	2.2

reads

$$\Gamma^2 = -\frac{2c\Delta^2 m^2[(\beta-1)m^2 + (\beta-3)q^2]}{(m^2+q^2)[\Delta^2(m^2+q^2)+\pi^2]} + \frac{2(\beta-1)\Delta^2 q^2 - c^2 m^2[\Delta^2(m^2-3q^2)+\pi^2]}{\Delta^2(m^2+q^2)+\pi^2}, \quad (22)$$

where $c = B_\phi/B_0 \approx$ const and $\Delta = 2\sigma/s_0$. In the limit $q \gg 1$, despite the uncertain approximation that we have performed, expression (23) differs by only 20% from the numerical solution.

It is interesting to notice that, by using (21) in the limit $q \gg 1$, we obtain the explicit expressions

$$\langle \boldsymbol{v}_1 \cdot \boldsymbol{\nabla} \times \boldsymbol{v}_1 \rangle \approx -\frac{4m\omega_B^2(\gamma^2 - m^2\omega_B^2)\langle v_{1s}^2 \rangle}{s_0^2 k_z (\gamma^2 + m^2\omega_B^2)^2}, \quad (23)$$

$$\langle \boldsymbol{B}_1 \cdot \boldsymbol{\nabla} \times \boldsymbol{B}_1 \rangle \approx \frac{4m B_\phi^2 \omega_B^2 \langle v_{1s}^2 \rangle}{s_0^4 k_z (\gamma^2 + m^2\omega_B^2)^2}, \quad (24)$$

where the symbol $\langle \cdot \rangle$ denotes volume averaging. It is therefore clear that, at the nonlinear level, eigenfunctions with nonzero m will produce both kinetic and magnetic helicity whose sign will depend on the sign of m. The relevant point is that modes with opposite m have an identical growth rate but opposite kinetic and magnetic helicity, and the fate of the final helicity is decided by the competition of modes with opposite azimuthal wave number.

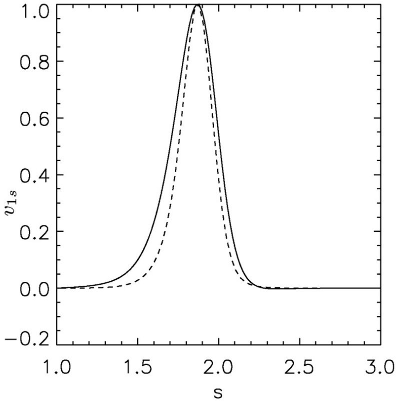

FIG. 3. Eigenfunction v_{1s} for the $m = 1$ mode for $q = 16$. The result of the simulation, model `Held` in Table I (solid line), is overplotted on the eigenfunction obtained solving (20) (dashed line); see [13] for more details. This is observed at $t/t_A = 9$, that is, during the linear growth of the instability.

Moreover, according to the oscillation theorem [27], as the $m = \pm 1$ are unstable, all the other modes with $m = \pm a$, where $a > 1$ is a positive integer, are also unstable, but with a smaller growth rate. As a consequence, although in the linear phase the $m = \pm 1$ modes dominate the linear growth, already in the weakly nonlinear phase the contribution of modes with $m \neq \pm 1$ can also be important for the selection of the final helical state.

The eigenfunctions appear clearly in our simulation and they fit quite well the eigenfunctions calculated by the linear model, as shown in Fig. 3. In our simulations, during the growing phase of the instability we observe a net increase of the helicity, as shown in Fig. 4, where we plot the time series of the normalized kinetic, current, and magnetic helicity. It is interesting to notice that while kinetic helicity decays on the viscous time scale, the current and magnetic helicities reach a nonzero value at very large times.

In actual simulations, we choose $\nu = 10^{-2}$ (in code units) so that the viscous time scale is $t_\nu = s^2/\nu \gg \gamma^{-1}$ and the actual value of ν does not play a significant role in the weakly nonlinear phase, as we verified in our simulations. Moreover, we decided to use a very small value for the magnetic diffusivity, $\eta = 10^{-9}$ (in code units). This is done to prevent the decay of the magnetic field by diffusion. In general, such small values of magnetic diffusivity would imply extremely large values of the magnetic Reynolds number which would be impossible to resolve with the resolutions we use. Nevertheless, we choose such values to have a toroidal field stable on time scales much longer than those of the instability. However, in our simulations no sharp gradients of the magnetic field develop, which is the reason why such small values of magnetic diffusivity are permissible.

We can now determine the coefficients γ, μ, and μ_* using the time evolution of $H(t)$ and $E(t)$ obtained with our DNS in solving the model (13). This can be done via a direct two-parameter χ^2 minimization because the exponent γ can easily be determined from the linear evolution and one is left with only the determination of μ and μ_*. An example of this approach is depicted in Fig. 5, where the agreement with our numerical simulations is explicitly shown. Note that around $t/t_A \approx 6.5$ we enter the deep nonlinear phase and our treatment does not apply anymore. We estimate this cutoff time for our simulations to be in the middle of the decay transition for $d \ln H/dt$ and $d \ln E/dt$ depicted in Fig. 5, and we have checked that the values of μ and μ_* are not strongly dependent on our cutoff time.

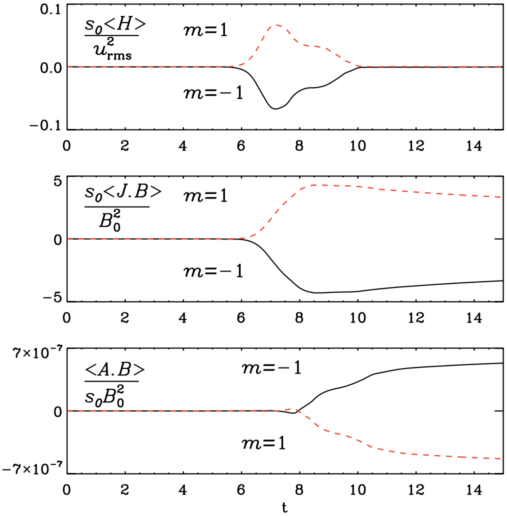

FIG. 4. (Color online) Kinetic, current, and magnetic helicities for two different runs (models `Hel` and `Helm1` in Table I) with helical perturbation and $m = \pm 1$. t is in units of the Alfvén travel time t_A. The viscous time is $t_\nu \approx 10^2 * t_A$ and the magnetic diffusion is $t_\eta \approx 10^9 * t_A$. The difference in the evolutions of the kinetic, current, and magnetic helicities can be clearly seen in the first, second, and third panel. These plots show how these quantities grow with the same rate, but different sign, depending on the sign of the initial perturbation, that is, the sign of m. Note that for each model, the magnetic helicity has an opposite sign to that of the kinetic and current helicities.

Our results are summarized in Table I. We see that the coefficients μ and μ_* are unchanged for models that differ only in the sign of m in the perturbation. This is what we expect and one of the symmetries we have used to write the Lagrangian (8). Model `Helc` shows that the growth rate depends on the value of c_s, but this does not change the values of μ and μ_*. Model `Helb` and model `Held` have a smaller growth rate due to a smaller v_A/c_s. `Helb` has μ and μ_* smaller than `Held` due to the fact that in the latter model, modes with higher k_z have been excited by the initial perturbation. Note that in our setup, the ratio v_A/c_s depends on B_0 but not on c_s. This is due to the fact that the model is isothermal and the initial radial balance is obtained through a pressure gradient that balances the Lorentz force. An increase of n_z of the perturbation, as in model `Heln10`, leads to a similar growth rate, but smaller μ and μ_*. This can be explained saying that, while in the linear phase this model evolves similarly to any $n_z = 1$ model, in the weakly nonlinear phase the evolution is different because of a faster growth of modes with higher k_z. In our models, we measure $2.2 \leqslant \mu_*/\mu \leqslant 2.6$.

IV. HOMOCHIRALITY IN BIOMOLECULES

It is instructive to consider Eqs. (12) as evolution equations for the concentration of two molecules of opposite handedness, L and R. Let us assume that L and R can be synthesized from

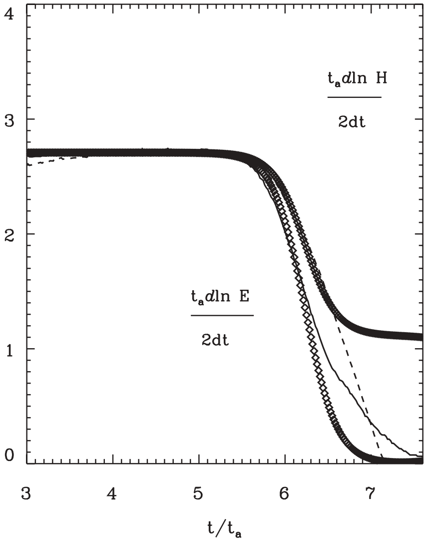

FIG. 5. Time evolution for the logarithmic derivative of kinetic energy (solid line) E and kinetic helicity H (dashed) as measured in DNS for models `Hel` and `Helm1` (see Table I). t is in units of the Alfvén travel time t_A. We overplot a fit of the model with Eqs. (13). The best fit is obtained for $\gamma = 2.71/t_A$, $\mu = 7.5 t_A/s_{\rm out}^2$, and $\mu_* = 18 t_A/s_{\rm out}^2$ and the solutions are overplotted on the DNS results.

a substrate S through autocatalytic reactions of the form

$$\mathsf{S} \xrightarrow{\mathsf{L}} \mathsf{L}, \quad \mathsf{S} \xrightarrow{\mathsf{R}} \mathsf{R}. \tag{25}$$

Autocatalytic reactions of this type have been confirmed in laboratory experiments [28]. Let us assume furthermore that L and R are capable of polymerizing to form homochiral dimers,

$$\mathsf{L}+\mathsf{L} \xrightarrow{\mu} \mathsf{LL}, \quad \mathsf{R}+\mathsf{R} \xrightarrow{\mu} \mathsf{RR}, \tag{26}$$

as well as heterochiral dimers,

$$\mathsf{L}+\mathsf{R} \xrightarrow{\mu_*} \mathsf{LR}. \tag{27}$$

Then the evolution equations for the various concentrations are

$$\frac{d[\mathsf{S}]}{dt} = -k_C[\mathsf{S}]([\mathsf{L}]+[\mathsf{R}]), \tag{28a}$$

$$\frac{d[\mathsf{L}]}{dt} = k_C[\mathsf{S}][\mathsf{L}] - 2k_S[\mathsf{L}]^2 - 2k_I[\mathsf{L}][\mathsf{R}], \tag{28b}$$

$$\frac{d[\mathsf{R}]}{dt} = k_C[\mathsf{S}][\mathsf{R}] - 2k_S[\mathsf{R}]^2 - 2k_I[\mathsf{L}][\mathsf{R}], \tag{28c}$$

$$\frac{d[\mathsf{LL}]}{dt} = k_S[\mathsf{L}]^2, \tag{28d}$$

$$\frac{d[\mathsf{RR}]}{dt} = k_S[\mathsf{R}]^2, \tag{28e}$$

$$\frac{d[\mathsf{LR}]}{dt} = k_I[\mathsf{L}][\mathsf{R}], \tag{28f}$$

which obeys the conservation law [24]

$$[\mathsf{S}] + [\mathsf{L}] + [\mathsf{R}] + 2[\mathsf{LL}] + 2[\mathsf{RR}] + 2[\mathsf{LR}] = \text{const.} \tag{29}$$

These equations represent a subset of a more general polymerization model [23]. Comparing with Sec. II, we see that Eqs. (28b) and (28c) are *identical* with Eqs. (12a) and (12b) when substituting $[\mathsf{L}] = E_L$ and $[\mathsf{R}] = E_R$, and identifying

$$k_C = 2\gamma, \quad k_S = 2\mu, \quad k_I = 2\mu_*. \tag{30}$$

Hence we demonstrate quantitatively that the spontaneous production of helicity from the fully nonlinear system of hydromagnetic equations can be described by the simple model equations (12), which in turn represent a simple set of chemical reactions (25)–(27).

The analogy with homochirality in biochemistry is useful because it helps to identify the phenomenon of mutual antagonism as the main cause of chiral symmetry breaking. This effect corresponds to a contribution to the nonlinear terms that result from the interaction between modes of opposite handedness. These are the terms proportional to μ_* and k_I in Eqs. (12) and (28), respectively. In the synthesis of polynucleotides, this is known as enantiomeric cross-inhibition and has been identified in laboratory experiments [29]. The synthesis of heterochiral dimers is essential in that it corresponds to the production of waste needed to eliminate building blocks of that handedness that is later to disappear completely.

V. CONCLUSIONS

We have shown how net helicity is produced by the addition of a small helical perturbation to a nonhelical system, thus driving the system to a final state characterized by a finite value of the helicities and, therefore, breaking the initial symmetry. We have shown further that this spontaneous symmetry breaking can be described by weakly nonlinear amplitude equations (13). Furthermore, we have numerically determined the coefficients appearing in the weakly nonlinear amplitude equations (13) for the Tayler instability. Direct numerical simulations show that the ratio between the coefficients describing the weakly nonlinear phase is almost constant. The agreement between the analytical model and the numerical solutions is rather good in the beginning of the weakly nonlinear phase, as shown in Fig. 5. This demonstrates quantitatively the close analogy between helicity production in hydromagnetic flows and the development of homochirality in biochemistry, which is described by the same system of equations as those resulting from the amplitude equations of the weakly nonlinear model of the Tayler instability. It will be useful to extend our analysis by means of a Landau-Ginzburg description of the amplitude equation by including a nonhomogeneous term in our Lagrangian to discuss the possible pattern formation in this type of spontaneous chiral symmetry breaking. We hope to address this issue in a future communication.

ACKNOWLEDGMENTS

The authors thank P. Chatterjee and M. Rheinhardt for useful discussions. A part of the work was performed when A.B. visited NORDITA under the program "Dynamo, Dynamical Systems and Topology." F.D.S. acknowledges HPC-EUROPA for financial support. Financial support from European Research Council under the AstroDyn Research Project 227952 is gratefully acknowledged.

[1] H. Umezawa, *Thermo Field Dynamics and Condensed States* (Elsevier, Amsterdam, 1982).

[2] N. D. Goldenfeld, *Lectures on Phase Transitions and the Renormalisation Group* (Addison-Wesley, Reading, MA, 1992).

[3] *Hydrodynamic Instabilities and the Transition to Turbulence*, 2nd ed., edited by H. L. Swinney and J. P. Gollub (Springer-Verlag, New York, 1985); M. C. Cross and P. C. Hohenberg, Rev. Mod. Phys. **65**, 851 (1993).

[4] W. W. Mullins and R. F. Sekerka, J. Appl. Phys. **35**, 444 (1964).

[5] E. Moses and V. Steinberg, Phys. Rev. A **34**, 693 (1986); A. J. Simon, J. Bechhoefer, and A. Libchaber, Phys. Rev. Lett. **61**, 2574 (1988); G. Faivre, S. de Cheveigne, C. Guthmann, and P. Kurowski, Europhys. Lett. **9**, 779 (1989); F. Melo and P. Oswald, Phys. Rev. Lett. **64**, 1381 (1990); H. Z. Cummins, L. Fourtune, and M. Rabaud, Phys. Rev. E **47**, 1727 (1993).

[6] J. V. Selinger, Z.-G. Wang, R. F. Bruinsma, and C. M. Knobler, Phys. Rev. Lett. **70**, 1139 (1993).

[7] A. Pinter, M. Lücke, and C. Hoffmann, Phys. Rev. Lett. **96**, 044506 (2006).

[8] P. Chatterjee, D. Mitra, A. Brandenburg, and M. Rheinhardt, Phys. Rev. E **84**, 025403(R) (2011); P. Chatterjee, D. Mitra, M. Rheinhardt, and A. Brandenburg, Astron. Astrophys. **534**, A46 (2011).

[9] M. Gellert, G. Rüdiger, and R. Hollerbach, Mon. Not. R. Astron. Soc. **414**, 2696 (2011).

[10] R. J. Tayler, Mon. Not. R. Astron. Soc. **161**, 365 (1973).

[11] R. J. Tayler and P. Markey, Mon. Not. R. Astron. Soc. **163**, 77 (1973).

[12] A. Bonanno and V. Urpin, Astron. Astrophys. **477**, 35 (2008).

[13] A. Bonanno and V. Urpin, Astron. Astrophys. **488**, 1 (2008).

[14] A. Bonanno and V. Urpin, Phys. Rev. E **84**, 056310 (2011).

[15] A. Bonanno and V. Urpin, Astrophys. J. **747**, 137 (2012).

[16] J. Braithwaite and Å. Nordlund, Astron. Astrophys. **450**, 1077 (2006).

[17] J. Braithwaite, Astron. Astrophys. **453**, 687 (2006).

[18] H. Spruit, Astron. Astrophys. **349**, 189 (1999).

[19] S. Fauve, S. Douady, and O. Thual, J. Phys. II **1**, 311 (1991).

[20] F. Quingzeng, Appl. Math. Mech. **18**, 865 (1997).

[21] L. D. Landau and E. M. Lifshitz, *Fluid Mechanics*, Volume 6 of Course of Theoretical Physics, 2nd English ed. (Pergamon, Oxford, 1987), Chap. 3 [Translated from *Gidrodinamika*, 3rd ed., "Nauka", Moscow, 1986].

[22] F. C. Frank, Biochim. Biophys. Acta **11**, 459 (1953).

[23] P. G. H. Sandars, Orig. Life Evol. Biosph. **33**, 575 (2003).
[24] A. Brandenburg, A. C. Andersen, S. Höfner, and M. Nilsson, Orig. Life Evol. Biosph. **35**, 225 (2005).
[25] J. Freidberg, Phys. Fluids **13**, 1812 (1970).
[26] J. P. Goedbloed, Physica **53**, 535 (1971).
[27] J. P. H. Goedbloed and S. Poedts, *Principles of Magnetohydrodynamics* (Cambridge University Press, Cambridge, 2004).
[28] K. Soai, T. Shibata, H. Morioka, and K. Choji, Nature (London) **378**, 767 (1995).
[29] G. F. Joyce, G. M. Visser, C. A. A. van Boeckel, J. H. van Boom, L. E. Orgel, and J. Westrenen, Nature (London) **310**, 602 (1984).

IV

PHYSICAL REVIEW E **81**, 036401 (2010)

Magnetic-field decay of three interlocked flux rings with zero linking number

Fabio Del Sordo, Simon Candelaresi, and Axel Brandenburg
NORDITA, AlbaNova University Center, Roslagstullsbacken 23, SE-10691 Stockholm, Sweden and Department of Astronomy, Stockholm University, SE 10691 Stockholm, Sweden

(Received 22 October 2009; revised manuscript received 27 January 2010; published 3 March 2010)

The resistive decay of chains of three interlocked magnetic flux rings is considered. Depending on the relative orientation of the magnetic field in the three rings, the late-time decay can be either fast or slow. Thus, the qualitative degree of tangledness is less important than the actual value of the linking number or, equivalently, the net magnetic helicity. Our results do not suggest that invariants of higher order than that of the magnetic helicity need to be considered to characterize the decay of the field.

DOI: 10.1103/PhysRevE.81.036401 PACS number(s): 52.65.Kj, 52.30.Cv, 52.35.Vd

I. INTRODUCTION

Magnetic helicity plays an important role in plasma physics [1–3], solar physics [4–6], cosmology [7–9], and dynamo theory [10,11]. This is connected with the fact that magnetic helicity is a conserved quantity in ideal magnetohydrodynamics [12]. The conservation law of magnetic helicity is ultimately responsible for inverse cascade behavior that can be relevant for spreading primordial magnetic field over large length scales. It is also likely the reason why the magnetic fields of many astrophysical bodies have length scales that are larger than those of the turbulent motions responsible for driving these fields. In the presence of finite magnetic diffusivity, the magnetic helicity can only change on a resistive time scale. Of course, astrophysical bodies are open, so magnetic helicity can change by magnetic helicity fluxes out of or into the domain of interest. However, such cases will not be considered in the present paper.

In a closed or periodic domain without external energy supply, the decay of a magnetic field depends critically on the value of the magnetic helicity. This is best seen by considering spectra of magnetic energy and magnetic helicity. The magnetic energy spectrum $M(k)$ is normalized such that

$$\int M(k)dk = \langle \boldsymbol{B}^2\rangle/2\mu_0, \tag{1}$$

where $\boldsymbol{B}$ is the magnetic field, μ_0 is the magnetic permeability, and k is the wave number (ranging from 0 to ∞). The magnetic helicity spectrum $H(k)$ is normalized such that

$$\int H(k)dk = \langle \boldsymbol{A}\cdot\boldsymbol{B}\rangle, \tag{2}$$

where $\boldsymbol{A}$ is the magnetic vector potential with $\boldsymbol{B}=\boldsymbol{\nabla}\times\boldsymbol{A}$. In a closed or periodic domain, $H(k)$ is gauge invariant, i.e., it does not change after adding a gradient term to $\boldsymbol{A}$. For finite magnetic helicity, the magnetic energy spectrum is bound from below [12] such that

$$M(k) \ge k|H(k)|/2\mu_0. \tag{3}$$

This relation is also known as the realizability condition [13]. Thus, the decay of a magnetic field is subject to a corresponding decay of its associated magnetic helicity. Given that in a closed or periodic domain the magnetic helicity changes only on resistive time scales [14], the decay of magnetic energy is slowed down correspondingly. More detailed statements can be made about the decay of turbulent magnetic fields, where the energy decays in a power-law fashion proportional to $t^{-\sigma}$. In the absence of magnetic helicity, $\langle \boldsymbol{A}\cdot\boldsymbol{B}\rangle=0$, we have a relatively rapid decay with $\sigma\approx 1.3$ [15], while with $\langle \boldsymbol{A}\cdot\boldsymbol{B}\rangle\neq 0$, the decay is slower with σ between 1/2 [9] and 2/3 [16].

The fact that the decay is slowed down in the helical case is easily explained in terms of the topological interpretation of magnetic helicity. It is well known that the magnetic helicity can be expressed in terms of the linking number n of discrete magnetic flux ropes via [13]

$$\int \boldsymbol{A}\cdot\boldsymbol{B}dV = 2n\Phi_1\Phi_2, \tag{4}$$

where

$$\Phi_i = \int_{S_i} \boldsymbol{B}\cdot d\boldsymbol{S} \quad (\text{for } i=1 \text{ and } 2) \tag{5}$$

are the magnetic fluxes of the two ropes with cross-sectional areas S_1 and S_2. The slowing down of the decay is then plausibly explained by the fact that a decay of magnetic energy is connected with a decay of magnetic helicity via the realizability condition (3). Thus, a decay of magnetic helicity can be achieved either by a decay of the magnetic flux or by magnetic reconnection. Magnetic flux can decay through annihilation with oppositely oriented flux. Reconnection on the other hand reflects a change in the topological connectivity, as demonstrated in detail in Ref. [17], p. 28.

The situation becomes more interesting when we consider a flux configuration that is interlocked, but with zero linking number. This can be realized quite easily by considering a configuration of two interlocked flux rings where a third flux ring is connected with one of the other two rings such that the total linking number becomes either 0 or 2, depending on the relative orientation of the additional ring, as is illustrated in Fig. 1. Topologically, the configuration with linking numbers of 0 and 2 are the same except that the orientation of the field lines in the upper ring is reversed. Nevertheless, the simple topological interpretation becomes problematic in the case of zero linking number, because then also the magnetic helicity is zero, so the bound of M from below disappears,

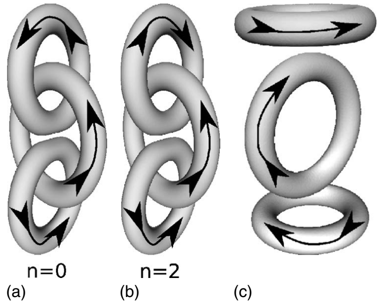

FIG. 1. Visualization of the triple ring configuration at the initial time. Arrows indicate the direction of the field lines in the rings, corresponding to a configuration with $n=0$ (left) and $n=2$ (center). On the right the noninterlocked configuration with $n=0$ is shown.

and M can now in principle freely decay to zero. One might expect that the topology should then still be preserved and that the linking number as defined above, which is a quadratic invariant, should be replaced with a higher-order invariant [18–20]. It is also possible that in a topologically interlocked configuration with zero linking number the magnetic helicity spectrum $H(k)$ is still finite and that bound (3) may still be meaningful. In order to address these questions we perform numerical simulations of the resistive magnetohydrodynamic equations using simple interlocked flux configurations as initial conditions. We also perform a control run with a noninterlocked configuration and zero helicity in order to compare the magnetic energy decay with the interlocked case.

Magnetic helicity evolution is independent of the equation of state and applies hence to both compressible and incompressible cases. In agreement with earlier work [21] we assume an isothermal gas, where pressure is proportional to density and the sound speed is constant. However, in all cases the bulk motions stay subsonic, so for all practical purposes our calculations can be considered nearly incompressible, which would be an alternative assumption that is commonly made [22].

II. MODEL

We perform simulations of the resistive magnetohydrodynamic equations for a compressible isothermal gas where the pressure is given by $p=\rho c_{\rm s}^2$, with ρ being the density and $c_{\rm s}$ being the isothermal sound speed. We solve the equations for $\boldsymbol{A}$, the velocity $\boldsymbol{U}$, and the logarithmic density $\ln\rho$ in the form

$$\frac{\partial \boldsymbol{A}}{\partial t} = \boldsymbol{U}\times\boldsymbol{B} + \eta\nabla^2\boldsymbol{A}, \tag{6}$$

$$\frac{\mathrm{D}\boldsymbol{U}}{\mathrm{D}t} = -c_{\rm s}^2\boldsymbol{\nabla}\ln\rho + \boldsymbol{J}\times\boldsymbol{B}/\rho + \boldsymbol{F}_{\rm visc}, \tag{7}$$

$$\frac{\mathrm{D}\ln\rho}{\mathrm{D}t} = -\boldsymbol{\nabla}\cdot\boldsymbol{U}, \tag{8}$$

where $\boldsymbol{F}_{\rm visc}=\rho^{-1}\boldsymbol{\nabla}\cdot 2\nu\rho\mathsf{S}$ is the viscous force; S is the traceless rate of strain tensor, with components $\mathsf{S}_{ij}=\frac{1}{2}(U_{i,j}+U_{j,i})-\frac{1}{3}\delta_{ij}\boldsymbol{\nabla}\cdot\boldsymbol{U}$; $\boldsymbol{J}=\boldsymbol{\nabla}\times\boldsymbol{B}/\mu_0$ is the current density; ν is the kinematic viscosity; and η is the magnetic diffusivity.

The initial magnetic field is given by a suitable arrangement of magnetic flux ropes, as already illustrated in Fig. 1. These ropes have a smooth Gaussian cross-sectional profile that can easily be implemented in terms of the magnetic vector potential. We use the PENCIL code [23], where this initial condition for $\boldsymbol{A}$ is already prepared, except that now we adopt a configuration consisting of three interlocked flux rings (Fig. 1) where the linking number can be chosen to be either 0 or 2, depending only on the field orientation in the last (or the first) of the three rings. Here, the two outer rings have radii $R_{\rm o}$, while the inner ring is slightly bigger and has the radius $R_{\rm i}=1.2R_{\rm o}$, but with the same flux. We use $R_{\rm o}$ as our unit of length. The sound travel time is given by $T_{\rm s}=R_{\rm o}/c_{\rm s}$.

In the initial state we have $\boldsymbol{U}=\boldsymbol{0}$ and $\rho=\rho_0=1$. Our initial flux, $\Phi=\int\boldsymbol{B}\cdot d\boldsymbol{S}$, is the same for all tubes with $\Phi=0.1c_{\rm s}R_{\rm o}^2\sqrt{\mu_0\rho_0}$. This is small enough for compressibility effects to be unimportant, so the subsequent time evolution is not strongly affected by this choice. For this reason, the Alfvén time, $T_{\rm A}=\sqrt{\mu_0\rho_0 R_{\rm o}^3}/\Phi$, will be used as our time unit. In all our cases we have $T_{\rm A}=10T_{\rm s}$ and denote the dimensionless time as $\tau=t/T_{\rm A}$. In all cases we assume that the magnetic Prandtl number ν/η is unity, and we choose $\nu=\eta=10^{-4}R_{\rm o}c_{\rm s}=10^{-3}R_{\rm o}^2/T_{\rm A}$. We use 256^3 mesh points.

We have chosen a fully compressible code, because it is readily available to us. Alternatively, as discussed at the end of Sec. I, one could have chosen an incompressible code by ignoring the continuity equation and computing the pressure such that $\boldsymbol{\nabla}\cdot\boldsymbol{U}=0$ at all times. Such an operation breaks the locality of the physics and is computationally more intensive, because it requires global communication.

III. RESULTS

Let us first discuss the visual appearance of the three interlocked flux rings at different times. In Fig. 2 we compare the three rings for the zero and finite magnetic helicity cases at the initial time and at $\tau=0.5$. Note that each ring shrinks as a result of the tension force. This effect is strongest in the core of each ring, causing the rings to show a characteristic indentation that was also seen in earlier inviscid and nonresistive simulations of two interlocked flux rings [21].

At early times, visualizations of the field show little difference, but at time $\tau=0.5$ some differences emerge in that the configuration with zero linking number develops an outer ring encompassing the two rings that are connected via the inner ring; see Fig. 2. This outer ring is absent in the configuration with finite linking number.

The change in topology becomes somewhat clearer if we plot the magnetic-field lines (see Fig. 3). For the $n=2$ configuration, at time $\tau=4$ one can still see a structure of three interlocked rings, while for the $n=0$ case no clear structure

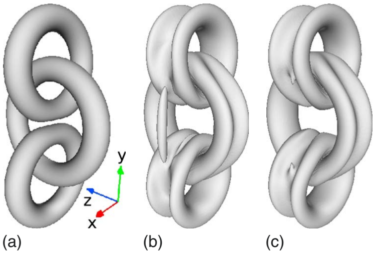

FIG. 2. (Color online) Visualization of the triple ring configuration at $\tau=0$ (left), as well as at $\tau=0.5$ with zero linking number (center) and finite linking number (right). The three images are in the same scale. The change in the direction of the field in the upper ring gives rise to a corresponding change in the value of the magnetic helicity. In the center we can see the emergence of a new flux ring encompassing the two outer rings. Such a ring is not seen on the right.

can be recognized. Note that the magnitude of the magnetic field has diminished more strongly for $n=0$ than for $n=2$. This is in accordance with our initial expectations.

The differences between the two configurations become harder to interpret at later times. Therefore, we compare in Fig. 4 cross sections of the magnetic field for the two cases. The xy cross sections show clearly the development of the new outer ring in the zero linking number configuration. From this figure it is also evident that the zero linking number case suffers more rapid decay because of the now *anti-aligned* magnetic fields (in the upper panel B_x is of opposite sign about the plane $y=0$ while it is negative in the lower panel).

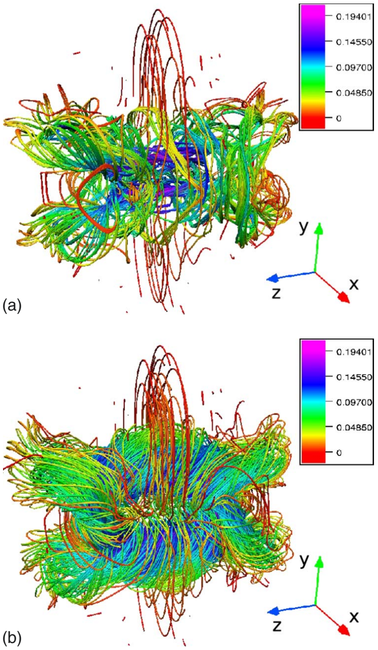

FIG. 3. (Color online) Magnetic flux tubes at time $\tau=4$ for the case of zero linking number (upper picture) and finite linking number (lower picture). The colors represent the magnitude of the magnetic field, where the scale goes from red (lowest) over green to blue (highest).

The evolution of magnetic energy is shown in Fig. 5 for the cases with zero and finite linking numbers. Even at the time $\tau\approx 0.6$, when the rings have just come into mutual contact, there is no clear difference in the decay for the two cases. Indeed, until the time $\tau\approx 2$ the magnetic energy evolves still similarly in the two cases, but then there is a pronounced difference where the energy in the zero linking number case shows a rapid decline (approximately like $t^{-3/2}$), while in the case with finite linking number it declines much more slowly (approximately like $t^{-1/3}$). However, power-law behavior is only expected under turbulent conditions and not for the relatively structured field configurations considered here. The energy decay in the zero linking number case is roughly the same as in a case of three flux rings that are not interlocked. The result of a corresponding control run is shown as a dotted line in Fig. 5. At intermediate times, $0.5<\tau<5$, the magnetic energy of the control run has diminished somewhat faster than in the interlocked case with $n=0$. It is possible that this is connected with the interlocked nature of the flux rings in one of the cases. Alternatively, this might reflect the presence of rather different dynamics in the noninterlocked case, which seems to be strongly controlled by oscillations on the Alfvén time scale. Nevertheless, at later times the decay laws are roughly the same for noninterlocked and interlocked nonhelical cases.

The time when the rings come into mutual contact is marked by a maximum in the kinetic energy at $\tau\approx 0.6$. This can be seen from Fig. 6, where we compare kinetic and magnetic energies separately for the cases with finite and zero linking numbers. Note also that in the zero linking number case magnetic and kinetic energies are nearly equal and decay in the same fashion.

Next we consider the evolution of magnetic helicity in Fig. 7. Until the time $\tau\approx 0.6$ the value of the magnetic helicity has hardly changed at all. After that time there is a gradual decline, but it is slower than the decline of magnetic energy. Indeed, the ratio $\langle \boldsymbol{A}\cdot\boldsymbol{B}\rangle/\langle \boldsymbol{B}^2\rangle$, which corresponds to a length scale, shows a gradual increase from $0.1R_{\text{o}}$ to nearly $0.6R_{\text{o}}$ at the end of the simulation. This reflects the fact that the field has become smoother and more space filling with time.

Given that the magnetic helicity decays only rather slowly, one must expect that the fluxes Φ_i of the three rings also only change very little. Except for simple configurations where flux tubes are embedded in field-free regions, it is in general difficult to measure the actual fluxes, as defined in Eq. (5). On the other hand, especially in observational solar physics, one often uses the so-called *unsigned* flux [24,25], which is defined as

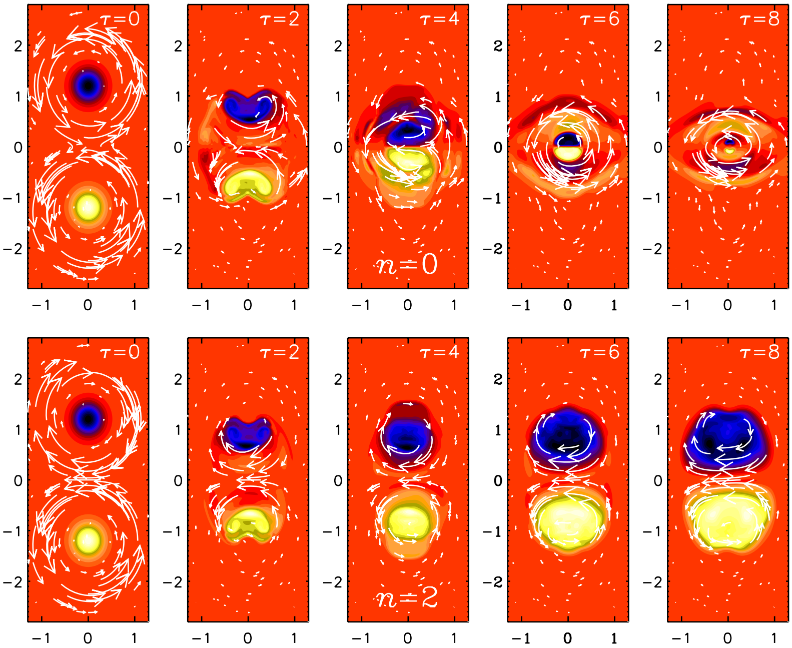

FIG. 4. (Color online) Cross sections in the *xy* plane of the magnetic field with zero linking number (upper row) and finite linking number (lower row). The *z* component (pointing out of the plane) is shown together with vectors of the field in the plane. Light (yellow) shades indicate positive values and dark (blue) shades indicate negative values. Intermediate (red) shades indicate zero value.

$$P_{2D}=\int_S |\boldsymbol{B}|dS. \tag{9}$$

For a ring of flux Φ that intersects the surface in the middle at right angles the net flux cancels to zero, but the unsigned flux gets contributions from both intersections, so $P_{2D}=2|\Phi|$. In three-dimensional simulations it is convenient to determine

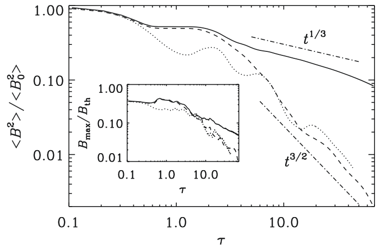

FIG. 5. Decay of magnetic energy (normalized to the initial value) for linking numbers of 2 (solid line) and 0 (dashed line). The dotted line gives the decay for a control run with noninterlocked rings. The dashed-dotted lines indicate $t^{1/3}$ and $t^{3/2}$ scalings for comparison. The inset shows the evolution of the maximum field strength in units of the thermal equipartition value, $B_{\rm th}=c_s(\rho_0\mu_0)^{1/2}$.

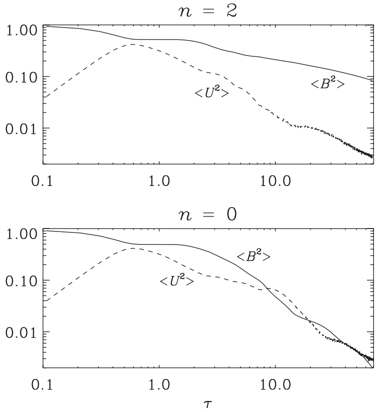

FIG. 6. Comparison of the evolution of kinetic and magnetic energies in the cases with finite and with vanishing linking numbers. Note that in both cases the maximum kinetic energy is reached at the time $\tau\approx 0.6$. The two cases begin to depart from each other after $\tau\approx 2$. In the nonhelical case the magnetic energy shows a sharp drop and reaches equipartition with the kinetic energy, while in the helical case the magnetic energy stays always above the equipartition value.

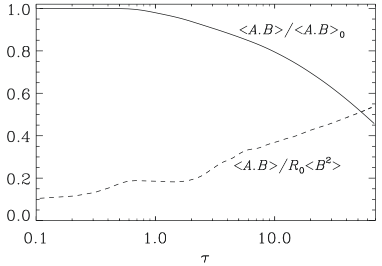

FIG. 7. Evolution of magnetic helicity in the case with finite linking number. In the upper panel, $\langle \boldsymbol{A}\cdot\boldsymbol{B}\rangle$ is normalized to its initial value (indicated by subscript 0) while in the lower panel it is normalized to the magnetic energy divided by R_0.

$$P = \int_V |\boldsymbol{B}| dV. \tag{10}$$

For several rings, all with radius R, we have

$$P = 2\pi R \sum_{i=1}^{N} |\Phi_i| = \pi N R P_{2\mathrm{D}}, \tag{11}$$

where N is the number of rings. In Fig. 8 we compare the evolution of P (normalized to the initial value P_0) for the cases with $n=0$ and 2. It turns out that after $\tau=1$ the value of p is nearly constant for $n=2$, but not for $n=0$.

Let us now return to the earlier question of whether a flux configuration with zero linking number can have finite spectral magnetic helicity, i.e., whether $H(k)$ is finite but of opposite sign at different values of k. The spectra $M(k)$ and $H(k)$ are shown in Fig. 9 for the two cases at time $\tau=5$. This figure shows that in the configuration with zero linking number $H(k)$ is essentially zero for all values of k. This is not the case and, in hindsight, is hardly expected; see Fig. 9 for the spectra of $M(k)$ and $k|H(k)|/2\mu_0$ in the two cases at $\tau=5$. What might have been expected is a segregation of helicity not in the wave-number space, but in the physical space for positive and negative values of y. It is then possible that magnetic helicity has been destroyed by locally generated magnetic helicity fluxes between the two domains in $y>0$ and $y<0$. However, this is not pursued further in this paper.

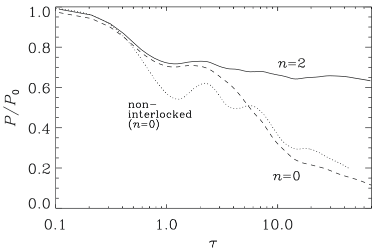

FIG. 8. Decay of the unsigned magnetic flux P (normalized to the initial value P_0) for the cases with $n=0$ and 2. The dotted line gives the decay for a control run with noninterlocked rings.

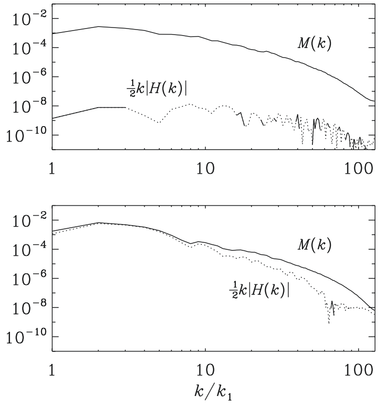

FIG. 9. Comparison of spectra of magnetic energy and magnetic helicity in the case with zero linking number (upper panel) and finite linking number (lower panel) at $\tau=5$. Stretches with negative values of $H(k)$ are shown as dotted lines.

In order to understand in more detail the way the energy is dissipated, we plot in Fig. 10 the evolution of the time derivative of the magnetic energy $E_\mathrm{M}=(1/2\mu_0)\int \boldsymbol{B}^2 dV$ (upper panel) and the kinetic energy $E_\mathrm{K}=\frac{1}{2}\int \rho \boldsymbol{U}^2 dV$ (lower panel). In the lower panel we also show the rate of work done by the Lorentz force, $W_\mathrm{L}=\int \boldsymbol{U}\cdot(\boldsymbol{J}\times\boldsymbol{B})dV$, and in the upper panel we show the rate of work done against the Lorentz force, $-W_\mathrm{L}$.

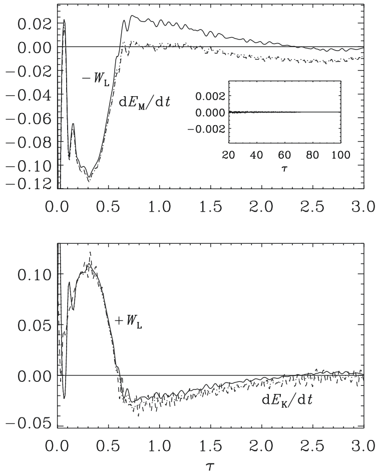

FIG. 10. Evolution of the rate of work done against the Lorentz force, $-W_\mathrm{L}$, together with dE_M/dt (upper panel), as well as the rate of work done by the Lorentz force, $+W_\mathrm{L}$, together with dE_K/dt (lower panel), all normalized in units of $E_\mathrm{M}/T_\mathrm{s}$, for the case with finite linking number. The inset shows $-W_\mathrm{L}$ at late times for the case with $n=0$ (solid line) and $n=2$ (dashed line).

All values are normalized by E_{M0}/T_s, where E_{M0} is the value of E_M at $\tau=0$.

The rates of magnetic and kinetic energy dissipations, ϵ_M and ϵ_K, respectively, can be read off as the difference between the two curves in each of the two panels in Fig. 10. Indeed, we have

$$-W_L - dE_M/dt = \epsilon_M, \tag{12}$$

$$W_L + W_C - dE_K/dt = \epsilon_K, \tag{13}$$

where the compressional work term $W_C=\int p \boldsymbol{\nabla} \cdot \boldsymbol{U} dV$ is found to be negligible in all cases. Looking at Fig. 10 we can say that at early times $(0<\tau<0.7)$ the magnetic field contributes to driving fluid motions $(W_L>0)$ while at later times some of the magnetic energy is replenished by kinetic energy $(W_L<0)$, but since magnetic energy dissipation still dominates, the magnetic energy is still decaying $(dE_M/dt<0)$. The maximum dissipation occurs around the time $\tau=0.7$. The magnetic energy dissipation is then about twice as large as the kinetic energy dissipation. We note that the ratio between magnetic and kinetic energy dissipations should also depend on the value of the magnetic Prandtl number $\mathrm{Pr}_M=\nu/\eta$, which we have chosen here to be unity. In this connection it may be interesting to recall that one finds similar ratios of ϵ_K and ϵ_M both for helical and nonhelical turbulence [26]. At smaller values of Pr_M the ratio of ϵ_K to $\epsilon_K+\epsilon_M$ diminishes like $\mathrm{Pr}_M^{-1/2}$ for helical turbulence [27]. In the present case the difference between $n=0$ and 2 is, again, small. Only at later times there is a small difference in W_L, as is shown in the inset of Fig. 10. It turns out that, for $n=2$, W_L is positive while for $n=0$ its value fluctuates around zero. This suggests that the $n=2$ configuration is able to sustain fluid motions for longer times than the $n=0$ configuration. This is perhaps somewhat unexpected, because the helical configuration $(n=2)$ should be more nearly force free than the nonhelical configuration. However, this apparent puzzle is simply explained by the fact that the $n=2$ configuration has not yet decayed as much as the $n=0$ configuration has.

IV. CONCLUSIONS

The present work has shown that the rate of magnetic energy dissipation is strongly constrained by the presence of magnetic helicity and not by the qualitative degree of knottedness. In our example of three interlocked flux rings we considered two flux chains, where the topology is the same except that the relative orientation of the magnetic field is reversed in one case. This means that the linking number switches from 2 to 0, just depending on the sign of the field in one of the rings. The resulting decay rates are dramatically different in the two cases, and the decay is strongly constrained in the case with finite magnetic helicity.

The present investigations reinforce the importance of considering magnetic helicity in studies of reconnection. Reconnection is a subject that was originally considered in two-dimensional studies of *X*-point reconnection [28,29]. Three-dimensional reconnection was mainly considered in the last 20 years. An important aspect is the production of current sheets in the course of field line braiding [30]. Such current sheets are an important contributor to coronal heating [31]. The crucial role of magnetic helicity has also been recognized in several papers [32,33]. However, it remained unclear whether the decay of interlocked flux configurations with zero helicity might be affected by the degree of tangledness. Our present work suggests that a significant amount of dissipation should only be expected from tangled magnetic fields that have zero or small magnetic helicity, while tangled regions with finite magnetic helicity should survive longer and are expected to dissipate less efficiently.

ACKNOWLEDGMENTS

We acknowledge the allocation of computing resources provided by the Swedish National Allocations Committee at the Center for Parallel Computers at the Royal Institute of Technology in Stockholm and the National Supercomputer Centers in Linköping. This work was supported in part by the European Research Council under the AstroDyn Research Project No. 227952 and the Swedish Research Council Grant No. 621-2007-4064.

---

[1] J. B. Taylor, Phys. Rev. Lett. **33**, 1139 (1974).
[2] T. H. Jensen and M. S. Chu, Phys. Fluids **27**, 2881 (1984).
[3] M. Berger and G. B. Field, J. Fluid Mech. **147**, 133 (1984).
[4] D. M. Rust and A. Kumar, Sol. Phys. **155**, 69 (1994).
[5] D. M. Rust and A. Kumar, Astrophys. J. **464**, L199 (1996).
[6] B. C. Low, Sol. Phys. **167**, 217 (1996).
[7] A. Brandenburg, K. Enqvist, and P. Olesen, Phys. Rev. D **54**, 1291 (1996).
[8] G. B. Field and S. M. Carroll, Phys. Rev. D **62**, 103008 (2000).
[9] M. Christensson, M. Hindmarsh, and A. Brandenburg, Astron. Nachr. **326**, 393 (2005).
[10] A. Pouquet, U. Frisch, and J. Léorat, J. Fluid Mech. **77**, 321 (1976).
[11] A. Brandenburg and K. Subramanian, Phys. Rep. **417**, 1 (2005).
[12] L. Woltjer, Proc. Natl. Acad. Sci. U.S.A. **44**, 489 (1958).
[13] H. K. Moffatt, J. Fluid Mech. **35**, 117 (1969).
[14] M. Berger, Geophys. Astrophys. Fluid Dyn. **30**, 79 (1984).
[15] M.-M. Mac Low, R. S. Klessen, and A. Burkert, Phys. Rev. Lett. **80**, 2754 (1998).
[16] D. Biskamp and W.-C. Müller, Phys. Rev. Lett. **83**, 2195 (1999).
[17] E. Priest and T. Forbes, *Magnetic Reconnection* (Cambridge University Press, Cambridge, England, 2000).
[18] A. Ruzmaikin and P. Akhmetiev, Phys. Plasmas **1**, 331 (1994).
[19] G. Hornig and C. Mayer, J. Phys. A **35**, 3945 (2002).
[20] R. Komendarczyk, Commun. Math. Phys. **292**, 431 (2009).
[21] R. M. Kerr and A. Brandenburg, Phys. Rev. Lett. **83**, 1155 (1999).

[22] R. Grauer and C. Marliani, Phys. Rev. Lett. **84**, 4850 (2000).
[23] http://pencil-code.googlecode.com
[24] C. Zwaan, Sol. Phys. **100**, 397 (1985).
[25] C. J. Schrijver and K. L. Harvey, Sol. Phys. **150**, 1 (1994).
[26] N. E. L. Haugen, A. Brandenburg, and W. Dobler, Astrophys. J. **597**, L141 (2003).
[27] A. Brandenburg, Astrophys. J. **697**, 1206 (2009).
[28] E. N. Parker, J. Geophys. Res. **62**, 509 (1957).
[29] D. Biskamp, Phys. Fluids **29**, 1520 (1986).
[30] M. A. Berger, Phys. Rev. Lett. **70**, 705 (1993).
[31] K. Galsgaard and Å. Nordlund, J. Geophys. Res. **101**, 13445 (1996).
[32] Y. Q. Hu, L. D. Xia, X. Li, J. X. Wang, and G. X. Ai, Sol. Phys. **170**, 283 (1997).
[33] Y. Liu, H. Kurokawa, C. Liu, D. H. Brooks, J. Dun, T. T. Ishii, and H. Zhang, Sol. Phys. **240**, 253 (2007).

V

IOP PUBLISHING PHYSICA SCRIPTA

Phys. Scr. **T142** (2010) 014028 (10pp) doi:10.1088/0031-8949/2010/T142/014028

Turbulent transport in hydromagnetic flows

A Brandenburg[1,2], P Chatterjee[1], F Del Sordo[1,2], A Hubbard[1],
P J Käpylä[1,3] and M Rheinhardt[1]

[1] NORDITA, Roslagstullsbacken 23, SE-10691 Stockholm, Sweden
[2] Department of Astronomy, Stockholm University, SE-10691 Stockholm, Sweden
[3] Department of Physics, FI-00014 University of Helsinki, Finland

E-mail: brandenb@nordita.org

Received 26 April 2010
Accepted for publication 1 June 2010
Published 31 December 2010
Online at stacks.iop.org/PhysScr/T142/014028

Abstract

The predictive power of mean-field theory is emphasized by comparing theory with simulations under controlled conditions. The recently developed test-field method is used to extract turbulent transport coefficients both in the kinematic and the nonlinear or quasi-kinematic cases. A striking example of the quasi-kinematic method is provided by magnetic buoyancy-driven flows that produce an α effect and turbulent diffusion.

PACS numbers: 91.25.Cw, 92.60.hk, 94.05.Lk, 96.50.Tf, 96.60.qd

(Some figures in this article are in colour only in the electronic version.)

1. Introduction

What happens when fluids mix? What if a fluid is moving in a magnetized environment? Are there analogies between the motion of a cloud in the sky, milk in a coffee cup and solar flares? The study of fluids and magnetic fields has always been a challenging branch of physics, leading to the development of tools of wide applicability, from meteorology to the study of galaxies. In particular, the connection between the existence of fluids in motion and the amplification of magnetic fields has been investigated both analytically and experimentally since the beginning of the 20th century. This generation of a magnetic field by dynamo action was already proposed by Larmor (1919), but a proper understanding of such a process requires both physical insight and a theoretical framework that describes the magneto-hydrodynamical (MHD) context in which the phenomena occur. The most common theoretical approach to MHD dynamos is the application of mean-field theory (Parker 1955, Steenbeck and Krause 1969, Moffatt 1978, Parker 1979, Krause and Rädler 1980). The core concept on which mean-field theory (hereafter MFT) rests is that turbulent systems (which include most natural MHD dynamos) are often amenable to a two-scale approach, where the velocity and magnetic fields are decomposed into mean and fluctuating components: $\boldsymbol{U}=\overline{\boldsymbol{U}}+\boldsymbol{u}$ and $\boldsymbol{B}=\overline{\boldsymbol{B}}+\boldsymbol{b}$. The mean parts $\overline{\boldsymbol{U}}$ and $\overline{\boldsymbol{B}}$ generally vary slowly both in space and time, and capture the global behavior of the system, which is often also the observable one. The fluctuating fields, on the other hand, describe irregular, often chaotic small-scale effects.

Using the aforementioned decomposition the equation for the time evolution of the magnetic field, known as the induction equation, can be rewritten as a set of two equations for mean and fluctuating quantities

$$\frac{\partial\overline{\boldsymbol{B}}}{\partial t}=\nabla\times\left(\overline{\boldsymbol{U}}\times\overline{\boldsymbol{B}}\right)+\nabla\times\overline{\boldsymbol{\mathcal{E}}}+\eta\nabla^2\overline{\boldsymbol{B}}, \qquad (1)$$

$$\frac{\partial\boldsymbol{b}}{\partial t}=\nabla\times\left(\overline{\boldsymbol{U}}\times\boldsymbol{b}\right)+\nabla\times\left(\boldsymbol{u}\times\overline{\boldsymbol{B}}\right)+\nabla\times(\boldsymbol{u}\times\boldsymbol{b})'+\eta\nabla^2\boldsymbol{b}, \qquad (2)$$

where η is the microphysical magnetic diffusivity of the fluid (here assumed uniform), while $\overline{\boldsymbol{\mathcal{E}}}\equiv\overline{\boldsymbol{u}\times\boldsymbol{b}}$ is the mean electromotive force, and $(\boldsymbol{u}\times\boldsymbol{b})'=\boldsymbol{u}\times\boldsymbol{b}-\overline{\boldsymbol{u}\times\boldsymbol{b}}$.

Correlations such as $\overline{\boldsymbol{u}\times\boldsymbol{b}}$ are at the heart of turbulent transport, and apply to a broad range of processes, from dynamos to the mixing of chemicals through stirring. For example, the evolution of the mean $\overline{C}$ of a chemical concentration $C=\overline{C}+c$ is governed by the mean flux $\overline{\boldsymbol{u}c}$ resulting from the interplay of the fluctuations. Likewise, the evolution of mean momentum, $\rho\overline{\boldsymbol{U}}$, is governed by the Reynolds stress, $\rho\overline{u_iu_j}$ (with constant density ρ). We return to the flux of chemicals at the end of section 4.1. Here, the key task consists in relating the mean emf $\overline{\boldsymbol{\mathcal{E}}}$ to the mean field $\overline{\boldsymbol{B}}$. Underlying symmetries that constrain the form of this relation are of significant help. $\overline{\boldsymbol{\mathcal{E}}}$ is a vector, so if the system is homogeneous and the turbulence isotropic, in what direction can it point? The answer is that in such a system $\overline{\boldsymbol{\mathcal{E}}}$ can have constituents pointing along the mean magnetic field $\overline{\boldsymbol{B}}$ and the mean current density $\overline{\boldsymbol{J}} = \nabla \times \overline{\boldsymbol{B}}/\mu_0$ (as well as higher-order spatial and time derivatives, see section 4.2), which leads to approximations such as

$$\overline{\boldsymbol{\mathcal{E}}} = \alpha \overline{\boldsymbol{B}} - \eta_t \mu_0 \overline{\boldsymbol{J}}. \tag{3}$$

The coefficients linking correlations to mean quantities are known unimaginatively as mean-field transport coefficients, with each one describing a distinct physical effect. In equation (3), α describes the (in)famous α effect that can drive a dynamo, while η_t quantifies the turbulent diffusion of the mean magnetic field (μ_0 is the vacuum permeability). Note that a much more general representation of $\overline{\boldsymbol{\mathcal{E}}}$ is given by the convolution integral

$$\overline{\boldsymbol{\mathcal{E}}}(\boldsymbol{x}, t) = \int_{t_0}^{t} \int \boldsymbol{G}(\boldsymbol{x}, \boldsymbol{x}', t, t')\, \overline{\boldsymbol{B}}(\boldsymbol{x}', t')\, \mathrm{d}^3x'\, \mathrm{d}t' \tag{4}$$

with an appropriate tensorial kernel $\boldsymbol{G}$.

Equation (2) contains terms that can sometimes be neglected. Most famously, in the case of fluids with small magnetic Reynolds number, that is $Re_\mathrm{M} = UL/\eta \ll 1$, or low Strouhal number $St = U\tau_c/L \ll 1$, we can drop $(\boldsymbol{u} \times \boldsymbol{b})'$ and can thus make an analytical calculation of the transport coefficients feasible. Under this approximation, known as the second order correlation approximation (SOCA), equation (2) takes for vanishing mean velocity the form

$$\frac{\partial \boldsymbol{b}}{\partial t} = \nabla \times \left(\boldsymbol{u} \times \overline{\boldsymbol{B}}\right) + \eta \nabla^2 \boldsymbol{b}. \tag{5}$$

In the limit of high Re_M (hence small St), the coefficients α and η_t reduce then to (Krause and Rädler 1980, Rädler and Rheinhardt 2007)

$$\alpha = -\frac{\tau_c}{3} \overline{\boldsymbol{u} \cdot (\nabla \times \boldsymbol{u})}, \qquad \eta_t = \frac{\tau_c}{3} \overline{\boldsymbol{u}^2}, \tag{6}$$

where τ_c is a characteristic turbulent correlation time.

2. The need for MFT: a status report

2.1. Motivation

In the astrophysical context, MFT has mainly been applied in order to understand and model the origin of the Sun's magnetic field and its differential rotation (Rüdiger and Hollerbach 2004). Direct simulations of convection in spherical shells begin to reproduce these phenomena to some extent (Brun *et al* 2004, Browning *et al* 2006, Brown *et al* 2010, Käpylä *et al* 2010a), but interpreting their results properly remains difficult. This task is approachable only in the framework of a reasonably accurate theory.

MFT is sometimes perceived as uncertain and even arbitrary owing to a large amount of parameters that are often chosen to reproduce 'whatever one wants'. Adjusting parameters at will is certainly risky and clearly not permissible in the long run, because it would imply a complete loss of predictive power of MFT. There are several reasons why the 'free parameter' approach has nevertheless often been adopted. Firstly, the conventional theory for computing turbulent transport coefficients is only accurate at low Reynolds numbers, but is not well tested at higher ones. Secondly, models of solar-like dynamos that are based on a straightforward application of mixing-length ideas to computing turbulent transport coefficients (Krivodubskii 1984) do not reproduce the Sun: the cycle periods are too short (Köhler 1973) and the migration of sunspots and other magnetic activity is poleward, not equatorward, which is also found in direct numerical simulations (Gilman 1983, Käpylä *et al* 2010a).

In this situation, it is sensible to reduce one's ambitions and focus on phenomena that are seen in direct simulations of simplified systems, but are nevertheless relevant for understanding the Sun. A useful goal consists then in reproducing such phenomena by mean-field models, thus obtaining a chance to trace down the reasons for discrepancies between both representations. This will be exemplified in section 3. First, however, we shall summarize the basic saturation phenomenology of mean-field dynamos.

2.2. Saturated dynamos and magnetic helicity fluxes

A recent discovery that is now well explained by MFT is the slow saturation behavior of an α^2 dynamo in a triply periodic box (Brandenburg 2001). Such systems are unphysical, but they make good test problems due to the ease of capturing them both numerically and analytically. Initially, both the mean and the fluctuating fields grow exponentially—as expected from kinematic theory. However, when the small-scale field becomes comparable to the equipartition value, i.e. $\overline{\boldsymbol{b}^2} \sim B_\mathrm{eq}^2$, the growth changes its nature: the fluctuating field saturates while the mean field, well below equipartition, continues to grow albeit extremely slowly. Finally, after multiple microphysical resistive times, the mean field itself reaches a steady, super-equipartition state; see figure 9.4 of Brandenburg and Subramanian (2005).

This behavior is one aspect of the 'catastrophic' α-quenching phenomenon, and has come to be understood in terms of the magnetic helicity density, $h \equiv \overline{\boldsymbol{A} \cdot \boldsymbol{B}}$, and the magnetic α effect of Pouquet *et al* (1976), $\alpha_\mathrm{M} \equiv \tau \overline{\boldsymbol{j} \cdot \boldsymbol{b}}/3\overline{\rho}$. It has usually the opposite sign of the α of equation (6), now marked α_K (kinetic), and grows with growing mean field, so that the net $\alpha = \alpha_\mathrm{K} + \alpha_\mathrm{M}$ would be reduced and the dynamo growth halted. This result has been extended to the dynamic α quenching phenomenology (Kleeorin and Ruzmaikin 1982, Field and Blackman 2002, Blackman and Brandenburg 2002), where the mean magnetic helicity in the fluctuating fields, $h_\mathrm{f} \equiv \overline{\boldsymbol{a} \cdot \boldsymbol{b}}$, is used as a proxy for the current helicity, $\overline{\boldsymbol{j} \cdot \boldsymbol{b}} \simeq k_\mathrm{f}^2 h_\mathrm{f}$, with k_f being the wavenumber of the energy-carrying eddies. In a system that disallows the divergence of the magnetic helicity flux, such as a triply periodic domain, the time evolution of h_f and the resulting dynamical α quenching equation can be written as

$$\frac{\mathrm{d}h_\mathrm{f}}{\mathrm{d}t} = -2\overline{\boldsymbol{\mathcal{E}}} \cdot \overline{\boldsymbol{B}} - 2\eta\mu_0 \overline{\boldsymbol{j} \cdot \boldsymbol{b}}, \tag{7}$$

$$\frac{\mathrm{d}\alpha_{\mathrm{M}}}{\mathrm{d}t} = -2\eta_{\mathrm{t}} k_{\mathrm{f}}^2 \left(\frac{\alpha \overline{\boldsymbol{B}}^2 - \eta_{\mathrm{t}}\mu_0 \overline{\boldsymbol{J}} \cdot \overline{\boldsymbol{B}}}{B_{\mathrm{eq}}^2} + \frac{\alpha_{\mathrm{M}}}{Re_{\mathrm{M}}} \right). \qquad (8)$$

The three phases of the α^2 dynamo in a triply periodic domain can now be understood. First the fields grow exponentially and the magnetic α effect grows with them until $\alpha_{\mathrm{M}} \sim -\alpha_{\mathrm{K}}$. This occurs rapidly enough that the magnetic helicity of the mean field (h_{m}) still obeys $h_{\mathrm{m}} \sim -h_{\mathrm{f}}$ and so $\overline{B}/B_{\mathrm{eq}} \simeq \sqrt{k_1/k_{\mathrm{f}}} < 1$ (Brandenburg 2001), where k_1 is the smallest possible wavenumber in the domain. During the resistive phase, the fluctuating fields are nearly steady but there is still a small excess of α over $\eta_{\mathrm{t}} k_1$ needed to replenish the field in the face of resistivity. This phase ends only when the time evolution of the total magnetic helicity reaches a steady state, which occurs when $\langle \boldsymbol{J} \cdot \boldsymbol{B} \rangle = 0$ or $\overline{B}/B_{\mathrm{eq}} \simeq \sqrt{k_{\mathrm{f}}/k_1} > 1$.

A short exponential growth phase yielding only weak mean fields poses severe problems for astrophysics as the subsequent resistive growth phase is generally prohibitively long. Real systems, however, allow for fluxes of magnetic helicity across their borders, and/or show spatial variations in the α effect, particularly regions where α has opposite signs separated, say, by an equator. This raises the possibility that the magnetic α will be exported from the system or transported to the equator and destroyed. Research into such transport is recent, but has already shown conclusively that there is a flux of h_{f} and that a larger residual α effect results due to it. It is not yet clear how large an effect this has on the final mean field strength.

3. Predictions versus realizations

In this section, we contrast the results of some computer realizations with corresponding mean-field predictions. We discuss examples from both linear and nonlinear regimes.

3.1. Parity and dependence on boundary conditions

A relatively old example is the emergence of oscillatory dynamo solutions in local models of accretion discs (Brandenburg *et al* 1995). Here, turbulence is driven by the magneto-rotational instability that generates a negative α effect in the upper half of the disc (Brandenburg *et al* 1995, Ziegler and Rüdiger 2000, Brandenburg 2005a, Gressel 2010). According to MFT, this negative α, for normal field (pseudo-vacuum) boundary conditions and radial shear, results in traveling wave solutions that are symmetric about the midplane and migrating toward the boundaries (Brandenburg and Campbell 1997). Conversely, when the boundary condition is changed to a perfect conductor, one expects non-oscillatory solutions that are antisymmetric about the midplane. Indeed, this dependence is borne out by simulations (Brandenburg 1998).

3.2. Onset of convective dynamo action depending on rotation rate

Large-scale dynamos due to turbulent convection are of particular interest in astrophysics. According to MFT, rotating inhomogeneous (usually due to stratification) turbulence leads to the generation of kinetic helicity and thus an α effect, which should enable the generation of large-scale fields. However, numerical simulations of rotating convection at first failed to show large-scale dynamo action (e.g. Brandenburg *et al* 1996, Cattaneo and Hughes 2006). Erroneously low values of α determined by what is now often called the imposed-field method seemed to confirm that the α effect does not work. In this method, a uniform magnetic field $\boldsymbol{B}_0$ is applied and one determines the resulting mean electromotive force, $\langle \boldsymbol{u} \times \boldsymbol{b} \rangle$, and further $\alpha = \langle \boldsymbol{u} \times \boldsymbol{b} \rangle \cdot \boldsymbol{B}_0 / B_0^2$; here the mean is defined as volume average (e.g. Cattaneo and Hughes 2006; see, however, Käpylä *et al* 2010b). On the other hand, when computing the turbulent transport coefficients for convection using the test-field method (see section 4.1), it was discovered that, as the rotation rate in non-shearing runs increases, the α effect increases and turbulent diffusion, η_{t}, decreases (Käpylä *et al* 2009a). Mean-field models (hereafter MFM), using these properly determined transport coefficients, then suggested that a large-scale dynamo should be excited when the Coriolis number, defined as the ratio of the rotation period to the convective turnover time, exceeds a value of ≈ 4. Subsequently, direct simulations in this parameter range confirmed this prediction (Käpylä *et al* 2009b). Again, this demonstrates that already kinematic MFT has predictive power and that very likely MFMs can give useful and new information about even more complex systems.

3.3. Helicity considerations

The helicity considerations outlined in section 2.2 provide further prognostic power. The shear-induced (non-diffusive) magnetic helicity flux, introduced by Vishniac and Cho (2001), has been particularly important in explaining the existence or the absence of a large-scale dynamo. For example, Tobias *et al* (2008) presented simulations of convection with vertical shear where no large-scale dynamo was excited although the necessary ingredients for an efficient dynamo (inhomogeneity, rotation and shear) were all present. However, in that case the shear-driven magnetic helicity flux is directed along the periodic x-direction and no net flux out of the system could occur. Using instead, in an otherwise similar setup, normal field boundary conditions, which do allow a net flux, Käpylä *et al* (2008) showed that a large-scale dynamo does exist and indeed saturates at near-equipartition field strengths; see the left panel of figure 1 where we show the effect of open versus periodic boundaries. Similar results have also been obtained for forced turbulence with a more complicated shear profile motivated by the differential rotation pattern of the Sun (Brandenburg 2005b). By imposing a toroidal magnetic field in a simulation with the same setup, the α effect has been determined and, for $Re_{\mathrm{M}} \gg 1$, it is also found to depend sensitively on whether the boundaries are open or closed (Brandenburg and Sandin 2004); see the right panel of figure 1.

Another issue approachable through magnetic helicity considerations is the convergence problem of the MRI, i.e. the steep decrease of the turbulence level with decreasing magnetic Prandtl number, Pr_{M}, for small values of Pr_{M} in fully periodic setups (e.g. Fromang *et al* 2007). An otherwise similar setup, however, that does allow a net magnetic helicity flux through the vertical boundaries produces indeed strong

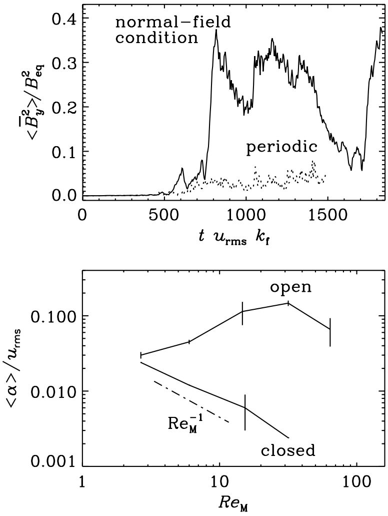

Figure 1. Upper plot: energy in the horizontally averaged streamwise magnetic field from two convection simulations with vertical shear $\overline{U}_y(z)$ and either normal field (solid line) or periodic (dotted line) magnetic boundary conditions in the x-direction. Adapted from Käpylä *et al* (2008). Lower plot: dependence of $\langle\alpha\rangle/u_{rms}$ on Re_M for open and closed boundaries. Note that for $Re_M \approx 30$ the α effect is about 30 times smaller when the boundaries are closed. Adapted from Brandenburg and Sandin (2004).

large-scale dynamo action, roughly independent of the value of Pr_M (Käpylä and Korpi 2010).

4. Computing mean-field transport coefficients

In view of such success stories, there should be an unbroken interest in MFMs both because of their descriptive capabilities and their predictive potential, but we have to realize that there are serious shortcomings of MFT that have persuaded many researchers to (re)turn to global direct numerical simulations instead of designing improved MFMs. This critical stage of MFT can be characterized by the following observations:

- The limitations of analytic approaches to calculating mean-field coefficients are clearly too restrictive as the interest has moved from pointing out the qualitative existence of certain effects to their quantitative reproduction and prediction. This is due to
    - the obvious insufficiency of SOCA in astrophysical contexts, as usually $Re_M \gg 1$ and $St \not\ll 1$;
    - the unclear aspects of closure approaches like the τ approximation (Rädler and Rheinhardt 2007);
    - the need for knowledge of velocity correlators like $\overline{u_i u_j \cdots u_n}$ even in mathematically well-established (systematic) higher-order correlation approximations.
- It is obvious that MFMs for realistic setups with predictive abilities need to employ transport coefficients that are
    - fully tensorial;
    - position dependent;
    - dependent on the mean quantities themselves, i.e. nonlinear;
    - non-local and non-instantaneous;
    - including magnetic background fluctuations.

  There is no longer any chance of obtaining powerful models by employing a few scalar coefficients, the basic structure of which can be derived analytically leaving a few free parameters to be adapted properly.

To find a way out of this impassé, one might look at how in other fields of physics/engineering, modeling and simulation of rather complex systems are being made possible if the full resolution of the microphysics is not affordable. Let us choose as an example the mechanics of elastic materials, say, metals. Their elastic properties can in principle be derived from the microphysics of their lattices, but it will perhaps never be possible to simulate the static and dynamic behavior of, say, a bridge by solving quantum physical lattice equations. Instead, one relies upon the equations of continuum mechanics in which the lattice physics enters via macrophysical material properties such as Young's modulus and the Poisson number (sufficient for an isotropic material). These are typically obtained by measurements in a series of standardized experiments with test bodies having simple geometries and being subject to clearly defined boundary conditions. Of course, for such an approach to be successful, a certain *locality* of the microphysics processes is necessary, which can be expressed by the principle that neighboring material elements of a structure 'communicate' only via forces at their common borders.

A widely analogous procedure with respect to the task of calculating transport coefficients for a certain type of turbulence would consist in creating it in a (small) test volume with well-defined boundary/environmental conditions (such as a penetrating magnetic and/or gravitational field) and to determine then the wanted coefficients somehow *by measurements*. Then a major theoretical challenge consists in specifying the set of experiments needed to find just these coefficients and in prescribing the computational recipe for extracting them from the measured quantities such as fluctuating magnetic fields and/or velocities.

This program has been implemented by the so-called *test-field methods* (Schrinner *et al* 2005, 2007) with the modification that the physical experiments are replaced by numerical ones. Clearly, there is an important difference compared to the continuum mechanics scheme: the same equations whose direct simulation was felt to be non-affordable, what just created the need for an MFM, have now, nevertheless, to be simulated within the numerical experiments. However, in two aspects the test-field approach can still be advantageous. Firstly, the 'experimental' volumes can represent small sections of the object that is to be globally analyzed. Hence, much finer structures can be resolved with the same numerical effort. Secondly, if an MFM is established once, it can thereafter be utilized for long-term global simulations, which would otherwise be prohibitively expensive.

The aforementioned locality of the actual physics here has to be with respect to correlation properties of the underlying fluctuating fields, say, a turbulent flow. For all conceivable astrophysical situations this condition can hardly be considered too restrictive. In practice, correlation lengths and times are the relevant quantities to be considered in defining the simulation box size and the integration time.

Computing turbulent transport tensors such as $\boldsymbol{\alpha}$ and $\boldsymbol{\eta}$ (see equation (9) below) from simulations has been performed with varying success over the last 20 years. Utilizing the imposed-field method for $\boldsymbol{\alpha}$ has led to either the confirmation of well-known results (for example, a positive horizontal α effect in the upper layers of convection in the Sun's Northern hemisphere) or the prediction of as yet unknown results (e.g. a reversed sign of the vertical α under the same conditions; see Brandenburg *et al* 1990) later confirmed by analytical calculations (Ferrière 1992, Rüdiger and Kitchatinov 1993).

After having explained the new test-field method in the next section, particular applications considering the nonlocality of turbulent transport in space and time will be discussed in section 4.2.

4.1. Test-field method

Let us return to equation (2) for the fluctuating magnetic field. The wanted mean electromotive force $\overline{\boldsymbol{\mathcal{E}}} = \overline{\boldsymbol{u} \times \boldsymbol{b}}$ is obviously a linear and homogeneous functional of $\overline{\boldsymbol{B}}$ and we may therefore write the ansatz

$$\overline{\boldsymbol{\mathcal{E}}} = \boldsymbol{\alpha}\overline{\boldsymbol{B}} - \boldsymbol{\eta}\nabla\overline{\boldsymbol{B}}, \tag{9}$$

strictly valid for stationary mean fields depending only linearly on position. The components of $\boldsymbol{\alpha}$ and $\boldsymbol{\eta}$ can be found by the following procedure:

(a) solve

$$\frac{\partial \boldsymbol{b}^k}{\partial t} - \eta\nabla^2\boldsymbol{b}^k - \mathrm{curl}\left[(\overline{\boldsymbol{U}} \times \boldsymbol{b}^k + \boldsymbol{u} \times \boldsymbol{b}^k)'\right] = \mathrm{curl}\,(\boldsymbol{u} \times \overline{\boldsymbol{B}}^k)$$

for given $\boldsymbol{u}$, $\overline{\boldsymbol{U}}$ and test fields $\overline{\boldsymbol{B}}^k$, $\quad k = 1, \ldots, N$;

(b) calculate $\overline{\boldsymbol{\mathcal{E}}}^k = \overline{\boldsymbol{u} \times \boldsymbol{b}^k}$;

(c) determine the components of $\boldsymbol{\alpha}$ and $\boldsymbol{\eta}$ by inverting

$$\overline{\boldsymbol{\mathcal{E}}}^k = \boldsymbol{\alpha}\overline{\boldsymbol{B}}^k - \boldsymbol{\eta}\nabla\overline{\boldsymbol{B}}^k. \tag{10}$$

The solution is unique if N is chosen appropriately and the test fields $\overline{\boldsymbol{B}}^k$ are sufficiently independent. Since we 'look at' the given velocity fields $\boldsymbol{u}$, $\overline{\boldsymbol{U}}$ not from only one perspective like in the case of the imposed-field method, but obtain instead different views represented by the different test solutions $\boldsymbol{b}^k$, the test-field approach could be characterized as 'holographic' instead of 'photographic'. Indeed, all of the information needed to specify an ansatz like (9) is extracted from the velocity fields.

For a number of explicitly given flows like those introduced by Roberts (1970) and Galloway and Proctor (1992), exact agreement of the determined tensors with SOCA results could be demonstrated. In the case of the Roberts flow there is agreement even with an analytic result for arbitrary magnetic Reynolds numbers (Rädler *et al* 2002, Rädler and Brandenburg 2009, Rheinhardt and Brandenburg 2010).

The method has now been applied to a number of different flows ranging from homogeneous forced turbulence without shear (Sur *et al* 2008, Brandenburg *et al* 2008a) to cases with shear (Brandenburg *et al* 2008b, Mitra *et al* 2009) and to inhomogeneous turbulence in stratified discs (Brandenburg 2005a, Gressel *et al* 2008) as well as convection (Käpylä *et al* 2009a). It has also been utilized in passive scalar transport, e.g. the transport of chemicals. Corresponding turbulent transport coefficients have been calculated for homogeneous turbulence under the influence of rotation or an applied magnetic field (Brandenburg *et al* 2009), as well as for homogeneous shear flows (Madarassy and Brandenburg 2010).

4.2. Nonlocality in space and time

Because the test fields are not native to the system, they can disentangle effects that can not otherwise be distinguished. However, for the same reason they can introduce temporal or spatial scales that are again not native to the system.

With respect to temporal scales the consequences of this mismatch can be seen in the *memory effect*: consider a dynamo system with a growing mean field. Turbulence creates a fluctuating field from the mean one and contributes to the mean electromotive force. If the mean field is growing, the small-scale field created in the past is weaker than it would be when created in the present. Thus, if the time behavior of the test fields is different from that of the 'real' mean field, the $\boldsymbol{\alpha}$ and $\boldsymbol{\eta}$ tensors from the test-field method will not be the actual ones that rule the evolution of the mean field. A similar problem occurs when the spatial scales of the test fields do not coincide with the spatial scale of the mean field to be modeled, due to *nonlocality* in space.

When the proper scales of the mean field are known, corresponding test fields can be used. Otherwise, the scales of the test fields, say, wavevector $\boldsymbol{k}$ and frequency ω, are considered independent parameters and the test-field method provides $\boldsymbol{\alpha}(\boldsymbol{k}, \omega)$ and $\boldsymbol{\eta}(\boldsymbol{k}, \omega)$, which exhaustively describe the response kernel introduced in (4).

The memory effect is demonstrated in figure 2 for the case of the Roberts flow (for details, see Hubbard and Brandenburg (2009). In the left plot, we see the difference between the growth rate of a dynamo and that calculated from the dispersion relation using $\boldsymbol{\alpha}$ and $\boldsymbol{\eta}$ determined by the test-field method with steady test fields. We can reconcile these growth rates by deriving them all from a proper kernel, which can be established by employing a set of test fields with different time dependences.

The memory effect and nonlocality in space have been studied using the integral kernel technique in Hubbard and Brandenburg (2009) and Brandenburg *et al* (2008a), respectively. Using test fields that oscillate sinusoidally in time, the Fourier transforms $\hat{\alpha}(\omega)$ of the integral kernels $\tilde{\alpha}(t)$ were found to fit the form:

$$\hat{\alpha}(\omega) = \alpha_0 \frac{1 - \mathrm{i}\omega\tau_\alpha}{(1 - \mathrm{i}\omega\tau_\alpha)^2 + \omega_\alpha^2\tau_\alpha^2}, \tag{11}$$

where τ_α is the memory time of the flow and ω_α is a fit parameter of order τ_α^{-1}. In turbulence, τ_α is comparable to the turnover time, but in steady flows, it can approach microphysical resistive time scales. In the right panel of figure 2, we present such a fit for the MW+flow of Otani (1993), being a flow pattern with wavenumber k_0 and amplitude u_0 that is modulated with frequency $\omega_\mathrm{f} = u_0 k_0$.

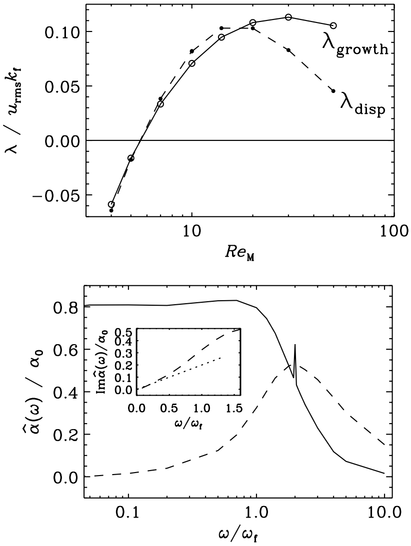

Figure 2. Upper plot: $Re_{\rm M}$ dependence of the dynamo growth rate for the Roberts flow as obtained from a direct calculation, $\lambda_{\rm growth}$, compared with the result of the dispersion relation, $\lambda_{\rm disp} = |\alpha k| - (\eta + \eta_{\rm t})k^2$, using a cube of size L^3; $k_1 = 2\pi/L$, $k_{\rm f} = \sqrt{2}k_1$. For this range of $Re_{\rm M}$, the most unstable mode has the largest possible wavelength ($k = k_1$). Lower plot: real (solid) and imaginary (dashed) parts of $\hat\alpha(\omega)$ for $k = 0$ using the Otani (1993) MW+ flow with $Re_{\rm M} = 1$. Normalization given by $\alpha_0 = u_0$. Inset: scaling of Im $\hat\alpha$ near the origin with slope 0.2, in agreement with the results of Hughes and Proctor (2010). Adapted from Hubbard and Brandenburg (2009).

This leads to an extra spike in $\hat\alpha(\omega)$ at $\omega = 2\omega_{\rm f}$. The slope of the imaginary part at the origin, $\mathrm{d}\,\mathrm{Im}\,\hat\alpha/\mathrm{d}\omega|_{\omega=0}$, represents the coefficient of the first order term with respect to an expansion in time. Its value of 0.2 is in agreement with that found by Hughes and Proctor (2010). The real-space integral kernel corresponding to (11) reads

$$\tilde\alpha(\tau) = \alpha_0\Theta(\tau)\mathrm{e}^{-\tau/\tau_\alpha}\cos\omega_\alpha\tau, \tag{12}$$

where τ is the time distance to the instant of consideration, and Θ is the Heaviside step function that preserves causality as the time integral kernel must only consider the past. Hubbard and Brandenburg (2009) have found similar expressions also for passive scalar transport.

The Fourier transform of the spatial integral kernels is somewhat simpler, being fit by a Lorentzian:

$$\hat\alpha(k) = \frac{\alpha_0}{1 + (a_\alpha k/k_{\rm f})^2}, \qquad \hat\eta_t(k) = \frac{\eta_{t0}}{1 + (a_\eta k/k_{\rm f})^2}, \tag{13}$$

whose amplitude is nearly independent of $Re_{\rm M}$ for $Re_{\rm M} \gg 1$. The k dependence is reasonably close to inverse quadratic for $k/k_{\rm f} > 2$; see figure 3. Here, $a_\alpha \approx 2a_\eta \approx 1$ are coefficients of the order of unity. The corresponding spatial integral kernels are simple exponential decays

$$\tilde\alpha(\zeta) = \alpha_0\frac{k_{\rm f}}{2a_\alpha}\mathrm{e}^{-(k_{\rm f}/a_\alpha)\zeta}, \qquad \tilde\eta_t(\zeta) = \eta_{t0}\frac{k_{\rm f}}{2a_\eta}\mathrm{e}^{-(k_{\rm f}/a_\eta)\zeta}, \tag{14}$$

where ζ is the distance from the point of consideration.

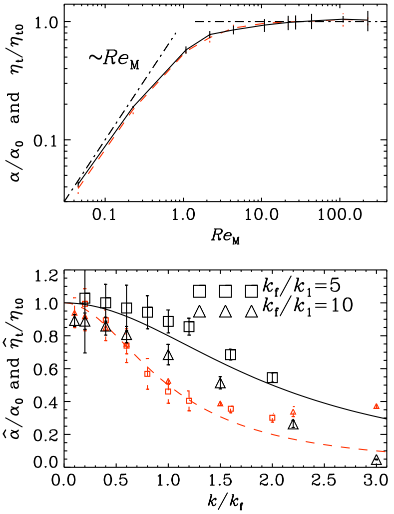

Figure 3. Upper plot: dependence of the normalized values of α (dashed or red line) and $\eta_{\rm t}$ (solid line) on $Re_{\rm M}$ for $k/k_{\rm f} = 0.2$ and $Re = 2.2$. Adapted from Sur *et al* (2008). Lower plot: dependences of the normalized $\hat\alpha$ (dashed or red line, small symbols) and $\hat\eta_{\rm t}$ (solid line, bigger symbols) on the normalized wavenumber $k/k_{\rm f}$ for turbulence forced with $k_{\rm f}/k_1 = 5$, $Re_{\rm M} = 10$ (squares) and $k_{\rm f}/k_1 = 10$, $Re_{\rm M} = 3.5$ (triangles). Lines give the Lorentzian fits (13). Adapted from Brandenburg *et al* (2008a).

5. From linear to nonlinear

When the velocity $\boldsymbol{U}$ is given, the tensors $\boldsymbol{\alpha}$ and $\boldsymbol{\eta}$ can be obtained by a mathematically well-founded procedure as outlined in section 4.1. Naturally, the question arises as to how one should proceed when the mean magnetic field has already acted upon this velocity. Inspecting equation (2) it can be concluded that $\overline{\boldsymbol{B}}$, considered as a functional of $\boldsymbol{U}$ and $\overline{\boldsymbol{B}}$, is always linear and homogeneous in the latter, irrespective of the effects that $\boldsymbol{U}$ was subjected to and, in particular, irrespective of whether or not a mean field had already acted upon it. That is, the presented test-field method continues to be valid without modification and as a tribute to this extension it is called the *quasi-kinematic method*. The turbulent transport coefficients are of course now depending on $\overline{\boldsymbol{B}}$, but this dependence is entirely conveyed by the dependence of $\boldsymbol{U}$ on $\overline{\boldsymbol{B}}$.

Clearly, a dynamically effective mean field represents an additional preferred direction. As a consequence, for an isotropic hydrodynamic background and a uniform $\overline{\boldsymbol{B}}$, the formerly isotropic tensor $\boldsymbol{\alpha}$ adopts now the shape

$$\alpha_{ij} = \alpha_1\delta_{ij} + \alpha_2\hat B_i\hat B_j, \quad i, j = 1, 2, \tag{15}$$

with $\hat{\boldsymbol{B}}$ being the unit vector in the direction of $\overline{\boldsymbol{B}}$. If this is, say, the x-direction we get $\alpha_{11} = \alpha_1 + \alpha_2$ and $\alpha_{22} = \alpha_1$. Both coefficients are of course functions of $\overline{B}$. Since $\overline{\boldsymbol{\mathcal{E}}} = \alpha_{11}\overline{\boldsymbol{B}}$, the effective scalar α effect is just given by α_{11}. As an example, the α quenching characteristic for the Roberts flow was determined exhibiting a $\overline{B}^{-4}$ asymptotic dependency, cf Rheinhardt and Brandenburg (2010) and figure 4. This

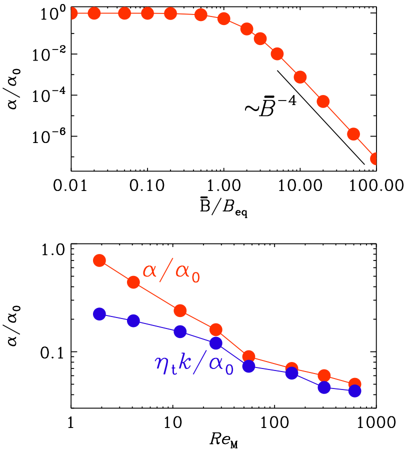

Figure 4. Upper plot: variation of α with $\overline{B}$ for the forced Roberts flow with $Re_M = 1/2\sqrt{2} \approx 0.35$ and $Pr_M = 1$. Adapted from Rheinhardt and Brandenburg (2010). Lower plot: Re_M dependence of α and η_t in the saturated state with $\overline{B} \approx B_{eq}$. Adapted from Brandenburg *et al* (2008c).

result is at odds with theoretical predictions, although it agrees with data for a forced ABC flow (Sur *et al* 2007).

Things become more involved if the direction of the mean current density $\overline{\boldsymbol{J}}$ enters as a second preferred direction. A situation in which this complication is circumvented, without being as simple as the former one, is given by the α^2 dynamo due to homogeneous isotropic helical (forced) turbulence. Here, the dynamo solution is a Beltrami field with $\overline{\boldsymbol{B}} \parallel \overline{\boldsymbol{J}}$ and constant modulus. Hence, $\overline{\boldsymbol{J}}$ is not providing an additional preferred direction and equation (15) remains valid. The solution has always Beltrami shape, regardless of at what level it eventually saturates. Consequently, α and η_t are independent of position for any field strength. The growth rate of the dynamo is given by $\lambda = |\alpha k| - (\eta + \eta_t)k^2$ and should approach zero in the course of saturation. Under these conditions it is possible to confirm the quasi-kinematic method in the way that $\alpha(\overline{B})$and $\eta_t(\overline{B})$ are determined in the saturated stage and checked for consistency against $\lambda = 0$. Indeed, this could be demonstrated to high accuracy for different values of Re_M; see Brandenburg *et al* (2008c). Figure 4 shows $\alpha(\overline{B})$ and $\eta_t(\overline{B})$ as functions of Re_M in the saturated state with $\overline{B} \approx B_{eq}$.

6. Quasi-kinematic method for magnetic-buoyancy-driven flows

So far, we have been dealing with situations in which a hydrodynamic background was provided independently and the mean magnetic field occurred as an additional, at most coequal participant. But what about cases in which the turbulence itself is a consequence of $\overline{\boldsymbol{B}}$? Examples are the magneto-rotational instability and the magnetic buoyancy instability (see below). Clearly, those setups do not know a kinematic stage on which the influence of $\overline{\boldsymbol{B}}$ is negligible. One might worry that in such a situation the quasi-kinematic test-field procedure fails (Courvoisier *et al* 2010). However, equation (2) continues to be valid and hence all conclusions drawn from it. Consequently, the quasi-kinematic method should be applicable. The only peculiarity occurring here is the fact that all components of $\boldsymbol{\alpha}$ and $\boldsymbol{\eta}$ vanish for $0 \leqslant \overline{B} \leqslant \overline{B}_{\text{threshold}}$, because a fluctuating velocity (and magnetic field) develops only after the instabilities have set in.

Let us now consider the magnetic buoyancy instability. It has been proposed by Moffatt (1978) that, once the dynamo-generated magnetic field in the overshoot layer of the Sun reaches appreciable strengths, this instability can set in and govern the dynamics thereafter. The buoyancy instability of a localized flux layer in the presence of stratification and rotation was later studied in detail by Schmitt (1984, 1985). A necessary but not sufficient condition for instability is

$$\frac{\partial}{\partial z}\log\left(\frac{B^2}{\rho^2}\right) < 0, \tag{16}$$

which essentially means that the magnetic field decreases faster with height than density. Using the imposed-field method, Brandenburg and Schmitt (1998) performed numerical calculations to determine the α effect of the resulting turbulence. Here we determine all components of $\boldsymbol{\alpha}$ and $\boldsymbol{\eta}$ using a version of the quasi-kinematic test-field method wherein mean fields are defined as xy averages.

Our setup is similar to that described in Brandenburg and Schmitt (1998). The computational domain is a cuboid of size $-1 \leqslant x \leqslant 1$, $-3 \leqslant y \leqslant 3$, $-0.5 \leqslant z \leqslant 1.5$, with gravity pointing in the negative z-direction, and rotation $\boldsymbol{\Omega}$ making an angle θ with the vertical. The pressure scale height is $H_P = 1$ (half-height of the box). The base state is a polytrope with index $m = 3$ (the adiabatic value here is 3/2), so that it is stable to convection. The initial condition comprises a horizontal magnetic layer of thickness $H_B = 0.1$ with the profile

$$B_y = v_{A0} H_B \frac{\partial}{\partial z} \tanh\left(\frac{z - 0.1}{H_B}\right), \tag{17}$$

where the ratio of the reference values of Alfvén and sound speed is $v_{A0}/c_{s0} = 0.5$. We modify the base state such that the density profile remains polytropic but the entropy profile is adjusted to obey magnetostatic equilibrium. The initial velocity consists of about 20 localized eddies with Mach numbers of about 10^{-5} at $z = 0.1$ in the xy-plane. We use stress-free boundary conditions for the velocity and the vertical field condition for the magnetic field, whereas with respect to entropy we keep the temperature at the top and the (radiative) heat flux at the bottom constant. All calculations have been done with $Pr = Pr_M = 4$ on a 64^3 grid. Figure 5(a) gives the temporal evolution of the volume averages $\langle u^2 \rangle$ and $\langle B_x^2 \rangle$ and figure 5(b) the evolution of the mean field $\overline{B}_x$. There is a short exponential growth phase followed by a slow decay on a resistive time scale.

When it comes to applying the test-field method, an aspect not discussed up to now is the intrinsic inhomogeneity of the flow both due to stratification and the background magnetic field itself. Within kinematics, that is, without the background field, no specific complication is connected to this, as from the stationary version of equation (4),

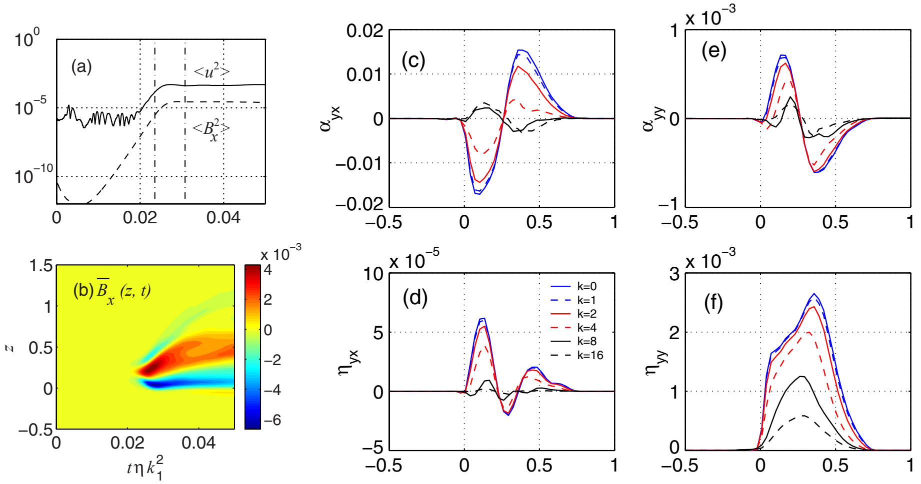

Figure 5. (a) Evolution of volume averaged velocity and B_x squares. (b) A 'butterfly diagram' for $\overline{B}_x$. (c–f) Selected tensorial components of $\hat{\boldsymbol{\alpha}}$ and $\hat{\boldsymbol{\eta}}$ for different wavenumbers k as explained in the legend in (d). Plots have been obtained by time averaging over the interval indicated by the dashed-dotted lines in (a).

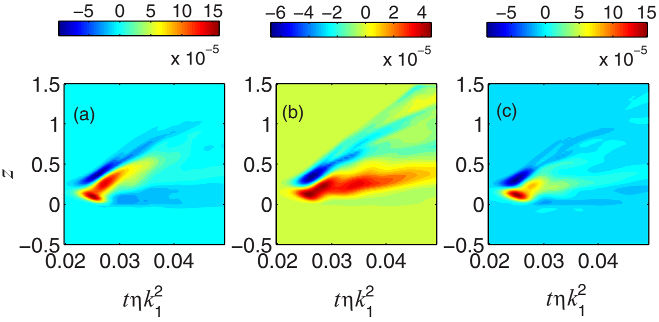

Figure 6. (a) The mean emf $\overline{\mathcal{E}}_y(z,t)$ calculated from the horizontal average $\overline{\boldsymbol{u}\times\boldsymbol{b}}$. (b) Reconstruction of $\overline{\mathcal{E}}_y(z,t)$ using only the $k=0$ contributions in (18). (c) The same as (b) but using all contributions $k=0,1,\ldots 8$.

$\boldsymbol{\alpha}$ and $\boldsymbol{\eta}$ emerge straightforwardly in a shape expressing inhomogeneity, that is, $\boldsymbol{\alpha}(\boldsymbol{x},\boldsymbol{x}')$, $\boldsymbol{\eta}(\boldsymbol{x},\boldsymbol{x}')$ or, equivalently, $\boldsymbol{\alpha}(\boldsymbol{x},\boldsymbol{x}-\boldsymbol{x}')$, $\boldsymbol{\eta}(\boldsymbol{x},\boldsymbol{x}-\boldsymbol{x}')$. When subjecting the latter to a Fourier transform with respect to their second argument, we arrive at $\hat{\boldsymbol{\alpha}}(\boldsymbol{x},\boldsymbol{k})$ and $\hat{\boldsymbol{\eta}}(\boldsymbol{x},\boldsymbol{k})$. In our case, harmonic test fields with different wavenumbers k in the z-direction can be employed to obtain $\hat{\boldsymbol{\alpha}}(z,k)$ and $\hat{\boldsymbol{\eta}}(z,k)$.

In the nonlinear situation, the Green's function approach remains valid if $\overline{\boldsymbol{\mathcal{E}}}$ is considered as a functional of $\boldsymbol{U}$ and $\overline{\boldsymbol{B}}$, which is then linear and homogeneous in the latter (cf section 5). However, we have to label $\boldsymbol{G}$ by the $\overline{\boldsymbol{B}}$ actually acting upon $\boldsymbol{U}$, that is, $\boldsymbol{G}(\boldsymbol{x},\boldsymbol{x}';\overline{\boldsymbol{B}})$, and can thus only make statements about the transport tensors for just the particular $\overline{\boldsymbol{B}}$ at hand. Hence, the tensors have to be labeled likewise: $\hat{\boldsymbol{\alpha}}\ (z,k;\overline{\boldsymbol{B}})$, $\hat{\boldsymbol{\eta}}\ (z,k;\overline{\boldsymbol{B}})$. As our initial mean magnetic field is in the y-direction, the instability will generate a $\overline{B}_x$ and we are mainly interested in the coefficients α_{yx}, α_{yy}, η_{yx} and η_{yy} with rank-2 tensor components $\eta_{ij}=-\eta_{ik3}\epsilon_{jk3}$; they are shown in figures 5(c)–(f). (Note that our rank-3 $\boldsymbol{\eta}$ tensor in equation (9) is defined with the opposite sign as, for example, in Brandenburg *et al* (2008a).)

Our goal now is to confirm that the relationship between $\overline{\boldsymbol{\mathcal{E}}}$ and $\overline{\boldsymbol{B}}$ taken directly from direct numerical simulations (DNS) can be represented by equation (9) with the transport tensors determined using the quasi-kinematic test-field method. In mathematical terms

$$\overline{\mathcal{E}}_i(z;\overline{\boldsymbol{B}}) \overset{?}{=} Re\left\{\sum_k \left[\hat{\alpha}_{ij}(z,k;\overline{\boldsymbol{B}}) - \mathrm{i}\pi k\,\hat{\eta}_{ij}(z,k;\overline{\boldsymbol{B}})\right] \times c_j^{(k)}\,\exp(\mathrm{i}\pi kz)\right\}, \tag{18}$$

with $2\boldsymbol{c}^{(k)}=\int\overline{\boldsymbol{B}}(z)\exp(-\mathrm{i}\pi kz)\,\mathrm{d}z$ and $\overset{?}{=}$ signifying the question whether the equation is indeed satisfied. We find that we can reasonably reconstruct the mean emf by truncating the infinite Fourier series already at $k=8$. The result of the assembly of $\overline{\boldsymbol{\mathcal{E}}}$ as formulated on the right-hand side of (18) is presented in figure 6(c) and turns out to be a faithful reproduction of $\overline{\mathcal{E}}$ from the DNS shown in figure 6(a), especially during the exponential growth phase. We conclude that the quasi-kinematic test-field method may be used for correctly calculating transport coefficients even in the presence of inhomogeneous turbulence driven by an initial mean magnetic field.

7. Conclusions

MFT still has a lot to offer in terms of new effects and quantitative precision by combining analytics with numerics in parameter regimes that were previously inaccessible. The list of examples goes on and on; here we have only mentioned some of the most striking cases. The unmentioned ones concern, for example, the Reynolds and Maxwell stresses that have important applications in accretion discs (Blackman 2010) and possibly sunspot formation (Brandenburg *et al* 2010). Also of particular interest is the transport of passive scalars, admixed chemicals for example, as was mentioned briefly in section 4.1. The test-field method has been applied successfully to such cases as well. One may anticipate that all these aspects of MFT will soon grow in significance in our voyage toward understanding astrophysical dynamos.

Acknowledgments

We are grateful for the allocation of computing resources provided by the Swedish National Allocations Committee at the Center for Parallel Computers at the Royal Institute of Technology in Stockholm and the National Supercomputer Center in Linköping as well as the Norwegian National Allocations Committee at the Bergen Center for Computational Science and the computing facilities hosted by CSC—IT Center for Science Ltd in Espoo, Finland, which are administered by the Finnish Ministry of Education. This work was supported in part by the European Research Council under the AstroDyn Research Project 227952, the Swedish Research Council (grant no. 621-2007-4064) and the Finnish Academy (grant no. 121431).

References

Blackman E G 2010 *Astron. Nachr.* **331** 101
Blackman E G and Brandenburg A 2002 *Astrophys. J.* **579** 359
Brandenburg A 1998 *Theory of Black Hole Accretion Discs* ed M A Abramowicz, G Björnsson and J E Pringle (Cambridge: Cambridge University Press) p 61
Brandenburg A 2001 *Astrophys. J.* **50** 824
Brandenburg A 2005a *Astron. Nachr.* **326** 787
Brandenburg A 2005b *Astrophys. J.* **625** 539
Brandenburg A and Campbell C G 1997 *Accretion Disks—New Aspects* ed H Spruit and E Meyer-Hofmeister (New York: Springer) p 109
Brandenburg A and Sandin C 2004 *Astron. Astrophys.* **427** 13
Brandenburg A and Schmitt D 1998 *Astron. Astrophys.* **338** L55
Brandenburg A and Subramanian K 2005 *Phys. Rep.* **417** 1
Brandenburg A, Nordlund Å, Pulkkinen P, Stein R F and Tuominen I 1990 *Astron. Astrophys.* **232** 277
Brandenburg A, Nordlund Å, Stein R F and Torkelsson U 1995 *Astrophys. J.* **446** 741
Brandenburg A, Jennings R L, Nordlund Å, Rieutord M, Stein R F and Tuominen I 1996 *J. Fluid Mech.* **306** 325
Brandenburg A, Rädler K-H and Schrinner M 2008a *Astron. Astrophys.* **482** 739
Brandenburg A, Rädler K-H, Rheinhardt M and Käpylä P J 2008b *Astrophys. J.* **676** 740
Brandenburg A, Rädler K-H, Rheinhardt M and Subramanian K 2008c *Astrophys. J.* **687** L49
Brandenburg A, Svedin A and Vasil G M 2009 *Mon. Not. R. Astron. Soc.* **395** 1599
Brandenburg A, Kleeorin N and Rogachevskii I 2010 *Astron. Nachr.* **331** 5
Brown B P, Browning M K, Brun A S, Miesch M S and Toomre J 2010 *Astrophys. J.* **711** 424
Browning M K, Miesch M S, Brun A S and Toomre J 2006 *Astrophys. J.* **648** L157
Brun A S, Miesch M S and Toomre J 2004 *Astrophys. J.* **614** 1073
Cattaneo F and Hughes D W 2006 *J. Fluid Mech.* **553** 401
Courvoisier A, Hughes D W and Proctor M R E 2010 *Proc. R. Soc.* A **466** 583
Ferrière K 1992 *Astrophys. J.* **389** 286
Field G B and Blackman E G 2002 *Astrophys. J.* **572** 685
Fromang S, Papaloizou J, Lesur G and Heinemann T 2007 *Astron. Astrophys.* **476** 1123
Galloway D J and Proctor M R E 1992 *Nature* **356** 691
Gilman P A 1983 *Astrophys. J. Suppl.* **53** 243
Gressel O 2010 *Mon. Not. R. Astron. Soc.* **405** 41
Gressel O, Ziegler U, Elstner D and Rüdiger G 2008 *Astron. Nachr.* **329** 619
Hubbard A and Brandenburg A 2009 *Astrophys. J.* **706** 712
Hughes D W and Proctor M R E 2010 *Phys. Rev. Lett.* **104** 024503
Käpylä P J, Korpi M J and Brandenburg A 2008 *Astron. Astrophys.* **491** 353
Käpylä P J, Korpi M J and Brandenburg A 2009a *Astron. Astrophys.* **500** 633
Käpylä P J, Korpi M J and Brandenburg A 2009b *Astrophys. J.* **697** 1153
Käpylä P J, Korpi M J, Brandenburg A, Mitra D and Tavakol R 2010a *Astron. Nachr.* **331** 73
Käpylä P J, Korpi M J and Brandenburg A 2010b *Mon. Not. R. Astron. Soc.* **402** 1458
Käpylä P J and Korpi M J 2010 *Mon. Not. R. Astron. Soc.* submitted
Kleeorin N I and Ruzmaikin A A 1982 *Magnetohydrodynamics* **18** 116
Köhler H 1973 *Astron. Astrophys.* **25** 467
Krause F and Rädler K-H 1980 *Mean-Field Magnetohydrodynamics and Dynamo Theory* (Oxford: Pergamon)
Krivodubskii V N 1984 *Sov. Astron.* **28** 205
Larmor J 1919 *Rep. Br. Assoc. Adv. Sci.* 159
Madarassy E J M and Brandenburg A 2010 *Phys. Rev.* E **82** 016304
Mitra D, Käpylä P J, Tavakol R and Brandenburg A 2009 *Astron. Astrophys.* **495** 1
Moffatt H K 1978 *Magnetic Field Generation in Electrically Conducting Fluids* (Cambridge: Cambridge University Press)
Otani N F 1993 *J. Fluid Mech.* **253** 327
Parker E N 1955 *Astrophys. J.* **122** 293
Parker E N 1979 *Cosmical Magnetic Fields* (Oxford: Clarendon)
Pouquet A, Frisch U and Léorat J 1976 *J. Fluid Mech.* **77** 321
Rädler K-H and Brandenburg A 2009 *Mon. Not. R. Astron. Soc.* **393** 113
Rädler K-H and Rheinhardt M 2007 *Geophys. Astrophys. Fluid Dyn.* **101** 11
Rädler K-H, Rheinhardt M, Apstein E and Fuchs H 2002 *Magnetohydrodynamics* **38** 41
Rheinhardt M and Brandenburg A 2010 *Astron. Astrophys.* **520** A28
Roberts G O 1970 *Phil. Trans. Roy. Soc.* A **266** 535
Rüdiger G and Hollerbach R 2004 *The Magnetic Universe* (Weinheim: Wiley-VCH)
Rüdiger G and Kitchatinov L L 1993 *Astron. Astrophys.* **269** 581
Schmitt D 1984 *The Hydromagnetics of the Sun* ed T D Guyenne and J J Hunt (ESA N85-25091 14-92) p 223

Schmitt D 1985 Dynamowirkung magnetostrophischer Wellen *PhD Thesis* University of Göttingen

Schrinner M, Rädler K-H, Schmitt D, Rheinhardt M and Christensen U 2005 *Astron. Nachr.* **326** 245

Schrinner M, Rädler K-H, Schmitt D, Rheinhardt M and Christensen U R 2007 *Geophys. Astrophys. Fluid Dyn.* **101** 81

Steenbeck M and Krause F 1969 *Astron. Nachr.* **291** 49

Sur S, Subramanian K and Brandenburg A 2007 *Mon. Not. R. Astron. Soc.* **376** 1238

Sur S, Brandenburg A and Subramanian K 2008 *Mon. Not. R. Astron. Soc.* **385** L15

Tobias S M, Cattaneo F and Brummell N H 2008 *Astrophys. J.* **685** 596

Vishniac E T and Cho J 2001 *Astrophys. J.* **550** 752

Ziegler U and Rüdiger G 2000 *Astron. Astrophys.* **356** 1141

VI

Mon. Not. R. Astron. Soc. **398,** 1891–1899 (2009) doi:10.1111/j.1365-2966.2009.15108.x

The α effect with imposed and dynamo-generated magnetic fields

A. Hubbard,[1]★ F. Del Sordo,[1,2] P. J. Käpylä[3] and A. Brandenburg[1,2]

[1]*NORDITA, AlbaNova University Center, Roslagstullsbacken 23, SE-10691 Stockholm, Sweden*
[2]*Department of Astronomy, Alba Nova University Center, Stockholm University, SE-10691 Stockholm, Sweden*
[3]*Observatory Tähtitorninmäki, PO Box 14, University of Helsinki, FI-00014 Helsinki, Finland*

Accepted 2009 May 12. Received 2009 May 12; in original form 2009 April 20

ABSTRACT

Estimates for the non-linear α effect in helical turbulence with an applied magnetic field are presented using two different approaches: the imposed-field method where the electromotive force owing to the applied field is used, and the test-field method where separate evolution equations are solved for a set of different test fields. Both approaches agree for stronger fields, but there are apparent discrepancies for weaker fields that can be explained by the influence of dynamo-generated magnetic fields on the scale of the domain that are referred to as meso-scale magnetic fields. Examples are discussed where these meso-scale fields can lead to both drastically overestimated and underestimated values of α compared with the kinematic case. It is demonstrated that the kinematic value can be recovered by resetting the fluctuating magnetic field to zero in regular time intervals. It is concluded that this is the preferred technique both for the imposed-field and the test-field methods.

Key words: hydrodynamics – magnetic fields – MHD – turbulence.

1 INTRODUCTION

The α effect is commonly used to describe the evolution of the large-scale magnetic field in hydromagnetic dynamos (Moffatt 1978; Parker 1979; Krause & Rädler 1980). However, the α effect is not the only known mechanism for explaining the generation of large-scale magnetic fields. Two more effects have been discussed in cases when there is shear in the system: the incoherent alpha-shear dynamo (Vishniac & Brandenburg 1997; Sokolov 1997; Silant'ev 2000; Proctor 2007) and the shear-current effect (Rogachevskii & Kleeorin 2003, 2004). In order to provide some understanding of the magnetic field generation in astrophysical bodies such as the Sun or the Galaxy, or at least in numerical simulations of these systems, it is of interest to be able to identify the underlying mechanism.

Astrophysical dynamos are usually confined to finite domains harbouring turbulent fluid motion. Both the Sun and the Galaxy are gravitationally stratified and rotating, which makes the turbulence non-mirror symmetric, thus leading to an α effect. In addition, the rotation is non-uniform, which leads to a strong amplification of the magnetic field in the toroidal direction, as well as other effects such as those mentioned above. Instead of simulating such systems with all their ingredients, it is useful to simplify the set-up by restricting oneself to Cartesian domains that can be thought to represent a part of the full domain. At low magnetic Reynolds numbers, i.e. when the effects of induction are comparable to those of magnetic diffusion, the α effect can clearly be identified in simulations of convection in Cartesian domains; see Brandenburg et al. (1990). Here, α has been determined by applying a uniform magnetic field across the simulation domain and measuring the resulting electromotive force. This method is referred to as the imposed-field method. However, in subsequent years simulations at larger magnetic Reynolds numbers have revealed problems in that the resulting α becomes smaller and strongly fluctuating in time. This was first found in simulations where the turbulence is caused by an externally imposed body force (Cattaneo & Hughes 1996; Hughes & Cattaneo 2008), but it was later also found for convection (Cattaneo & Hughes 2006). This suggested that the mean-field approach may be seriously flawed (Cattaneo & Hughes 2009).

Meanwhile, there have been a number of simulations of convection where large-scale magnetic fields are being generated. Such systems include simulations not only in spherical shells (Browning et al. 2006; Brown et al. 2007), but also in Cartesian domains (Käpylä, Korpi & Brandenburg 2008, 2009a; Hughes & Proctor 2009). However, the absence of a significant α effect in some of these simulations led Hughes & Proctor (2009) to the conclusion that such magnetic fields can only be explained by other mechanisms such as the incoherent alpha-shear dynamo or the shear-current effect. Such an explanation seems to be in conflict with earlier claims of a finite α effect as determined by the test-field method of Schrinner et al. (2005, 2007), and in particular with recent results for convection (Käpylä, Korpi & Brandenburg 2009b). The purpose of the present paper is therefore to discuss possible reasons for conflicting results that are based on different methods. The idea is to compare measurements of the α effect using both the imposed-field method and the test-field method. We consider here the case of helically forced turbulence in a triply periodic domain. This case is believed to be well understood. We expect

---

★E-mail: hubbard@pas.rochester.edu

α to be catastrophically quenched, i.e. α is suppressed for field strengths exceeding the Zeldovich (1957) value of $R_{\mathrm{m}}^{-1/2} B_{\mathrm{eq}}$, where B_{eq} is the equipartition field strength where kinetic and magnetic energy densities are comparable. The importance of the Zeldovich field strength was emphasized by Gruzinov & Diamond (1994) in connection with catastrophic quenching resulting from magnetic helicity conservation.

In this paper we focus on the case of moderate values of R_{m} of around 30. This is small by comparison with astrophysical applications, but it is large compared with the critical value for dynamo action in fully helical turbulence (Brandenburg 2001), which occurs for $R_{\mathrm{m}} \gtrsim 1$ in our definition of R_{m} based on the wavenumber of the scale of the energy carrying eddies, i.e. the forcing wavenumber. In addition, we only consider cases with a magnetic Prandtl number of unity. However, this should not worry us too much, because we know that the large-scale dynamo works independently of the value of the magnetic Prandtl number (Mininni 2007; Brandenburg 2009).

2 HELICAL TURBULENCE AND α EFFECT

2.1 Forced turbulence simulations

Throughout this paper we consider hydromagnetic turbulence in the presence of a mean magnetic field $\boldsymbol{B}_0$ using triply periodic boundary conditions. The total magnetic field is written as $\boldsymbol{B}_0 + \nabla \times \boldsymbol{A}$, where $\boldsymbol{A}$ is the magnetic vector potential. We employ an isothermal equation of state where the pressure is proportional to the density, $p = \rho c_{\mathrm{s}}^2$, with c_{s} being the isothermal sound speed. The governing evolution equations for logarithmic density $\ln \rho$, velocity $\boldsymbol{U}$, together with $\boldsymbol{A}$, are given by

$$\frac{\mathrm{d} \ln \rho}{\mathrm{d}t} = -\nabla \cdot \boldsymbol{U}, \tag{1}$$

$$\frac{\mathrm{d}\boldsymbol{U}}{\mathrm{d}t} = \boldsymbol{J} \times (\boldsymbol{B}_0 + \boldsymbol{B})/\rho + \boldsymbol{f} + \boldsymbol{F}_{\mathrm{visc}} - c_{\mathrm{s}}^2 \nabla \ln \rho, \tag{2}$$

$$\frac{\partial \boldsymbol{A}}{\partial t} = \boldsymbol{U} \times (\boldsymbol{B}_0 + \boldsymbol{B}) + \eta \nabla^2 \boldsymbol{A}, \tag{3}$$

where $\boldsymbol{B}_0 + \boldsymbol{B}$ is the total magnetic field, but since $\boldsymbol{B}_0 = \mathrm{const}$ it does not enter in the mean current density, which is given by $\boldsymbol{J} = \nabla \times \boldsymbol{B}/\mu_0$, where μ_0 is the vacuum permeability. Furthermore, $\mathrm{d}/\mathrm{d}t = \partial/\partial t + \boldsymbol{U} \cdot \nabla$ is the advective derivative, $\boldsymbol{F}_{\mathrm{visc}} = \rho^{-1} \nabla \cdot 2\rho\nu\boldsymbol{S}$ is the viscous force, ν is the kinematic viscosity, $\mathsf{S}_{ij} = (1/2)(U_{i,j} + U_{j,i}) - (1/3)\delta_{ij} \nabla \cdot \boldsymbol{U}$ is the traceless rate of strain tensor and $\boldsymbol{f}$ is a random forcing function consisting of plane transversal waves with random wavevectors $\boldsymbol{k}$ such that $|\boldsymbol{k}|$ lies in a band around a given forcing wavenumber k_{f}. The vector $\boldsymbol{k}$ changes randomly from one time-step to the next. This method is described for example in Haugen, Brandenburg & Dobler (2004). The forcing amplitude is chosen so that the Mach number $\mathrm{Ma} = u_{\mathrm{rms}}/c_{\mathrm{s}}$ is about 0.1.

We consider a domain of size $L_x \times L_y \times L_z$. We use $L_x = L_y = L_z = 2\pi/k_1$ in all cases. Our model is characterized by the choice of magnetic Reynolds and Prandtl numbers, defined here via

$$R_{\mathrm{m}} = u_{\mathrm{rms}}/\eta k_{\mathrm{f}}, \quad P_{\mathrm{m}} = \nu/\eta. \tag{4}$$

We start the simulations with zero initial magnetic field, so the field is entirely produced by the imposed field. The value of the magnetic field will be expressed in units of the equipartition value

$$B_{\mathrm{eq}} = \langle \mu_0 \rho \boldsymbol{u}^2 \rangle^{1/2}. \tag{5}$$

We consider values of B_0/B_{eq} from 0.06 to 20 along with a magnetic Reynolds number of about 26, adequate to support dynamo action.

2.2 α from the imposed-field method

The present simulations allow us to determine directly the α effect under the assumption that the relevant mean field is given by volume averages, denoted here by angular brackets. Given that the magnetic field is written as $\boldsymbol{B} = \nabla \times \boldsymbol{A}$ where $\boldsymbol{A}$ is also triply periodic, we have $\langle \boldsymbol{B} \rangle = \boldsymbol{0}$. We can determine the volume-averaged electromotive force:

$$\langle \boldsymbol{\mathcal{E}} \rangle = \langle \boldsymbol{\mathcal{E}} \rangle (t) \equiv \langle \boldsymbol{u} \times \boldsymbol{b} \rangle, \tag{6}$$

where $\boldsymbol{u} = \boldsymbol{U} - \langle \boldsymbol{U} \rangle$ and $\boldsymbol{b} = \boldsymbol{B}$ are the fluctuating components of velocity and magnetic field, and $\langle \boldsymbol{B} \rangle = \langle \nabla \times \boldsymbol{A} \rangle = \boldsymbol{0}$.

For mean fields defined as volume averages, and because of periodic boundary conditions, we have $\langle \boldsymbol{J} \rangle = \boldsymbol{0}$. Under isotropic conditions there is therefore only the α effect connecting $\langle \boldsymbol{\mathcal{E}} \rangle$ with $\boldsymbol{B}_0$ via $\langle \boldsymbol{\mathcal{E}} \rangle = \alpha_{\mathrm{imp}} \boldsymbol{B}_0$, so

$$\alpha_{\mathrm{imp}} = \langle \boldsymbol{\mathcal{E}} \rangle \cdot \boldsymbol{B}_0 / B_0^2. \tag{7}$$

In all cases reported below we assume $\boldsymbol{B_0} = (B_0, 0, 0)$. Note that $\nabla \times \langle \boldsymbol{\mathcal{E}} \rangle = \boldsymbol{0}$ and therefore our time-constant imposed field is self-consistent.

2.3 α from the test-field method

A favoured method of determining the full α_{ij} tensor is by using the test-field method (Schrinner et al. 2005, 2007), where one solves, in addition to equations (1)–(3), a set of equations. In the special case of volume averages this set of equations simplifies to

$$\frac{\partial \boldsymbol{a}^q}{\partial t} = \overline{\boldsymbol{U}} \times \boldsymbol{b}^q + \boldsymbol{u} \times (\boldsymbol{B}_0 + \overline{\boldsymbol{B}}^q) + \boldsymbol{u} \times \boldsymbol{b}^q - \overline{\boldsymbol{u} \times \boldsymbol{b}^q} + \eta \nabla^2 \boldsymbol{a}^q, \tag{8}$$

where $\boldsymbol{b}^q = \nabla \times \boldsymbol{a}^q$ with $q = 1$ or 2 denotes the response to each of the two test fields $\overline{\boldsymbol{B}}^q$. Throughout this paper, overbars denote planar averages. Later we consider arbitrary planar averages and denote their normals by superscripts, but here we restrict ourselves to xy averages. We use two different constant test fields:

$$\overline{\boldsymbol{B}}^1 = (\mathcal{B}, 0, 0), \quad \overline{\boldsymbol{B}}^2 = (0, \mathcal{B}, 0), \tag{9}$$

where $\mathcal{B} = \mathrm{const}$ is the magnitude of the test field, but its actual value is of no direct significance, because the $\mathcal{B}$ factor cancels in the calculation of α.

However, given that the test-field equations are linear in $\boldsymbol{b}^q$, this field can grow exponentially due to dynamo action. When $|\boldsymbol{b}^q|$ becomes larger than about 20 times the value of $\mathcal{B}$, the determination of α becomes increasingly inaccurate, so it is advisable to reset $\boldsymbol{b}^q$ to zero in regular intervals (Sur, Brandenburg & Subramanian 2008). We calculate the corresponding values of the electromotive force $\langle \boldsymbol{\mathcal{E}} \rangle^q = \langle \boldsymbol{u} \times \boldsymbol{b}^q \rangle$ to determine the components

$$\alpha_{iq} = \langle \mathcal{E} \rangle_i^q / \mathcal{B}. \tag{10}$$

This corresponds to the special case $k = 0$ when considering sinusoidal and cosinusoidal test functions described elsewhere (Brandenburg, Rädler & Schrinner 2008a).

Even though the test-field equations themselves are linear, the flow field is affected by the actual magnetic field (which is different from the test field), so the resulting α tensor is being affected ('quenched') by the magnetic field. This was successfully demonstrated in Brandenburg et al. (2008b), where α_{ij} takes the form

$$\alpha_{ij} = \alpha_1 \delta_{ij} + \alpha_2 \hat{B}_i \hat{B}_j. \tag{11}$$

Here $\hat{\boldsymbol{B}} = \overline{\boldsymbol{B}}/|\overline{\boldsymbol{B}}|$ is the unit vector of the relevant mean magnetic field. In the induction equation the α effect occurs only in the combination

$$\alpha_{ij}\overline{B}_j = (\alpha_1 + \alpha_2)\overline{B}_i, \tag{12}$$

and this is also what is determined by the imposed-field method, but it is different from the mean values of the components of the α_{ij} tensor. On the other hand, in the case of a passive vector field it is the mean components of α_{ij} rather than the components of $\alpha_{ij}\overline{B}_j$ that are of immediate importance (Tilgner & Brandenburg 2008).

2.4 α in the presence of meso-scale fields

The *relevant* mean field may not just be the imposed field with wavenumber $k = 0$, but it may well be a field with wavenumber $k = k_1$. Such a field would vanish under volume averaging, but it would still produce finite values of $\langle \hat{B}_i \hat{B}_j \rangle$. For the diagonal components of $\langle \alpha_{ij} \rangle$ we can write

$$\langle \alpha_{xx} \rangle = \alpha_1 + \epsilon_x \alpha_2, \quad \langle \alpha_{yy} \rangle = \alpha_1 + \epsilon_y \alpha_2, \tag{13}$$

where the factors

$$\epsilon_x = \langle \hat{B}_x^2 \rangle \quad \text{and} \quad \epsilon_y = \left\langle \hat{B}_y^2 \right\rangle \tag{14}$$

quantify the weight of the α_2 term. For a purely uniform field pointing in the x direction we have $\epsilon_x = 1$ and $\epsilon_y = 0$, while for a Beltrami field of the form $\overline{\boldsymbol{B}} = (\cos kz, \sin kz, 0)$ we have $\epsilon_x = \epsilon_y = 1/2$.

In practice we will have a mixture between the imposed field (below sometimes referred to as large-scale field) and a dynamo-generated magnetic field with typical wavenumber $k = k_1$ (below sometimes referred to as meso-scale magnetic field). The solution to the test-field equations, $\boldsymbol{b}^q$, can also develop meso-scale fields with wavevectors in the x or y directions, but not in the z direction, because that component is removed by the term $\overline{\boldsymbol{u} \times \boldsymbol{b}^q}$ in equation (8). Table 1 highlights the difference between imposed, meso-scale and test fields. We denote the ratio of the strengths of imposed and meso-scale fields as $\beta = B_0/B_1$ and distinguish three (and later four) different cases, depending on the direction of the wavevector of the Beltrami field.

The first case is referred to as the X branch, because the wavevector of the Beltrami field points in the x direction. To calculate ϵ_x there is, in addition to the imposed field B_0, a Beltrami field $B_1(0, \cos kx, \sin kx)$, which does not have a component in the x direction. Thus, $B_x = B_0$, and since $\boldsymbol{B} = (B_0, B_1 \cos kx, B_1 \sin kx)$, we have $\boldsymbol{B}^2 = B_0^2 + B_1^2$, so $\epsilon_x = \hat{B}_x^2 = B_0^2/(B_0^2 + B_1^2)$, or $\epsilon_x = \beta^2/(1 + \beta^2)$. Likewise, with $B_y = B_1 \cos kx$ we find for the volume average or, in this case, the x average $\langle B_y^2 \rangle = B_1^2/2$, so $\epsilon_y = 1/[2(1 + \beta^2)]$.

The next case is referred to as the Y branch, because the wavevector of the Beltrami field points in the y direction. Thus, we have $\boldsymbol{B} = (B_0 + B_1 \sin ky, 0, B_1 \cos ky)$, so $\boldsymbol{B}^2 = B_0^2 + 2B_0 B_1 \sin ky + B_1^2$. This is no longer independent of position, so the volume average or, in this case, the y average has to be obtained by integration. Thus, we write $\epsilon_x = I_1(\beta)$ where we have defined

$$I_1(\beta) = \int_0^{2\pi} \frac{(\beta + \sin\theta)^2}{\beta^2 + 2\beta\sin\theta + 1}\,\mathrm{d}\theta = \begin{cases} 1/2 & \beta^2 \le 1, \\ 1 - 1/2\beta^2 & \beta^2 > 1, \end{cases}$$

where $\theta = ky$ has been introduced as dummy variable. Since $B_y = 0$ in this case, we have $\epsilon_y = 0$.

Table 1. Overview of the different types of fields and their meaning.

Field	Symbol	Magn	Induct. eqn	Test-field eqn
Imposed field	$\boldsymbol{B}_0$	B_0	Yes	Yes
Meso-scale field	$\overline{\boldsymbol{B}}$	B_1	Yes	–
Test field	$\overline{\boldsymbol{B}}^q$	$\mathcal{B}$	–	Yes
Test field response	$\boldsymbol{b}^q$		–	Yes

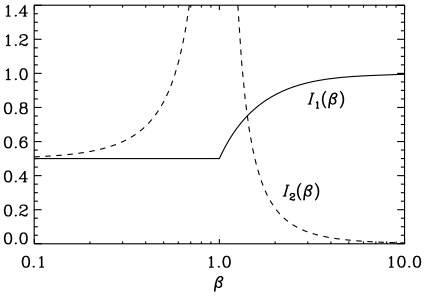

Figure 1. Plot of the integrals $I_1(\beta)$ and $I_2(\beta)$.

Finally, for the Z branch, where the wavevector of the Beltrami field points in the z direction, we have $\boldsymbol{B} = (B_0 + B_1 \cos kz, B_1 \sin kz, 0)$, we find $\epsilon_x = I_1(\beta)$ and $\epsilon_y = I_2(\beta)$ with

$$I_2(\beta) = \int_0^{2\pi} \frac{\cos^2\theta}{\beta^2 + 2\beta\cos\theta + 1}\,\frac{\mathrm{d}\theta}{2\pi} = \begin{cases} I_0(\beta) & \beta^2 < 1, \\ I_0(\beta)/\beta^2 & \beta^2 > 1, \end{cases}$$

where $I_0(\beta) = (1 + \beta^2)/[2(1 - \beta^2)]$ and $\theta = kz$ has been used as a dummy variable. A graphical representation of the integrals is given in Fig. 1 and a summary of the expressions for $\epsilon_x(\beta)$ and $\epsilon_y(\beta)$ as well as $\epsilon_x(0)$ and $\epsilon_y(0)$ for the X, Y and Z branches is given in Table 2. The singularity in $I_0(\beta)$ could potentially affect α_{yy}. However, the results shown below show that, at least for stronger fields, α_2 goes to zero near the singularity of $I_0(\beta)$ such that α_{yy} remains finite.

3 RESULTS

We have performed simulations for values of B_0 in the range $0.06 \le R_\mathrm{m}^{1/2} B_0/B_\mathrm{eq} \le 20$ for $R_\mathrm{m} \approx 26$ and $P_\mathrm{m} = 1$. In all cases we use $k_\mathrm{f}/k_1 = 3$, which is big enough to allow a meso-scale magnetic field of wavenumber k_1 to develop within the domain; see Fig. 2. We did not initially anticipate the importance of the meso-scale fields. Different runs were found to exhibit rather different behaviour which turned out to be related to their random positioning on different branches. We used the existing results from different branches as initial conditions for neighbouring values of B_0.

In this paper, error bars are estimated from the averages obtained from any of three equally long subsections of the full time series.

Table 2. Summary of the expressions for $\epsilon_x(\beta)$ and $\epsilon_y(\beta)$ as well as $\epsilon_x(0)$ and $\epsilon_y(0)$ for the X, Y and Z branches.

Branch	$\epsilon_x(\beta)$	$\epsilon_y(\beta)$	$\epsilon_x(0)$	$\epsilon_y(0)$
X	$\beta^2/(1 + \beta^2)$	$1/[2(1 + \beta^2)]$	0	1/2
Y	$I_1(\beta)$	0	1/2	0
Z	$I_1(\beta)$	$I_2(\beta)$	1/2	1/2

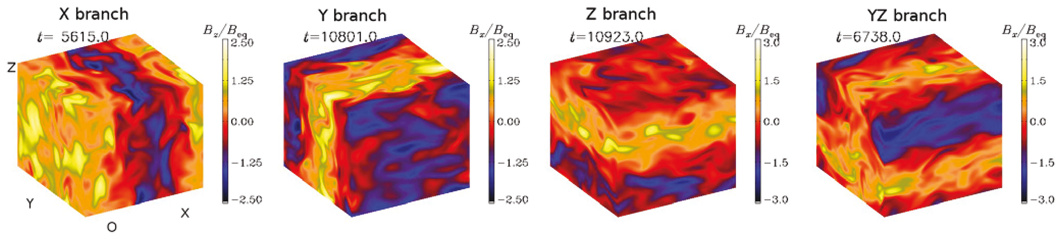

Figure 2. Visualization of B_z on the periphery of the computational domain for the X branch and B_x for the Y, Z and YZ branches. The coordinate directions are indicated on the first panel.

The error bars are comparable with the typical scatter of the data points, but they are not shown because they would make the figure harder to read. Note that the results in this section consider saturated fields. The opposite case will be considered in Section 4.

3.1 Different branches

The resulting values of α are shown in Fig. 3. For strong imposed magnetic fields, $R_{\rm m}\boldsymbol{B}_0^2/B_{\rm eq}^2 > 1$, the resulting dependence of α on B_0 obeys the standard catastrophic quenching formula for the case of a uniform magnetic field (Vainshtein & Cattaneo 1992):

$$\alpha_{\rm fit} = \frac{\alpha_0}{1+\tilde{R}_{\rm m}\overline{\boldsymbol{B}}^2/B_{\rm eq}^2} \quad (\text{for } \overline{\boldsymbol{B}} = \boldsymbol{B}_0 = \text{const only}), \tag{15}$$

where $\alpha_0 = -(1/3)\,u_{\rm rms}$ is the relevant kinematic reference value for fully helical turbulence with negative helicity and $R_{\rm m} > 1$ (Sur et al. 2008). We treat $\tilde{R}_{\rm m}$ as an empirical fit parameter that is proportional to $R_{\rm m}$ and find that $\tilde{R}_{\rm m}/R_{\rm m} \approx 0.4$ gives a reasonably good fit; see the dash–dotted line in Fig. 3. The existence of such an empirical factor might be related to fact that the relevant quantity could be the width of the magnetic inertial range, and that this is not precisely equal to $R_{\rm m}$. For $R_{\rm m}\boldsymbol{B}_0^2/B_{\rm eq}^2 > 1$, a similar result is also reproduced using the test-field method, although α_{xx} is typically somewhat larger than $\alpha_{\rm imp}$.

For weak imposed magnetic fields, $R_{\rm m}\boldsymbol{B}_0^2/B_{\rm eq}^2 < 1$, apparent discrepancies are found between the imposed-field method and the test-field method. In fact, in the graphical representation in Fig. 3 the results can be subdivided into four different branches that we refer to as branches X, Y, Z and YZ. These names have to do with the orientation of a dynamo-generated magnetic field. These dynamo-generated magnetic fields take the form of Beltrami fields that vary in the x, y and z directions for branches X, Y and Z, while for branch YZ the field varies both in the y and z directions. Earlier work without imposed fields has shown that branch YZ can be accessed during intermediate times during the saturation of the dynamo, but it is not one of the ultimate stable branches X, Y or Z.

Branches Y and Z show the sudden onset of suppression of $\alpha_{\rm imp}$ for *weak* magnetic fields. This has to do with the fact that for weak imposed magnetic fields a dynamo-generated field of Beltrami type is being generated. Such fields quench the α effect, even though they do not contribute to the volume-averaged mean field. On branch YZ the α effect is only weakly suppressed, while on branch X the imposed field $\alpha_{\rm imp}$ increases with decreasing values of B_0.

The test-field method reveals that on branches X, Y and YZ the α_{yy} component is nearly independent of B_0, and always larger than the α_{xx} component. However, on branch Z and for $R_{\rm m}\boldsymbol{B}_0^2/B_{\rm eq}^2 < 1$ we find that $\alpha_{xx} = \alpha_{yy}$ and only weakly suppressed.

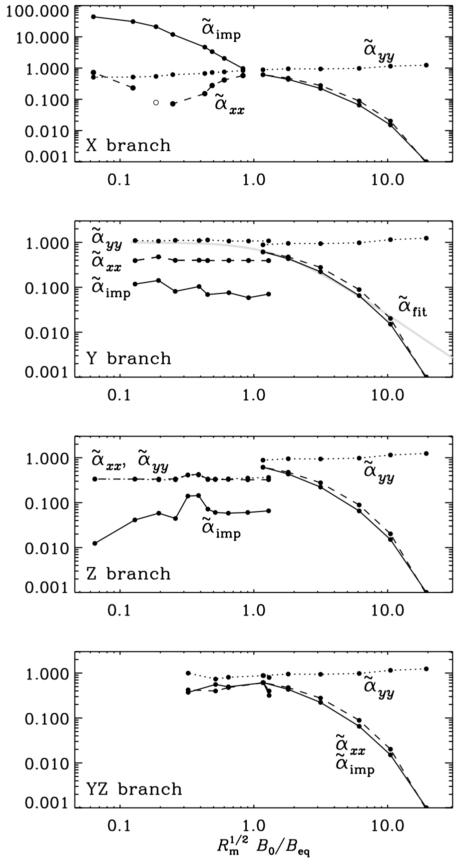

Figure 3. Volume-averaged values of $\alpha_{\rm imp}$, α_{xx} and α_{yy}. A tilde indicates that the values are normalized by α_0, i.e. $\tilde{\alpha}_{\rm imp} = \alpha_{\rm imp}/\alpha_0$ (solid line), $\tilde{\alpha}_{xx} = \langle\alpha_{xx}\rangle/\alpha_0$ (dashed line), $\tilde{\alpha}_{yy} = \langle\alpha_{yy}\rangle/\alpha_0$ (dotted line) and $\tilde{\alpha}_{\rm fit} = \alpha_{\rm fit}/\alpha_0$ (thick grey line, but only shown in the second panel). The two open symbols in the top panel indicate that the values of α_{xx}/α_0 are negative.

A comment regarding the discontinuities in Fig. 3 near $R_{\rm m}\boldsymbol{B}_0^2/B_{\rm eq}^2 = 1$ is here in order. The systems considered here are in saturated states. To the left of the discontinuities the system has a saturated meso-scale dynamo, while to the right there is none.

Intermediate states are simply not possible. Hence, the discontinuities are caused by the effects of the meso-scale magnetic fields on $u_{\rm rms}$ and thus on $R_{\rm m}$.

3.2 Relation to α_1 and α_2

In the following we will try to interpret the results presented above in terms of equation (11) and determine α_1 and α_2 for the different branches. For small values of B_0, a magnetic field with $k = k_1$ and hence a finite planar average can develop. Compared with the large-scale field B_0, we refer to this dynamo-generated field as meso-scale magnetic field. As demonstrated in Brandenburg (2001), three types of such mean fields are possible in the final saturated state. These fields correspond to Beltrami fields of the form

$$\frac{\overline{\boldsymbol{B}}^{(x)}}{B_1} = \begin{pmatrix} 0 \\ c_x \\ s_x \end{pmatrix}, \quad \frac{\overline{\boldsymbol{B}}^{(y)}}{B_1} = \begin{pmatrix} s_y \\ 0 \\ c_y \end{pmatrix}, \quad \frac{\overline{\boldsymbol{B}}^{(z)}}{B_1} = \begin{pmatrix} c_z \\ s_z \\ 0 \end{pmatrix}, \tag{16}$$

where $c_\xi = \cos(k_1\xi + \phi)$ and $s_\xi = \sin(k_1\xi + \phi)$ denote cosine and sine functions as functions of $\xi = x$, y or z, with an arbitrary phase shift ϕ.[1] The precise value of B_1 emerges as a result of the simulation, but based on simulations in a periodic domain (Brandenburg 2001) we know that $B_1/B_{\rm eq}$ should be about $(k_{\rm f}/k_1)^{1/2}$ times the equipartition value. This is also confirmed by the present calculations.

Let us now discuss separately the different branches. As can be seen from Fig. 4, the weak-field regime is characterized by the presence of meso-scale magnetic fields that vary either in the x direction (the X branch), the y direction (Y branch), the z direction (Z branch) or in both the y and z directions (YZ branch).

In order to get some idea about the values α_1 and α_2 on the various branches, we consider two limiting cases. For strong imposed fields, $\beta \to \infty$, the results lie formally on the YZ branch, because such a field has only very little variation in the x direction. However, $\langle \hat{B}_i \hat{B}_j \rangle$ will be dominated only by the uniform field in the x direction, so we have $\epsilon_x = 1$ and $\epsilon_y = 0$; see Section 2.3. This means that $\tilde{\alpha}_{\rm imp} = \tilde{\alpha}_{xx} = \tilde{\alpha}_1 + \tilde{\alpha}_2$ and $\tilde{\alpha}_{yy} = \tilde{\alpha}_1$, so we can calculate

$$\tilde{\alpha}_1 = \tilde{\alpha}_{yy}, \quad \tilde{\alpha}_2 = \tilde{\alpha}_{\rm imp} - \tilde{\alpha}_{yy}, \tag{17}$$

where a tilde indicates normalization by α_0. For weak imposed fields, $\beta \to 0$, we can calculate $\tilde{\alpha}_1$ and $\tilde{\alpha}_2$ on the X branch by using the relations

$$\tilde{\alpha}_{xx} = \tilde{\alpha}_1, \tag{18}$$

$$\tilde{\alpha}_{yy} = \tilde{\alpha}_1 + \frac{1}{2}\tilde{\alpha}_2, \tag{19}$$

$$\tilde{\alpha}_{\rm imp} = \tilde{\alpha}_1 + \tilde{\alpha}_2. \tag{20}$$

However, on the X branch $\tilde{\alpha}_{xx}$ is ill determined, as seen in Fig. 3 and discussed in Section 4.1. Therefore, we use only equations (19) and (20) to calculate

$$\tilde{\alpha}_1 = 2\tilde{\alpha}_{yy} - \tilde{\alpha}_{\rm imp}, \quad \tilde{\alpha}_2 = 2\tilde{\alpha}_{\rm imp} - 2\tilde{\alpha}_{yy}. \tag{21}$$

For the Y, Z and YZ branches, on the other hand, these relations have to be substituted by

$$\tilde{\alpha}_1 = 2\tilde{\alpha}_{xx} - \tilde{\alpha}_{\rm imp}, \quad \tilde{\alpha}_2 = 2\tilde{\alpha}_{\rm imp} - 2\tilde{\alpha}_{xx}. \tag{22}$$

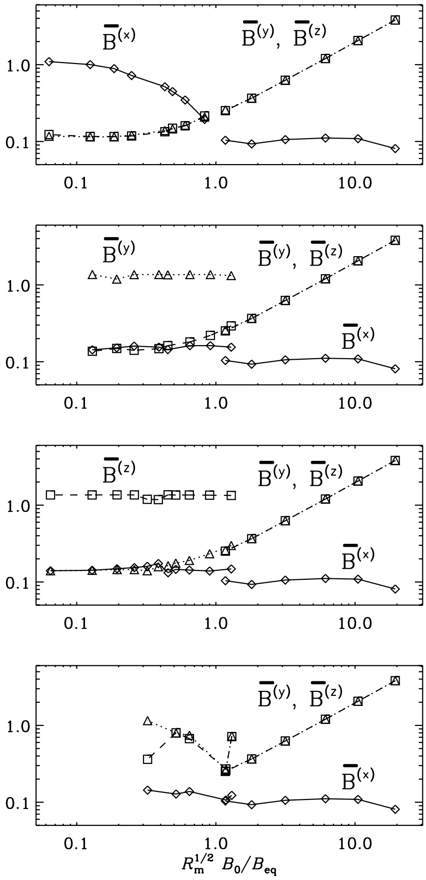

Figure 4. Root-mean-square values of the mean magnetic fields as functions of the imposed field for turbulence with $R_{\rm m} = 26$ for the X, Y, Z and YZ branches in the same order as in Fig. 3. Diamonds, triangles and squares denote $\overline{\boldsymbol{B}}^{(x)}$, $\overline{\boldsymbol{B}}^{(y)}$ and $\overline{\boldsymbol{B}}^{(z)}$, respectively.

The resulting values of $\tilde{\alpha}_1$ and $\tilde{\alpha}_2$ are plotted in Fig. 5 for each of the four branches. On the Y branch one can, as a test, also use the independent relation $\tilde{\alpha}_1 = \tilde{\alpha}_{yy}$. The resulting values are about 50 per cent larger than the values shown in Fig. 5, suggesting that there could be additional contributions in the simplified relation $\tilde{\alpha}_{yy} = \tilde{\alpha}_1$. On the Z branch, of course, $\tilde{\alpha}_{xx} = \tilde{\alpha}_{yy}$, so here too we have to use the equations (22).

In all cases we find that $\tilde{\alpha}$ is quenched by $\tilde{\alpha}_1$ and $\tilde{\alpha}_2$ having opposite signs and their moduli approaching each other. This is particularly clear in the case of strong fields where $\tilde{\alpha}_1$ and $-\tilde{\alpha}_2$ become indistinguishable, while each of them is still increasing. We note that the turbulence itself is not strongly affected (Brandenburg & Subramanian 2005a). On the Y and Z branches both $\tilde{\alpha}_1$ and $\tilde{\alpha}_2$ are of order unity, but on the X branch they can reach rather large values when the imposed field is weak. The behaviour on the YZ branch is somewhat unsystematic, suggesting that this branch is really just the result of a long-term transient, as was already found in the absence of an imposed field (Brandenburg 2001). However, we decided not

---

[1] Unlike the case considered by Brandenburg et al. (2008b), here the test field has $k = 0$, and there is no relative phase to be considered.

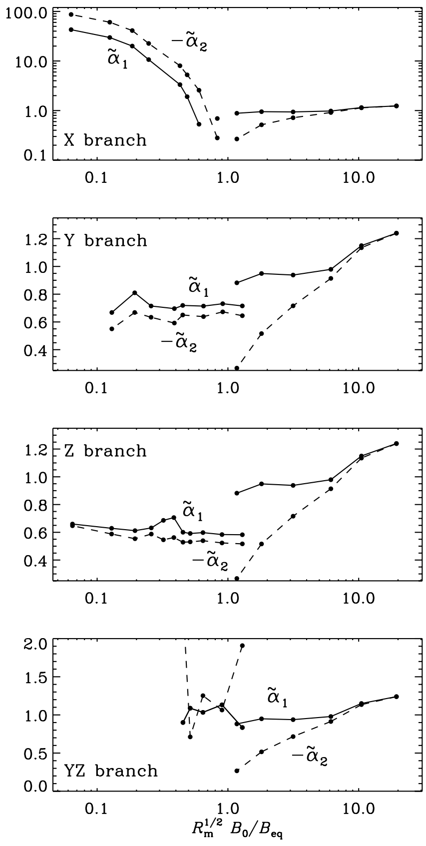

Figure 5. Dependence of α_1 and α_2 on B_0 for the X, Y, Z and YZ branches in the same order as in Fig. 3.

to discard this branch, because it is likely that transient solutions on this branch may become even more long-lived as the magnetic Reynolds number is increased further.

3.3 Enhancement of α_imp in the field-aligned case

The suppression of $\alpha = \alpha_1 + \alpha_2$ by the magnetic field is not surprising. What is unexpected, however, is the dramatic enhancement of both α_1 and $-\alpha_2$ for weak imposed fields and equipartition-strength meso-scale fields that vary in the x direction (the field-aligned case or X branch). In this case the interactions of the current density associated with the Beltrami field and the imposed field generate a force varying along x, perpendicular to the components of the meso-scale Beltrami field. This generates a meso-scale velocity that in turn damps the Beltrami field, resulting in the slower rise in $\overline{\boldsymbol{B}}^{(x)}$ as B_0/B_eq is decreased. Further, the cross-product of the meso-scale velocity field with the Beltrami field generates a large-scale electromotive force in the x direction. This is seen both in α_imp and in α_{xx}. A rough estimate of this electromotive force can be obtained by considering the fields

$$\boldsymbol{B}_0 = \begin{pmatrix} B_0 \\ 0 \\ 0 \end{pmatrix}, \quad \boldsymbol{B}_1 = B_1 \begin{pmatrix} 0 \\ \cos kx \\ \sin kx \end{pmatrix}, \tag{23}$$

so that $\mu_0 \boldsymbol{J}_1 = -k\boldsymbol{B}_1$, where subscript 1 denotes meso-scale fields. The meso-scale current density and the imposed field will generate a meso-scale Lorentz force which will drive a meso-scale velocity field $\boldsymbol{U}_1$. We estimate $\boldsymbol{U}_1$ by balancing

$$\boldsymbol{J}_1 \times \boldsymbol{B}_0/\rho + \nu_\mathrm{t}\nabla^2 \boldsymbol{U}_1 \approx 0, \tag{24}$$

where ν_t is the turbulent viscosity. We therefore expect that $\boldsymbol{U}_1$ will saturate for

$$\boldsymbol{U}_1 = \frac{B_0 B_1/\rho\mu_0}{\nu_\mathrm{t} k} \begin{pmatrix} 0 \\ \sin kx \\ -\cos kx \end{pmatrix}. \tag{25}$$

This velocity field will generate an $\boldsymbol{\mathcal{E}}_0$ parallel to $\boldsymbol{B}_0$ in conjunction with $\boldsymbol{B}_1$:

$$\boldsymbol{\mathcal{E}}_0 \equiv \langle \boldsymbol{U}_1 \times \boldsymbol{B}_1 \rangle = \alpha_\mathrm{meso} \boldsymbol{B}_0, \tag{26}$$

with $\alpha_\mathrm{meso} = B_1^2/(\rho\mu_0\nu_\mathrm{t}k)$. We then expect the total α_imp to be

$$\alpha_\mathrm{imp} = \alpha + \frac{B_1^2/\rho\mu_0}{\nu_\mathrm{t}k}. \tag{27}$$

Normalizing by $\alpha_0 = -u_\mathrm{rms}/3$ and assuming $\nu_\mathrm{t} \approx u_\mathrm{rms}/3k_\mathrm{f}$ we find for small imposed field and a meso-scale dynamo that varies along x:

$$\frac{\alpha_\mathrm{imp}}{\alpha_0} \approx 1 + 9\,\frac{k_\mathrm{f}}{k_1}\left(\frac{B_1}{B_\mathrm{eq}}\right)^2. \tag{28}$$

Given that $k_\mathrm{f}/k_1 = 3$ and noting that B_1/B_eq reaches values up to 1.2, we find that $\alpha_\mathrm{imp}/\alpha_0 \approx 40$, which is still somewhat below the actual value of 53; see the top panel of Fig. 3. The remaining discrepancy may be explicable by recalling that the actual value of ν_t may well be reduced due to the presence of an equipartition-strength magnetic field.

3.4 Comment on wavenumber dependence

In previous work on the test-field method we used test fields with wavenumbers different from zero. It turned out that in the kinematic regime, α is proportional to $1/[1 + a(k/k_\mathrm{f})^2]$, where $a = 0.5, \ldots, 1$ (Brandenburg et al. 2008a; Mitra et al. 2009). It was shown that the variation of α with k represents non-locality in space. In order to get some idea about the dependence of α_{xx} and α_{yy} on k in the present case we compare in Table 3 the results for $k = k_0$ with those for $k = 0$. It turns out that both values decrease by 30 per cent on the X branch, and increase by less than 10 per cent on the Z branch.

Table 3. Examples of the dependence of $\tilde{\alpha}_{xx}$ and $\tilde{\alpha}_{yy}$ on the wavenumber k of the test field. Note that the field strength is different in both cases.

Branch	k/k_0	$\tilde{\alpha}_{xx}$	$\tilde{\alpha}_{yy}$	$R_\mathrm{m}^{1/2} B_0/B_\mathrm{eq}$
X	0	0.72 ± 0.14	0.51 ± 0.16	0.06
	1	0.61 ± 0.02	0.37 ± 0.01	0.06
Z	0	0.34 ± 0.02	0.32 ± 0.02	0.2
	1	0.35 ± 0.01	0.35 ± 0.02	0.2

The k dependence for the Z branch is minor, although one would have expected a small decrease rather than an increase. Nevertheless, within error bars, this result is possibly still compatible with the dependence in the kinematic case. For the X branch the error bars for $k = 0$ are larger. This is because of the strong interaction between the imposed uniform field and a Beltrami field varying along the same direction, as discussed in Section 3.3. It is therefore not clear whether the k dependence is here significant and how to interpret it.

4 RESETTING THE FLUCTUATIONS

4.1 Effectiveness of resetting the fields

The evolution equations used both in the imposed-field method and in the test-field method allow for dynamo action. This led Ossendrijver et al. (2002) and Käpylä et al. (2006) to the technique of resetting the resulting magnetic field in regular intervals. This method is now also routinely used in the test-field approach (Sur et al. 2008), and we have also used it throughout this work. The lack of resetting the magnetic field may also be the main reason for the rather low values of α found in the recent work of Hughes & Proctor (2009); see the corresponding discussion in Käpylä et al. (2009b).

In this section we employ the method of resetting $\boldsymbol{B}$ to obtain better estimates for α for weak imposed fields, and to compare this with results from the test-field method. The result is shown in Fig. 6 where we show the dependence of $\alpha_{\rm imp}$ on B_0 and on the reset interval Δt. We note that, in units of the turnover time, the reset interval $\Delta t u_{\rm rms} k_{\rm f}$ has a weak dependence both on B_0 and Δt, because small values of B_0 and Δt quench $u_{\rm rms}$ only weakly. The resetting technique has eliminated the branching for weak fields. For weak fields we find that the value of $\alpha_{\rm imp}$ is slightly below α_0, but this is partly because for finite scale separation there is an additional factor $(1 + k_{\rm f}^2/k_1^2)^{-1} \approx 0.9$ (Brandenburg et al. 2008a). The actual value of $\alpha_{\rm imp}$ is somewhat smaller still, which may be ascribed to other systematic effects.

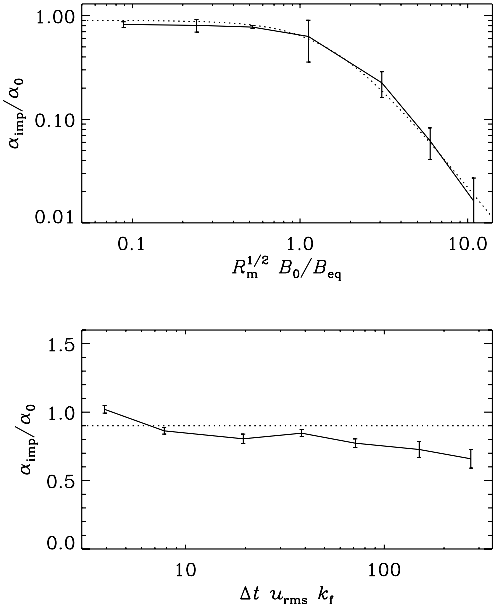

Figure 6. Dependence of $\alpha_{\rm imp}$ (solid lines) and $\alpha_{\rm fit}$ (dotted lines) on the imposed field strength with fixed reset time $\Delta t u_{\rm rms} k_{\rm f} = 50, \dots, 70$ (upper panel) and the dependence of $\alpha_{\rm imp}$ on the reset time for $R_{\rm m}^{1/2} B_0/B_{\rm eq} = 0.1$ (lower panel). In all cases we have $R_{\rm m} \approx 30$.

Table 4. Comparison of the results for $\tilde{\alpha}_{xx}$ and $\tilde{\alpha}_{yy}$ for two different reset times Δt for the examples of the X and Z branches with $R_{\rm m}^{1/2} B_0/B_{\rm eq} = 0.2$. The reset time is normalized by the inverse turnover time $(u_{\rm rms} k_{\rm f})^{-1}$.

Branch	$\Delta t u_{\rm rms} k_{\rm f}$	$\tilde{\alpha}_{xx}$	$\tilde{\alpha}_{yy}$
X	25	-0.08 ± 0.13	0.54 ± 0.02
	50	-0.98 ± 0.09	0.70 ± 0.04
Z	25	0.34 ± 0.02	0.32 ± 0.02
	50	0.32 ± 0.01	0.33 ± 0.03

It turns out that over a wide range of reset intervals the resulting values of $\alpha_{\rm imp}$ are not dependent in a systematic way on the reset interval (see also Mitra et al. 2009), although it is clear that the error bars increase for larger values of Δt. The same is true for the values of α_{xx} and α_{yy} obtained using the test-field method, except for the case of weak fields on the X branch where the values of α_{xx} are ill determined; see Table 4, where we compare the values of α_{xx} and α_{yy} for two different reset times in the case where α_{xx} is found to change sign ($R_{\rm m}^{1/2}\boldsymbol{B}_0/B_{\rm eq} \approx 0.2$). The increasing fluctuations for longer reset intervals occur as the system exits the kinematic regime. It might therefore be possible to find indicators of when the kinematic regime has been exited and resetting becomes necessary. However, we have not pursued this further in this work.

For even larger values of Δt there is enough time for the mesoscale magnetic field to develop. An example is shown in Fig. 7 where 18 intervals of length $\Delta t u_{\rm rms} k_{\rm f} = 270$ are shown. For half of these intervals the wavevector of the Beltrami field begins to develop in the x direction, so $\alpha_{\rm imp}$ is heading toward the X branch. In the other half of these cases the magnetic field is weak and $\alpha_{\rm imp}$ lies on one of the other branches. None of these cases reproduce the correct kinematic value of α, because we are not really considering a kinematic problem in this case. This underlines the importance of choosing reset intervals that are not too long.

Our results support the hypothesis that the precise value of the reset time interval is not critical except for the field-aligned case

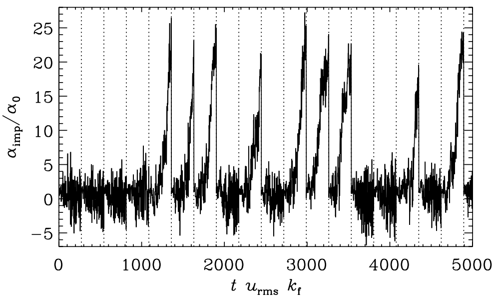

Figure 7. Time series of $\alpha_{\rm imp}$ for $\Delta t u_{\rm rms} k_{\rm f} = 270$ with $R_{\rm m}^{1/2} B_0/B_{\rm eq} = 0.1$. The reset intervals are indicated by dotted vertical lines. In all cases we have $R_{\rm m} \approx 30$.

where the diagonal components of the α_{ij} tensor are large and quite uncertain, as indicated also by the large error bars. The sign change found for α_{xx} at low or intermediate field strengths might therefore not be real.

4.2 Time averaging in the test-field method

We have already demonstrated that the length of the reset interval is not critical for the value of α, but longer reset times tend to lead to larger errors. In the present section we demonstrate this for the test-field method using the idealized case where the turbulent flow velocity is replaced by simple stationary flow given by the equation

$$\boldsymbol{U} = k_\mathrm{f}\varphi\hat{\boldsymbol{z}} + \nabla \times (\varphi\hat{\boldsymbol{z}}), \tag{29}$$

with

$$\varphi = \varphi(x, y) = u_0 \cos k_0 x \cos k_0 y, \tag{30}$$

which is known as the Roberts flow.

When the magnetic Reynolds number exceeds a certain critical value of around 60, some kind of dynamo action of $\boldsymbol{b}^q$ commences. This type of dynamo is often referred to as small-scale dynamo action (Brandenburg et al. 2008b; Sur et al. 2008; Cattaneo & Hughes 2009), but this name may not always be accurate. In the case of the Roberts flow there would be no such dynamo action if the wavenumber of the test field is zero, $k = 0$, as assumed here. However, for $k = k_0$, for example, dynamo action for the test-field equation is possible. The test fields are therefore chosen to be

$$\frac{\overline{\boldsymbol{B}}^1}{\mathcal{B}} = \begin{pmatrix} \cos kz \\ 0 \\ 0 \end{pmatrix}, \quad \frac{\overline{\boldsymbol{B}}^2}{\mathcal{B}} = \begin{pmatrix} \sin kz \\ 0 \\ 0 \end{pmatrix}, \tag{31}$$

$$\frac{\overline{\boldsymbol{B}}^3}{\mathcal{B}} = \begin{pmatrix} 0 \\ \cos kz \\ 0 \end{pmatrix}, \quad \frac{\overline{\boldsymbol{B}}^4}{\mathcal{B}} = \begin{pmatrix} 0 \\ \sin kz \\ 0 \end{pmatrix}, \tag{32}$$

see Sur et al. (2008). Since now the mean fields are also functions of z, the term $\boldsymbol{u} \times \boldsymbol{b}^q$ cannot be omitted in equation (8).

As stressed by Brandenburg et al. (2008a), in the expression for the electromotive force there is in general also a contribution $\overline{\boldsymbol{\mathcal{E}}}_0$ that is independent of the mean field. Given that test fields $\overline{\boldsymbol{B}}^q$ are independent of time, we have

$$\overline{\boldsymbol{\mathcal{E}}}^q(z, t) = \overline{\boldsymbol{\mathcal{E}}}_0^q(z, t) + \alpha(z)\overline{\boldsymbol{B}}^q(z) - \eta_\mathrm{t}(z)\mu_0\overline{\boldsymbol{J}}^q(z), \tag{33}$$

where overbars denote xy averages (not volume averages), so there is also a term $\eta_\mathrm{t}\mu_0\overline{\boldsymbol{J}}^q$, where η_t is the turbulent magnetic diffusivity. We have assumed that α and η_t are independent of time, and in this case they are also independent of z. The $\overline{\boldsymbol{\mathcal{E}}}_0^q(z, t)$ term can be eliminated by averaging over time, i.e. $\langle\overline{\boldsymbol{\mathcal{E}}}_0^q\rangle = \boldsymbol{0}$, so

$$\langle\overline{\boldsymbol{\mathcal{E}}}^q\rangle = \alpha\overline{\boldsymbol{B}}^q - \eta_\mathrm{t}\mu_0\overline{\boldsymbol{J}}^q. \tag{34}$$

In Fig. 8 we show the evolution of α for the Roberts flow with $R_\mathrm{m} = 65$ and 55. In the case with $R_\mathrm{m} = 65$ there are exponentially growing oscillations corresponding to a wave travelling in the z direction. In general such fields can be a superposition of waves travelling in the positive and negative z directions. It is seen quite clearly that the running time average is stable and well defined. The results for $R_\mathrm{m} = 65$ and 55 are close together ($\alpha/\alpha_0 = 0.096$ and 0.090, respectively), suggesting continuity across the point where dynamo action sets in. This supports the notion that averaging over time is a meaningful procedure.

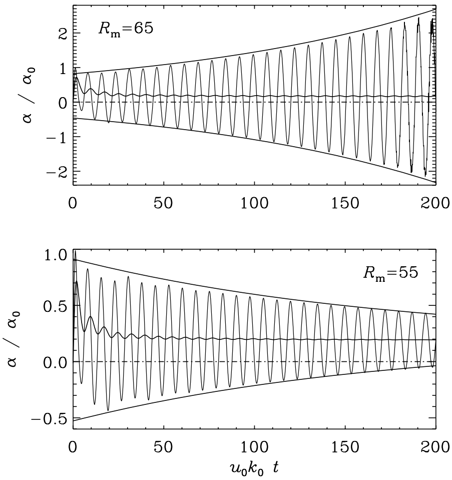

Figure 8. Plot of the instantaneous α for $R_\mathrm{m} = 65$ (upper panel) and $R_\mathrm{m} = 55$ (lower panel). In both cases running means are overplotted and converge to nearly the same value of about −0.096 in the upper panel and −0.090 in the lower one. The envelope functions are well described by exponentials and are also overplotted. Note, however, the different scales on the ordinate of both panels. The dash–dotted line shows the zero level.

5 CONCLUSIONS

The present simulations have shown that the imposed-field method leads to a number of interesting and unexpected results. For imposed fields exceeding the value $R_\mathrm{m}^{-1/2}B_\mathrm{eq}$ one recovers the catastrophic quenching formula of Vainshtein & Cattaneo (1992); see equation (15). We emphasize once more, however, that this formula is only valid for completely uniform large-scale fields in a triply periodic domain. This is clearly artificial, but it provides an important benchmark.

A number of surprising results have been found for weaker fields of less than $R_\mathrm{m}^{-1/2}B_\mathrm{eq}$. In virtually none of those cases does the imposed-field method recover the kinematic value of α. Instead, α_imp can attain strongly suppressed values, but it can actually also attain strongly enhanced values. This is caused by the unavoidable emergence of meso-scale dynamo action. In principle, such meso-scale dynamo action could have been suppressed by restricting oneself to scale-separation ratios, k_f/k_1, of less than 2 or so. This was done, for example, in some of the runs of Brandenburg & Subramanian (2005a). In the present case of a triply periodic box, four different magnetic field configurations can emerge. The first three correspond to Beltrami fields, where the wavevector points in one of the three coordinate directions. The fourth possibility is also a Beltrami field, but one that varies diagonally in a direction perpendicular to the direction of the imposed field. The latter was found to be unstable in the absence of an imposed field, but they can be long-lived in the present case of an imposed field.

In this paper, we have used the term meso-scale fields to refer to the Beltrami fields naturally generated by the helicity-driven dynamo in our system. A more general definition of meso-scale fields would encompass all fields that break isotropy, average to zero, and yet do not time-average to zero. In the absence of such fields, mean-field theory can be applied in a straightforward manner. This is indeed the case that one is normally interested in. However, when such meso-scale fields exist, they must be understood for determining turbulent transport coefficients, because those coefficients apply then to the particular case of saturated meso-scale fields.

The results obtained with the imposed-field method reflect correctly the circumstances in the non-linear case where the α effect is suppressed by dynamo-generated meso-scale magnetic fields whose scale is smaller than that of the imposed field, but comparable to the scale of the domain. Especially in the case of closed or periodic domains the resulting α is catastrophically quenched, which is now well understood (Blackman & Brandenburg 2002; Field & Blackman 2002). This effect is particularly strong in the case where one considers volume averages, and thus ignores the effects of turbulent magnetic diffusion. With magnetic diffusion included, both α and $\eta_{\rm t}$ have only a mild dependence on $R_{\rm m}$ (Brandenburg et al. 2008b). However, astrophysical dynamos are expected to operate in a regime where magnetic helicity fluxes alleviate catastrophic quenching; see Brandenburg & Subramanian (2005b) for a review.

Determining the nature of the dynamo mechanism is an important part in the analysis of a successful simulation showing large-scale field generation. Our present analysis shows that meaningful results for α can be obtained using either the imposed-field or the test-field methods provided the departure of the magnetic field from $\boldsymbol{B}_0$ is reset to zero to eliminate the effects of dynamo-generated meso-scale magnetic fields. Conversely, if such fields are not eliminated, the results can still be meaningful, as demonstrated here, but they need to be interpreted correspondingly and bear little relation to the imposed field. On the other hand, for strong imposed magnetic fields ($R_{\rm m}\boldsymbol{B}_0^2/B_{\rm eq}^2 > 1$), meso-scale magnetic fields tend not to grow, so the resetting procedure is then neither necessary nor would it make much of a difference when the test-field method is used. However, when the imposed-field method is used, the resetting of the actual field reduces the quenching of $u_{\rm rms}$. This affects the normalizations of B_0 and α_{ij} with $B_{\rm eq}$ and α_0, respectively, because both are proportional to $u_{\rm rms}$.[2]

Throughout this paper we have considered relatively moderate values of $R_{\rm m}$, but we computed a large number of different simulations. In the beginning of this study we started with larger values of $R_{\rm m}$ and found that the resulting $\alpha_{\rm imp}$ seemed inconsistent. In hindsight it is clear what happened: the few cases that we had in the beginning were all scattered around different branches. Only later, by performing a large number of simulations at smaller values of $R_{\rm m}$ it became clear that there are indeed different branches. This highlights the importance of studying not just one or a few models of large $R_{\rm m}$, but rather a larger systematic set of intermediate cases of moderate $R_{\rm m}$ where it is possible to understand in detail what is going on. It will be important to continue exploring the regime of larger $R_{\rm m}$, and we hope that the new understanding that emerged from studying cases of moderate $R_{\rm m}$ proves useful in this connection. According to the results available so far, we can say that for larger values of $R_{\rm m}$ the turbulent transport coefficients are only weakly affected (see Brandenburg et al. 2008b, for $R_{\rm m} \le 600$) for fields of equipartition strength, or not affected at all (Sur et al. 2008, for $R_{\rm m} \le 220$) if the field is in the kinematic limit.

ACKNOWLEDGMENTS

We thank the referee for making a number of constructive remarks on the paper. We acknowledge the use of computing time at the Center for Parallel Computers at the Royal Institute of Technology in Sweden and CSC – IT Center for Science in Espoo, Finland. This work was supported in part by the European Research Council under the AstroDyn Research Project 227952 (FDS), the Academy of Finland grant 121431 (PJK) and the Swedish Research Council grant 621-2007-4064 (AB).

REFERENCES

Blackman E. G., Brandenburg A., 2002, ApJ, 579, 359

Brandenburg A., 2001, ApJ, 550, 824

Brandenburg A., 2009, ApJ, 697, 1206

Brandenburg A., Subramanian K., 2005a, A&A, 439, 835

Brandenburg A., Subramanian K., 2005b, Phys. Rep., 417, 1

Brandenburg A., Nordlund A., Pulkkinen P., Stein R. F., Tuominen I., 1990, A&A, 232, 277

Brandenburg A., Rädler K.-H., Schrinner M., 2008a, A&A, 482, 739

Brandenburg A., Rädler K.-H., Rheinhardt M., Subramanian K., 2008b, ApJ, 687, L49

Brown B. P., Browning M. K., Brun A. S., Miesch M. S., Nelson N. J., Toomre J., 2007, in Stancliffe R. J., Houdek G., Martin R. G., Tout C. A., eds, AIP Conf. Proc. 948. Unsolved Problems in Stellar Physics. Am. Inst. Phys., New York, p. 271

Browning M. K., Miesch M. S., Brun A. S., Toomre J., 2006, ApJ, 648, L157

Cattaneo F., Hughes D. W., 1996, Phys. Rev. E, 54, R4532

Cattaneo F., Hughes D. W., 2006, J. Fluid Mech., 553, 401

Cattaneo F., Hughes D. W., 2009, MNRAS, 395, L48

Field G. B., Blackman E. G., 2002, ApJ, 572, 685

Gruzinov A. V., Diamond P. H., 1994, Phys. Rev. Lett., 72, 1651

Haugen N. E. L., Brandenburg A., Dobler W., 2004, Phys. Rev. E, 70, 016308

Hughes D. W., Cattaneo F., 2008, J. Fluid Mech., 594, 445

Hughes D. W., Proctor M. R. E., 2009, Phys. Rev. Lett., 102, 044501

Käpylä P. J., Korpi M. J., Ossendrijver M., Stix M., 2006, A&A, 455, 401

Käpylä P. J., Korpi M. J., Brandenburg A., 2008, A&A, 491, 353

Käpylä P. J., Korpi M. J., Brandenburg A., 2009a, ApJ, 697, 1153

Käpylä P. J., Korpi M. J., Brandenburg A., 2009b, A&A, 500, 633

Krause F., Rädler K.-H., 1980, Mean-Field Magnetohydrodynamics and Dynamo Theory. Pergamon Press, Oxford

Mininni P. D., 2007, Phys. Rev. E, 76, 026316

Mitra D., Käpylä P. J., Tavakol R., Brandenburg A., 2009, A&A, 495, 1

Moffatt H. K., 1978, Magnetic Field Generation in Electrically Conducting Fluids. Cambridge Univ. Press, Cambridge

Ossendrijver M., Stix M., Brandenburg A., Rüdiger G., 2002, A&A, 394, 735

Parker E. N., 1979, Cosmical Magnetic Fields. Clarendon Press, Oxford

Proctor M. R. E., 2007, MNRAS, 382, L39

Rogachevskii I., Kleeorin N., 2003, Phys. Rev. E, 68, 036301

Rogachevskii I., Kleeorin N., 2004, Phys. Rev. E, 70, 046310

Schrinner M., Rädler K.-H., Schmitt D., Rheinhardt M., Christensen U., 2005, Astron. Nachr., 326, 245

Schrinner M., Rädler K.-H., Schmitt D., Rheinhardt M., Christensen U., 2007, Geophys. Astrophys. Fluid Dyn., 101, 81

Silant'ev N. A., 2000, A&A, 364, 339

Sokolov D. D., 1997, Astron. Rep., 41, 68

Sur S., Brandenburg A., Subramanian K., 2008, MNRAS, 385, L15

Tilgner A., Brandenburg A., 2008, MNRAS, 391, 1477

Vainshtein S. I., Cattaneo F., 1992, ApJ, 393, 165

Vishniac E. T., Brandenburg A., 1997, ApJ, 475, 263

Zeldovich Ya. B., 1957, Sov. Phys. JETP, 4, 460

---

[2] This explains why $\Delta t u_{\rm rms} k_{\rm f}$ is 70 in Fig. 6 and 50 in Table 4 under otherwise comparable conditions, except that here only the test field is reset and not the actual fluctuating one.

This paper has been typeset from a TEX/LATEX file prepared by the author.

VII

Turbulent dynamos with advective magnetic helicity flux

F. Del Sordo[1,2]* and G. Guerrero[3,1] and A. Brandenburg[1,2]
[1] *Nordita, KTH Royal Institute of Technology and Stockholm University, Roslagstullsbacken 23, SE 10691 Stockholm Sweden*
[2] *Department of Astronomy, AlbaNova University Center, Stockholm University, SE 10691 Stockholm, Sweden*
[3] *Solar Physics, HEPL, Stanford University, Stanford, CA, 94305-4085, USA*

10 October 2012

ABSTRACT

Many astrophysical bodies harbor magnetic fields that are thought to be sustained by a dynamo process. However, it has been argued that the production of large-scale magnetic fields by mean-field dynamo action is strongly suppressed at large magnetic Reynolds numbers owing to the conservation of magnetic helicity. This phenomenon is known as *catastrophic quenching.* Advection of magnetic fields by stellar and galactic winds toward the outer boundaries and away from the dynamo is expected to alleviate such quenching. Here we explore the relative roles played by advective and turbulent–diffusive fluxes of magnetic helicity in the dynamo. In particular, we study how the dynamo is affected by advection. We do this by performing direct numerical simulations of a turbulent dynamo of α^2 type driven by forced turbulence in a Cartesian domain in the presence of a flow toward the upper and lower borders of the domain. Our results indicate that in the presence of advection the dynamo, otherwise stationary, becomes oscillatory. We confirm an earlier result for turbulent–diffusive magnetic helicity fluxes that for small magnetic Reynolds numbers ($\mathrm{Rm} \lesssim 200$, based on the wavenumber of the energy-carrying eddies) the magnetic helicity flux scales less strongly with magnetic Reynolds number ($\mathrm{Rm}^{-1/2}$) than the term describing magnetic helicity destruction by resistivity (Rm^{-1}). Our new results now suggest that for $\mathrm{Rm} \gtrsim 200$ there are different scalings. We show for the first time that the advective magnetic helicity flux term becomes comparable to the resistive term for $\mathrm{Rm} \gtrsim 1000$, which is necessary for alleviating catastrophic quenching.

Key words: magnetic fields — MHD — hydrodynamics – turbulence

1 INTRODUCTION

A theoretical framework for explaining the large-scale magnetic fields observed in many astrophysical bodies is mean-field dynamo theory. Its basic idea is that the inductive effects of turbulent motions are able to amplify a weak magnetic field and maintain it on timescales longer than the magnetic diffusion time (Moffatt 1978). Gradients in the large-scale velocity field, like shear motions, can also contribute significantly to the amplification of the magnetic field. In mean-field dynamo theory the contribution of the turbulent scales is parameterized through the electromotive force which depends on the large-scale magnetic field as well as its derivatives (Krause & Rädler 1980). The coefficients in front of the magnetic field and its derivatives are called turbulent transport coefficients. They can be either turbulent–diffusive (with turbulent diffusion $\propto \eta_t$) or non-diffusive (e.g., the α effect or turbulent pumping).

Under some approximations (e.g., in the low conductivity limit for small magnetic Reynolds number, $\mathrm{Rm} \leqslant 1$, or in the high conductivity limit for small Strouhal number, $\mathrm{St} \leqslant 1$), theories like the first order smoothing approximation are able to predict the functional form of the expressions and the correct values of the coefficients. Within their limits of validity, these results present a remarkably good agreement with the computation of the transport coefficients through direct numerical simulations (DNS); see, e.g., Sur et al. (2008). However, not enough is known about the functional form of these coefficients at large values of Rm (i.e., small values of the microphysical magnetic diffusivity) and about the saturation process when the magnetic field becomes dynamically important. Understanding the behavior of the dynamo in these regimes has remained an important problem for several decades. Although many recent works have contributed to understanding dynamo saturation at large magnetic Reynolds numbers, more work is still necessary to have a complete picture of the dynamo excitation and saturation mechanisms.

Among the turbulent transport coefficients the α effect

---

* E-mail: fabio@nordita.org (FDS)

is particularly important, because it allows a closed dynamo loop for regenerated both poloidal and toroidal magnetic fields. It has been suspected, however, that in closed or triply periodic domains the α effect can be strongly suppressed at higher magnetic Reynolds numbers and might scale like $\alpha \propto \mathrm{Rm}^{-1}$ (Vainshtein & Cattaneo 1992; Cattaneo & Hughes 1996). An explanation for this was proposed by Gruzinov & Diamond (1994), who used the α effect derived by Pouquet et al. (1976), which has, in addition to the kinetic helicity density, a contribution proportional to the current helicity density. It is this quantity which builds up as the dynamo saturates.

This is a consequence of magnetic helicity conservation and can be explained as follows: the large-scale magnetic field generated by the α effect is helical, but in order to satisfy the conservation of total magnetic helicity, a small-scale field with magnetic helicity of opposite sign, but equal magnitude, must be generated in the system. The small-scale magnetic helicity is responsible for the creation of a magnetic α effect ($\alpha_{\rm M}$) which contributes with opposite sign to the kinetic α. This basic idea led Kleeorin & Ruzmaikin (1982) to propose the dynamical quenching model at a time well before simulations saw any indications of catastrophic quenching. Even nowadays the issue is quite unclear when it comes to making predictions about the high-Rm regime. The final amplitude that the magnetic α effect acquires depends on the geometry of the system and on the value of the magnetic Reynolds number. For highly turbulent astrophysical objects (high Rm) like the Sun or the Galaxy, $\alpha_{\rm M}$ could get higher amplitudes decreasing the dynamo efficiency. However the dynamics of $\alpha_{\rm M}$ also depends on the ability of the system to get rid of the small-scale magnetic helicity responsible for its creation. In a closed or triply periodic domain, magnetic helicity annihilation depends critically on the microscopic magnetic diffusivity. This is a very slow process given the scales and diffusivity values under consideration. However, an obvious solution to this catastrophic (Rm-dependent) quenching is to allow the system to get rid of helical small-scale magnetic fields.

In real astrophysical systems, this processes is generally expected to happen in a number of different ways. Among the various mechanisms for removing magnetic helicity from the system we focus here on the role played by the turbulent–diffusive magnetic helicity flux and by the presence of advective flows or winds. The role of these magnetic helicity fluxes has been tested in the context of mean-field dynamo models through a dynamical equation for the magnetic α-effect (Kleeorin et al. 2000; Brandenburg & Subramanian 2005; Sur et al. 2007; Brandenburg et al. 2009; Guerrero et al. 2010; Chatterjee et al. 2011). These models have demonstrated the importance of magnetic helicity fluxes in solving the catastrophic quenching problem.

Verifying the validity of these results in DNS is more complicated since obtaining higher Rm in the numerical models requires high resolution and large computational resources. Various attempts have, however, succeeded in verifying the role of magnetic helicity conservation in the saturation of the dynamo. For instance, Brandenburg (2001) studied the saturation in triply periodic helically forced dynamos of α^2 type. The role of open magnetic boundary conditions for convective dynamos has been studied in Käpylä et al. (2008, 2009, 2010). Mitra et al. (2010a) (hereafter MCCTB) have verified the existence of turbulent–diffusive magnetic helicity fluxes in α^2 dynamo models in the presence of an equator and Hubbard & Brandenburg (2010) (hereafter HB) did the same for a dynamo region embedded inside a highly conducting halo which provided a more realistic boundary condition. In both cases it was found that a fit to a Fickian diffusion law can account for this flux and that the diffusivity value is comparable to or below the value of the turbulent magnetic diffusivity $\eta_{\rm t}$. The resulting Fickian diffusion coefficient was found to be approximately independent of Rm. By considering a statistically steady state, and noting that the local value of the magnetic helicity density was also statistically steady, their result became then also independent of the gauge chosen to define the magnetic vector potential.

In addition, shear flows have been argued to be effective in alleviating catastrophic quenching (Vishniac & Cho 2001) and allowing significant saturation levels of the dynamo (Käpylä et al. 2008), although it appears now plausible that their result could also be explained through a change in the excitation conditions of the dynamo. Indeed, recent DNS have failed to demonstrate the presence of the Vishniac-Cho flux (Hubbard & Brandenburg 2011). Yet another possibility are advective magnetic helicity fluxes. In the context of the galactic dynamo, alleviation of catastrophic quenching thanks to a wind has been studied in mean-field models by Shukurov et al. (2006) and Sur et al. (2007). Mitra et al. (2011) studied the role of a wind in solar mean-field dynamo models. The models studied in the present paper allow us to compare with their results and to determine the importance of magnetic helicity fluxes in the dynamical evolution of the magnetic α-effect. To our understanding the study of advective fluxes in DNS of a dynamo is an outstanding problem. With this paper we intend to close this gap.

We perform DNS leading to α^2-type dynamo action in a domain with kinetic helicity of opposite signs on both sides of the equator. We use a relaxation term to include a large-scale flow that advects the large-scale magnetic field. Furthermore, we consider periodic boundary conditions in the horizontal directions, zero-gradient conditions for the velocity and vertical field conditions for the magnetic field. In this way we allow for the removal of magnetic helicity through advection. For the sake of simplicity and to study these effects separately in a clear way, we do not include here large-scale shear. Nevertheless the results presented here should also be applicable in the context of the galactic dynamo and, in principle, also to the solar dynamo, where large-scale winds have been shown in mean-field models to play a role in carrying magnetic helicity outside its bounds (Mitra et al. 2011).

This paper is organized as follows. In Sect. 2 we describe the physical model considered here and present the equations governing its evolution. In Sect. 3 we present the results of the simulations. First we describe the properties of the solutions without the wind. Next, we explore the effects that the wind has on the characteristics of the dynamo solution. Finally we determine the magnetic helicity fluxes present in the model and verify their balance with the production terms to prevent the quenching of what corresponds to the α effect in the corresponding mean-field description. We conclude and summarize the results in Sect. 4.

2 THE MODEL

2.1 Governing equations

We use the Pencil Code [1] to solve the following set of compressible hydromagnetic equations in an isothermal layer:

$$\frac{\partial \boldsymbol{A}}{\partial t} = \boldsymbol{U} \times \boldsymbol{B} - \mu_0 \eta \boldsymbol{J}, \tag{1}$$

$$\frac{\mathrm{D} \ln \rho}{\mathrm{D}t} = -\boldsymbol{\nabla} \cdot \boldsymbol{U} + q_\rho, \tag{2}$$

$$\frac{\mathrm{D}\boldsymbol{U}}{\mathrm{D}t} = -c_\mathrm{s}^2 \boldsymbol{\nabla} \ln \rho + \frac{1}{\rho} \boldsymbol{J} \times \boldsymbol{B} + \frac{1}{\rho} \boldsymbol{\nabla} \cdot 2\nu\rho \mathsf{S} + \boldsymbol{f}_\mathrm{w} + \boldsymbol{f}, \tag{3}$$

where $\mathrm{D}/\mathrm{D}t = \partial/\partial t + \boldsymbol{U} \cdot \boldsymbol{\nabla}$ is the advective derivative, $\boldsymbol{A}$ is the magnetic vector potential, $\boldsymbol{B} = \boldsymbol{\nabla} \times \boldsymbol{A}$ is the magnetic field, $\boldsymbol{J} = \boldsymbol{\nabla} \times \boldsymbol{B}/\mu_0$ is the current density, μ_0 is the magnetic permeability, η and ν are magnetic diffusivity and kinematic viscosity, respectively, $c_\mathrm{s} =$ const is the sound speed, $\boldsymbol{U}$ is the velocity, ρ is the density, S is the rate of strain tensor given by

$$\mathsf{S}_{ij} = \tfrac{1}{2}(U_{i,j} + U_{j,i}) - \tfrac{1}{3}\delta_{ij} \boldsymbol{\nabla} \cdot \boldsymbol{U}, \tag{4}$$

where the commas denote derivatives, $\boldsymbol{f}_\mathrm{w}$ provides a forcing for the wind [see Eq. (8) in 2.2], q_ρ is a source term in Eq. (2) needed to replenish the resulting mass loss, $\boldsymbol{f}$ is a time-dependent random δ-correlated forcing function of the form

$$\boldsymbol{f} = \boldsymbol{f}(\boldsymbol{x}, t; \sigma(z)), \tag{5}$$

where σ is related to its local helicity density,

$$\langle \boldsymbol{f} \cdot \boldsymbol{\nabla} \times \boldsymbol{f} \rangle / \langle k_\mathrm{f} \boldsymbol{f}^2 \rangle = 2\sigma/(1+\sigma^2), \tag{6}$$

and is chosen to vary like $\sigma(z) = \sin(2\pi z/L_z)$ with a sign change across the equator at $z = 0$. This forcing drives turbulence in a band of wavenumbers around k_f^{-1}. The modulation $\sigma(z)$ of this forcing is similar to that used by Warnecke et al. (2011) to simulate a sign change of helicity in forced turbulence in a spherical wedge.

We consider a computational domain of size $L_x \times L_y \times L_z$, with quadratic horizontal extent, $L_x = L_y$, using periodic boundary conditions and a vertical extent that is twice as big, $L_z = 2L_x$, with $|z| \leqslant L_z/2$ (i.e., $-L_z/2 \leqslant z \leqslant L_z/2$) and an equator at $z = 0$. Our boundary conditions are

$$U_{x,z} = U_{y,z} = U_z - \overline{U}_\mathrm{w} = A_{x,z} = A_{y,z} = A_z = 0 \tag{7}$$

on the top and bottom boundaries at $z = \pm L_z/2 \equiv \pm z_\mathrm{top}$. $\overline{U}_\mathrm{w}$ is the wind profile, defined in Eq. (9). The lowest horizontal wavenumber in the domain is $k_1 = 2\pi/L_x$. In the following, we use k_1 as our inverse length unit, so $|k_1 z| \leqslant 2\pi$. To eliminate boundary effects, we restrict most of the analysis to a diagnostic layer, $|z| \leqslant L_*$ with $k_1 L_* = 3$. For all our runs we choose $k_\mathrm{f}/k_1 = 4$, which is a compromise between it being large enough to allow a large-scale magnetic field to be generated and yet small enough to achieve sufficiently large values of Rm.

We set c_s to unity in the code, so our dimensionless time is in units of the sound travel time, $(c_\mathrm{s} k_1)^{-1}$. However, the relevant physics is not governed by compressibility effects, so it is more natural to quote time in turnover times, i.e., we quote instead the value of $t u_\mathrm{rms} k_\mathrm{f}$. In most of the cases reported below, the turbulent Mach number, $\mathrm{Ma} = \mathrm{u_{rms}/c_s}$, is around 0.1.

2.2 Generating the wind

The advective term, or wind, in our model is given by the forcing function in Eq. (8),

$$\boldsymbol{f}_\mathrm{w} = -\frac{1}{\tau_\mathrm{w}} \left[\overline{\boldsymbol{U}} - \overline{\boldsymbol{U}}_\mathrm{w}(z) \right], \tag{8}$$

where $\overline{\boldsymbol{U}}$ is the horizontally averaged velocity field, and

$$\overline{\boldsymbol{U}}_\mathrm{w}(z) = U_0 \frac{\boldsymbol{z}}{z_\mathrm{top}} \tag{9}$$

is the wind profile that increases linearly toward the z boundaries. The wind profile can be modified by the turbulence and the magnetic field, but the original outflow profile is restored on a timescale τ_w. The presence of a wind leads to mass loss across the vertical boundaries with mass loss rate that depends on U_0.

Stellar winds are the main agents of mass loss in stars. In a galactic environment it is possible to observe galactic winds as well as galactic fountains. These mechanisms can be driven by the explosions of supernovae in the galactic disc. In this case a direct estimate of the mass loss rate is more complicated, given also that it is expected to be very small. However, to have stationary conditions, we keep the mass in the domain constant using the source term q_ρ in Eq. (2). This source term restores the density at each spatial point of the domain to its initial value ρ_0 on a timescale $\tau_\mathrm{s} = \tau_\mathrm{w}$. Thus, analogously to Eq. (8) we write $q_\rho = -\tau_s^{-1}(\ln \overline{\rho} - \ln \overline{\rho}_0)$.

We study the dependence of the model on the dimensionless wind speed and the magnetic Reynolds number of the turbulence,

$$S_W = \frac{\boldsymbol{\nabla} \cdot \overline{U}_\mathrm{w}}{u_\mathrm{rms} k_\mathrm{f}}, \quad \mathrm{Rm} = \frac{u_\mathrm{rms}}{\eta k_\mathrm{f}}. \tag{10}$$

In all cases, we use a magnetic Prandtl number of unity, i.e., $\nu/\eta = 1$.

2.3 Magnetic helicity fluxes

In our model we expect two different kinds of magnetic helicity fluxes: those caused by the wind, i.e. *advective* magnetic helicity fluxes, and those due to turbulence in the presence of a mean gradient of the magnetic helicity density, i.e. *turbulent–diffusive* magnetic helicity fluxes. To assess their relative importance, we now consider the magnetic helicity equation in the Weyl gauge which is used in Eq. (1), i.e.,

$$\frac{\partial}{\partial t} \overline{\boldsymbol{A} \cdot \boldsymbol{B}} = -2\eta\mu_0 \overline{\boldsymbol{J} \cdot \boldsymbol{B}} - \boldsymbol{\nabla} \cdot \overline{\boldsymbol{\mathcal{F}}}, \tag{11}$$

where overbars denote averages over x and y and $\overline{\boldsymbol{\mathcal{F}}} = \overline{\boldsymbol{E} \times \boldsymbol{A}}$ is the total magnetic helicity flux, with $\boldsymbol{E} = \eta\mu_0 \boldsymbol{J} - \boldsymbol{U} \times \boldsymbol{B}$ being the electric field. This equation is evidently gauge-dependent; see for instance Candelaresi et al. (2011). In particular, since $\overline{\boldsymbol{A} \cdot \boldsymbol{B}}$ is not a physical quantity, it could drift – even in the steady state; see Fig. 2 of Brandenburg et al. (2002) for an example. However, if $\overline{\boldsymbol{A} \cdot \boldsymbol{B}}$ is constant in a particular gauge, then we have

$$\boldsymbol{\nabla} \cdot \overline{\boldsymbol{\mathcal{F}}} = -2\eta\mu_0 \overline{\boldsymbol{J} \cdot \boldsymbol{B}}, \tag{12}$$

---

[1] `http://pencil-code.googlecode.com/`

where now $\boldsymbol{\nabla}\cdot\overline{\boldsymbol{\mathcal{F}}}$ must be gauge-independent, because $\boldsymbol{J}$ and $\boldsymbol{B}$ are gauge-invariant. This argument was invoked by MCCTB and HB to determine turbulent–diffusive contributions to the magnetic helicity flux.

In the present work, we are interested in two contributions to $\overline{h} = \overline{\boldsymbol{A}\cdot\boldsymbol{B}}$, one from the mean fields, $\overline{h}_{\rm m} = \overline{\boldsymbol{A}}\cdot\overline{\boldsymbol{B}}$, and one from the fluctuating fields, $\overline{h}_{\rm f} = \overline{\boldsymbol{a}\cdot\boldsymbol{b}}$. Their sum gives the total mean magnetic helicity density, i.e., $\overline{h} = \overline{h}_{\rm m} + \overline{h}_{\rm f}$. Note, however, that only $\overline{h}_{\rm f}$ is the component directly relevant for the study of catastrophic quenching, because it is approximately proportional to the current helicity density, $\overline{\boldsymbol{j}\cdot\boldsymbol{b}}$, which in turn determines the magnetic contribution to the α effect. [The approximate proportionality of magnetic and current helicities is non-trivial and will need to be re-assessed below; see also Fig. 3 of MCCTB and Table 2 of HB for earlier examples.]

The evolution equation for $\overline{h}_{\rm f}$ is

$$\frac{\partial \overline{h}_{\rm f}}{\partial t} = -2\overline{\boldsymbol{\mathcal{E}}}\cdot\overline{\boldsymbol{B}} - 2\eta\mu_0\,\overline{\boldsymbol{j}\cdot\boldsymbol{b}} - \boldsymbol{\nabla}\cdot\overline{\boldsymbol{\mathcal{F}}}_{\rm f}, \tag{13}$$

where, as mentioned above, we allow two contributions to the flux of magnetic helicity from the fluctuating field $\overline{\boldsymbol{\mathcal{F}}}_{\rm f}$: an advective flux due to the wind, $\overline{\boldsymbol{\mathcal{F}}}_{\rm f}^{\rm\,w} = \overline{h}_{\rm f}\overline{\boldsymbol{U}}_{\rm w}$, and a turbulent–diffusive flux due to turbulence, modelled here by a Fickian diffusion term down the gradient of $\overline{h}_{\rm f}$, i.e., $\overline{\boldsymbol{\mathcal{F}}}_{\rm f}^{\rm\,diff} = -\kappa_h\boldsymbol{\nabla}\overline{h}_{\rm f}$. Here, $\overline{\boldsymbol{\mathcal{E}}} = \overline{\boldsymbol{u}\times\boldsymbol{b}}$ is the electromotive force of the fluctuating field.

In the steady state, and if $\overline{h}_{\rm f}$ is then also constant (which is not guaranteed to be the case because $\overline{h}_{\rm f}$ is *a priori* gauge-dependent), we have

$$\boldsymbol{\nabla}\cdot\overline{\boldsymbol{\mathcal{F}}}_{\rm f} = -2\overline{\boldsymbol{\mathcal{E}}}\cdot\overline{\boldsymbol{B}} - 2\eta\mu_0\,\overline{\boldsymbol{j}\cdot\boldsymbol{b}}. \tag{14}$$

Again, although $\boldsymbol{\nabla}\cdot\overline{\boldsymbol{\mathcal{F}}}_{\rm f}$ is in principle gauge-dependent, it can now be determined by measuring $\overline{\boldsymbol{\mathcal{E}}}\cdot\overline{\boldsymbol{B}}$ and $\overline{\boldsymbol{j}\cdot\boldsymbol{b}}$, that are manifestly gauge-independent quantities. This means that $\boldsymbol{\nabla}\cdot\overline{\boldsymbol{\mathcal{F}}}_{\rm f}$ must be gauge-independent as well. We assume that $\overline{\boldsymbol{\mathcal{F}}}_{\rm f}$ has a component only in the vertical direction, we can obtain its z dependence through integration via

$$\overline{\mathcal{F}}_{\rm fz} = \int_0^z \boldsymbol{\nabla}\cdot\overline{\boldsymbol{\mathcal{F}}}_{\rm f}\,{\rm d}z'. \tag{15}$$

The assumption of only a z component of $\overline{\boldsymbol{\mathcal{F}}}_{\rm f}$ would break down in the presence of shear, where cross-stream fluxes with finite divergence are possible; see Hubbard & Brandenburg (2011).

For discussion of our results presented below, let us contrast our present simulations with those of MCCTB. In their case, the outer boundary condition at $z = \pm L_z/2$ was a perfect conductor (P.C.) one and the most easily excited mode was antisymmetric about the midplane with dynamo waves propagating toward the equator. This antisymmetry results in permitting a flux of magnetic helicity through the equatorial plane and in this sense has the same effect as the vertical field (V.F.) boundary condition. This, together with the fact that the magnetic helicity density is antisymmetric about the equator, is the reason why in their case the turbulent–diffusive flux can play a measurable role. However, because $\overline{\mathcal{F}}_{{\rm f}z}$ has vanishing vertical derivative at the equator, $\boldsymbol{\nabla}\cdot\overline{\boldsymbol{\mathcal{F}}}_{\rm f} = 0$ at the equator. This is different in the model of HB, in which the helicity is arranged to be symmetric about the midplane, which is therefore not an equator in the usual sense. Here the field is symmetric about the midplane, corresponding thus to a P.C. condition, and thus $\boldsymbol{\nabla}\cdot\overline{\boldsymbol{\mathcal{F}}}_{\rm f} \neq 0$. The boundary conditions and their properties are summarized in Table 1 for MCCTB and HB and compared with those used in the present work.

Table 1. Comparison of boundary conditions and other properties of the simulations of MCCTB and the present work.

	MCCTB	HB	present work
boundary	P.C. $\overline{\mathcal{F}}_{{\rm f}z} = 0$ $\boldsymbol{\nabla}\cdot\overline{\boldsymbol{\mathcal{F}}}_{\rm f} \neq 0$	halo $\overline{\mathcal{F}}_{{\rm f}z} \neq 0$ $\boldsymbol{\nabla}\cdot\overline{\boldsymbol{\mathcal{F}}}_{\rm f} = 0$	V.F. $\overline{\mathcal{F}}_{{\rm f}z} \neq 0$ $\boldsymbol{\nabla}\cdot\overline{\boldsymbol{\mathcal{F}}}_{\rm f} = 0$
equator/ midplane	antisymmetry (like V.F.) $\overline{\mathcal{F}}_{{\rm f}z} \neq 0$ $\boldsymbol{\nabla}\cdot\overline{\boldsymbol{\mathcal{F}}}_{\rm f} = 0$	symmetry (like P.C.) $\overline{\mathcal{F}}_{{\rm f}z} = 0$ $\boldsymbol{\nabla}\cdot\overline{\boldsymbol{\mathcal{F}}}_{\rm f} \neq 0$	symmetry (like P.C.) $\overline{\mathcal{F}}_{{\rm f}z} = 0$ $\boldsymbol{\nabla}\cdot\overline{\boldsymbol{\mathcal{F}}}_{\rm f} = 0$

Unlike MCCTB, in the present work the V.F. condition is applied on the outer boundaries, in which case the most easily excited mode is symmetric about the equator with dynamo waves travelling away from the midplane. This is similar to a P.C. condition at the midplane, for which the magnetic helicity flux vanishes. However, because $\overline{h}_{\rm f}$ is antisymmetric about the equator, it must have a turning point there, so its second derivative vanishes so that $\boldsymbol{\nabla}\cdot\overline{\boldsymbol{\mathcal{F}}}_{\rm f} = 0$.

3 RESULTS

3.1 Model without advective flux

We begin by describing the results for a dynamo in the absence of an advective flux ($S_W = 0$). The solution for this particular setup is a steady magnetic field mainly concentrated around the equator of the domain, where the magnetic helicity changes its sign. In Figure 1 we show the B_y and B_z components of the magnetic field in the saturated phase of a model without wind and ${\rm Rm} = 206$ (later referred to as Model N3). Note that $B_x = B_y = 0$ on the top and bottom boundaries, owing to the use of vertical-field boundary conditions. Both of them, as well as B_z, do not show any significant temporal change once $b_{\rm rms}$ has reached its saturation value. This can be observed in the top panel of Figure 2, where the vertical distribution of $\overline{B}_y$ is depicted as a function of time.

3.2 Model with advective flux

Let us now turn to models in which a wind is included ($S_W \neq 0$). An example of the resulting wind profile as well as the vertical distribution of $u_{\rm rms}$ is shown in Figure 3. Even with just a weak wind the dynamo becomes oscillatory; see Figure 2. Note that the cycle period decreases as the wind speed is increased. We observe oscillatory solutions of even parity, that is $\overline{B}_x$ and $\overline{B}_y$ are symmetric with respect to the midplane $z = 0$, with dynamo waves migrating away from $z = 0$. This is expected based on mean-field models in similar setups (Brandenburg et al. 2009) provided the outer boundary condition is a vacuum or vertical field condition, as is the case here.

In Figure 4 we can see how the actual $B_y(x, y, z, t)$,

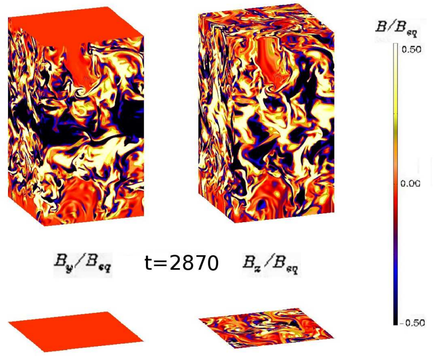

Figure 1. Visualization of B_y (left) and B_z (right) on the borders of the domain for model N3 in the saturated phase of the simulation (t is time in turnover times).

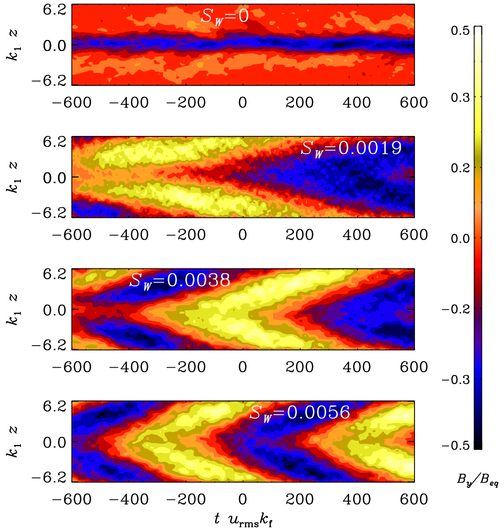

Figure 2. Space-time diagrams of $\overline{B}_y$ for different wind intensities S_W corresponding to Models N3, W3, M2, and S2 from top to bottom. The time axes have been shifted such that for each run about 1200 turnover times are being displayed. Note that the cycle period decreases with increasing wind speed.

as opposed to its horizontal average $\overline{\boldsymbol{B}}_y(z,t)$, evolves during half a period in the saturated phase of the simulations, changing gradually from negative to positive polarity. In Table 2 we summarize important output parameters that characterize the simulations and, in particular, details regarding the magnetic helicity balance. Note that all table entries are non-dimensionalized by normalizing with relevant quantities such as $B_{\rm eq}$; see the table caption for details. Magnetic helicity and the various production terms are antisymmetric

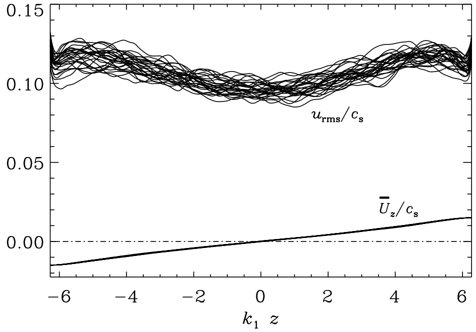

Figure 3. Resulting vertical profile of $\overline{U}_z$ together with the rms velocity as a function of height. Different lines correspond to different times. In this case $U_0 = 0.015c_{\rm s}$, corresponding to $S_W = 0.0055$.

about the midplane. Within the range $|z| \leqslant L_*$, all these quantities vary approximately linearly with z. Therefore we characterize their values by their slope. An appropriate normalization is therefore $k_1\eta_{\rm t0}B_{\rm eq}^2$. The numerical resolution in the x direction, N_x, is given in the last column. This is also the resolution used in the y direction, while that in the z direction is always twice as large. Our resolution is increased with increasing values of Rm, so the largest resolution used in this paper is $1024 \times 1024 \times 2048$ meshpoints.

As can be seen from the bottom panel of Figure 5, the difference between total and turbulent–diffusive fluxes is roughly constant with z, so that its divergence is small. This shows that in this particular setup the turbulent–diffusive magnetic helicity flux has actually *no* contribution in balancing the rhs of Eq. (14) to zero. This is different form the case studied by HB, in which a finite magnetic helicity flux across the equator was possible, playing thus a measurable role; see Table 1.

To characterize the magnitude of the magnetic helicity, we give its value averaged over the range $|z| \leqslant L_*$. To compare this value with that from advective magnetic helicity fluxes, we should multiply the table entry for $\boldsymbol{\nabla}\cdot\overline{\boldsymbol{\mathcal{F}}}_{\rm f}$ by L_*, which is about half the full vertical extent of the domain. Note that $\boldsymbol{\nabla}\cdot\overline{\boldsymbol{\mathcal{F}}}_{\rm f}$ and $k_1\overline{\mathcal{F}}_z^{\rm diff}$ are actually comparable, even though $\overline{\mathcal{F}}_z^{\rm diff}$ can have no effect in the present geometry and gives zero divergence.

We recall that $\overline{\boldsymbol{j}\cdot\boldsymbol{b}}$ and $\overline{\boldsymbol{a}\cdot\boldsymbol{b}}$ are approximately proportional to each other. This is also borne out by the present simulations where $k_{\rm eff}^2 \equiv \overline{\boldsymbol{j}\cdot\boldsymbol{b}}/\overline{\boldsymbol{a}\cdot\boldsymbol{b}}$ is constant and $k_{\rm eff}/k_{\rm f} \approx 2$. This confirms earlier findings of MCCTB and HB, where a similar value of $k_{\rm eff}$ was found. Under isotropic conditions, this ratio is approximately unity (Brandenburg 2001). However, for Model N3, the correlation between $\overline{\boldsymbol{j}\cdot\boldsymbol{b}}$ and $\overline{\boldsymbol{a}\cdot\boldsymbol{b}}$ is poor, giving formally a negative value, so $k_{\rm eff}$ is given as imaginary in Table 2.

The quantity $\overline{\boldsymbol{j}\cdot\boldsymbol{b}}/k_{\rm f}B_{\rm eq}^2$ is systematically below unity, suggesting that the dynamo can only be expected to produce mean fields where $\overline{\boldsymbol{B}}^2 \approx B_{\rm eq}^2$. Finally, we also give the values of the flux divergence of the mean field $\boldsymbol{\nabla}\cdot\overline{\boldsymbol{\mathcal{F}}}_{\rm m}$. These values are typically about 10 times larger than the flux divergence

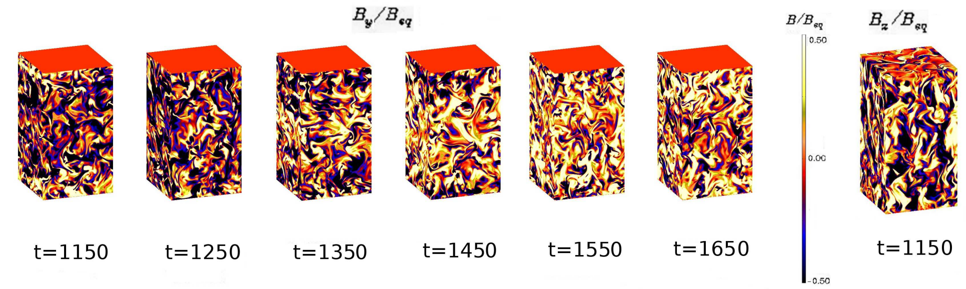

Figure 4. Visualization of B_y (left) at six different times during the evolution of the system, for Model S3. It is visible its variability, being this component of the magnetic field prevalently negative in the first snapshot and gradually turning positive in the others. Time is given in turnover times and spans over half a cycle. On the right, B_z is visualized on the borders of the domain for model S3. It does not show any relevant variability during its evolution.

Table 2. Characteristic output parameters of the simulations. Here, S_W characterizes the wind speed, $\overline{\boldsymbol{B}}_{\rm rms}$ is the rms value of the *mean* field normalized by $B_{\rm eq}$, $2\overline{\boldsymbol{\mathcal{E}}}\cdot\overline{\boldsymbol{B}}$, $2\eta\overline{\boldsymbol{j}\cdot\boldsymbol{b}}$, and $\boldsymbol{\nabla}\cdot\overline{\boldsymbol{\mathcal{F}}}_{\rm f}$ give magnetic helicity production, dissipation, and flux divergence in units of $k_{\rm f}\eta_{\rm t0}B_{\rm eq}^2$, $\overline{\mathcal{F}}_z^{\rm diff}$ is the turbulent–diffusive magnetic helicity flux in units of $\eta_{\rm t0}B_{\rm eq}^2$, characterized by the diffusion coefficient $\kappa_{\rm f}/\eta_{\rm t}$, $k_{\rm eff}$ is normalized by $k_{\rm f}$, $\overline{\boldsymbol{j}\cdot\boldsymbol{b}}$ is normalized by $k_{\rm f}B_{\rm eq}^2$, and $\boldsymbol{\nabla}\cdot\overline{\boldsymbol{\mathcal{F}}}_{\rm m}$ is the flux divergence of the mean field in units of $k_{\rm f}\eta_{\rm t0}B_{\rm eq}^2$. The strongest outflows we examine are those of Models S1, S2 and S3, in which the maximum value of the wind speed is $U_0 \approx 0.15\cdot u_{\rm rms}$. N_x indicates the number of mesh points in the x direction. (In all cases we have $N_y = N_x$ and $N_z = 2N_x$.)

Model	S_W	Rm	$\overline{\boldsymbol{B}}_{\rm rms}$	$2\overline{\boldsymbol{\mathcal{E}}}\cdot\overline{\boldsymbol{B}}$	$2\eta\overline{\boldsymbol{j}\cdot\boldsymbol{b}}$	$\boldsymbol{\nabla}\cdot\overline{\boldsymbol{\mathcal{F}}}_{\rm f}$	$\overline{\mathcal{F}}_z^{\rm diff}$	$\kappa_{\rm f}/\eta_{\rm t}$	$k_{\rm eff}$	$\overline{\boldsymbol{j}\cdot\boldsymbol{b}}$	$\boldsymbol{\nabla}\cdot\overline{\boldsymbol{\mathcal{F}}}_{\rm m}$	Ma	N_x
T1	0.0000	9	0.58	0.066	−0.069	0.004	0.007	−0.3 ± 0.7	1.22	−0.03	0.06	0.18	64
T2	0.0000	23	0.48	0.032	−0.035	0.004	0.002	−0.5 ± 0.4	1.16	−0.03	0.03	0.19	64
N1	0.0000	37	0.53	0.048	−0.047	0.001	0.004	0.1 ± 0.2	1.48	−0.07	0.05	0.15	64
N2	0.0000	81	0.58	0.023	−0.022	0.000	0.002	−0.0 ± 0.2	1.37	−0.07	0.02	0.16	128
N3	0.0000	206	0.27	0.001	−0.002	0.001	−0.003	0.0 ± 0.2	0.97i	−0.01	−0.00	0.17	256
N4	0.0000	397	0.27	0.000	−0.001	−0.000	−0.000	0.1 ± 0.2	0.84i	−0.01	−0.00	0.16	512
N5	0.0000	722	0.18	0.00	−0.01	0.01	0.017	0.1 ± 0.3	2.34	−0.16	−0.02	0.15	1024
N6	0.0054	1073	0.11	0.01	−0.01	−0.02	0.019	0.0 ± 0.3	2.83	−0.28	0.02	0.11	1024
W1	0.0020	24	0.61	0.205	−0.196	−0.008	0.013	0.4 ± 0.1	1.17	−0.19	0.19	0.10	128
W2	0.0019	51	0.42	0.094	−0.088	−0.005	0.011	0.5 ± 0.1	1.45	−0.18	0.09	0.10	128
W3	0.0019	129	0.36	0.047	−0.043	−0.004	0.010	0.4 ± 0.2	1.60	−0.23	0.05	0.10	256
M2	0.0038	51	0.36	0.090	−0.082	−0.006	0.008	0.4 ± 0.2	1.48	−0.17	0.09	0.10	128
S1	0.0060	24	0.40	0.167	−0.152	−0.012	0.019	0.8 ± 0.2	1.27	−0.15	0.16	0.10	64
S2	0.0056	51	0.31	0.085	−0.074	−0.007	0.015	0.5 ± 0.4	1.52	−0.16	0.08	0.10	128
S3	0.0055	133	0.20	0.034	−0.029	−0.005	0.007	0.6 ± 0.3	2.23	−0.16	0.03	0.11	256
S4	0.0053	271	0.17	0.023	−0.018	−0.005	0.013	0.3 ± 0.4	2.35	−0.20	0.02	0.11	512
S5	0.0053	548	0.15	0.015	−0.011	−0.005	0.012	0.1 ± 0.2	2.39	−0.25	0.02	0.11	1024
S6	0.0054	1063	0.14	0.013	−0.007	−0.006	0.010	0.1 ± 0.2	2.70	−0.32	0.01	0.11	1024
I1	0.0112	26	0.18	0.064	−0.060	−0.002	0.009	1.1 ± 1.2	2.01	−0.06	0.06	0.10	64
I2	0.0105	55	0.13	0.029	−0.027	−0.002	0.007	−0.0 ± 1.2	9.11	−0.06	0.03	0.11	128

of magnetic helicity of the small-scale field, $\boldsymbol{\nabla}\cdot\overline{\boldsymbol{\mathcal{F}}}_{\rm f}$, but it is of course only the latter that is relevant for alleviating catastrophic quenching.

All simulations with wind show that the rms value of the mean field, $\overline{\boldsymbol{B}}_{\rm rms}$, declines slowly with increasing wind speed; see Figure 6. This result might just be a consequence of a gradual increase of the critical value of Rm above which dynamo action is possible. However, it could also be an indication that a fraction of the mean magnetic field is being removed from the domain by the flow – as found in the mean-field models of Shukurov et al. (2006).

In Figure 7 we see how $\overline{\boldsymbol{B}}_{\rm rms}$ decreases with increasing Rm. The scalings $\mathrm{Rm}^{-0.4}$ and $\mathrm{Rm}^{-0.17}$ are given for orientation and show that in the presence of advection $\overline{\boldsymbol{B}}_{\rm rms}$ varies much slower than Rm^{-1}, which is the slope anticipated from catastrophic quenching models without a wind (Brandenburg & Subramanian 2005). Note, however, that DNS always gave a shallower slope (Brandenburg & Dobler 2001) and, at larger values of Rm, $\overline{\boldsymbol{B}}_{\rm rms}$ may have been already independent of Rm (Hubbard & Brandenburg 2012). Indeed, without a wind ($S_W = 0$) the Rm dependence is compatible with a steeper $\mathrm{Rm}^{-1/2}$ law, but it is less certain in this case. Looking at Figure 8, we can also see there there is no significant change of the cycle period with Rm.

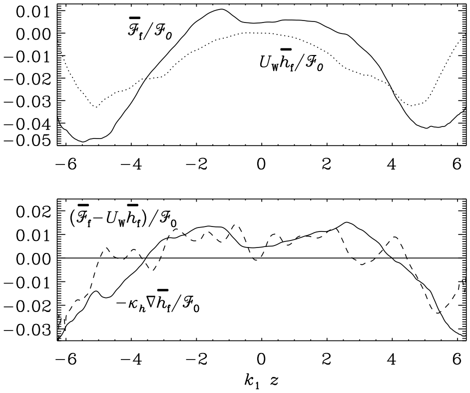

Figure 5. Contributions to the magnetic helicity flux for Model W3. Upper panel: vertical profiles of magnetic helicity fluxes of the fluctuating field (solid line), compared with the contribution from the mean flow (dashed line). Lower panel: residual between the two aforementioned fluxes (solid line) compared with a fit to the gradient of the magnetic helicity density from the small-scale field (dashed line). The fluxes are normalized by $\overline{\mathcal{F}}_0 = \eta_{t0}B_{\rm eq}^2$.

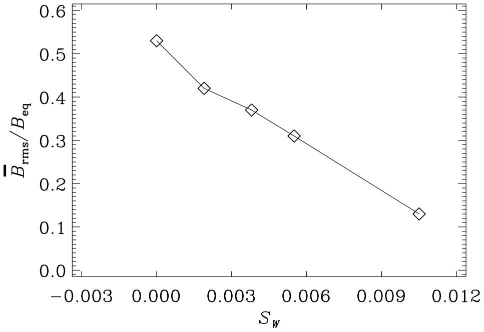

Figure 6. Root-mean-square value of the mean magnetic field, $\overline{\boldsymbol{B}}_{\rm rms}$, as function of S_W for models N3, W2, M2, S2 and I2, which have Rm ≈ 50.

The high-resolution runs with Rm = 544 and 1061 are too short to cover a magnetic cycle, but one can see that the slope of the structure, which corresponds to the speed of the dynamo wave, is approximately unchanged. In the high-Rm models the fluctuations are more pronounced, but the peak-to-peak contrast is about the same for all runs.

Table 2 shows that $2\overline{\boldsymbol{\mathcal{E}}}\cdot\overline{\boldsymbol{B}}$, $2\eta\mu_0\,\overline{\boldsymbol{j}\cdot\boldsymbol{b}}$, and $\boldsymbol{\nabla}\cdot\overline{\boldsymbol{\mathcal{F}}}_{\rm f}$ balance approximately to zero, confirming that the results represent a statistically steady state. All three quantities have approximately the same (nearly linear) z dependence for $|z| < L_*$, so that also the values of their three slopes must balance to zero, which is indeed the case. In Figure 9 we show the scaling properties of the aforementioned quantities for Models W1–W3 and S1–S6: for Rm $\lesssim$ 200 the first two quantities decrease approximately like ${\rm Rm}^{-1}$, while the latter decreases only like ${\rm Rm}^{-1/2}$, which is in agreement with the values obtained by HB; see also Figure 10 of Candelaresi et al. (2011) for a corresponding plot.

However, for Rm $\gtrsim$ 200 the scaling of $2\overline{\boldsymbol{\mathcal{E}}}\cdot\overline{\boldsymbol{B}}$ changes into an ${\rm Rm}^{-1/2}$ scaling; $\boldsymbol{\nabla}\cdot\overline{\boldsymbol{\mathcal{F}}}_{\rm f}$ is at first below $2\eta\mu_0\,\overline{\boldsymbol{j}\cdot\boldsymbol{b}}$, but for high enough Rm increases to reach an absolute value similar to that of $2\overline{\boldsymbol{\mathcal{E}}}\cdot\overline{\boldsymbol{B}}$. This suggests that the simple expec-

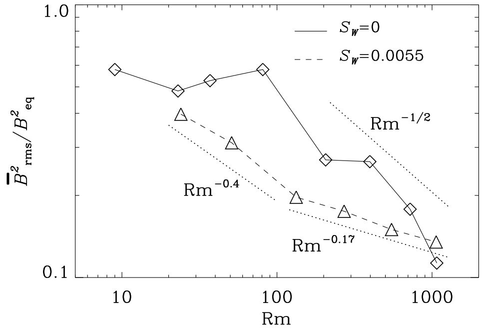

Figure 7. $\overline{\boldsymbol{B}}^2_{\rm rms}$ as a function of Rm in absence (solid line, Models T1, T2, N1–N6) and in presence (dashed line, Models S1–S6) of advective flux. The two dotted lines give the slopes −0.5, −0.4, and −0.17 for orientation.

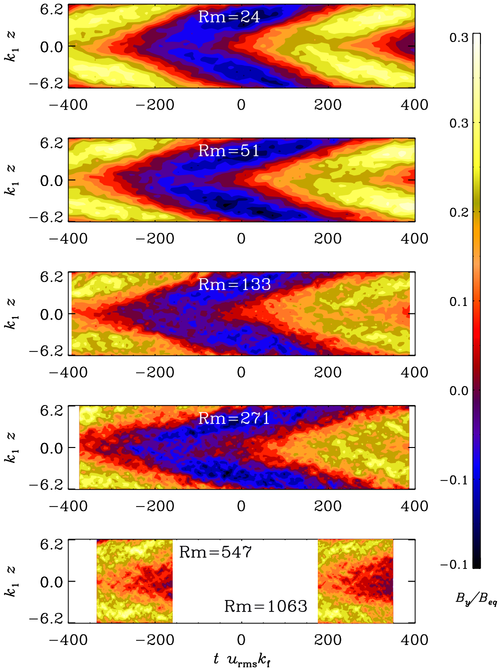

Figure 8. Space-time diagrams of $\overline{B}_y$ for wind $U_0 = 0.015c_{\rm s}$ (corresponding to $S_W \approx 0.0055$) for Models S1–S6 for different magnetic Reynolds numbers. From the top: Rm = 24, 51, 133, 271, as well as 547 (bottom left) and 1063 (bottom right).

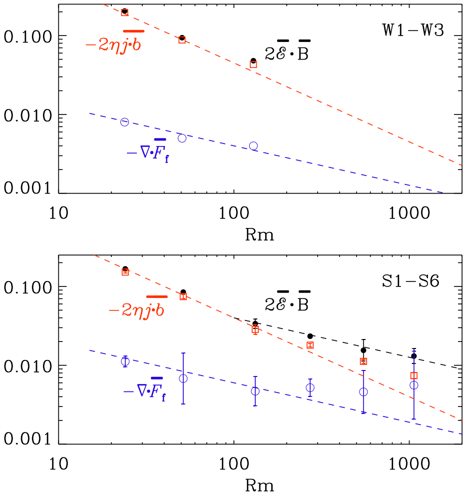

Figure 9. Scaling properties of the vertical slopes of $2\overline{\boldsymbol{\mathcal{E}}}\cdot\overline{\boldsymbol{B}}$, $-2\eta\mu_0\overline{\boldsymbol{j}\cdot\boldsymbol{b}}$, and $-\boldsymbol{\nabla}\cdot\overline{\boldsymbol{\mathcal{F}}}_{\rm f}$ for Models W1, W2 and W3 (upper panel) and for Models S1–S6 (lower panel). (Given that the three quantities vary approximately linearly with z, the three labels indicate their non-dimensional values at $k_1 z = 1$.) The second panel shows that a stronger wind decreases the value of Rm for which the contribution of the advective term becomes comparable to that of the resistive term.

tation based on the naive extrapolation given from a linear fit is misleading, and that catastrophic quenching might be alleviated already for Rm $\gtrsim$ 1000. In the absence of a wind and for large magnetic Reynolds numbers (Models N4–N6), the divergence of the magnetic helicity flux shows strong fluctuations about zero, making it harder to determine an accurate magnetic helicity balance of small-scale fields.

4 CONCLUSIONS

In the present work we have examined the effects of an advective magnetic helicity flux in DNS of a turbulent dynamo. The present simulations without shear yield an oscillatory large-scale field owing to the spatially varying kinetic helicity profile with respect to the equatorial plane. We emphasize in this context that the possibility of oscillatory dynamos of α^2 type is not new (Baryshnikova & Shukurov 1987; Rädler & Bräuer 1987), but until recently all known examples were restricted to spherical shell dynamos where α changes sign in the radial direction. The example found by Mitra et al. (2010b) applies to a spherical wedge with latitudinal variation of α changing sign about the equator. Similar results have also been obtained in a mean-field dynamo with a linear variation of $\alpha(z) \propto z$ (Brandenburg et al. 2009). Our present simulations are probably the first DNS of such a dynamo in Cartesian geometry. Closest to our simulations are those of MCCTB who used perfectly conducting outer boundary conditions without wind, and also found oscillatory solutions. Surprisingly, however, oscillation are here only obtained if there is at least a slight outflow.

One would have expected that catastrophic quenching can be alleviated if magnetic helicity is removed from the domain at a rate larger than its diffusion rate, that is, the advective term $\boldsymbol{\nabla}\cdot\overline{\boldsymbol{\mathcal{F}}}_{\rm f}$ dominates over the resistive term, $2\eta\mu_0\overline{\boldsymbol{j}\cdot\boldsymbol{b}}$. Figure 9 shows that, for Rm $\lesssim$ 200, the latter term decreases linearly with decreasing η, while the former only decreases proportional to $\eta^{1/2}$, i.e., proportional to $\mathrm{Rm}^{-1/2}$. This would have led us to the estimate that for Rm $\approx 4\cdot 10^3$ the catastrophic quenching can be alleviated by a wind with $S_W \approx 0.0055$. Our new results suggest that this can happen already for smaller values of Rm. The reason for this is still unclear. It is possible that catastrophic quenching was an artefact of intermediate values of Rm, as suggested by Hubbard & Brandenburg (2012), or that a magnetic helicity flux can have an effect even though it is weak compared with diffusive terms.

Finally, we should emphasize that we have only examined here the case of subsonic advection. In real astrophysical cases, like galactic and stellar winds, the outflow is instead supersonic and can, thus, play a decisive role in alleviating the catastrophic quenching through the advection of magnetic helicity.

ACKNOWLEDGEMENTS

FDS acknowledges HPC-EUROPA for financial support. Financial support from European Research Council under the AstroDyn Research Project 227952 is gratefully acknowledged. The computations have been carried out at the National Supercomputer Centre in Umeå and at the Center for Parallel Computers at the Royal Institute of Technology in Sweden.

REFERENCES

Baryshnikova I., Shukurov A., 1987, Astron. Nachr., 308, 89
Brandenburg A., 2001, ApJ, 550, 824
Brandenburg A., Candelaresi S., Chatterjee P., 2009, MNRAS, 398, 1414
Brandenburg A., Dobler W., 2001, A&A, 369, 329
Brandenburg A., Dobler W., Subramanian K., 2002, Astron. Nachr., 323, 99
Brandenburg A., Subramanian K., 2005, Astron. Nachr., 326, 400
Candelaresi S., Hubbard A., Brandenburg A., Mitra D., 2011, Phys. Plasmas, 18, 012903
Cattaneo F., Hughes D. W., 1996, Phys. Rev. E, 54, 4532
Chatterjee P., Guerrero G., Brandenburg A., 2011, A&A, 525, A5
Gruzinov A. V., Diamond P. H., 1994, Phys. Rev. Lett., 72, 1651
Guerrero G., Chatterjee P., Brandenburg A., 2010, MNRAS, 409, 1619
Hubbard A., Brandenburg A., 2010, Geophys. Astrophys. Fluid Dyn., 104, 577 (HB)
Hubbard A., Brandenburg A., 2011, ApJ, 727, 11
Hubbard A., Brandenburg A., 2012, ApJ, 748, 51
Käpylä P. J., Korpi M. J., Brandenburg A., 2008, A&A, 491, 353

Käpylä P. J., Korpi M. J., Brandenburg A., 2009, A&A, 500, 633
Käpylä P. J., Korpi M. J., Brandenburg A., 2010, A&A, 518, A22
Kleeorin N., Moss D., Rogachevskii I., Sokoloff D., 2000, A&A, 361, L5
Kleeorin N. I., Ruzmaikin A. A., 1982, Magnetohydrodynamics, 18, 116
Krause F., Rädler K., 1980, Mean-field magnetohydrodynamics and dynamo theory. Pergamon Press, Oxford
Mitra D., Candelaresi S., Chatterjee P., Tavakol R., Brandenburg A., 2010a, Astron. Nachr., 331, 130 (MCCTB)
Mitra D., Tavakol R., Käpylä P. J., Brandenburg A., 2010b, ApJL, 719, L1
Mitra D., Moss D., Tavakol R., Brandenburg A., 2011, A&A, 526, A138
Moffatt H. K., 1978, Magnetic field generation in electrically conducting fluids. Cambridge Univ. Press, Cambridge
Pouquet A., Frisch U., Leorat J., 1976, J. Fluid Mech., 77, 321
Rädler K.-H., Bräuer H.-J., 1987, Astron. Nachr., 308, 101
Shukurov A., Sokoloff D., Subramanian K., Brandenburg A., 2006, A&A, 448, L33
Sur S., Brandenburg A., Subramanian K., 2008, MNRAS, 385, L15
Sur S., Shukurov A., Subramanian K., 2007, MNRAS, 377, 874
Vainshtein S. I., Cattaneo F., 1992, ApJ, 393, 165
Vishniac E. T., Cho J., 2001, ApJ, 550, 752
Warnecke J., Brandenburg A., Mitra D., 2011, A&A, 534, A11